INFORMATION TO USERS

This manuscript has been reproduced from the microfilm master. UMI films the text directly from the original or copy submitted. Thus, some thesis and dissertation copies are in typewriter face, while others may be from any type of computer printer.

The quality of this reproduction is dependent upon the quality of the copy submitted. Broken or indistinct print, colored or poor quality illustrations and photographs, print bleedthrough, substandard margins, and improper alignment can adversely affect reproduction.

In the unlikely event that the author did not send UMI a complete manuscript and there are missing pages, these will be noted. Also, if unauthorized copyright material had to be removed, a note will indicate the deletion.

Oversize materials (e.g., maps, drawings, charts) are reproduced by sectioning the original, beginning at the upper left-hand corner and continuing from left to right in equal sections with small overlaps.

Photographs included in the original manuscript have been reproduced xerographically in this copy. Higher quality 6" x 9" black and white photographic prints are available for any photographs or illustrations appearing in this copy for an additional charge. Contact UMI directly to order.

ProQuest Information and Learning
300 North Zeeb Road, Ann Arbor, MI 48106-1346 USA
800-521-0600

3-D Seismic Investigations of Northern Cascadia Marine Gas Hydrates.

by

Michael Riedel
Diploma in Geophysics, University of Kiel, 1998

A Thesis submitted in Partial Fulfillment of the
Requirements for the Degree of

DOCTOR OF PHILOSOPHY

in the

SCHOOL OF EARTH AND OCEAN SCIENCE

We accept this thesis as conforming
to the required standard

Dr. R. D. Hyndman, Supervisor (School of Earth and Ocean Science)

Dr. N. R. Chapman, Co-Supervisor (School of Earth and Ocean Science)

Dr. G. D. Spence, Departmental Member (School of Earth and Ocean Science)

Dr. S. E. Dosso, Additional Member (School of Earth and Ocean Sciences)

Dr. N. Djilali, Outside Member (Department of Mechanical Engineering)

Dr. S. Holbrook, External Examiner (Department of Geology and Geophysics, University of Wyoming)

Supervisor: Dr. R. D. Hyndman

Abstract

This dissertation presents results from 3-D (parallel 2-D) high resolution seismic surveys and associated studies over an area with deep sea gas hydrate occurrence. The study area is located on the accretionary prism of the northern Cascadia subduction zone offshore Vancouver Island, Canada.

The major objectives of this study were the imaging of a gas/fluid vent field found in the study area and detailed mapping of the tectonic setting and geological controls on fluid/gas venting. Secondary objectives were the characterization of the gas hydrate occurrence and constraints on the seismic nature of the bottom-simulating reflector (BSR) and its spatial distribution.

The main grid was 40 lines at 100 m spacing with eight perpendicular crossing lines of multichannel and single channel seismic reflection, and 3.5 kHz subbottom profiler data. In addition to the main 3-D seismic grid, two smaller single channel grids (25 m spacing) were collected over the vent field. The multichannel seismic data acquired with the Canadian Ocean Acoustic Measurement System (COAMS) streamer required correction for irregular towing depth and shot point spacing. A new array element localization (AEL) technique was developed to calculate receiver depth and offset. The individual receiver depths along the COAMS streamer varied between 10–40 m, which resulted in the occurrence of a prominent receiver ghost that could not be completely removed from the seismic data. The ghost resulted in limited vertical resolution and a coarse velocity-depth function.

The vent field is characterized by several blank zones that are related to near-surface deformation and faulting. These zones are 80–400 m wide and can be traced downward through the upper 100–200 m thick slope sediment section until they are lost in the accreted sediments that lack coherent layered reflectivity. The blank zones are also characterized by high amplitude rims that are concluded to result from the interference effect of diffractions. These diffractions result due to relatively sharp discontinuities in the sediment physical properties at the blank zone boundary. 2-D vertical incidence seismic modeling suggests an increase in P-wave velocity inside of the blank zone with only minor changes in density.

Blanking is believed to be mainly the effect of increased hydrate formation within the fault planes. The faults are conduits for upward migrating fluids and methane gas that is converted into hydrate once it reaches the hydrate stability field. Carbonate formations at the seafloor can also contribute to blanking especially at higher frequencies. Free gas may be present in case of full hydrate saturation or strong fluid flow. Geochemical analyses of pore water and water-column samples carried out in cooperation with Scripps Institute of Oceanography indicate relatively low fluid fluxes of less than 1 mm/yr and there is no heat flow anomaly present over the vent field. Methane concentrations of 20 n-moles/L (about 8 times the ocean background concentration) were detected in water-column samples of the first 100–200 m above the main blank zone of the vent field. Venting is also believed to be strongly episodic with a recently more quiet time. However, the observed carbonate crusts indicate a long-term activity of the vents.

Examiners:

Dr. R. D. Hyndman, Supervisor (School of Earth and Ocean Science)

Dr. N. R. Chapman, Co-Supervisor (School of Earth and Ocean Science)

Dr. G. D. Spence, Departmental Member (School of Earth and Ocean Science)

Dr. S. E. Dosso, Additional Member(School of Earth and Ocean Science)

Dr. N. Djilali, Outside Member (Department of Mechanical Engineering)

Dr. S. Holbrook, External Examiner (Department of Geology and Geophysics,University of Wyoming)

Table of Contents

1 Introduction **2**

1.1 General Overview 2

1.2 Gas Hydrates - What are they? 4

1.2.1 Gas Hydrate Formation and Stability 5

Organic Geochemistry of the Methane Source 8

In situ Formation Model 8

Fluid-Expulsion Model 9

Free-gas Model 9

1.3 Global Distribution of Gas Hydrates 10

1.3.1 Gas Hydrates in Oceanic Environments 11

1.3.2 Gas Hydrates in Permafrost Regions 13

1.4 Why are Gas Hydrates Important? 13

1.4.1 Gas Hydrates as a Potential Energy Resource 13

1.4.2 Gas Hydrates and Climate Change 14

Global Warming 14

Global Cooling 15

1.4.3 Gas Hydrate as Geologic Hazard 16

1.5 Field Survey and Downhole Evidence for Gas Hydrate 18

2 Previous Gas Hydrate Studies Offshore Vancouver Island **20**

2.1 General Tectonic Setting 20

2.1.1 Tectonic Interpretation Near ODP Site 23

2.2 Previous Geophysical Studies 24

2.2.1 The BSR: Distribution and Reflection Pattern 26

2.2.2 Seismic Velocities and Hydrate Concentration 28
2.2.3 Amplitude-Versus-Offset Studies and Full Wave Form Inversion 30
2.3 Fluid Venting and Carbonate Pavement 32

3 The COAMS-99 Experiment **34**
3.1 3-D Seismic Survey Design 34
3.2 Seismic Data Sets Acquired 38
3.3 Seismic Systems 39
3.3.1 Seismic Source 41
3.3.2 COAMS Multichannel Streamer 43
3.3.3 Teledyne Single Channel Streamer 49
3.3.4 3.5 kHz Subbottom Profiler 50
3.3.5 12 kHz Echosounder 50
3.3.6 Navigation 50
3.3.7 DTAGS 52

4 COAMS Multichannel Seismic Data Processing **54**
4.1 Introduction 54
4.2 Pre-processing 55
4.2.1 Array Element Localization (AEL) 55
4.2.2 Geometry Definition 60
4.3 The Problem of the Ghost 60
4.4 Multichannel Processing Scheme 62
4.4.1 Processing in Shot-gather Domain 62
4.4.2 Processing in CMP Domain 63
4.4.3 Velocity Analysis 67
Velocity Error Estimation 69
4.4.4 Interval Velocities and Hydrate Concentration 73

4.4.5 Stacking 75
4.5 Post-stack Processing 76
4.5.1 Crossline Static 76
4.5.2 2-D Migration 76
4.5.3 Ghost-removal 77
4.6 2.5-D Migration 80
4.7 3-D Binning Procedure 83
4.8 Single Channel Processing for the Teledyne Array 83

5 Regional Seismic Analyses **85**
5.1 Introduction 85
5.1.1 Methodology of Reflection Coefficient Calculations 86
5.2 COAMS-99 studies 88
5.2.1 Bathymetry 88
5.2.2 Seafloor Reflection Coefficients 90
5.2.3 Area With High Reflection Coefficients 93
What Causes the Frequency Dependent Reflection Coefficients? 95
Carbonate Pavement, Erosion or Sand Layers? 98
Conclusion 102
5.2.4 Boundary Between Accreted and Slope Sediments 103
ODP Results and Seismostratigraphy 104
Results From COAMS-99 107
5.3 Combination With Regional Seismic Studies SC-93 and MC-96 116
5.3.1 Combined Bathymetry and Seafloor Reflection Coefficients . . 116
5.3.2 Boundary Between Accreted and Slope Sediments 119
5.4 COAMS-99 BSR Studies 121
5.4.1 Distribution 121
5.4.2 BSR Vertical Incidence Reflection Coefficient 124

5.4.3 Heat Flow Derived From BSR Depth 127
Methodology of Heat Flow Calculations 128
5.4.4 Heat Flow Pattern 130

6 Seismic Blank Zones - Active Cold-Vents? 136

6.1 Introduction 136
6.2 Seismic Observations at the Vent Field 138
6.2.1 12 kHz Echosounder 138
6.2.2 Parasound (4 kHz) and 3.5 kHz Subbottom Profiler 140
6.2.3 DTAGS 143
6.2.4 COAMS 144
6.2.5 Teledyne Single Channel Data 148
3-D Analysis of the 1999 SC Data 150
3-D Analysis of the 2000 SC Data 152
6.3 Frequency Dependence of Amplitude Reduction 157
6.4 Piston Coring at Blank Zones 1 and 4 160
6.4.1 Hydrate Recovery 162
6.5 Carbonates Occurrences 163
6.6 Heat Flow 167
6.7 Geochemistry From Piston Cores 171
6.8 Other Fault-Related Blanking 173
6.9 Evidence of Wide-Spread Venting Associated With Thrust Faults . . 179
6.9.1 Introduction 179
6.9.2 Seismic Observations 180
6.9.3 ROPOS Observations 183
6.10 Amplitude-Versus-Offset (AVO) Analyses 185
6.10.1 Elastic 1-D Inversion 188
6.10.2 2-D Viscoelastic Modeling 189

6.11 Seismic Modeling of Blanking and High Amplitude Rim 191
6.11.1 Amplitude Variations in MC and SC Airgun Seismic Data . . 192
6.11.2 1-D AVO Model 196
6.11.3 Surface Carbonates 197
6.11.4 Hydrate Formation 199
6.11.5 Conclusions From Seismic Modeling 204
6.12 Possible Mechanisms of Blanking 206
6.12.1 Free Gas Model 206
6.12.2 Porosity Increase Model 208
6.12.3 Fluid Migration and Mud Volcanos 208
6.12.4 Surface Transmission Loss Model 209
6.12.5 Hydrate Formation Model 210
6.13 Tectonic Interpretation of the Vent Field Blank Zones 212

7 Modeling of Elastic Properties of Hydrate-bearing Sediments and Amplitude-Versus-Offset (AVO) Modeling 217

7.1 Introduction 217
7.2 Marine Sediments and Gas Hydrate Formation 220
7.2.1 Elastic Properties of Sediments at ODP Site 889/890 220
7.2.2 Reference-Profile for P- and S-wave velocities 221
7.2.3 Hydrate Formation in the Pore Space 222
7.2.4 Hydrate Formation as Part of the Sediment Frame 222
7.2.5 Hydrate Formation as Grain Cement 225
7.3 General AVO and Crossplotting Theory 228
7.3.1 Shuey-Approximation and Intercept-Gradient Crossplotting . 228
7.4 AVO Modeling 230
7.4.1 Hydrate Replacement in Marine Sediments 230
7.4.2 Results From Line 89-08 and 89-10 233

7.4.3 BSR AVO-response 236
BSR Crossplots: Hydrate, Gas and Cementation Vector 237
7.4.4 Data Examples 241
7.5 Frequency Dependent Reflection Coefficients and AVO Tuning 242

8 Summary and Conclusions **247**
8.1 Fluid Venting - Cold Vents and Blank Zones 247
8.2 Estimating Hydrate Concentrations and BSR AVO Modeling 249

References **251**

Appendix A Array Element Localization - Theory **262**

Appendix B Geometry Definition in ITA/Insight **269**

Appendix C ITA-Insight Programs for Seismic Data Processing **272**

Appendix D Fast Phase-shift Migration in ITA **276**

Appendix E Modeling Elastic Properties of Hydrate-bearing Sediments **278**
E.1 The Baseline Model for Water-saturated Sediments 278
E.2 Hydrate Formation in the Pore Fluid 280
E.3 Hydrate Formation in the Frame 281
E.4 Sediments With Free Gas 281
E.5 Cementation Model by Dvorkin and Nur (1993) 282

Appendix F List of Abbreviations **284**

List of Tables

3.1 Seismic data sets acquired in 1999 and 2000. 39

3.2 Bias of depth sensors. 43

3.3 Position of sheet lead added to the COAMS array. 47

3.4 Color code used for echo strength representation of the Simrad EA-500 12 kHz echosounder. 52

5.1 Parameter values for modeling a negative impedance-contrast effect. . 95

5.2 Computed ratios of frequency dependent reflection amplitude to normal reflectivity without second layer. 98

6.1 Isotopic composition ($\delta^{18}O_{PDB}$ and $\delta^{13}C_{PDB}$) of carbonate rocks sampled at blank zone 1. 166

6.2 Measured heat flow values, bottom water temperatures and thermal conductivities. 170

6.3 Range limits for elastic AVO inversion. 188

6.4 Elastic 1-D AVO inversion results inside and outside blank zone. . . . 189

6.5 Modeling parameters for the Carbonate pavement. 199

6.6 Modeling parameters for the hydrate fill model. 204

7.1 Elastic properties of sediment solid phase components and pore fluid. 221

B.1 Header words updated in geometry definition. 271

List of Figures

1.1 Gas hydrate structure I. 4
1.2 Stability region for marine gas hydrates. 6
1.3 The P/T phase diagram for methane hydrate stability field. 7
1.4 Illustration of fluid expulsion model. 10
1.5 Map showing world-wide locations of known and inferred gas hydrate occurrences. 11
1.6 Map showing area of gas hydrate occurrence on the Northern Cascadia Margin. 12
1.7 Diagram illustrating the effect of global warming on polar gas hydrate deposits. 16
1.8 Diagram illustrating the effect of P/T changes on submarine gas hydrates and the resulting sea floor failures and gas release. 18

2.1 General plate tectonic setting and bathymetry of the Cascadia subduction zone. 21
2.2 Detailed multibeam bathymetry around ODP Site 889/890. 22
2.3 Part of migrated seismic line 89-08 showing westward dipping thrust fault. 24
2.4 Location of detailed seismic surveys around ODP Leg 146. 25
2.5 Frequency dependent BSR vertical incidence reflection coefficients. . . 27
2.6 Seismic interval velocities, downhole sonic logs and reference velocity-depth profile at OPD Site 889/890. 29
2.7 Hydrate concentrations at ODP Sites 889/890. 29
2.8 AVO modeling of BSR from Yuan *et al.* 1999. 31
2.9 Final full-waveform inversion result from Yuan *et al.*, 1999. 32

3.1 Track lines for main 3-D grid. 35
3.2 Single channel seismic track lines around vent field (Teledyne 1999 and 2000). 36
3.3 Derivation of the threshold frequency for spatial aliasing. 38
3.4 Summary of field data geometry. 40
3.5 Source signature and frequency spectrum. 42
3.6 Nominal geometry of the COAMS array. 44
3.7 Directivity pattern of the COAMS front array with 5 hydrophones per group. 45
3.8 Directivity pattern of the COAMS far offset array with 10 hydrophones per group. 46
3.9 Analysis of compass reading of COAMS inline 17. 48
3.10 Source wavelet of the 3.5 kHz subbottom profiler and corresponding power-spectrum. 51

4.1 Geometry of the AEL inverse problem. 56
4.2 Simplified sound velocity profile and representative direct and reflected ray paths. 57
4.3 Reflected ray offset x and travel time t as a function of ray parameter p. 58
4.4 Inverted hydrophone group positions using the AEL algorithm. 59
4.5 Example of a shot gather. 61
4.6 Comparison of unprocessed and processed shot gather with AEL applied. 64
4.7 Comparison of unprocessed and processed amplitude spectrum. . . . 65
4.8 Comparison of unprocessed and processed auto correlations. 65
4.9 Comparison of a CMP before and after applying trim statics. 66
4.10 Semblance on SCMP without and with τ–p filter and AGC applied. . 68
4.11 Comparison of seismic velocity spectra. 69
4.12 Section of stacked COAMS inline 27 with *rms* and interval velocities. 71

4.13 SCMP gathers and corresponding velocity spectra and semblance plots to investigate error in velocity estimation. 72
4.14 Corresponding NMO corrected SCMP gathers. 73
4.15 Comparison of interval velocities derived from MC-89, DTAGS, and COAMS inline 40. 74
4.16 Stacked section of inline 27. 78
4.17 Migrated section of COAMS inline 27 without post-stack deconvolution. 79
4.18 Migrated section of COAMS inline 27 with post-stack deconvolution applied. 81
4.19 2.5-D migration results from COAMS crossline 205 and 615. 82

5.1 Color-coded bathymetry defined from COAMS 3-D seismic data. . . . 89
5.2 Seafloor reflection coefficients defined from COAMS migrated zero-offset sections. 91
5.3 Seafloor reflection coefficient defined from COAMS migrated zero-offset sections and bathymetry overlay. 92
5.4 3-D perspective view of the step in seafloor topography associated with a trace of high reflection coefficients. 94
5.5 Comparison of reflection coefficients and migrated seismic section of COAMS inline 27. 96
5.6 Comparison of reflection coefficients and migrated seismic section of COAMS inline 30. 97
5.7 3.5 kHz subbottom profiler seismic section from inline 27. 99
5.8 Detailed section of 3.5 kHz seismic section of inline 27 at area with high reflection coefficients. 100
5.9 Detailed section of 3.5 kHz seismic section of inline 30 at area with high reflection coefficients. 101
5.10 Detail of migrated line 89-08 in vicinity to ODP site 889. 105

5.11 Seismostratigraphy and interpretation from ODP Site 889A. 106
5.12 Seismic amplitude and envelope section of COAMS inline 40. 108
5.13 Seismic amplitude and envelope section of COAMS line XL-06. 109
5.14 Large scale tectonic interpretation of the area around ODP Site 889/890. 110
5.15 Section of seismic amplitude and envelope from COAMS inline 15. . . 111
5.16 Color-coded map of the depth of the boundary between accreted and slope sediments. 112
5.17 Timeslices of seismic and envelope from the COAMS 3-D cube. 113
5.18 Combined bathymetry and seafloor reflection coefficients from all regional grids in area around ODP Site 889/890. 118
5.19 Combined topography of the boundary between accreted and slope sediments. 120
5.20 Part of COAMS line XL-01 showing a well developed BSR in slope basin sediments. 122
5.21 BSR distribution around ODP Site 889A. 123
5.22 BSR reflection coefficients from COAMS data around ODP Site 889A. 125
5.23 Map with interpolated and smoothed BSR topography. 131
5.24 Heat flow and depth of BSR determined from interpolated BSR. . . . 132
5.25 Calculated heat flow values and seismic sections of COAMS inline 02. 133
5.26 Heat flow from BSR depth estimates and from in situ measurements along COAMS line XL-06. 134
5.27 Simplified heat flow responses. 135

6.1 Part of 12 kHz echosounder recording from inline 27. 139
6.2 12 kHz echosounder recording from inline 14 of the July 2000 3-D grid. 140
6.3 Parasound recording from inline 27. 141
6.4 Parasound recording across the center of blank zone 1. 142
6.5 3.5 kHz recording across the vent field. 143

6.6 DTAGS line BC-03. 144
6.7 COAMS inline 27 and xline 07. 145
6.8 Example of two NMO corrected SCMP gathers. 147
6.9 Examples of unmigrated single channel seismic data. 149
6.10 Linedrawing of blank zones from Teledyne line SC-18. 150
6.11 3-D analysis of 1999 single channel seismic data. 151
6.12 Crosslines from the 2000 single channel seismic data showing hydrate cap. 153
6.13 Slices of instantaneous amplitude from unprocessed 2000 3-D data. . 154
6.14 Seafloor reflection coefficient around blank zone 1 with core locations. 155
6.15 3-D analysis of 2000 single channel seismic data. 157
6.16 3-D perspective view of blank zone 1 from July 2000 3-D seismic data. 158
6.17 Frequency dependent amplitude reduction. 160
6.18 Location of core sites around blank zone 1 and 4. 161
6.19 Hydrate samples recovered from piston cores. 163
6.20 Examples of carbonate formations around blank zone 1 and 3. 164
6.21 Examples of the observed active part of the vent (blank zone 1). . . . 166
6.22 Heat flow profile across the vent field. 168
6.23 Heat flow measurements (in mW/m^2) at core positions at blank zone 1 and 4. 169
6.24 Extrapolated depth of no sulphate and corresponding methane and fluid fluxes. 172
6.25 Methane concentration in the water column above core site C-4. . . . 173
6.26 Blank zone from COAMS inline 5 at the SW flank of the western main ridge of accreted sediment. 174
6.27 Part of COAMS inline 27 showing fault associated amplitude reduction. 176
6.28 Timeslice of instantaneous amplitude at 1.89 s TWT showing fault traces. 177

6.29 Example of small faults with reduced seismic amplitudes. 178
6.30 Detailed view of the swath bathymetry around mound structure (Cucumber Ridge). 179
6.31 Migrated multichannel COAMS line XL-01. 180
6.32 3.5 kHz record of ridge structure. 181
6.33 Detailed view of 12 kHz profile recorded during ROPOS dive 585. . . 182
6.34 Images from bottom-video observation over the ridge structure. . . . 184
6.35 Amplitude versus offset (AVO) analysis of COAMS data around blank zone 2. 187
6.36 Observed amplitude variation over the vent field from COAMS data. 193
6.37 Detailed view of amplitude variations the blank zones. 194
6.38 Observed amplitude variation over the vent field from single channel seismic data. 195
6.39 Modeling results for the 1-D AVO model. 197
6.40 Synthetic seismograms for the 1-D AVO Model. 198
6.41 Modeling results for the carbonate pavement model. 200
6.42 Synthetic seismograms for the carbonate pavement model. 201
6.43 Modeling results for the hydrate-fill model. 202
6.44 Synthetic seismograms for the hydrate fill model. 203
6.45 Simplified model of the blank zones. 214

7.1 Modeling results of P-wave velocity for the 'hydrate in pore-space' model.223
7.2 Modeling results of P-wave velocity for the 'hydrate in frame' model. 224
7.3 Modeling results of S-wave velocity for the 'hydrate in frame' model.. 226
7.4 Modeling results of P-wave velocity using the cementation model for a pure quartz sand of 40 % porosity. 227
7.5 Modeling results of S-wave velocity using the cementation model for a pure quartz sand of 40 % porosity. 227

7.6 Crossplot of Intercept and Gradient for the *hydrate-in-frame* and cementation model for a two-layer system. 231
7.7 Crossplot of Intercept and Gradient for the *hydrate-in-pore-space* model for a two-layer system. 232
7.8 AVO trend of the four layers from seismic line 89-08 in the deep sea basin. 233
7.9 Crossplot of non-calibrated Intercept and Gradient of four layers in the deep sea basin. 234
7.10 AVO trend of two (hydrate-bearing) layers from seismic line 89-10. . . 235
7.11 Crossplot of non-calibrated Intercept and Gradient of two (hydrate-bearing) layers of line 89-10. 236
7.12 Crossplot of Intercept and Gradient for a BSR by using the *hydrate-in-frame* and *hydrate-in-pore* model. 238
7.13 Crossplot of Intercept and Gradient for a BSR by using the *hydrate-in-frame* model and two scenarios for additional cementation. 239
7.14 Simplified effects of increasing hydrate and gas concentrations plus cementation effects on a BSR Intercept-Gradient Crossplot. 240
7.15 Example of extracted intercept and gradients from MC line 89-10 and COAMS. 241
7.16 Four examples of the AVO trend of a BSR in COAMS data. 242
7.17 Frequency dependent intercept-gradient crossplot for a BSR gradient layer. 245

Acknowledgments

First, I would like to thank my supervisors Roy Hyndman and Ross Chapman for their support during the thesis and many helpful discussions. I also would like to thank my committe members George Spence, Stan Dosso and Nedjib Djilali for their support and suggestions during the thesis. I especially enjoyed to work with George and Ross at sea during exciting cruises onboard CCGS JP Tully. At this point I would also like to thank the crew on CCGS JP Tully for their support during the different surveys.

I wish to thank all technicians, here especially Bob Macdonald. I also want to acknowledge all other people being involved in helping to make the COAMS-99 survey a successful cruise: Ivan Frydecky, Brian Nichols, Bob Chappel and Bill Hill.

I want to thank the University of Victoria for financial support by the University fellowship and graduate teaching fellowships. The seismic work carried out would be impossible without state of the art seismic processing software. Many thanks to Seismic Micro Technology for donating the *Kingdom-Suite*-package to the seismology group and many thanks to DigiRule for donating the software *OUTRIDER*.

This is also the point to remember my friends in the seismology lab for interesting scientific and philosophical discussions, social lunches, and lots of coffee: here first of all Kumar, Ruben, Ivana and especially Samantha (and of course the entire E-Hut crew).

At the end of this long list I want to thank my parents and my brother for their support and patience with me being so far away from home. Without them this work would have never been possible.

Ich möchte mich an dieser Stelle ganz herzlich bei meinen Eltern und meinem Bruder für ihre Unterstützung bedanken. Ohne diese Hilfe wäre meine Arbeit nie zustande gekommen. Vielen Dank für Alles während meiner gesamten Studienzeit von den ersten Schritten in Clausthal über Kiel bis schliesslich nach Victoria in Kanada.

Chapter 1

Introduction

1.1 General Overview

This dissertation presents results from 3-D (parallel 2-D) high resolution multichannel seismic surveys and associated studies over an area with deep sea gas hydrate occurrence. The study area is located on the accretionary prism of the northern Cascadia subduction zone offshore Vancouver Island, Canada. The area of investigation has been the focus of many detailed studies, especially 2-D multichannel seismic (MCS), regional widely-spaced single channel seismic (SCS) surveys and scientific ocean drilling (Ocean Drilling Program (ODP) Leg 146, Site 889/890).

The major objectives of this study were:

1. the imaging of a gas/fluid vent field found in the study area,
2. mapping of the detailed tectonic setting and geological controls on fluid venting,
3. characterization of the gas hydrate occurrence, and
4. further constraints on the seismic nature of the bottom-simulating reflector (BSR) and its spatial distribution.

The 3-D survey performed in August 1999 was carried out with a single 40 in^3 (0.65 l) sleeve gun as primary seismic source and the Canadian Ocean Acoustic Measurement System (COAMS) multichannel streamer. On a total of 40 lines at 100 m spacing of the main grid and eight additional lines crossing the main grid perpendicular, multichannel and single channel seismic reflection and 3.5 kHz subbottom profiler data were collected. In addition to the main 3-D seismic grid, two smaller

single channel grids (25 m spacing) were collected over a vent field characterized by several blank zones. The two single channel 3-D data sets provide a high resolution image of the seismic structures of the vent field. Based on the results from the 3-D seismic analyses, a piston coring program was carried out at the vent field in July 2000 providing information about the physical properties and chemical state of the shallow sediments. The coring was complemented by video observations and seafloor sampling in September 2000 and May 2001 using the unmanned submersible ROPOS. These data sets provide ground truth for the seismic data and give detailed insight into the mechanism of fluid/gas venting.

The first chapter of this thesis will give a general background introduction to gas hydrate research followed by chapter 2 with a detailed review of the geophysical studies carried out so far in the area around the ODP Site 889/890. The 3-D seismic survey and data acquisition is described in chapter 3 followed by a detailed outline of the seismic processing carried out in chapter 4. Results from regional seismic analyses are described in chapter 5 including (a) reflection coefficient studies of the seafloor and BSR, (b) seismostratigraphic characterization of the sediments and tectonic interpretation, and (c) heat flow estimates from BSR-depth variations. Chapter 6 discusses the seismic character of the vent field and other fault-related blank zones. In this chapter a summary of preliminary results from the physical properties and geochemical analyses and heat flow measurements is given. Also first results from the video-observation and bottom sampling surveys with ROPOS are shown. Chapter 7 discusses the use of rock-physics models to calculate elastic properties of hydrate-bearing sediments. The models are used to carry out a comprehensive AVO study of the BSR, including the effect of frequency dependent AVO tuning.

1.2 Gas Hydrates - What are they?

Gas hydrate is a naturally occurring solid comprised of a three-dimensional lattice framework structure of water ice with open cages, into which various gas molecules can fit (Figure 1.1). Gas hydrate will form usually with about 90% of the cages filled giving a volume ratio of methane gas to solid hydrate of about 160:1 (Hunt, 1979). The first scientific observation of hydrates was done by Davy (1811), reporting the formation of a 'yellow precipitate' as a result of chlorine gas bubbling through water. In the 1930's gas hydrates became a problem in the oil and gas industry blocking gas pipelines in colder regions. The first clear evidence of natural marine gas hydrates was found over the Blake Outer Ridge off the south east of the United States of America by Markl *et al.* (1970).

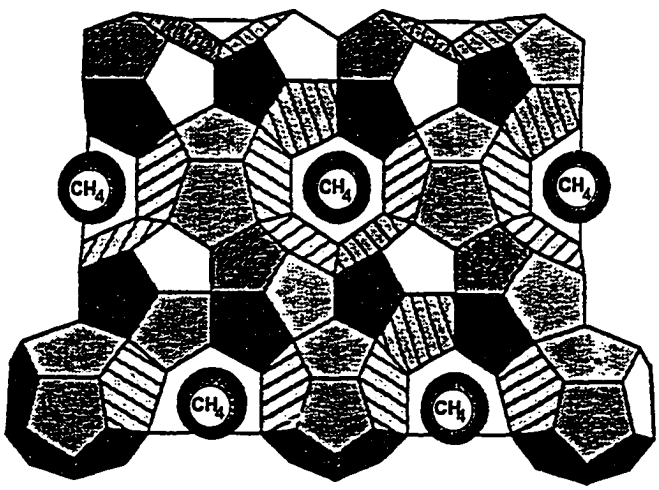

Figure 1.1 Gas hydrate structure I. Each methane molecule is trapped in rigid cages of water molecules. The structure is stable if about 90% of cages are filled (from Kvenvolden, 1993).

1.2.1 Gas Hydrate Formation and Stability

Thermodynamic conditions for the stability of gas hydrate are strongly dependent on the size and shape of the gas component. The gas molecules must be small enough to fit into the cavities of the lattice framework, but large enough to give stability to the overall structure. Three gas hydrate structures are known to occur in natural environments: structures I, II and H. Structure I is the most common form where methane is the main hydrate-forming gas. Structures II and H have been reported when larger gas molecules are included from thermogenic gas produced at greater depth, for example in the Gulf of Mexico (Sassen and MacDonald, 1994; Brooks, 1986).

Provided sufficient methane concentrations are present, the stability of hydrate is primarily controlled by temperature and pressure as illustrated in Figure 1.2. The region where hydrate is stable is defined by the intersection of the phase boundary with the local temperature profile. Thus hydrate is not stable in shallow waters nor at greater depths exceeding about 2.5 km. A detailed view of the phase diagram for gas hydrates is illustrated in Figure 1.3. Hydrate typically forms if the concentration of methane exceeds the critical concentration close to the local solubility threshold. If the concentration of methane falls below the critical concentration, hydrate dissociates until the equilibrium methane concentration is reached in the fluid. Second order controls on hydrate stability include the concentration of gases other than methane, the salinity of the pore water and the composition of the host sediment (e.g. Clennell *et al.*, 1999).

Xu and Ruppel (1999) formulated an analytical model to predict the occurrence, distribution and evolution of methane gas hydrate in porous marine sediments. From their model it can be seen that the base of the zone in which gas hydrate actually occurs will not usually coincide with the base of hydrate stability and can lie substantially shallower than the base of the stability zone. If the bottom-simulating reflector

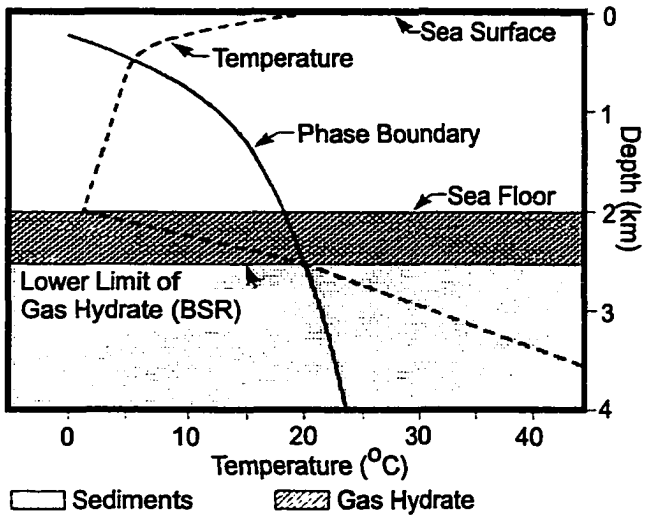

Figure 1.2 Stability region for marine gas hydrates. The phase boundary is indicated by the heavy line. A simplified temperature profile is shown as dashed line. The field of hydrate stability is defined by the intersection of the temperature profile with the phase boundary. In this example hydrates are stable between 500 m and 2500 m (from Dillon and Max, 2000).

(BSR) marks the top of the free gas zone, then the BSR should occur substantially deeper than the base of the stability zone. But if the BSR marks the base of the methane hydrate bearing layer, then the BSR may occur within the methane hydrate stability zone. The BSR could therefore occur at pressure and temperature conditions lower than those at the base of the methane hydrate stability zone.

The occurrence of methane hydrates and their concentration is affected by the amount of fluid flux in the general region of methane hydrate stability. Diffusive end-member gas hydrate systems are characterized by a thin layer of gas hydrate located near the base of the stability zone. Advective end-member systems have thicker layers of gas hydrate and, for high flux rates, greater concentrations near the base of the

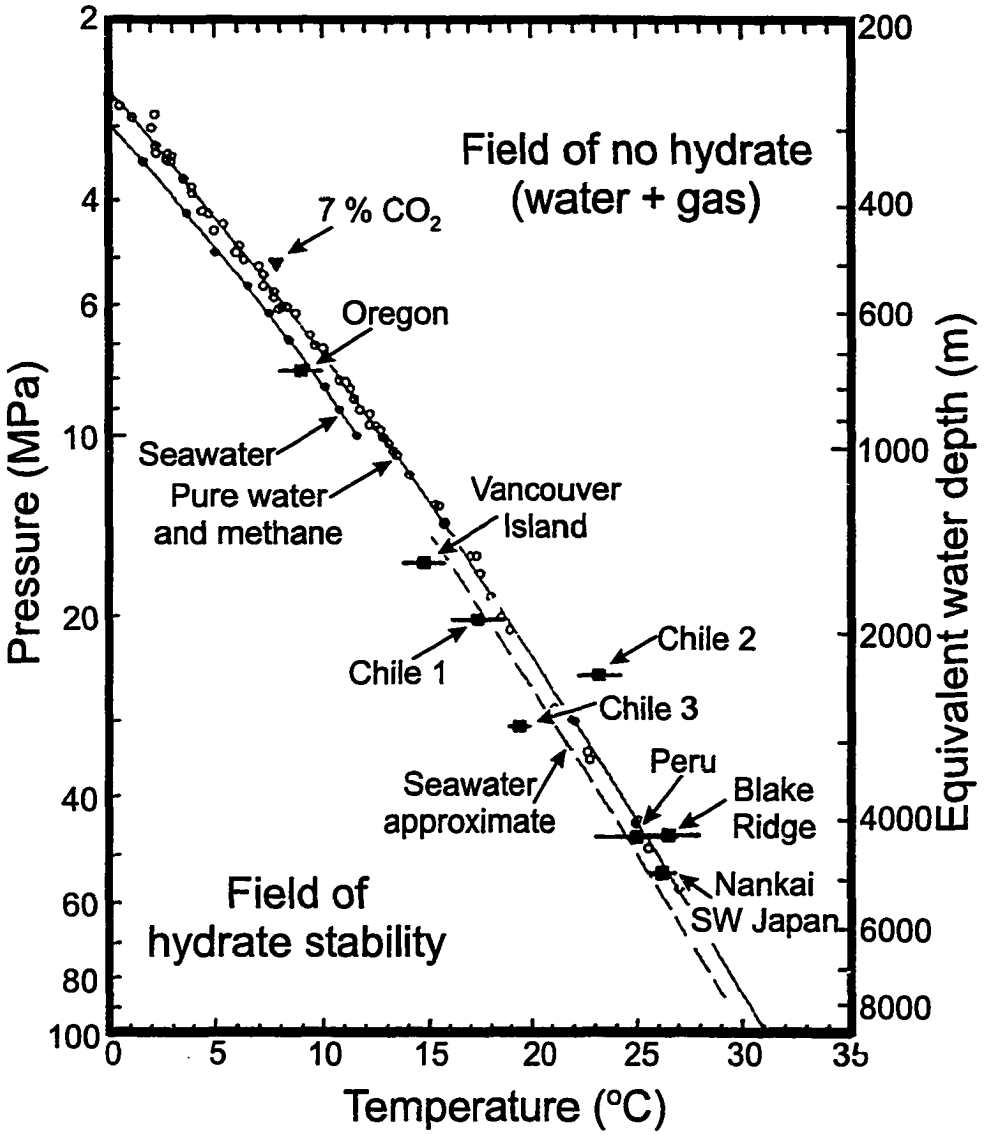

Figure 1.3 The pressure-temperature phase diagram for methane hydrate stability field. The solid line (seawater curve) is from the equation-of-state computation by Englezos and Bishnoi (1988) and Dickens and Quinby-Hunt (1994). Estimates of in situ P-T conditions at the base of hydrate stability field measured at DSDP/ODP sites (solid squares) agree with the laboratory data (after Hyndman *et al.* 1994.)

hydrate bearing layer than shallower in the sediments (Xu and Ruppel, 1999).

Organic Geochemistry of the Methane Source

The isotopic composition of methane recovered from most deep sea hydrate samples is consistent with that for gases produced from low temperature biological processes. The $\delta^{13}C$ value of biogenic methane is usually lighter than $-60°/_{oo}$ relative to the PDB standard (Claypool and Kvenvolden, 1983). If the hydrocarbon gases are produced by thermal conversion of organic matter, the isotopic signature is relatively heavy. Also generally more ethane and propane are generated. Fractionation, i.e. a trend to incorporate the lighter gas, may occur during hydrate formation, but is generally not sufficient to explain the high $\delta^{13}C$ observations (Thiery *et al.*, 1998). Thus the majority of gas hydrates near the Earth's surface is probably the result of biogenic conversion of organic matter into methane gas.

In situ Formation Model

Paull *et al.* (1994) postulated a hydrate-formation model based on hydrate production from in situ local organic carbon. Microbial methane production occurs below the depth of sulphate reduction and if methane saturation is reached, additional methane production results in the generation of either gas hydrate or free gas, depending on the temperature and pressure conditions present. However, this model does not explain the high concentrations of hydrate accumulations observed in some areas, such as offshore Vancouver Island, that have low sediment organic carbon content.

Sediments at the Blake-Bahama Ridge contain 1–1.5% organic carbon (Kvenvolden and Barnard, 1983) with a fraction available for methanogenesis of about 50% (Paull *et al.*, 1994). Using in situ organic carbon as the only source, gas concentration exceeds the solubility by only a factor of 3. This supply of methane gas is insufficient

to fill more than a few percent of the pore volume with hydrate. The hydrate concentrations at the Blake-Bahama Ridge are only a few percent, thus the model by Paull *et al.* (1994) might be applicable for the Blake Ridge. But the larger observed hydrate accumulations for the Cascadia Margin require a larger influx of methane into the stability zone for hydrate formation because only 0.5% organic carbon is contained in the sediments.

Fluid-Expulsion Model

The problem of the source of high methane concentrations is resolved by the fluid-expulsion model proposed by Hyndman and Davis (1992), which involves methane migration into the stability zone by an upward fluid flow from greater depth (Figure 1.4). In this model, most of the methane is produced biogenically at greater depth below the level of hydrate stability. As the methane-rich (but probably still unsaturated) fluids are carried upward by fluid expulsion, methane is removed from the fluids to form hydrate. The hydrate zone builds gradually upward from the base of the stability field forming a sharp discontinuity at the bottom and a gradational top. This models explains the source for large quantities of methane to form the observed amounts of hydrate and predicts that the largest concentrations of hydrate are located just above the base of the stability field.

Free-gas Model

A third model was proposed by Minshull *et al.* (1994) who suggested the formation of hydrate by upward migration of free methane gas bubbles. It was argued that this mechanism is consistent with gas concentrations seen over structural highs offshore Columbia. Gas bubbles may travel some distance into the hydrate stability field before hydrate is nucleated. Once the first hydrate is formed it may build downward as more gas migrates upward. Evidence that free gas migration does occur through the hydrate stability zone comes from hydrates recovered in piston cores in the Gulf

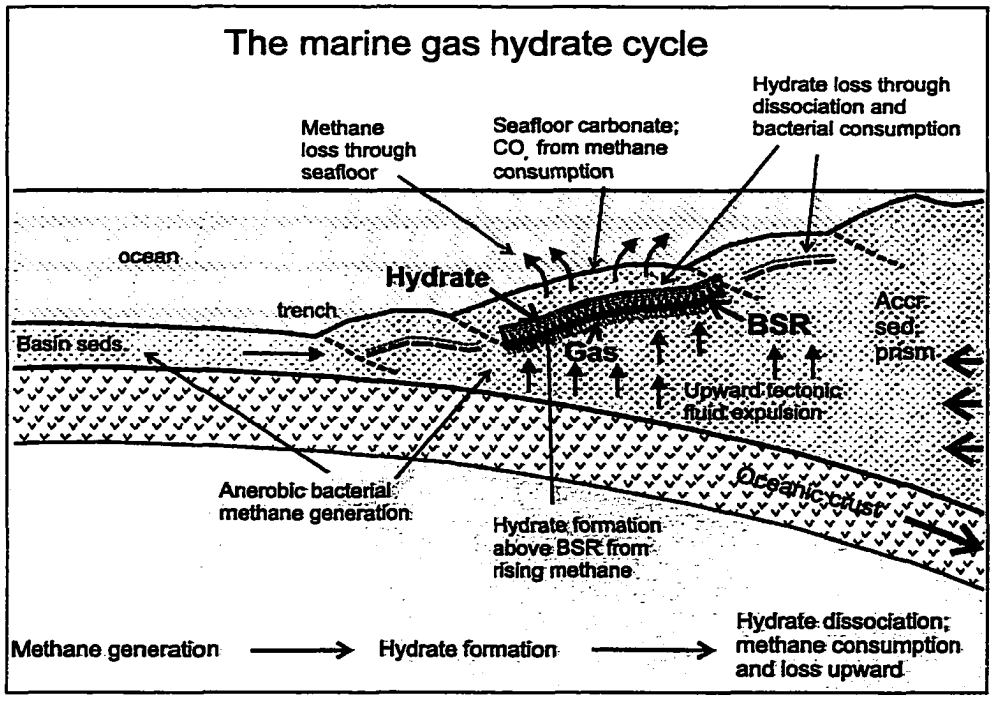

Figure 1.4 Illustration of fluid expulsion model (after Hyndman *et al.*, 2001).

of Mexico (Brooks *et al.*, 1984). However, this model seems not very likely to be applicable for most widespread hydrate occurrences since gas in the vapor phase is thermodynamically strongly unstable in the hydrate stability zone (e.g. Buffett, 1999).

1.3 Global Distribution of Gas Hydrates

Natural gas hydrates occur worldwide but due to the nature of the hydrate stability field, hydrate is mainly found in marine sediments on continental margins and in polar regions (Figure 1.5). In polar regions, gas hydrate is normally found where there is permafrost both onshore in continental sediments, and offshore on polar continental shelves. Samples of gas hydrate have been recovered on land in the western

Prudhoe Bay oil field in Alaska (Collett, 1993) and in the MacKenzie Delta of Canada (Dallimore *et al.*, 1999). Thus far, gas hydrate has been recovered at about 30 oceanic locations (e.g. Kvenvolden *et al.*, 1993; Ginsburg and Soloviev, 1998) including the Northern Cascadia Margin offshore Vancouver Island (Spence *et al.*, 2000).

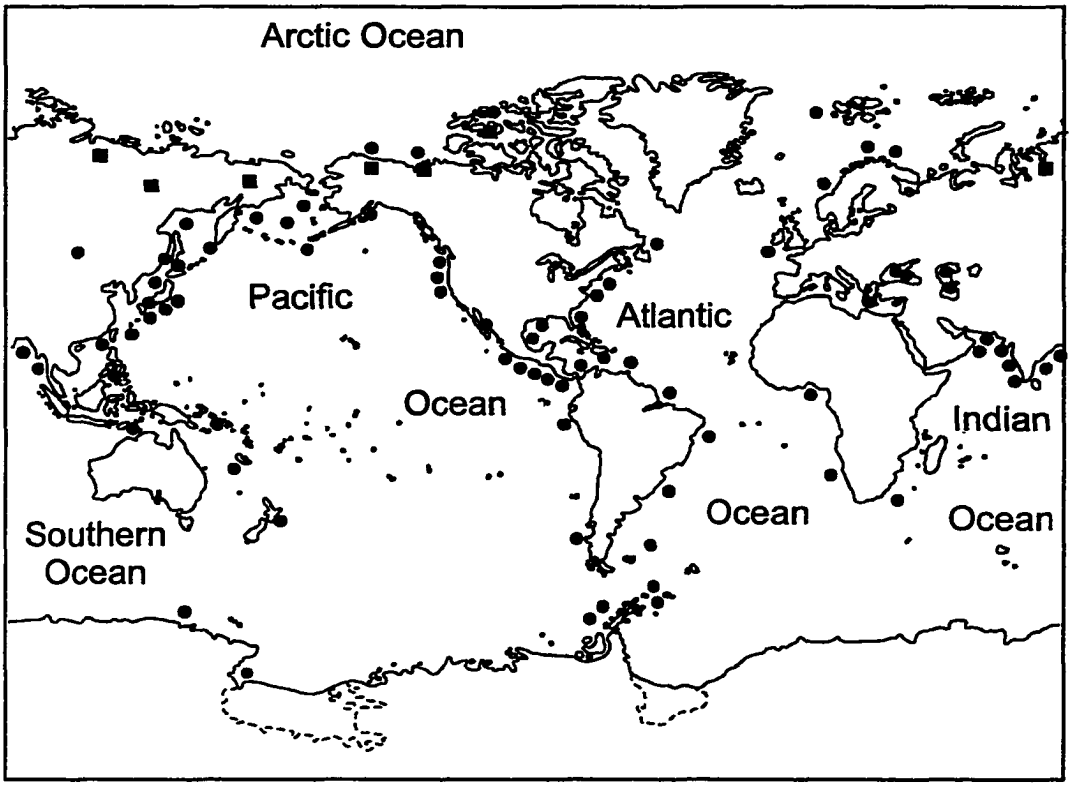

Figure 1.5 Map showing world-wide locations of known and inferred gas hydrate occurrences in marine sediments (solid circles) and in continental (permafrost) regions (squares) as up to May 2000 (from Kvenvolden, 2000).

1.3.1 Gas Hydrates in Oceanic Environments

Most of the oceanic occurrences of gas hydrate have been inferred from the presence of the bottom-simulating reflector (BSR) which marks the base of the hydrate stability field. Various marine geophysical surveys, the Deep Sea Drilling Project

(DSDP) and the Ocean Drilling Program (ODP) confirm the presence of hydrate in almost 10% of the global oceanic area (Kvenvolden, 2000), but their presence is restricted to the rise and slope of continental margins at water depths usually greater than about 500 m. A comprehensive list and description of the various geophysical studies worldwide can be found in Ginsburg and Soloviev (1998) and references therein.

Gas hydrates observed offshore Vancouver Island on the Northern Cascadia Margin are found at water depths between 500 and 2000 m and are mainly stable within the uppermost 200–300 m of sediments (Figure 1.6). The Northern Cascadia Margin is the best studied accretionary sediment prism hydrate occurrence, while the Blake-Outer Ridge region of the Atlantic Ocean offshore the south-eastern U.S. is the most investigated site of oceanic gas hydrate on a passive margin.

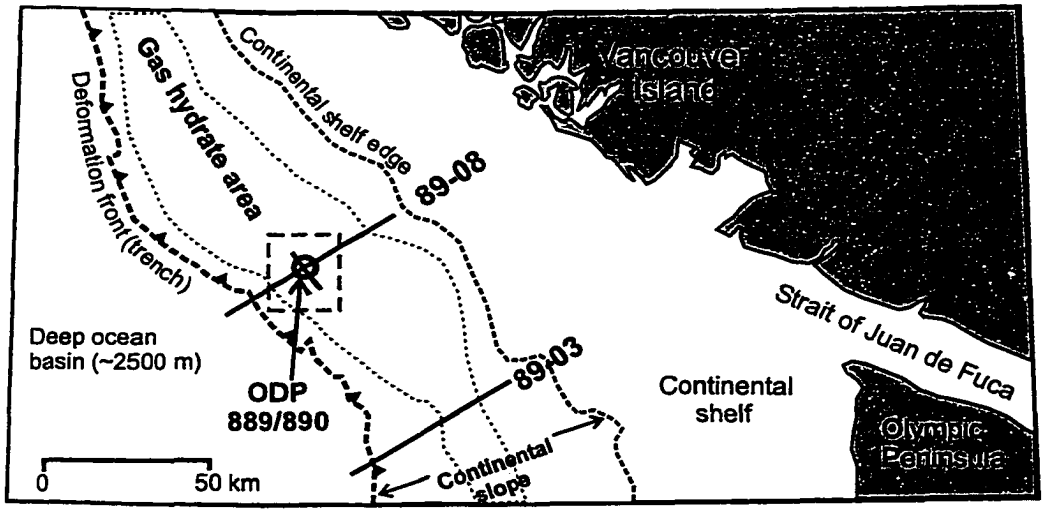

Figure 1.6 Map showing area of gas hydrate occurrence (shaded area) on the Northern Cascadia Margin as inferred from BSR mapping (after Hyndman *et al.* 1994).

1.3.2 Gas Hydrates in Permafrost Regions

The cold surface temperatures in polar regions allow gas hydrate to form as shallow as 130 m (MacDonald, 1983). Onshore gas hydrates are known to occur at the Messoyakha gas field in western Siberia (Makogon *et al.*, 1972) and it is believed that they also occur in many other permafrost areas of northern Russia (Chersky *et al.*, 1985). Permafrost associated gas hydrates are also widely present in the North American Arctic (Collett and Dallimore, 2000). The Mallik gas hydrate well in the MacKenzie Delta of Canada is the most well-studied site (Dallimore *et al.*, 1999). Several other arctic land hydrate accumulations have been inferred mainly by well-log responses of electrical resistivity and sonic velocity (e.g. Bily and Dick, 1974).

In addition to the known onshore accumulations, gas hydrates are known to exist within the offshore permafrost areas of the Beaufort Sea shelf of Canada (Neave *et al.*, 1978) and the continental shelf of Siberia (Bell, 1983). Gas hydrates may also occur in offshore and onshore permafrost regions of Antarctica but few data are available (e.g. Lodolo and Camerlenghi, 2000).

1.4 Why are Gas Hydrates Important?

Gas hydrates became of major interest during the last 20 years because (a) they might represent a future energy resource, (b) they may play a role in global climate change, and (c) they represent a potential geological hazard.

1.4.1 Gas Hydrates as a Potential Energy Resource

Several estimates of the total carbon content in marine and permafrost gas hydrates have been made and although these numbers are highly speculative, methane hydrate may represent a large reservoir of hydrocarbons that will dwarf all known fossil fuel deposits combined (e.g. Collett, 2000; Kvenvolden, 1993). However, the

role that gas hydrates might play in contributing to the world's energy requirements depends on the availability of sufficient gas hydrates and the costs of extraction. There is considerable disagreement in the total volume of gas hydrate accumulations as well as the concentration of gas hydrates in the host sediments. Even though gas hydrates are known to occur in numerous marine and permafrost regions, little is known about the technology required to extract the gas from hydrate. Several methods were proposed for gas recovery from hydrate, such as (a) thermal stimulation, i.e. 'melting' the in situ gas hydrate by hot water or steam injection, (b) decreasing the pressure below hydrate equilibrium or (c) injection of an inhibitor into the reservoir (e.g. methanol) to move the hydrate to outside of the stability conditions. Thermal stimulation and inhibitor ('antifreeze') injection have been proven to be technically feasible (Sloan, 1998) but the enormous economical and environmental costs associated with these techniques appear to be prohibitive. The most promising extraction technique considered is the depressurization of the reservoir. However, the extraction of gas may be hampered by re-formation of gas hydrate due to the nature of the gas hydrate dissociation (cooling).

1.4.2 Gas Hydrates and Climate Change

Methane is a strong greenhouse gas with a global warming potential 20 times larger than that for an equivalent volume of carbon dioxide (Shine, 1990). The amount of methane trapped in gas hydrate globally is approximately 3000 times the amount of methane present in the atmosphere (MacDonald, 1990). Thus the release of methane from gas hydrate dissociation might have a significant effect on global climate.

Global Warming

During global warming glaciers and ice caps melt, contributing water to the oceans. Oceans also thermally expand. The sea level rise causes an increase of hydrostatic pressure that stabilizes submarine gas hydrate deposits. At the same

time increasing atmospheric temperatures act to destabilize continental gas hydrates on a time scale of hundreds to thousands of years, and perhaps also marine hydrates. The released methane eventually reaches the atmosphere causing more global warming (positive feedback). Water temperatures also increase during global warming, although deep water bottom temperatures generally change slowly due to the large heat-capacity of the ocean. Thus for the deep-water gas hydrates (at depths greater than 300–500 m), the effect on hydrate stability caused by increasing sea level should outweigh the destabilization effects of an increase in water temperatures. However, at a critical depth of around 300–500 m hydrate deposits are most vulnerable to changes in bottom-water temperatures and changes in ocean circulation (Kennett *et al.*, 2000). The warming of these intermediate waters might occur faster than the sea level rise and might trigger the release of methane and a positive feedback to global warming. However, the ocean is generally depleted in methane causing immediate methane oxidization. Only if gas hydrate is released rapidly in huge amounts (maybe during a slumping event) can considerable amounts of methane reach the atmosphere.

Another positive feedback mechanism is expected for hydrate underlying polar continental shelves. First, increasing air temperatures increase shallow water temperatures. Second, even more important is the increase in ground surface temperature caused by the transgression of the polar ocean over the exposed, colder continental coastal surface as sea level rises. Flooding the land with relatively warm waters offsets the effects of increasing pressure due to the sea level rise and gas hydrates of the polar coastal land are destabilized (Figure 1.7).

Global Cooling

During global cooling, growing glaciers and ice caps remove water from the oceans and the ocean thermally contracts. The result is a sea level fall and regression of the oceans from continental shelves. During regression the pressure on marine gas hydrate deposits decreases and the hydrates dissociate. However, over longer time periods the

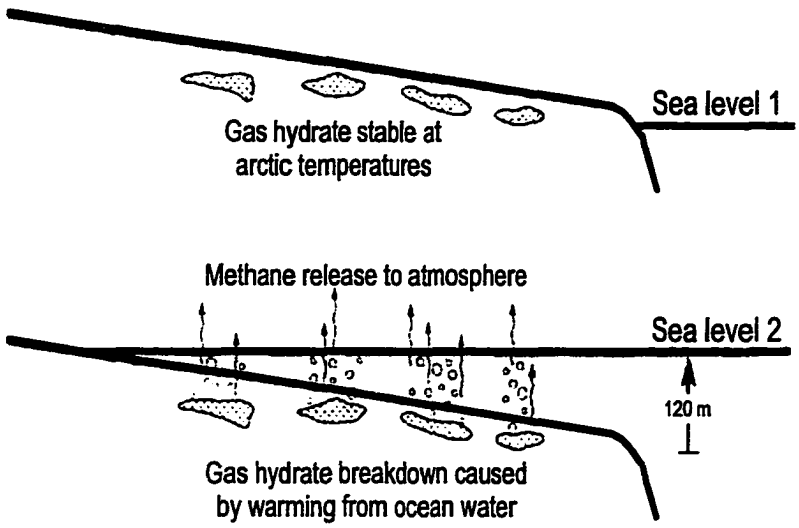

Figure 1.7 Diagram illustrating the effect of global warming on polar gas hydrate deposits (from Dillon and Max, 2000).

decrease in water temperatures re-stabilizes the hydrate deposits, offsetting the effect of decreased pressure. In polar regions the growing glaciers and ice caps increase the pressure on the gas hydrates and enforce stabilization. The drop in sea-level also exposes large areas of coastal regions to the colder surface temperatures stabilizing underlying hydrate deposits.

In summary, during global warming and/or cooling periods gas hydrate deposits should respond to pressure and temperature changes; however, the responses are complex and the extent of the influence that methane from gas hydrate dissociation has on global climate is still uncertain.

1.4.3 Gas Hydrate as Geologic Hazard

Since gas hydrates can be destabilized easily by pressure and temperature changes, they are a potential seafloor geohazard. The formation and dissociation of gas hydrate

has a significant influence on the mechanical properties of marine sediments. The replacement of pore water by hydrate will increase the shear strength as well as reduce the porosity and permeability of the sediment (Paull *et al.*, 2000). In turn during gas hydrate dissociation, free gas and water will be released, decreasing the shear strength making the sediment more prone to failure. The process of gas hydrate decomposition will also affect the pore pressure of the sediments (Kayen and Lee, 1993). During gas hydrate dissociation in sediments having pore fluids saturated with methane, the water and free gas released into the pore space will usually exceed the volume that was previously occupied by the hydrate. The net effect is either an increase in pressure (if the sediments are well sealed by a low permeability cap) or an increase in volume if the additional pressure can escape by fluid flow. Gas hydrate dissociation can occur due to changes in the pressure/temperature conditions, as outlined above, or due to continued sedimentation. The associated increase in pore pressure, expansion of sediment volume and the development of free gas bubbles all have the potential to weaken the sediment. Failure could be triggered by gravitational loading (continued sedimentation) or seismic disturbances (earthquakes), yielding slumps, debris flows and slides as illustrated in Figure 1.8.

The possible connection between gas hydrate occurrence and submarine slides was first recognized by McIver (1982). Many authors have later related major slumps on continental margins to instability associated with the break down of hydrates, including surficial slides and slumps on the continental slope and rise of South West Africa (Summerhayes *et al.*, 1979), slumps on the U.S. Atlantic continental slope (Carpenter, 1981), large submarine slides on the Norwegian margin (Jansen *et al.*, 1987), and massive bedding-plane slides and rotational slumps on the Alaska Beaufort Sea continental margin (Kayen and Lee, 1993).

Submarine mud-volcanoes have also been attributed to the release of gas from gas hydrate dissociation (Ginsburg *et al.*, 1992).

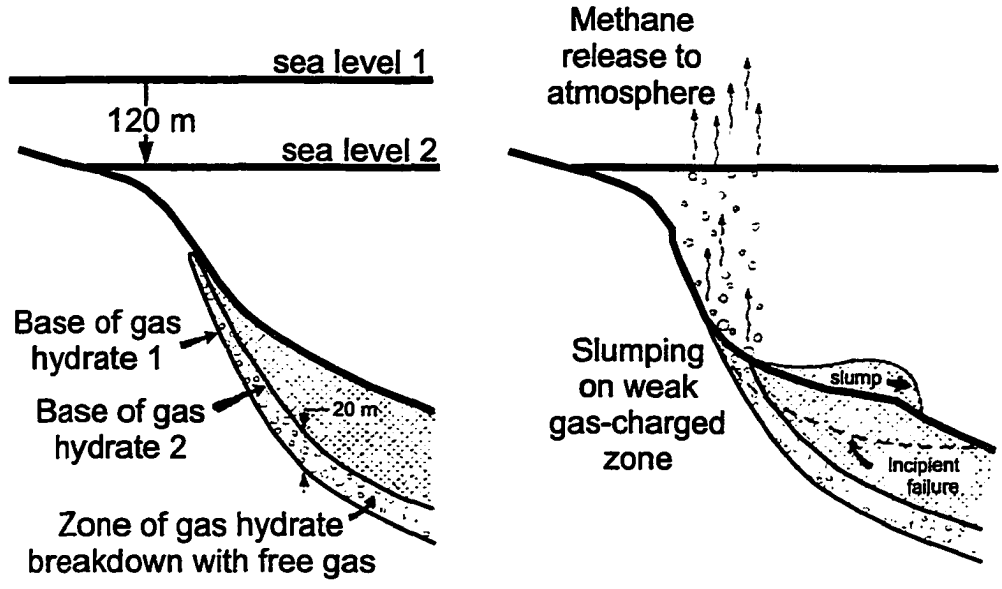

Figure 1.8 Diagram illustrating the effect of P/T changes on submarine gas hydrates and the resulting sea floor failures and gas release (from Dillon and Max, 2000).

1.5 Field Survey and Downhole Evidence for Gas Hydrate

Gas hydrates can be detected seismically and electrically. The two most important seismic characteristics of hydrate occurrence are the presence of a bottom-simulating reflector (BSR) and/or increased P-wave velocities compared to a no-hydrate reference. Other seismic indicators include a change in reflection pattern (blanking) and a change in the amplitude-versus-offset (AVO) response as outlined in chapter 7.

The BSR is characterized by an opposite reflection polarity compared to the seafloor reflection. The BSR polarity is due to a negative impedance contrast. Since density is not expected to change much in hydrate bearing sediments, the negative contrast is mainly due to a decrease in seismic velocity. The BSR might mark the top of the first occurrence of free gas, but not necessarily the base of the gas hydrate stability zone (Ruppel, 1997). Gas hydrate can coexist with free gas over a limited depth range as suggested for the Blake Ridge hydrate site. For the Cascadia hydrates,

Yuan *et al.* (1996) concluded that the observed BSR is mainly the result of hydrates above and no hydrates below the BSR, and free gas is only a minor contributor.

If hydrate forms in the sediments, it mainly replaces pore fluid and reduces the porosity. The result is an increase in the seismic P-wave velocity. This increase can be detected by careful multichannel interval velocity analysis, downhole sonic logging and vertical seismic profiling (Yuan *et al.* 1996; MacKay *et al.*, 1994). An increase in seismic S-wave velocity is to be expected if the hydrate forms in such a way that the overall sediment matrix is stiffened (Guerin *et al.*, 1999; Dvorkin and Nur, 1993).

Hydrate can also be detected by a change in electrical resistivity (Hyndman *et al.*, 1999; Yuan and Edwards, 2000). This field method is especially important if there is no BSR. During the formation of hydrate the conductive saline pore water is replaced by more resistive solid hydrate containing little salt and the porosity available for conduction is reduced as approximately described by Archie's Law. Hydrate concentrations can be inferred from electrical resistivity data, but for accurate results the data have to be corrected for the effect of varying in situ salinity in the remaining pore fluid. A geochemical marker that hydrate was present in cores before recovery is pore water freshening. The formation of hydrate increases the salinity of the remaining pore water at the initial phase of formation (Hyndman *et al.*, 1999). If there is sufficient permeability of the host sediment, the increase in salinity yields a salinity gradient which is brought back to equilibrium by the diffusion or fluid flux of fresher normal salinity pore waters into the hydrate zone. If a core containing hydrate is recovered, the dissociation of hydrate results in release of methane and nearly pure water, i.e. a pore water freshening. The amount of freshening can then be used as an indicator for the amount of hydrate that was present in the sediments, if the in situ pore fluid salinity can be estimated.

Chapter 2

Previous Gas Hydrate Studies Offshore Vancouver Island

The Vancouver Island margin area of investigation has been the focus of many geophysical studies since 1985 to characterize the gas hydrate occurrence. Within this chapter the major results from these previous studies is given and discussed in relation to the new seismic data acquired as part of this thesis study.

2.1 General Tectonic Setting

The area of this investigation is on the accretionary prism of the Cascadia subduction zone (Figure 2.1). The Juan de Fuca plate converges nearly orthogonally to the North American plate at a present rate of about 45 mm/year (e.g. Riddihough, 1984). Seaward of the deformation front, the Cascadia basin consists of pre-Pleistocene hemipelagic sediments overlain by a rapidly deposited Pleistocene turbidite for a total sediment thickness of about 2500 m. Most of the incoming sediment is scraped off the oceanic crust and folded and thrust upward to form elongated anticlinal ridges with elevations as high as 700 m above the adjacent basin. The thrust faults near the deformation front penetrate nearly the entire sediment section (Davis and Hyndman, 1989).

Landward from the deformation front, the seafloor rises rapidly to a water depth of 1400–1500 m where there is a bathymetric bench. The 12 km by 8 km area of detailed investigation is located near two topographic highs, which rise 200 m over the surrounding seafloor (Figure 2.2). The area between the topographic highs forms a 350 m deep trough filled with slope basin sediments.

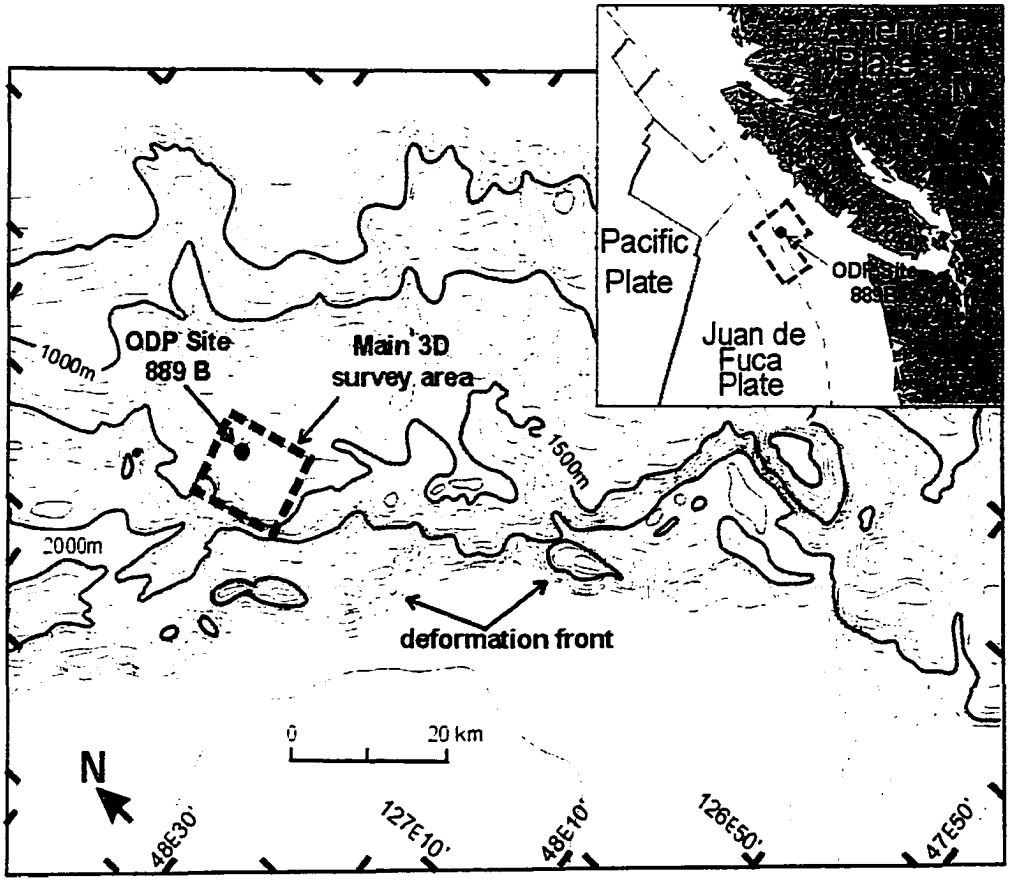

Figure 2.1 General plate tectonic setting and bathymetry of the Cascadia subduction zone.

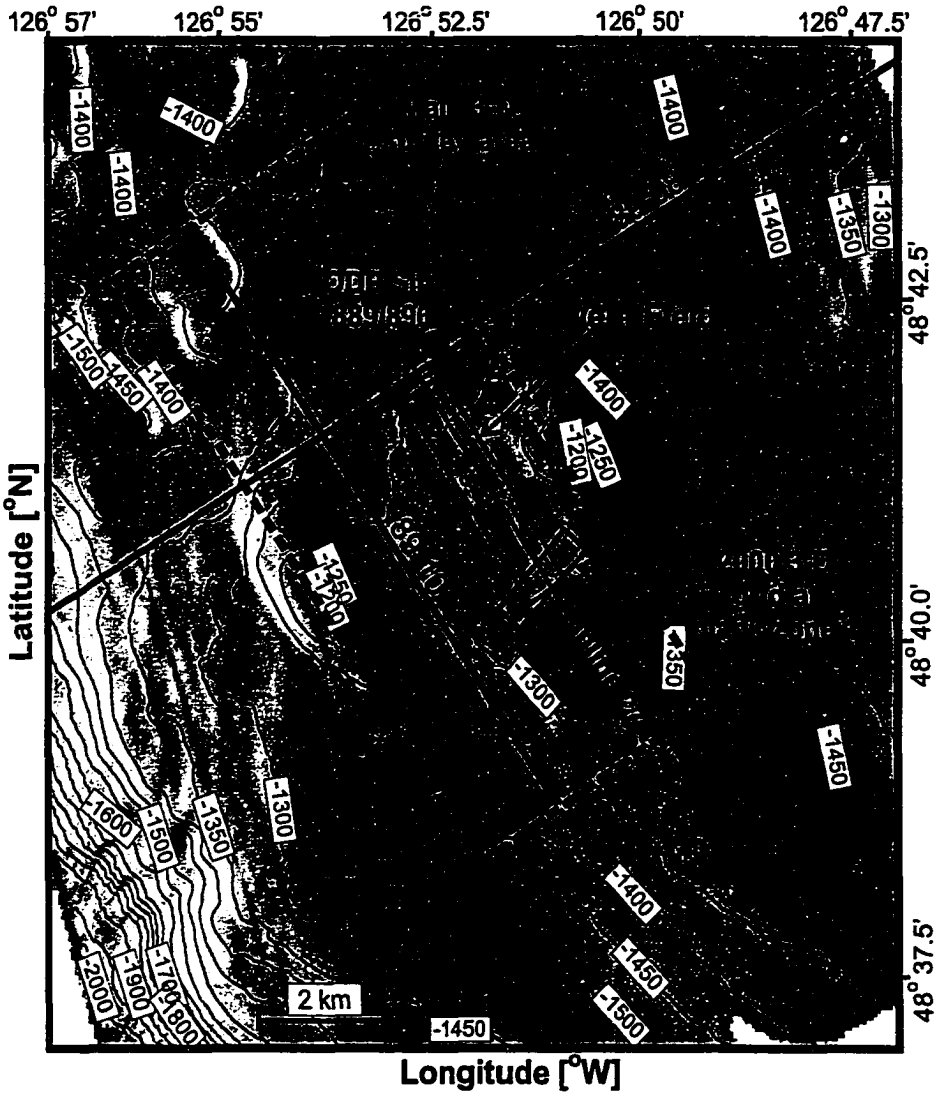

Figure 2.2 Detailed multibeam bathymetry around ODP Site 889/890 (from German cruise Sonne 111, provided by V. Spiess). Location of the main 3-D grid, the 1999 vent field grid and the 2000 grid around blank zone 1 are indicated.

At ODP Site 889, sediments in the upper 128 m below the seafloor are silty clays and clayey silts interbedded with fine sand turbidites. This sequence was interpreted as little-deformed slope basin sediments, deposited in place (Westbrook *et al.*, 1994). The sediments below this sequence are more deformed, compacted and cemented, and were interpreted as accreted Cascadia Basin sediments.

2.1.1 Tectonic Interpretation Near ODP Site

ODP Sites 889/890 lie on a plateau on the accretionary prism near the two topographic highs. The area around site 889/890 was undergoing deformation during the period that the basin sediments were deposited. This results in complicated deformation structures with a mixture of erosional unconformaties, faults and onlaps. The plateau of accreted sediment is generally covered with a layer of bedded sediments that thicken into basins formed in synclines on the footwall side of thrust faults. Seismically, the accreted sediments are almost transparent and show no seismic coherency, whereas the younger basin sediments show stronger continuous reflectivity. To the east of the ODP site, a broad slope basin has developed with up to 0.5 s TWT thick sediment fill. The basin is divided into several sub-basins by ridges of accreted sediment. Uplift of the ridges resulted in thinned and locally deformed sequences over the ridges between thicker less deformed sequences in the basins. As shown in Figure 2.3 the southwestern margin of the basin is an eastward facing fault scarp outcrop. This fault appears to be westward dipping based on the asymmetry of the sediment deformation and the uplift of the ridge (Westbrook *et al.*, 1994). However, the observed deformation features can be explained only if the ridges are brought up "along many small thrust faults that lie within them" (Westbrook *et al.*, 1994).

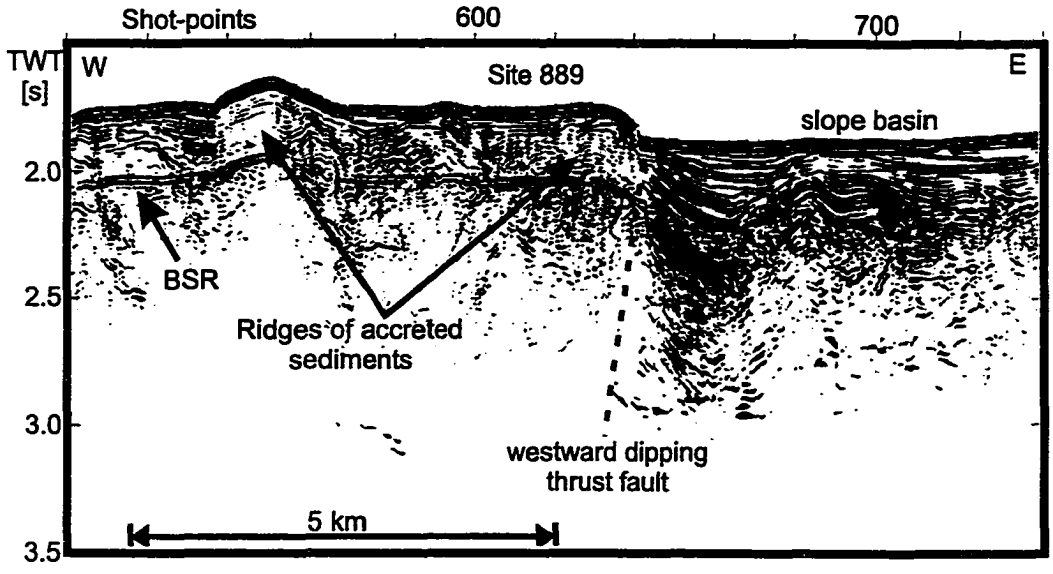

Figure 2.3 Part of migrated seismic line 89-08 showing westward dipping thrust fault at western side of slope basin (after Hyndman *et al.*, 1994).

2.2 Previous Geophysical Studies

The area investigated in this thesis has been the focus of many detailed study programs to investigate natural gas hydrates in a deep-sea environment. Natural gas hydrates on the northern Cascadia margin were first inferred in 1985 from a BSR in seismic data (Davis and Hyndman, 1989). A number of conventional multichannel seismic lines were acquired along the Vancouver Island margin in 1989 providing more detailed insight into the BSR distribution across the margin (Hyndman *et al.*, 1994). Based mainly on the 1989 seismic data, ODP Leg 146 drilled several wells in 1992 through the gas hydrate zone on the continental slope as well as a no-hydrate/gas reference site in the deep ocean basin seaward of the deformation front (Westbrook *et al.*, 1994).

A variety of detailed geophysical studies have been carried out since then including surface towed single and multichannel seismic surveys, deep-towed high-resolution

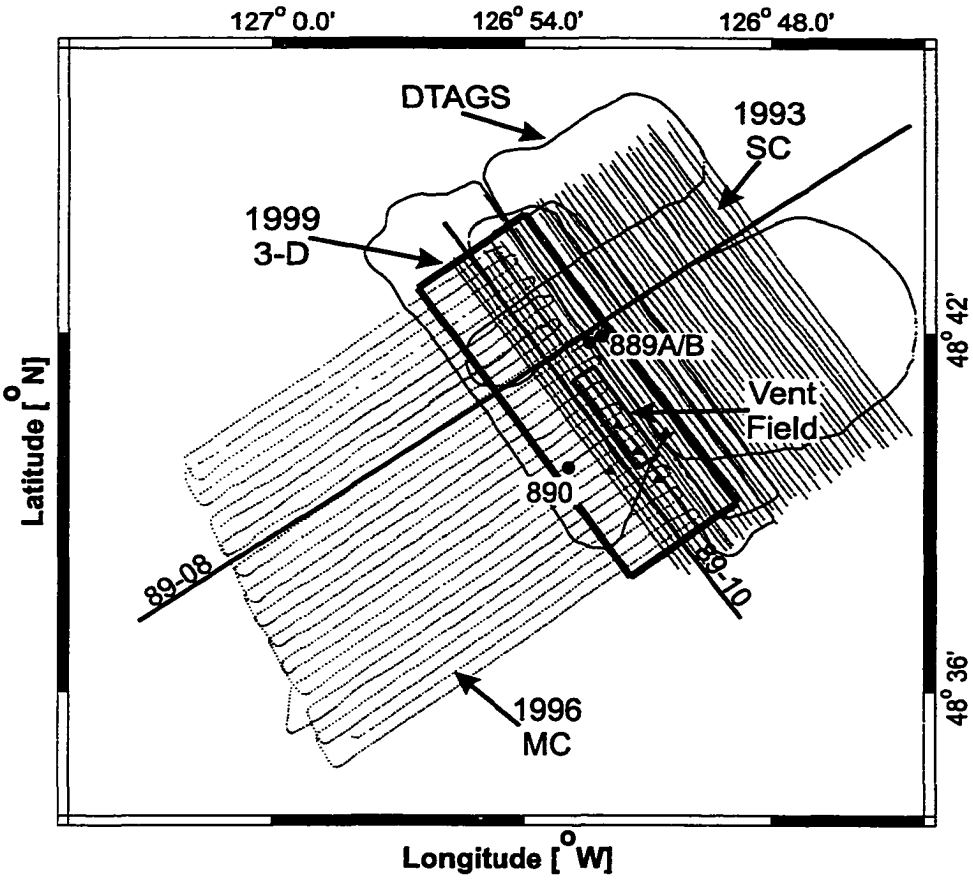

Figure 2.4 Location of detailed seismic surveys around ODP Leg 146. Circles are ODP Sites 889/890, triangles indicate OBS location from 1999 survey.

seismic surveys (Deep Tow Acoustic Geophysics System: DTAGS), Ocean Bottom Seismometer (OBS) studies, high-resolution acoustic echosounder (12 kHz) and sub-bottom profiling (3.5 kHz), electrical surveys, swath bathymetry, piston corer seafloor sampling and heat flow studies. The location of the detailed seismic studies are shown on Figure 2.4.

2.2.1 The BSR: Distribution and Reflection Pattern

The occurrence of a BSR is an unambiguous seismic indicator of marine gas hydrate. In Cascadia a clear BSR is generally observed in deformed accreted sediments whereas it is not apparent in the well-bedded slope basin sediments (Figure 2.3). Although a clear BSR reflector is not observed in those latter areas, substantial hydrate concentration was inferred from multichannel interval velocities and electrical resistivity profiling (Yuan *et al.*, 1996; Yuan and Edwards, 2000). This is an apparent contradiction to the conclusion by Yuan *et al.* (1996) that the BSR is due to hydrate only. The BSR first appears on the continental slope 5–10 km landward of the deformation front. There is no BSR in the deep sea Cascadia basin. The BSR disappears on the upper slope for water depths of less than 600–800 m.

The BSR reflection pattern shows the following characteristics in conventional low-frequency (20–30 Hz) seismic data:

1. The BSR is a single reflector with reflection polarity opposite to that of the seafloor reflection.

2. The BSR waveform is a single symmetric pulse.

3. The BSR reflection coefficients are generally large (up to about 50% of the seafloor reflection coefficient).

These characteristics are consistent with a simple single interface model for the BSR, where the decrease in seismic impedance occurs over a depth range less than the seismic wavelength (about 50 m for conventional MCS). Since the density is not expected to change significantly by replacement of pore fluid by up to a few 10's % hydrate or few percent gas, the negative impedance contrast is believed to be mainly a velocity effect. The lower seismic velocities can be either the effect of free gas or just the absence of high-velocity hydrate in the sediments below the interface.

However, these characteristics were only observed clearly in the low-frequency seismic data. The BSR reflection coefficient has been found to decrease with increasing frequency for airgun data over a range from 15–175 Hz (Fink and Spence, 1999). An even larger decrease was observed using the high-resolution DTAGS system, which operates over a frequency range of 250–650 Hz (Chapman *et al.*, 2001). An explanation suggested is that the frequency dependent behaviour of the BSR is a consequence of a gradational velocity contrast over a depth interval of about 10 m. The thickness of this gradient layer is too small to influence the low-frequency seismic data, but is larger than the wavelength of the DTAGS system. The frequency-dependence of the BSR was modeled using synthetic seismograms over the frequency range of 15–500 Hz as shown in Figure 2.5. A boundary thickness of 6–10 m and a velocity decrease of 250 m/s was found to best explain the observed reflection coefficients at all frequencies.

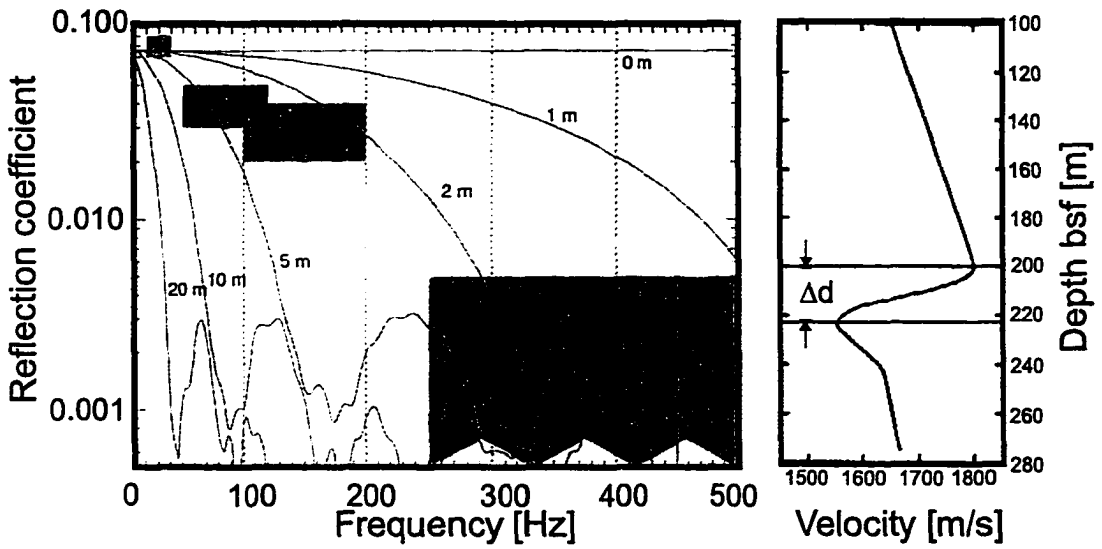

Figure 2.5 Frequency dependent BSR vertical incidence reflection coefficients. (a) Observed BSR reflection coefficients with varying frequency (shaded areas). The solid lines are modeled reflection coefficients for different gradient layer thickness Δd (b) Velocity depth function for the BSR (from Chapman *et al.*, 2001).

2.2.2 Seismic Velocities and Hydrate Concentration

Multichannel interval velocities provide one of the main quantitative constraints on hydrate concentration. Interval velocities derived from reflectors inside the hydrate stability zone above the BSR have to be compared to a no-hydrate/gas reference velocity profile (Yuan *et al.*, 1996). This reference was obtained from regional multichannel seismic data by extrapolating the deeper trend to the seafloor (Figure 2.6). This extrapolation can be done since the sediment section is quite uniform at seismic wavelengths. However, there is variability at a smaller thickness scale of turbidite layering. Multichannel interval velocities within the hydrate zone are higher than the reference velocity profile and are in good agreement with the ODP sonic logs. The shift towards increased compressional velocities is an indicator for the presence of hydrate, and can be used to estimate the hydrate concentration. Assuming that hydrate formation replaces the pore fluid in the pore space, the velocity increase due to hydrate can be approximated with several models. The simplest model is a porosity reduction using a velocity-porosity function for the Cascadia sediments. Hydrate concentrations calculated near the ODP Site 889/890 are shown in Figure 2.7 (Yuan *et al.*, 1996).

Downhole electrical resistivity data were also used to estimate the hydrate concentration. A reference no-hydrate/gas profile was obtained from the Cascadia basin Site 888. The increased resistivities observed around Site 889/890 may be due to lower than normal in situ pore fluid salinity and a correction must be carried out using core data (Hyndman *et al.*, 1999). A simple model using Archie's law of corrected resistivity versus hydrate gives a hydrate concentration of about 30% pore saturation just above the BSR, which is slightly higher than the concentration derived from seismic velocities. Similar resistivities and inferred hydrate concentrations were obtained by seafloor electrical sounding (Yuan and Edwards, 2000).

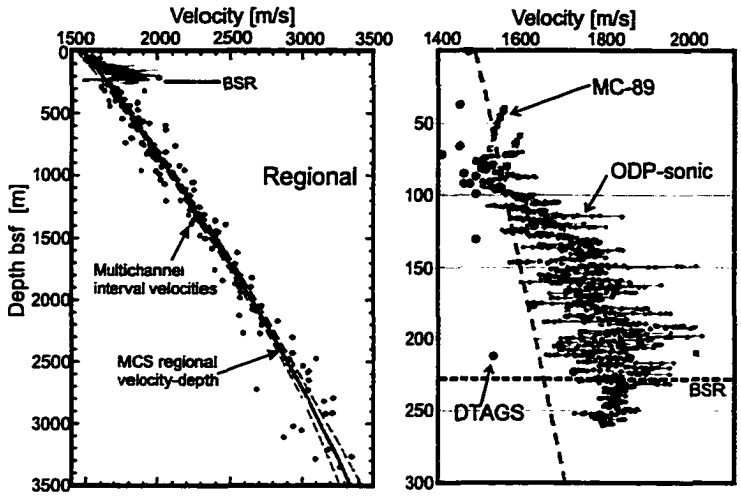

Figure 2.6 (a) MCS interval velocities from within 10 km of ODP Sites 889/890 that provide the no-hydrate/gas reference (from Yuan *et al.*, 1996), (b) Detailed view of the MC-89 and DTAGS interval velocities and sonic log data.

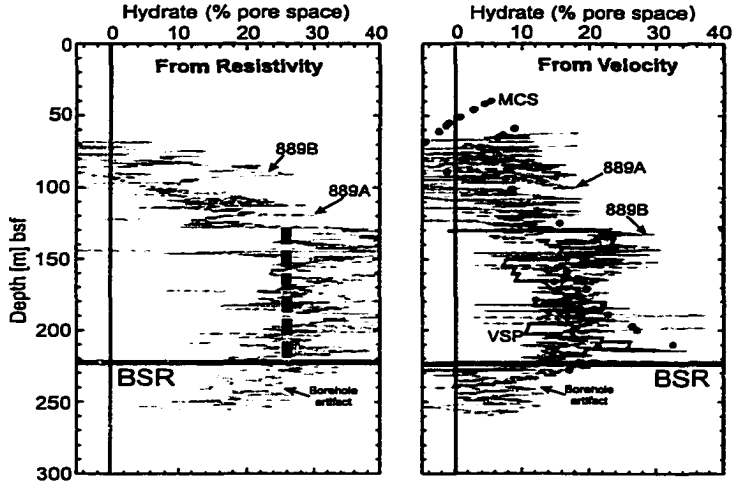

Figure 2.7 Hydrate concentrations at ODP Sites 889/890 computed from (a) resistivity data (Hyndman *et al.*, 1999) and (b) seismic data. The dashed line in (a) indicates an average hydrate concentration estimated from seafloor electrical sounding (Yuan and Edwards, 2000).

2.2.3 Amplitude-Versus-Offset Studies and Full Wave Form Inversion

Amplitude Versus Offset (AVO) investigations are an important tool in sediment classification and in hydrocarbon exploration. AVO methods are based on measuring the reflection coefficient of seismic waves at a particular interface as a function of the angle of incidence. The AVO response is primarily a function of the physical properties (i.e. P-wave and S-wave velocity and density) of the sediments above and below the interface. However the detailed structure of the interface, especially layer thickness, can contribute to the overall AVO effect or add false tuning effects and has to be taken into consideration if AVO is used in an inversion scheme to estimate the physical properties of the sediments. The AVO method might provide insight into the BSR and constrain the question of whether the impedance decrease at the BSR is the effect of free gas below or the effect of the higher hydrate concentrations above the interface. Yuan *et al.* (1999) calculated the AVO response for three different models: (a) free gas only, (b) hydrate only, and (c) free gas and hydrate (Figure 2.8). Only small differences were observed between the different AVO responses, with the hydrate-only model giving the best fit to the observed AVO data. However, there are significant differences in the near to mid-offset range of the AVO responses between the gas-only and hydrate-only models, which might help to further constrain the range of physical properties of the sediments above and below the interface (see chapter 7 for new analyses).

The AVO method is based only on the observed amplitudes of the BSR, normally picked from the peak or trough amplitudes of the BSR. Additional information can be obtained by modeling the complete waveform. Full wave form inversion was implemented for the area around ODP Sites 889/890 (Yuan *et al.*, 1999; Singh and Minshull, 1994; Minshull *et al.*, 1994). The inversion technique tries to find a P-wave velocity-depth function such that the synthetic seismograms fit amplitude and waveform (phase) of the observed data within a common mid point gather. In the

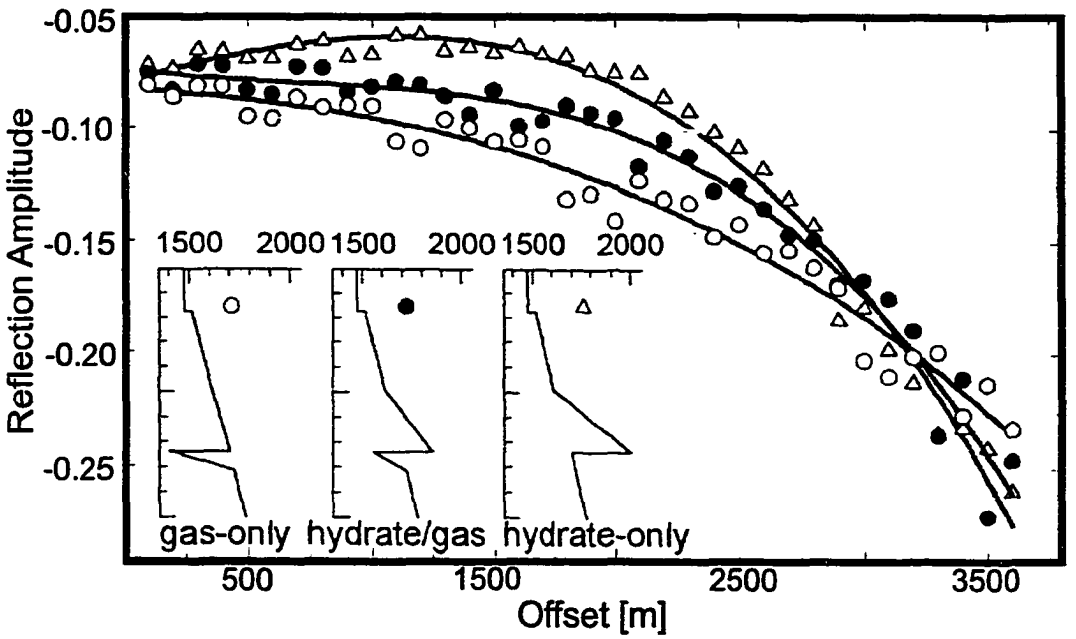

Figure 2.8 Reflection coefficients as function of offset from synthetic seismograms for three different BSR models shown in the insets (from Yuan *et al.* 1999).

study by Yuan *et al.* (1999) S-wave velocity and density were calculated from the P-wave velocity by using empirical relations (Castagna *et al.* 1985; Hamilton 1978). Attenuations were kept fixed at $Q_p = 200$ and $Q_s = 25$ (Minshull *et al.*, 1994). The inversion result was found to be very sensitive to the starting model and there was poor control of the absolute velocities. However, a good general agreement with the multichannel seismic interval velocities and with the ODP downhole sonic logs was found (Figure 2.9).

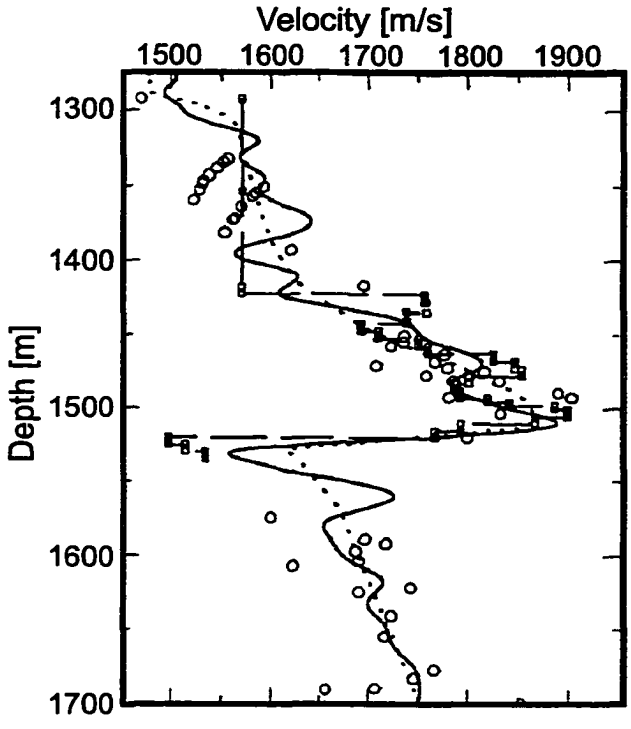

Figure 2.9 Final full-waveform inversion result for the hydrate+gas model (solid line). Velocities from MCS (open circles) and VSP (dashed line with symbols) are also shown (from Yuan *et al.*, 1999).

2.3 Fluid Venting and Carbonate Pavement

The overall accretion process results in shortening and tectonic thickening of the incoming sediment column. The thickening results in an underconsolidated section that re-establishes an equilibrium porosity-depth relation through consolidation and fluid expulsion (Hyndman and Davis, 1992). Fluid venting and associated mud volcanism have been reported from many accretionary prisms (Suess *et al.*, 1999; Suess *et al.*, 1998; Elderfield *et al.*, 1990; Henry *et al.*, 1990; Le Pichon *et al.*, 1990). The fluids often are inferred to be discharged along major faults (including the decollement), and only a small amount expelled pervasively. This is in contrast to the interpretation for the accretionary prism offshore Vancouver Island where the lack of strong

local thermal anomalies at the deformation front and the absence of pronounced BSR depth disturbances suggest that only minor concentrations of fluids are expelled up faults and other hydrologic conduits (Davis *et al.*, 1990; Ganguly *et al.*, 2000).

Fluid expulsion and venting are often associated with near-surface diagenetic processes such as carbonate formation. Widespread carbonate sedimentation in the general area was interpreted from high-amplitude backscattering on GLORIA side-scan images (Carson *et al.*, 1994). Carbonate slabs, nodules and chimneys were collected on the Cascadia margin off Oregon by submersibles or grab samplers (Kulm and Suess, 1990; Bohrmann *et al.*, 1998). Fink and Spence (1999) interpreted local seafloor amplitude anomalies observed in multifrequency single channel seismic data around ODP Site 889/890 as the result of a thin carbonate crust. However, no evidence for carbonate pavements were found in piston cores acquired over that region during a 1996 cruise (Mi, 1998).

Chapter 3

The COAMS-99 Experiment

Within this chapter the details of the 3-D seismic survey and data acquisition is described. The design and acquisition parameters, such as line direction and spacing, control the limit of the seismic interpretation carried out. Also a detailed description of all different seismic acquistion equipments used is given.

3.1 3-D Seismic Survey Design

An important part of this thesis study was the 3-D seismic survey in the area of ODP Leg 146, Site 889/890 including the COAMS multichannel system and the Teledyne high-resolution single channel array. The location of the COAMS-99 3-D seismic experiment was chosen in the vicinity of the sites 889/890, based on the results of the previous seismic surveys. The location is between the two nearby prominent topographic highs and also covered the area where blank zones were observed during the DTAGS cruise (Figure 2.2). The line direction for the main 3-D grid was SE–NW parallel to MCS seismic line 89–10 and DTAGS line BC–03. A minimum topographic change is observed in this direction, minimizing imaging problems of the type observed on data acquired in a perpendicular direction (Zühlsdorff *et al.*, 2000). A total of 41 seismic lines were acquired for the main 3-D grid (inline 1 was not used due to a failure of the seismic source), plus eight perpendicular lines for crossline reference (Figure 3.1).

The multichannel reflection seismic experiment was complemented by five Ocean Bottom Seismometers (OBS) from Dalhousie University. The OBSs were deployed

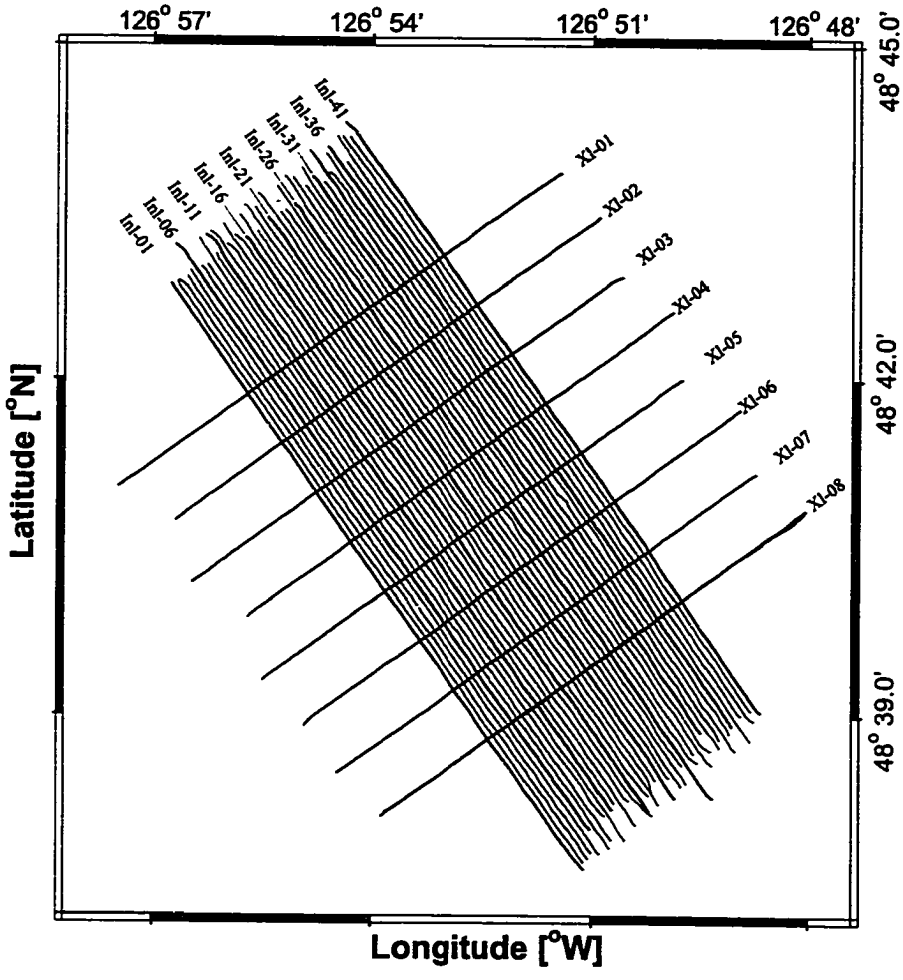

Figure 3.1 Track lines for main 3-D grid.

in a star configuration separated by 1000 m that covers the area of blank zone one (Figure 3.2). During the first two days of data acquisition (maximum data storage capacity of the OBS) the complete area of investigation was covered to allow full 3-D seismic tomography.

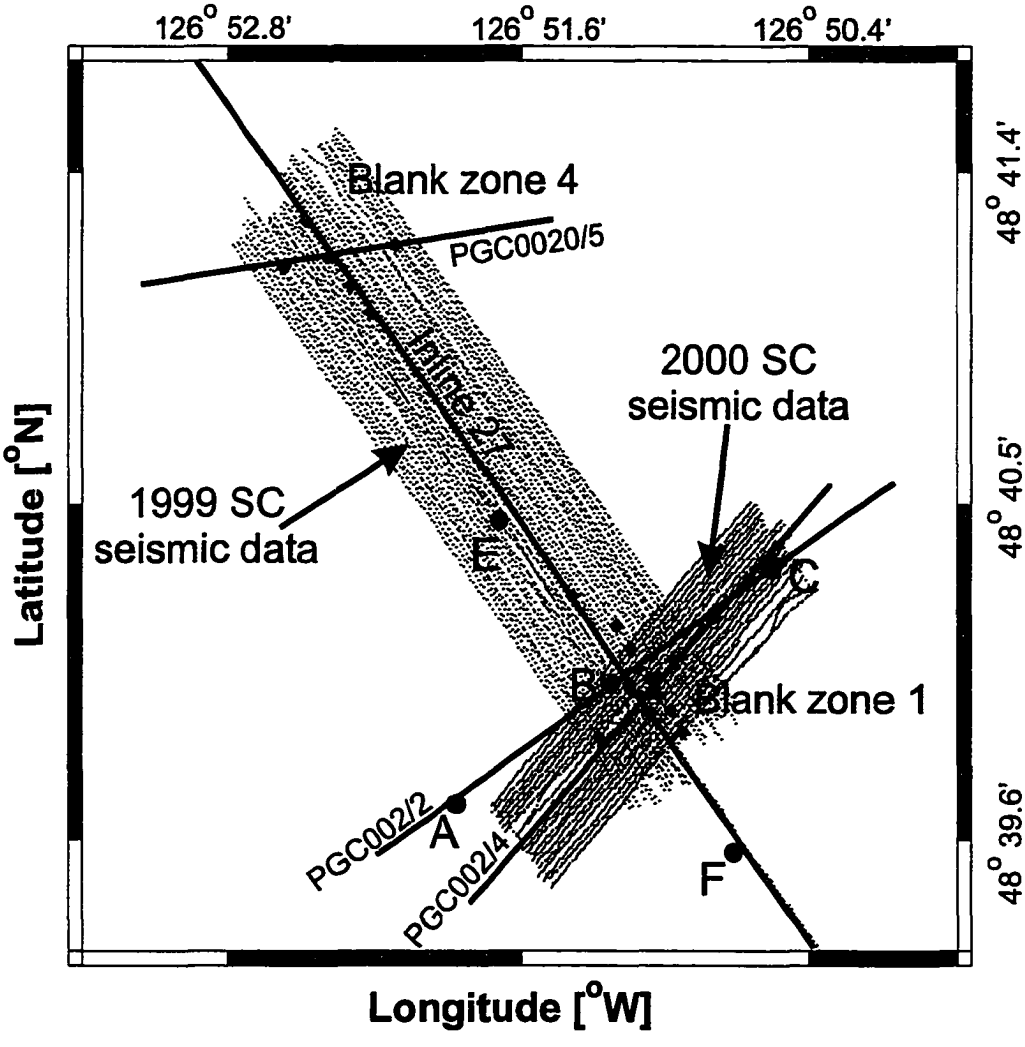

Figure 3.2 Single channel seismic track lines around vent field (Teledyne 1999 and 2000). Position of inline 27 from the main grid is included for reference. OBS positions from 1999 deployment are shown as circles. OBSs are labeled from A–F. Selected piston-core locations (triangles) at blank zone 1 and 4 are also shown.

This survey was limited by the time available and the maximum survey speed of 4 knots (about 2 m/s) during data acquisition. In 3-D seismic data acquisition the spacing between adjacent inlines is the most critical parameter for unaliased depth imaging. Industry-type 3-D seismic surveys are commonly done with several closely spaced parallel streamers. The COAMS-99 seismic experiment was carried out with one streamer only. Thus, no crossline information is available for velocity and anisotropy due to the lack of multiple azimuths. Also, data processing of this kind of data set has to be carried out very carefully to avoid artifacts such as survey line footprints, i.e. striations due to small data offsets between adjacent lines.

The maximum frequency (f_{thresh}) to be used in 3-D processing to avoid spatial aliasing can be calculated from the average dip of sedimentary layers (θ) and an average velocity (V) found in the area of interest for any given line spacing (δx) (Figure 3.3):

$$f_{thresh} = \frac{V}{(4 \cdot \delta x \cdot sin(\theta))} \tag{3.1}$$

Using a velocity of e.g. 1650 m/s, a maximum dip of about 6° as defined from previous cruises, and a line spacing of 100 m, the maximum frequency to be used is about 40 Hz.

The survey 100 m inline spacing allowed covering the main area of investigation and maintaining the possibility of full, albeit low frequency, 3-D seismic data processing. The seismic lines were acquired in stages so that always a regular grid was available for interpretation if the system failed, i.e. starting with a grid of 400 m line spacing and then subsequently filling in the lines towards a 200 m and 100 m grid. During the first 2 days of the survey, the 200 m grid was completed and fully recorded on the five OBS.

Each line of the main 3-D grid consists of an alignment length of 500 m at the

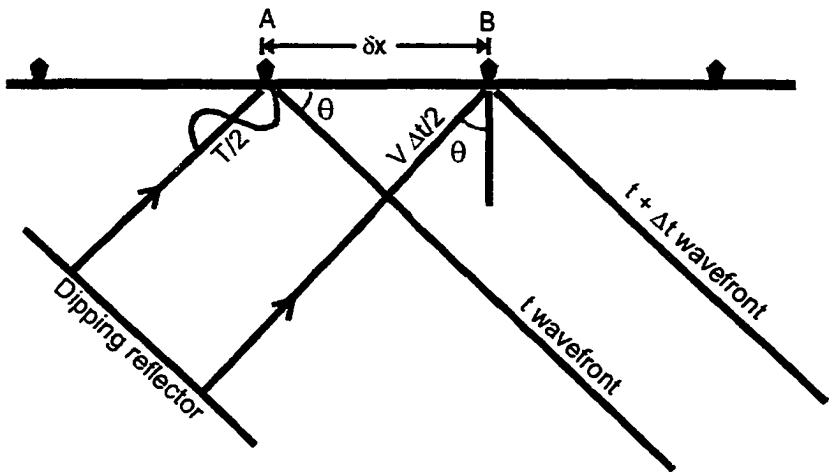

Figure 3.3 Derivation of the threshold frequency for spatial aliasing. Aliasing occurs when the time difference between the arrivals at receivers A and B is one-half the period (T/2) apart (after Yilmaz, 1987).

beginning of each line to ensure that the streamer has straightened behind the ship before entering the main survey area (see also section about compass data). The length of this buffer was estimated from previous experience using the COAMS streamer but was found to be too short for complete alignment. An actual length of minimum 1500 m (about the length of the COAMS array) is needed, limiting the useful data set to a total length of about nine kilometers per line.

3.2 Seismic Data Sets Acquired

A total of 48 COAMS multichannel seismic lines were acquired, 40 lines forming the main grid and eight perpendicular lines. On all lines single channel seismic and high-resolution 3.5 kHz subbottom profiler data also were acquired. Due to severe weather conditions, little 3.5 kHz data was obtained on some of the main grid lines. The data quality was commonly poor into the sea but was better on lines with the

Year	Area	Seismic equipment	Spacing
1999	Main grid	COAMS	100 m
1999	Main grid	Teledyne	100 m
1999	Main grid	3.5 kHz	100 m
1999	Vent field	Teledyne	25 m
1999	Vent field	3.5 kHz	25 m
2000	Blank zone 1	Teledyne	25 m
2000	Blank zone 1	3.5 kHz	25 m

Table 3.1 Seismic data sets acquired in 1999 and 2000.

sea. The blank zones were subsequently covered with a single channel-only seismic grid of 31 lines at 25 m spacing (Figure 3.2). Based on preliminary results of the 3-D analysis, a cruise in July 2000 acquired 26 piston cores over the vent field. As part of this survey, a second single channel seismic grid of 21 lines was acquired perpendicular to the 1999 grid using similar acquisition parameters (Figure 3.2), covering the most prominent blank zone. Table 3.1 summarizes the seismic reflection and 3.5 kHz data sets collected in 1999 and 2000.

3.3 Seismic Systems

Figure 3.4 shows in summary the field data acquisition geometry for the COAMS-99 experiment. Position of the two streamers, airgun, shotpoint hydrophone and high-resolution subbottom profiler are indicated and relative distances to the stern of the ship are added.

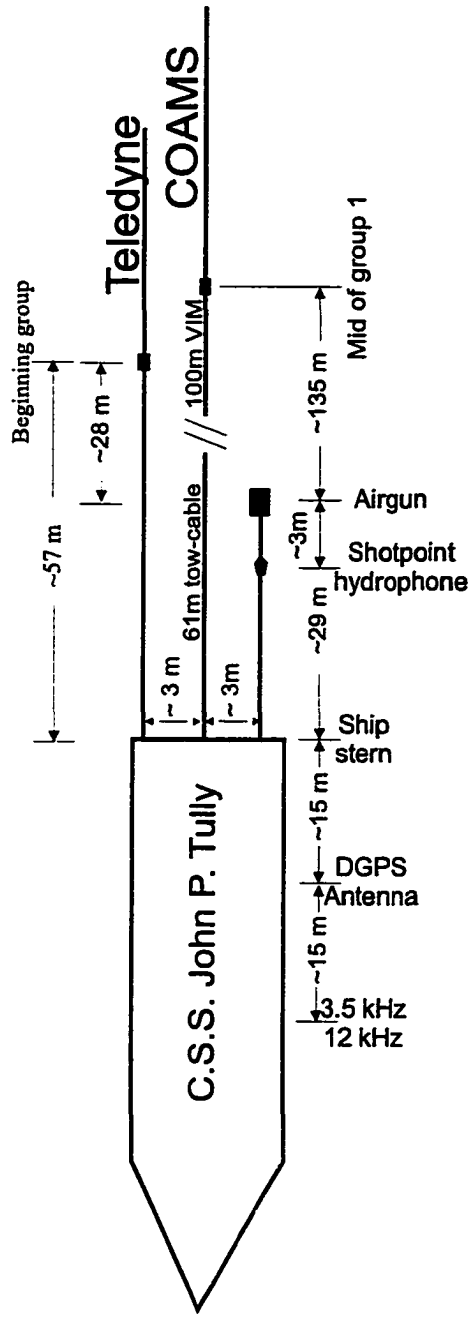

Figure 3.4 Summary of field data geometry.

3.3.1 Seismic Source

The seismic source for the COAMS multi- and single channel surveys was a single 40 in^3 (0.65 l) sleeve gun with a wave shape kit. The wave shape kit uses 50% of the volume to reduce the bubble collapse energy by injecting 20 in^3 of air a few milliseconds after the first release.

A shot point hydrophone was towed about 3 m below and 3 m in front of the sleeve gun to record the airgun source signature (Figure 3.5) for modeling studies and data processing. The trigger time delay of each shot can be calculated from the approximate position of the shot point hydrophone relative to the seismic source. Observed variations in the trigger time delay are mostly due to varying relative distances between the gun and the shot point hydrophone. No consistent drift of the trigger time delay was identified, and was therefore set to an average of 18.6 ms for the entire survey.

With the use of a flotation device the gun was towed at a nominal depth of about 2 m below the sea surface. In the frequency spectrum shown in Figure 3.5b, calculated from the shot point hydrophone recordings, the first frequency notch occurs at about 450 Hz. This frequency notch (f_{notch}) corresponds to a depth of 1.7 m (or approximately 2 m) using the following equation:

$$f_{notch} = \frac{V}{2d}, \tag{3.2}$$

where V represents an average sound speed in the water (1500 m/s) and d is the gun depth below sea surface.

The shot point distance was planned to be at about 19 m, which is four times the hydrophone spacing of the front part of the COAMS array, as defined in section 3.3.2. However, the actual shot point distance varied between 16 m and 32 m during the entire survey. This distance was found to be highly dependent on the line direction and wind speed. Originally it was planned to control the shot point distance from the geophysical navigation system. The newly developed acquisition computer provided

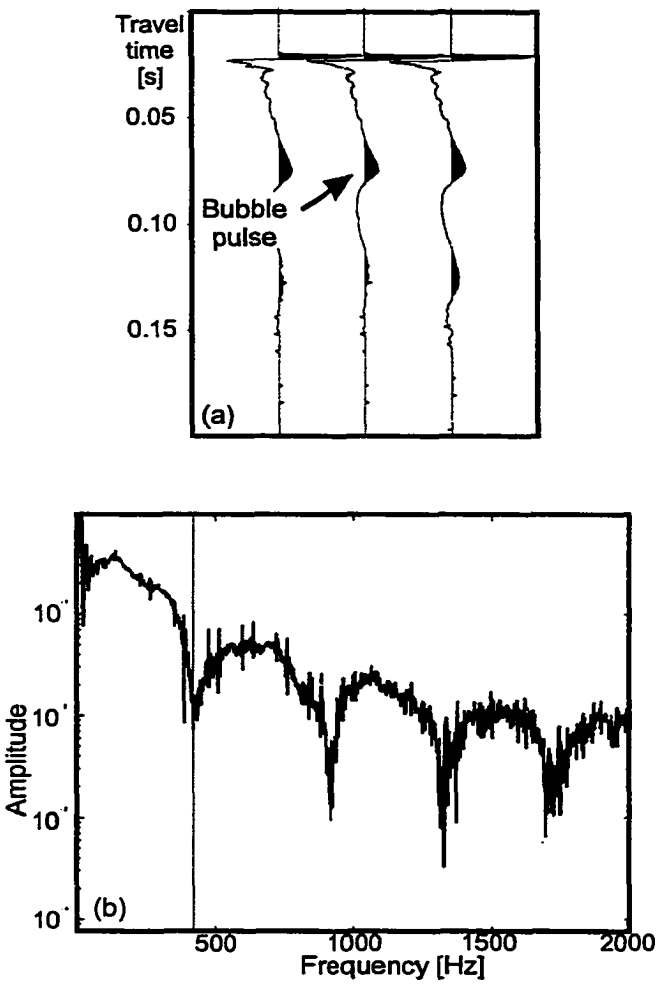

Figure 3.5 (a) Source signature and (b) frequency spectrum for three sleeve gun records. The first notch at about 450 Hz corresponds to a gun depth of about 2 m.

was not able to use the external trigger pulse provided by the geophysical navigation system. Therefore the COAMS acquisition computer itself was used to trigger the gun and data recording. However, shot point distance was not calculated consistently. The shot point distance was based on the GPS position of the ship, conversion to UTM coordinates (Clarke-80 datum) and a smoothing operator to allow for GPS position scatter.

3.3.2 COAMS Multichannel Streamer

The oilfilled COAMS streamer (Figure 3.6) consists of 15 sections, each 76 m long. The active length is 1140 m with a total of 102 hydrophone groups. A vibration insulation module (VIM) is attached to the front and end of the array. The hydrophone groups of the first four sections consist of five sub-groups spaced at 1.19 m giving a group spacing of 4.76 m. Each sub-group contains 5 single hydrophones of a total group length of 10 cm. The hydrophone groups in sections five to fifteen consist of 10 hydrophone sub-groups. The 5 individual hydrophones within a sub-group are so closely spaced that they do not produce a directivity pattern noticeable in the seismic frequency range. The 1.19 m spacing for each major group however results in a significant directivity pattern, especially for the channels 65–102, where 10 sub-groups are summed to one channel. The directivity patterns for the two different settings are visualized in Figure 3.7 and Figure 3.8.

The spacing of the hydrophone groups increases along the array to 9.52 m in sections five and six, 19.04 m in sections seven and eight and 38.08 m in sections nine to 15. There are also five depth sensors along the array and a heading sensor at the tail of the array for monitoring of the streamer position. The depth sensors were calibrated by towing the streamer at the surface for about 5 minutes. The readings were then averaged to estimate the bias of the depth sensor (Table 3.2).

	Sensor 1	Sensor 2	Sensor 3	Sensor 4	Sensor 5
Bias [m]	13	12	11	10	12

Table 3.2 Bias of depth sensors.

From an earlier experiment with the COAMS streamer in 1998, it was known that the streamer has strong positive buoyancy and was floating at the surface for most of the survey making seismic recordings almost impossible. To balance the streamer at a greater depth, sheet lead was added along the streamer for the COAMS-99 experiment

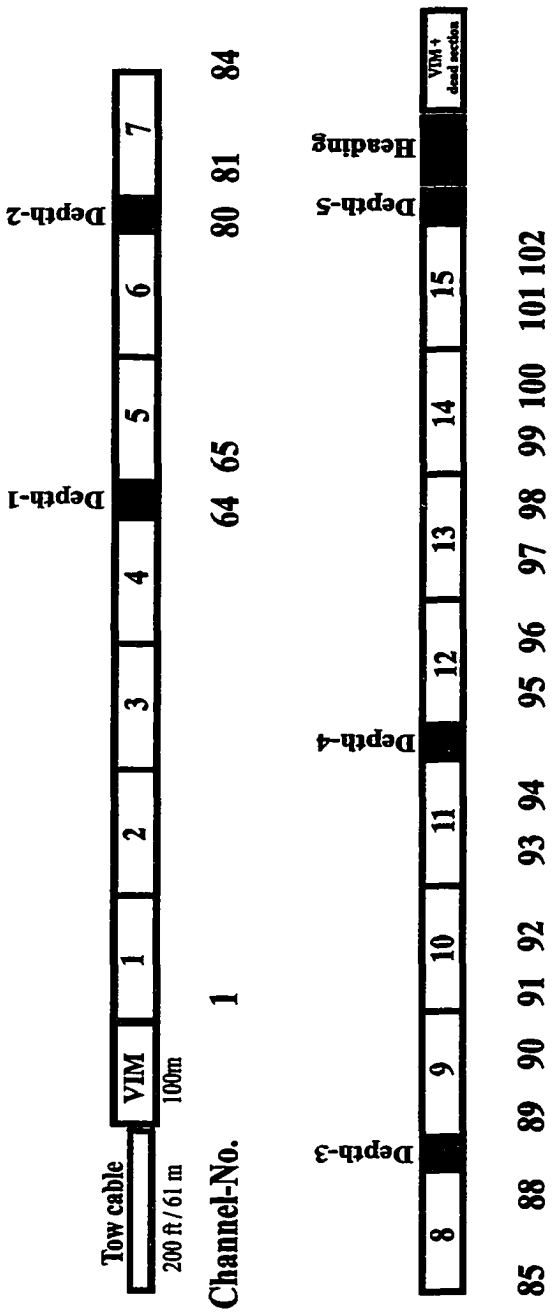

Figure 3.6 Nominal geometry of the COAMS array.

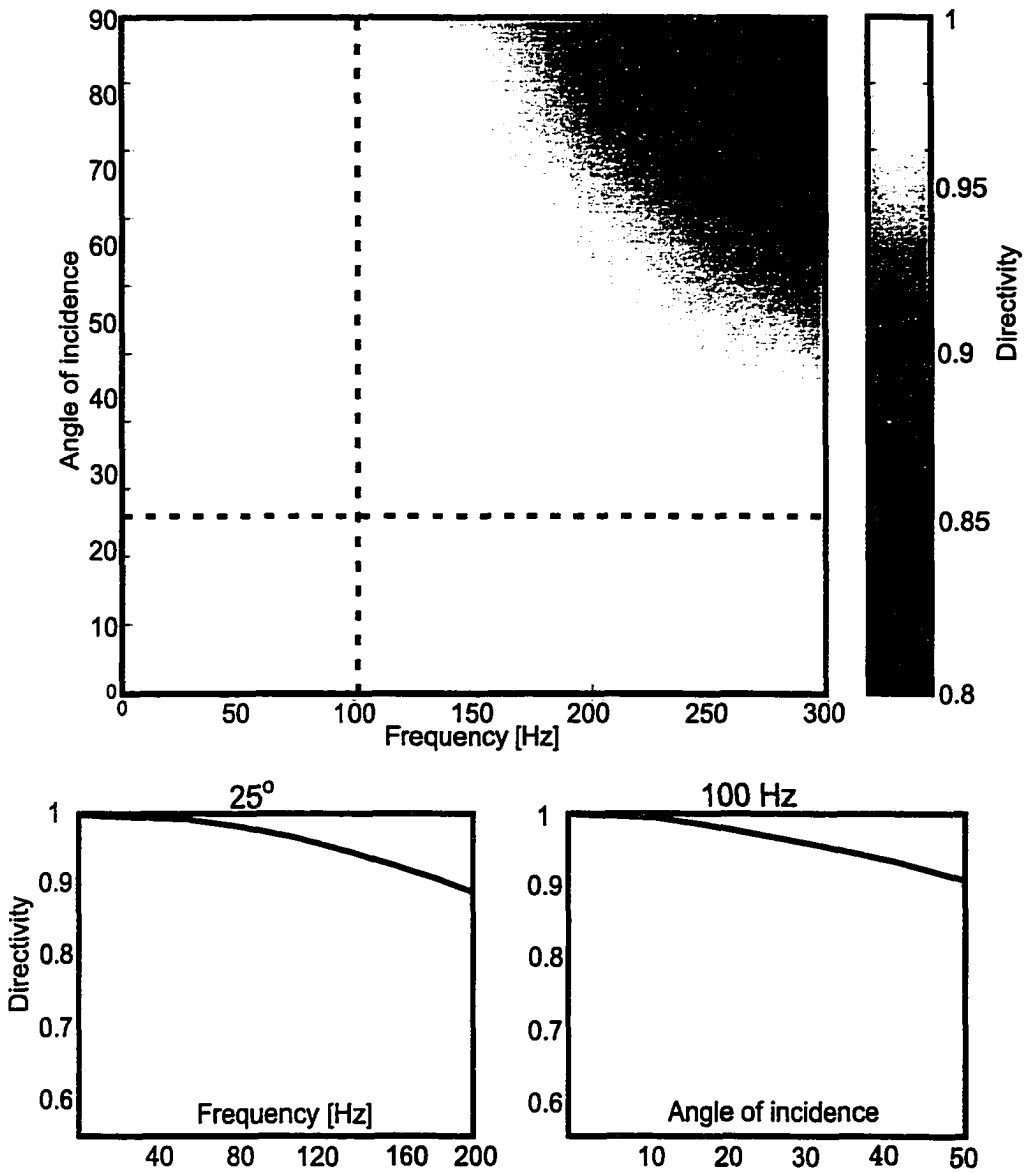

Figure 3.7 Directivity pattern of the COAMS front array with 5 hydrophones per group. For the maximum frequency content (200 Hz) and estimated maximum angle of incidence (50°) the signal attenuation due to the directivity does not exceed 10%.

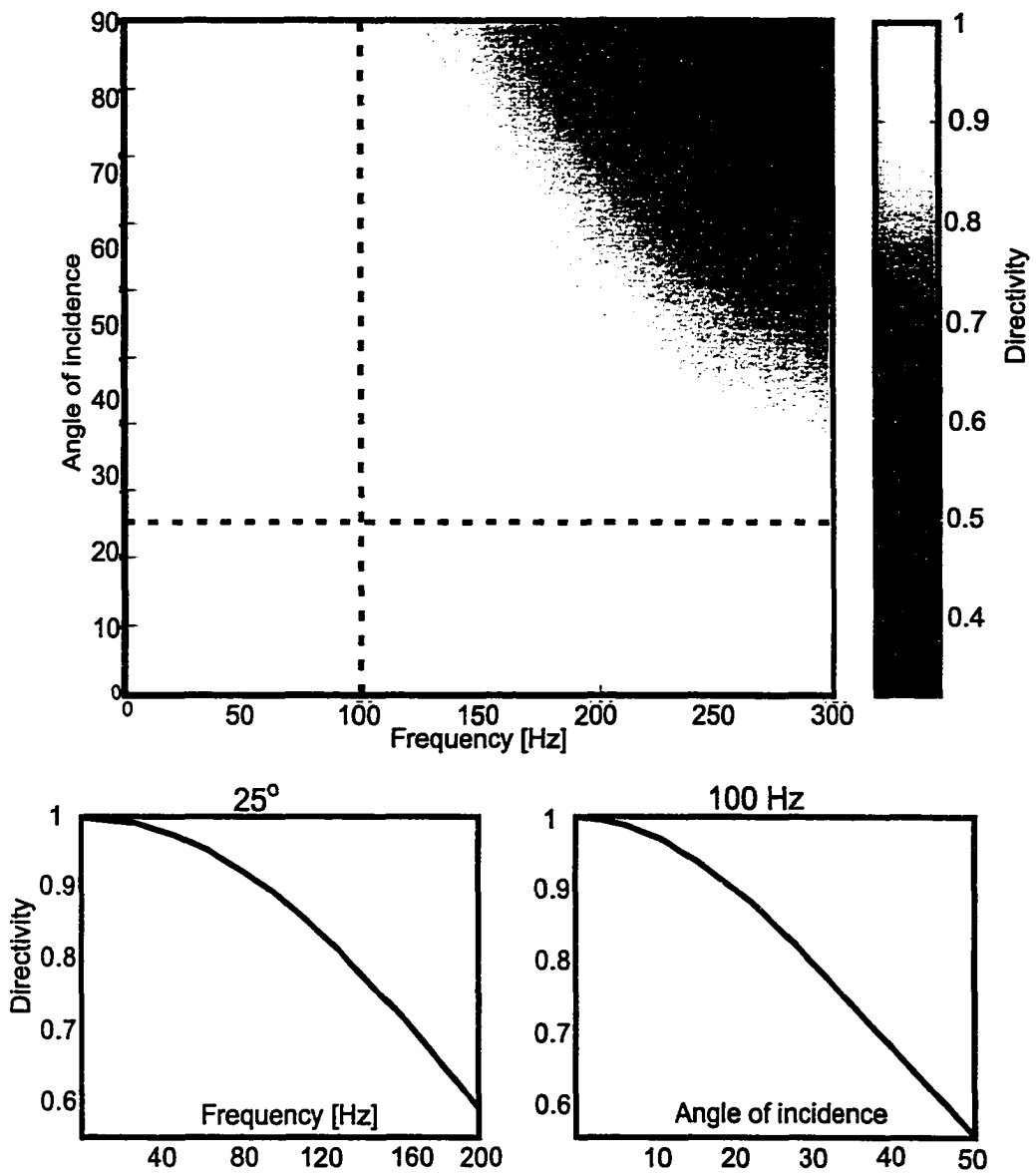

Figure 3.8 Directivity pattern of the COAMS far offset array with 10 hydrophones per group. Attenuation of the signal at far offsets (beyond channel 64, 440 m) can be up to 45% for the maximum frequency (200 Hz) and estimated angle of incidence (50°).

Section	Distance from front of section [m]
8	25, 50
9	13, 25, 37, 50, 63, 75
10	13, 25, 37, 50, 63, 75
11	0, 25, 37, 50, 63, 75
12	0, 25, 37, 50, 63, 75
13	25, 50, 75
14	25, 50, 75
15	25, 50, 75
Dead section	25, 75
Aft VIM	0, 50

Table 3.3 Position of sheet lead added to the COAMS array.

(Table 3.3). The streamer was trimmed by this method to a depth between 10 m to 40 m below the sea surface.

The tail compass was not calibrated separately. A typical plot of the compass reading and a comparison to the ship heading is shown in Figure 3.9. The ship heading and compass reading are in good agreement after the streamer equilibrated to the new line direction after a turn.

A mean heading was calculated for the ship heading and streamer compass separately. Since the compass accuracy is not known and the ship heading varied by about 2°, streamer equilibration was defined as the position when the streamer compass deviates less than 2° from the mean of the streamer compass calculated from the last 4 km of the line. There is no information on the shape of the COAMS array in the x-y plane. If we assume a straight array, a deviation of 2° is equivalent to a crossline deviation distance of about 45 m for a total offset of 1300 m. This distance

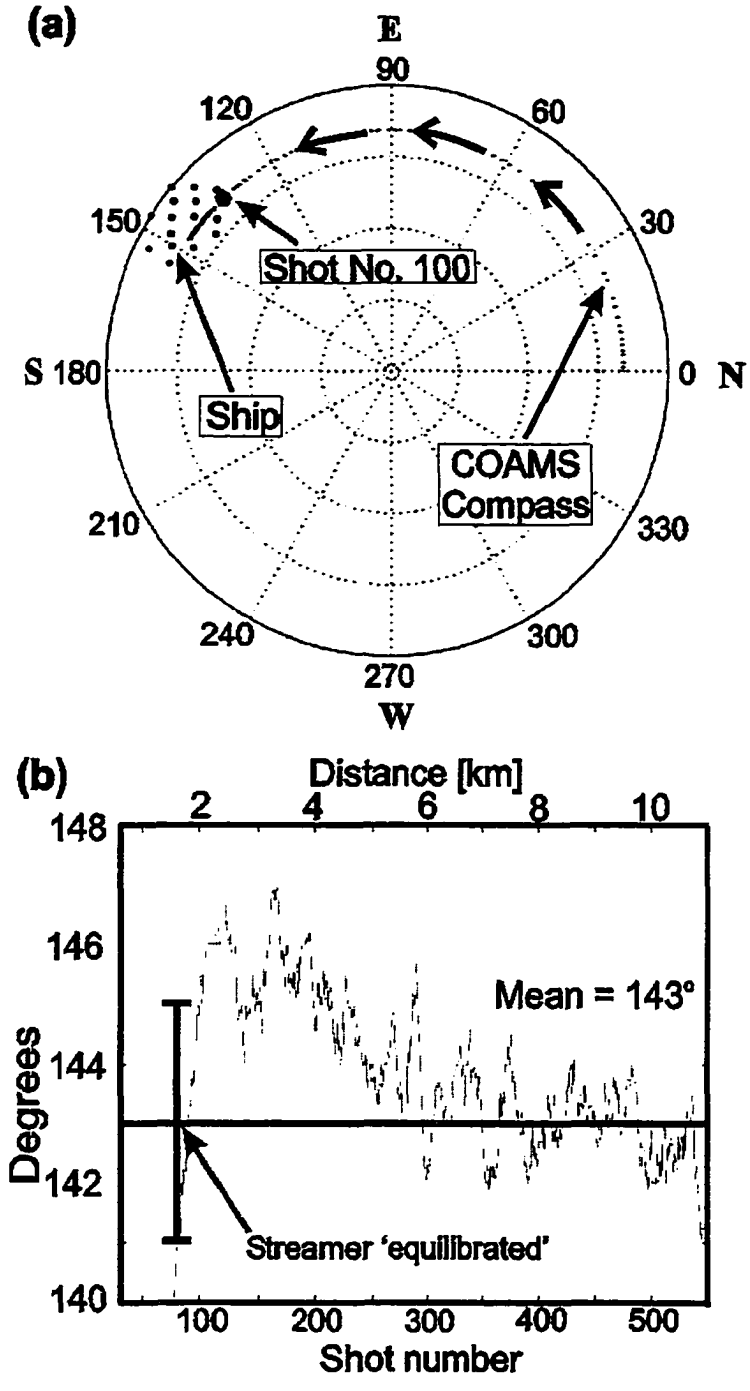

Figure 3.9 Analysis of compass reading of COAMS inline 17. (a) Polar diagram and (b) compass heading along seismic line. Average heading and compass readings are both 143 °.

is less than half the inline spacing.

Feathering can be used positively to obtain true 3-D seismic information (e.g. Yilmaz, 2001), but very good array positioning is necessary. This is not possible with only a tail compass, and therefore seismic processing was done in 2-D only, i.e. a projection of the data onto the inline direction.

Streamer equilibration to 2° took on average about 80 shots or 1500 m, which is almost three times the expected value of 500 m initially used for the safety buffer during acquisition. From each seismic line recorded, about 1500 m from the start of the line has to be omitted in the full-offset analyses to avoid false interpretation. Since for final stacking only the front part of the array was used (first 64 channels, maximum offset 460 m) a total of 1000 m was omitted from the start of the array to maximize the area available for interpretation.

The analog pressure signals of the hydrophones were digitized onboard in the lab at a frequency of 700 Hz, i.e. the maximum frequency content in the COAMS data is 350 Hz. The system contains a built-in analog filter to avoid aliasing. The corner frequencies were set to 10 Hz and 200 Hz. From these corner frequencies the amplitudes are attenuated so that the amplitudes at 0 and 350 Hz are at -30 dB respectively.

3.3.3 Teledyne Single Channel Streamer

The Teledyne hydrophone array is a 50 m long oilfilled streamer, composed of a 15 m vibration isolation module (VIM), a 25 m long active section with 50 hydrophones spaced every 0.5 m and a tail 10 m long VIM. The head of the array was towed 42 m behind the stern of the ship and its estimated depth was 4 m based on the notch at 175 Hz in the frequency spectrum using equation (3.2). A preamplifier in the streamer had a lowcut filter set to 60 Hz. The signal was then filtered with a Krohn-Hite filter at 70–2000 Hz. Except for the first three lines, the Teledyne was recorded on the

COAMS system on channel 83 at a sampling frequency of 700 Hz.

3.3.4 3.5 kHz Subbottom Profiler

Each line of the COAMS-99 survey was recorded by a 3.5 kHz subbottom profiler (ORE Model 140 transceiver), which is mounted inside the hull of the ship. The system consists of 16 individual transceivers combined to one sea chest with an array size of 82 cm × 82 cm. The combined transmitting beam has a opening width of 30°. The transmitted signal was sent at a four second repetition rate. Recording length was 1310 ms at a maximum recording delay of 1310 ms. The sampling frequency was 39 μs. The outgoing pulse was recorded once for further processing and interpretation (Figure 3.10). Plotting of the 3.5 kHz data is done using the envelope.

3.3.5 12 kHz Echosounder

The 12 kHz Simrad EA-500 echosounder was used during the COAMS-99 cruise and the July 2000 3-D seismic survey. Data were plotted on the ship's HP color inkjet only. No digital information could be acquired. The reflected echos were analyzed based on the internal settings of the signal output level, time-varying gain, and receiver characteristics and converted to a color-coded reflection strength. The color code used for plotting the reflection strength is defined in table 3.4. The echo strength is divided into twelve color categories. The scale is logarithmic with a 3-dB step between each color, which gives the color scale a range of 36 dB from the weakest to the strongest signal.

3.3.6 Navigation

The primary GPS navigation was by a GBX GPS/Beacon Receiver (SNR 25) installed for the survey. The antenna was located 15 m from the stern at the ships aft mast. The system recorded at one second intervals longitude, latitude, day, time

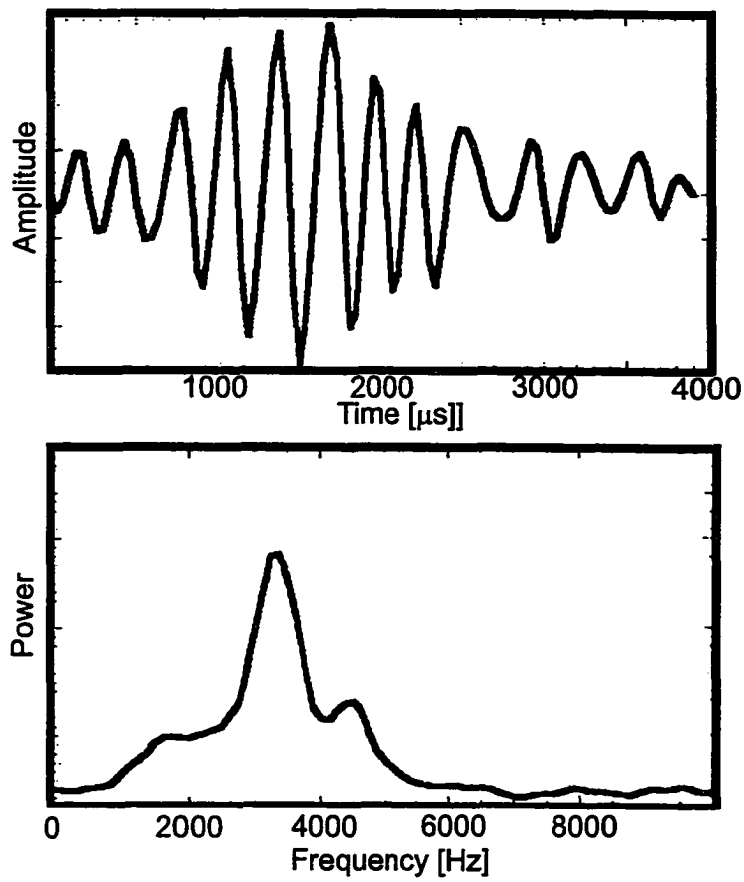

Figure 3.10 Source wavelet of the 3.5 kHz subbottom profiler and corresponding power-spectrum.

and water depth as determined from the automatic bottom picker on the shipboard 12 kHz echo sounder. The water depth was calculated by using a fixed mean water speed of 1492.6 m/s. Bathymetry was later corrected to true depth by using the measured sound speed profile (see also section 4.1). The sound profile was measured once at the end of the cruise with a velocimeter (Applied Microsystems Ltd.). The velocimeter measures the traveltime of an acoustic signal that is emitted by the system

Black/White	from weak signal to -44 dB
Blue	-44 to -41 dB
	-41 to -38 dB
	-38 to -35 dB
	-35 to -32 dB
	-32 to -29 dB
	-29 to -26 dB
	-26 to -23 dB
	-23 to -20 dB
	-20 to -17 dB
	-17 to -14 dB
	-14 to -11 dB
Red	from -11 dB to very strong signal

Table 3.4 Color code used for echo strength representation of the Simrad EA-500 12 kHz echosounder.

and reflected from a metal plate, mounted 15 cm below the emitter. Simultaneously temperature and pressure were recorded.

3.3.7 DTAGS

The DTAGS (Deep Tow Acoustic Geophysics System) was deployed in the area of investigation around the ODP Site in 1997 (Chapman *et al.*, 2001). Data from this survey and reprocessed data by W. Wood, NRL, are used in the study of the blank zones (Chapter 5 and 6). The DTAGS system consists of a Helmholtz transducer source emitting a chirp-like sweep signal of frequencies from 250 - 650 Hz and a 600 m long hydrophone streamer with two subarrays each containing 24 hydrophone groups (Gettrust and Ross 1990; Gettrust *et al.*, 1999; Chapman *et al.* 2001). The

original sweep was not recorded and a synthetic sweep was used for cross-correlation. Source waveform and amplitude after correlation proved to be quite unstable. The tilt of the DTAGS streamer varied considerably so careful source and receiver geometry corrections were required for the short wavelengths of 2–6 m (Walia and Hannay, 1999). In this study only the first five near offset traces were used to create a stack without applying normal moveout corrections.

Chapter 4

COAMS Multichannel Seismic Data Processing

4.1 Introduction

The goal of multichannel seismic data processing is to obtain a seismic image of the subsurface for geological/structural interpretation and to characterize the subsurface lithology by seismic interval velocities. Seismic velocities are also an important tool to identify gas hydrate deposits as outlined in Chapters 1 and 2.

In this study, 40 multichannel lines spaced at 100 m and eight lines crossing the main grid perpendicular were acquired with the COAMS array. Special problems in processing arise due to the irregular hydrophone spacing of the array, the irregular towing depth and the irregular shot spacing. This requires a careful pre-processing sequence for determining the survey geometry by an array element localization (AEL).

The irregular towing depth of the COAMS array also results in a receiver ghost which destructively interferes with primary reflections. The effect of the receiver ghost is a loss in vertical resolution as well as distorted velocity spectra. Several techniques were tested to suppress the receiver ghost and only a combination of several pre- and post-stack/migration commands were able to reduce the ghost by about 50%.

Each of the 48 lines had to be processed with the same sequence of commands to allow for 3-D interpretation and the goal of the processing was to find a sequence of commands that on average performs well on all lines.

4.2 Pre-processing

4.2.1 Array Element Localization (AEL)

The first processing step was the definition of the survey geometry, the x, y and z- coordinate of each shot and receiver. Sheet lead along the streamer stabilized the overall shape compared to the earlier COAMS-98 cruise, but changes in depth of 20–40 m were still observed.

If the depth changes were small (1–2 m), the static correction can be ignored and a lateral coherency filter used after normal moveout (NMO) correction (trim statics). Since the depth changes are large, a full static correction to a fixed datum must be performed for the depth and range of each receiver within the array. This information can be inferred from the navigation and the acoustic traveltimes of the direct wave and seafloor reflection.

A new technique was developed as part of this study to estimate depth and offset of the hydrophones based on a linearized inversion of the acoustic data using regularization to minimize array curvature (Dosso and Riedel, 2001). The depth information recorded on the five pressure sensors along the COAMS array were used as a priori information in the inversion. Prior to inversion a database was created containing a piece-wise 2-D linear representation of the seafloor and the hand-picked traveltimes of the direct wave and seafloor reflection of each shot.

Changes in seafloor topography can create convergence (two or more arrivals) and shadow (no arrivals) zones, as illustrated in Figure 4.1. Due to the piece-wise linear representation of the seafloor, additional artificial shadow and convergence zones are created by the ray theory (Figure 4.2). These zones can easily be identified in a range and/or time versus ray parameter plot (Figure 4.3). In the case of a shadow zone, receivers within this zone are not used and the regularization, i.e. the smoothness of the model, will *fill* the gap. In case of a convergence zone the first arrival has to be used, i.e. the smallest traveltime.

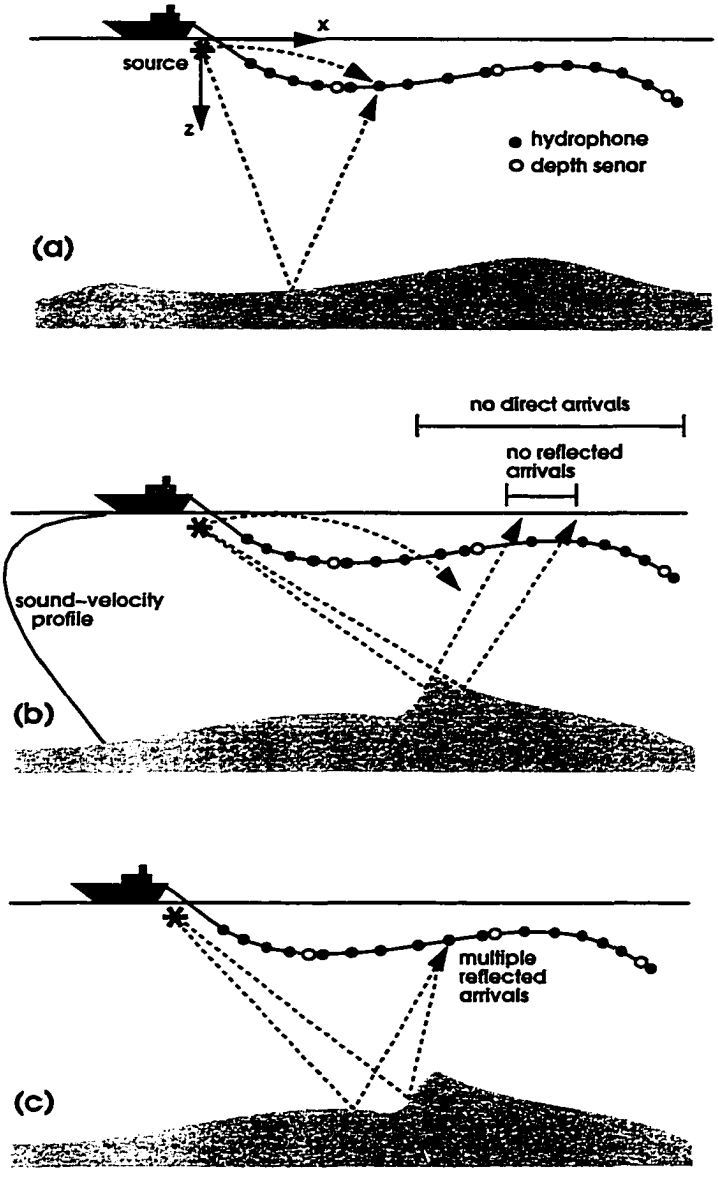

Figure 4.1 Geometry of the AEL inverse problem is illustrated in (a). Shadow zones for direct and reflected arrivals are illustrated in (b). Convergent zones for reflected arrivals are shown in (c).

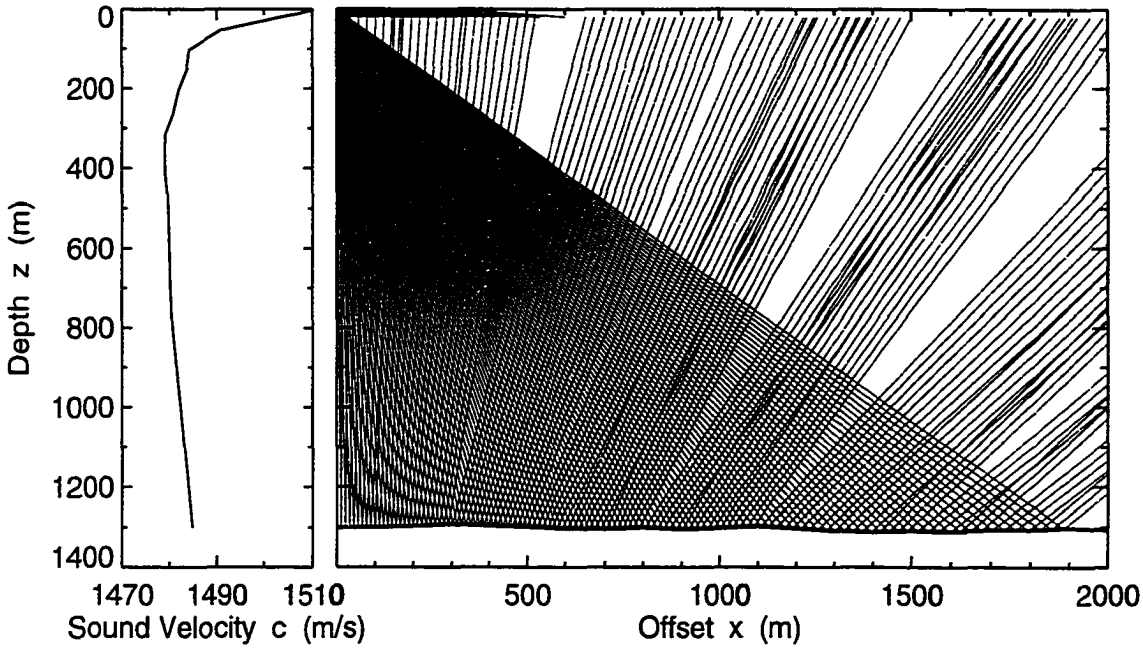

Figure 4.2 Simplified sound velocity profile and representative direct and reflected ray paths for nominal source and receiver depths of 2 and 20 m, respectively. Bathymetry was chosen arbitrarily.

A problem arises from downward refraction of the acoustic waves emitted from the source. The direct arrival is lost at a range of about 600 m because the streamer is towed in a strong thermocline. The sound speed decreases from 1505 m/s to 1480 m/s over a depth range of about 100 m. The front part of the array has two arrivals, the direct and reflected rays, and can therefore be controlled much better than the far end of the array. Beyond an offset of about 600 m, only the seafloor reflection can be used, along with the depth sensors and the regularization constraint.

The accuracy of the AEL inversion was limited to several meters, especially for the far end of the array. The lack of a direct wave and the picking accuracy of the travel time for the reflected arrival yield an error for the depth estimates of about 2–4 m, or 3–8 ms two way travel time (TWT). This residual error is small enough to

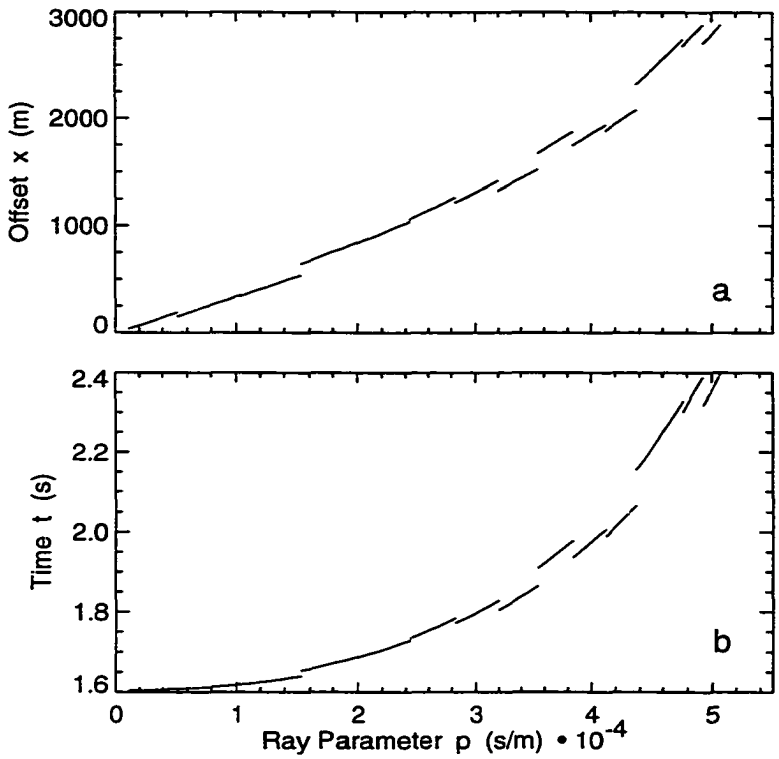

Figure 4.3 Reflected ray offset x and travel time t as a function of ray parameter p for a synthetic inversion example.

be corrected by an automated trim statics. The static correction based on the AEL results was carried out for vertical ray paths. The time difference between a full slant path and the vertical path is less than the uncertainty of the AEL method and was often below the sampling rate of the seismic data (1.43 ms).

Since only one source was used, which was in line with the streamer, the y-deviation of the streamer cannot be identified from the acoustical data. The compass gives directional data from the tail end of the streamer only. No information is available of the total shape of the array. The compass reading showed that the streamer followed the ship direction after it equilibrated within $\pm$ 2°. Only those data where the streamer is $\pm$ 2° directly behind the ship are used in this study.

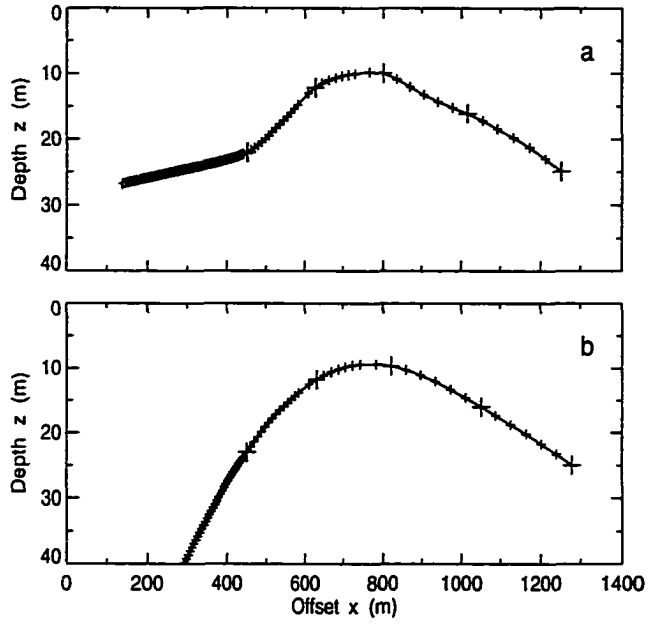

Figure 4.4 (a) Inverted hydrophone group positions using the AEL algorithm; (b) positions determined via cubic spline interpolation of the five depth sensor readings. Positions with large crosses indicate those hydrophones closest to a depth sensor.

The AEL was performed at every 20th shot on each line. The results were then linear interpolated for all shots in a line. The general shape of the streamer did not change significantly during the cruise. A comparison of an inverted array position versus the positions derived from cubic spline interpolation of the depth sensor readings is shown in Figure 4.4.

Due to the heavy tow cable at the front of the array and only one VIM of 100 m length attached to the tow cable, the front of the array was exposed to the greatest changes in towing depth. The far end of the array was almost de-coupled from the heave of the ship.

A complete description of the mathematical aspects of this inversion technique can be found in Dosso and Riedel (2001). A brief outline of the inversion procedure

is given in Appendix A.

4.2.2 Geometry Definition

Seismic data processing was done with the ITA/Insight system. Due to the complicated shape of the COAMS array and the non-regular shot point spacing a standard marine geometry definition could not be performed. Several programs were developed for geometry definition in ITA/Insight using the navigation data and the results from the AEL inversion for depth and offset of each individual hydrophone group in a shot gather. Each hydrophone group was assigned a common mid point (CMP) location based on a simplified geometry (flat array) to increase CMP fold. The actual offset and depth information as derived from the inversion for each receiver is still maintained. An example of a typical ITA/Insight pre-stack job file for geometry definition and all seismic header words accessed is given in Appendix B.

4.3 The Problem of the Ghost

The minimum depth of the COAMS array was constrained to around 10 m by adding sheet lead to the cable as explained in Section 3.3.2. The effect of towing the streamer at such a depth is a receiver ghost as a separate reflection as illustrated in Figure 4.5. The receiver ghost is a reflection from the sea surface that has opposite polarity to the regular/primary reflection. The ghost interferes destructively with the primary reflections and generally decreases vertical resolution (see also Section about velocity determination). The arrival time of the ghost varies along the array (see e.g. Figure 4.5). Since the array has a simplified shape of an *upside-down U*, the ghost gets close to the primary reflections at the shallowest part of the cable. Also, the waveform of reflections, including the ghost, changes along the array, mainly due to the effect of having five hydrophones per channel within the first 64 groups and

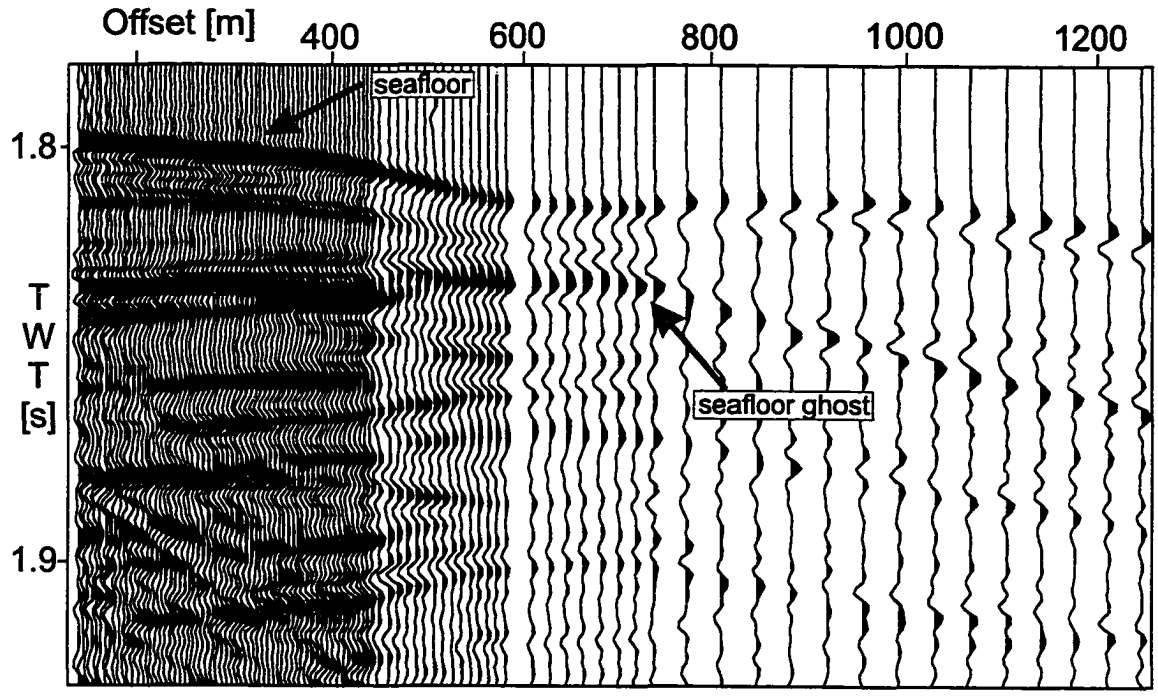

Figure 4.5 Example of a shot gather (after processing step 1) containing the receiver ghost (no static shift derived from AEL applied).

ten for the far end groups. A second change in waveform arises due to the change in shape/tilt of the array. This results in a slightly different angle of incidence of the wavefronts approaching the cable and therefore in a different summation output.

The following processing techniques have been used to suppress the ghost:

- predictive deconvolution in pre-stack domain,
- predictive deconvolution in post-stack domain,
- velocity filtering via slant-stack.

None of the above techniques was able to completely remove the ghost alone. A combination of pre-stack deconvolution, slant-stack and post-stack (post-migration) predictive deconvolution gave the best result.

The optimum towing depth of a multichannel streamer is mainly a function of the frequency of the seismic source used. To minimize the ghost, the streamer should always be towed as shallow as possible. If the frequency of the seismic source is below 40–50 Hz, a depth of even 5 m might be acceptable. The problem of a near-surface towed streamer is the proximity to the ocean swell, which reduces the signal-to-noise ratio. Another possibility of avoiding a ghost-interference is towing the streamer at a greater depth, so that primary and ghost reflectors are separated out. However, depth and x-y deviation control of a streamer towed at a depth of 400–500 m might be a challenging task.

4.4 Multichannel Processing Scheme

The main 3-D data set was processed using the same command sequence (see Appendix C for ITA command files). The pre-stack processing sequence can be divided into three major stages after including the geometry information in the header of the seismic data. Stage 1 is done in the shot-gather domain followed by CMP sorting and trim static correction. The last stage is velocity definition using the semblance technique.

4.4.1 Processing in Shot-gather Domain

The objectives of the processing sequence in the shot-gather domain are to perform the static correction and to enhance the signal-to-noise ratio by using bandpass filters and prediction deconvolution operators.

The first three steps of processing in the shot gather domain include amplitude correction for spherical divergence (by multiplying with corresponding TWT), static correction (vertical shift) for receiver depth as determined from the AEL and correction for trigger time delay. The next step is bandpass filtering and predictive

deconvolution for airgun bubble and receiver ghost attenuation. The bandpass corner frequencies determined from amplitude spectra were set to 10, 20, 160 and 200 Hz before and 20, 30, 160, 200 Hz after the deconvolution. An example of the raw data is given in Figure 4.6. A strong low frequency (5–25 Hz) flow noise generated at the various bulk heads along the array dominates the data set (Figures 4.6 and 4.7).

The parameters of the predictive deconvolution were determined from the autocorrelation function (Figure 4.8.):

- 10 ms gap length,
- 500 ms operator length,
- 0.1% stabilization noise.

The predictive deconvolution works on the auto correlation function (ACF) of the seismic data by leaving the elements of the output's ACF which belong to the window from 0 to 'gap' unaltered, but minimizing the rest of the ACF. An example of the ACF of a typical bandpass filtered shot gather is given in Figure 4.8. From this figure it can be seen that the signal corresponding to the ghost always arrives after 10 ms. Although the output ACF does not show any strong signal corresponding to the ghost, it is still prominent in the seismic data. The operator length of 500 ms gave the best overall results and was chosen based on a series of deconvolution tests with varying operator lengths. The amount of 0.1% stabilization noise is recommended by the ITA system. An increase of this parameter would result in higher frequencies on the output seismic shot-gather, which have to be filtered out afterwards.

4.4.2 Processing in CMP Domain

After bandpass filtering and deconvolution the data were sorted into common mid point (CMP) gathers. Residual positioning errors remained in the data after the AEL inversion due to the resolution limits of the method. These residual errors are less

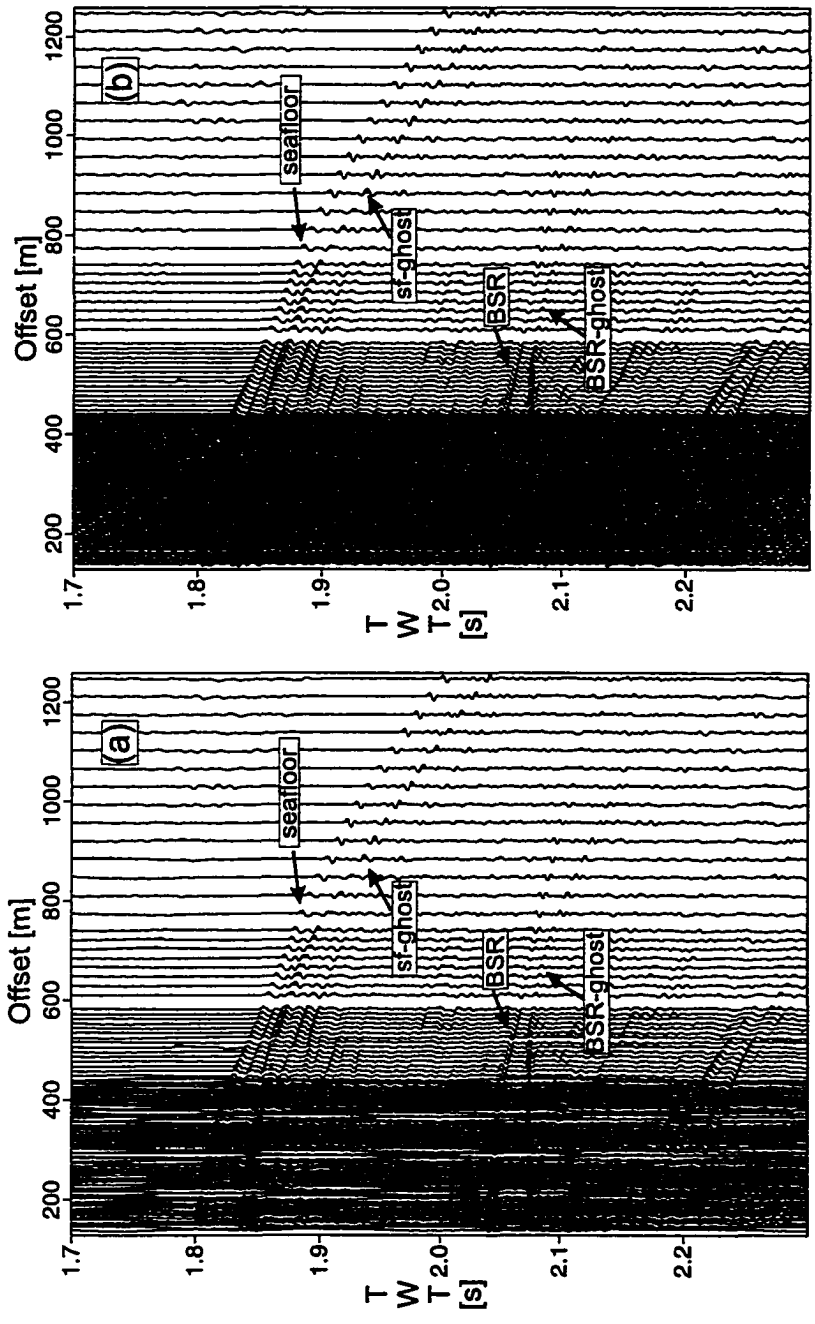

Figure 4.6 Comparison of (a) unprocessed and (b) processed shot gather after stage 1 of processing sequence with AEL based static shifts applied. For plotting purposes an AGC with 100 ms window length was used.

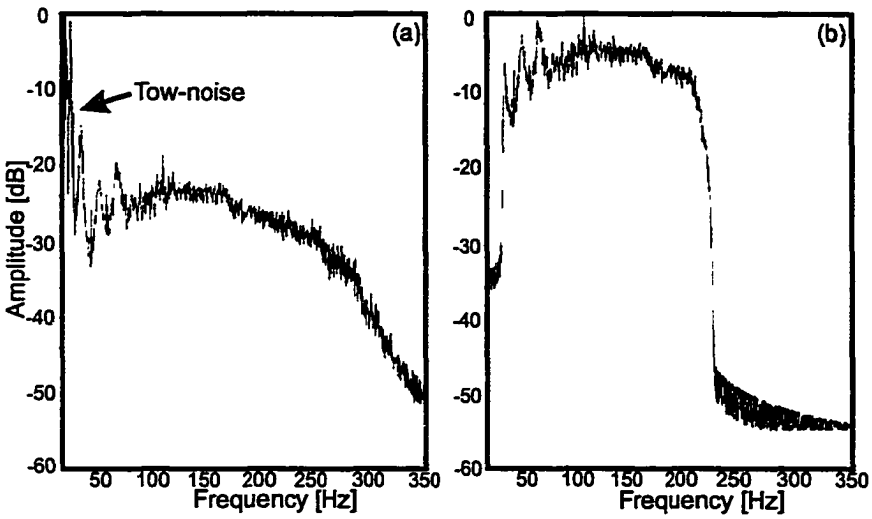

Figure 4.7 Comparison of (a) unprocessed amplitude spectrum and (b) processed amplitude spectrum after stage 1 of processing sequence.

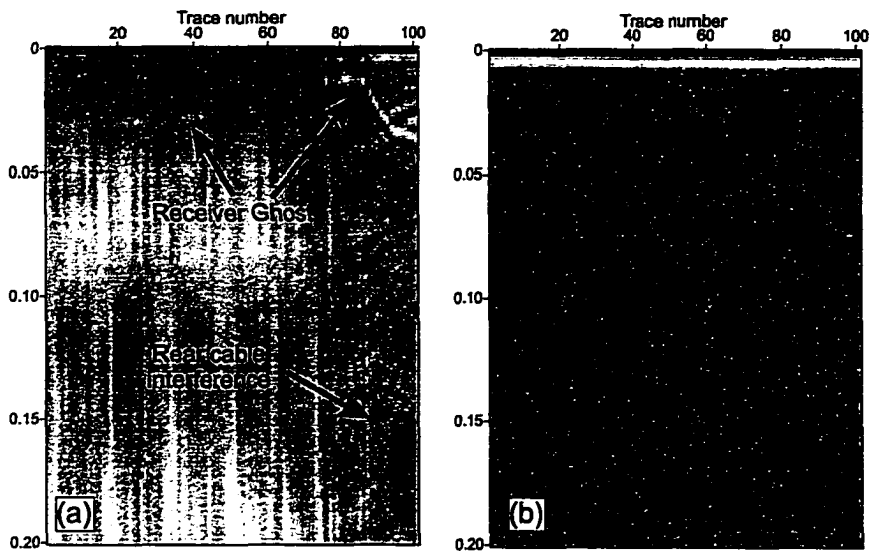

Figure 4.8 Comparison of (a) unprocessed and (b) processed auto correlations after stage 1 of processing sequence.

than 10 ms TWT. To remove these errors, an automated trim static correction was performed. Using an average velocity profile a normal moveout (NMO) correction

was carried out mainly to flatten the seafloor reflection. The trim statics, optimized to a time window around the seafloor reflection, calculates the time shifts needed on each trace to maximize the stacked power along the flattened reflection. This calculation was performed three times with different search parameters for the time shifts to optimize the result. After trim statics the inverse NMO was performed. The improvement of using the trim statics is illustrated in Figure 4.9.

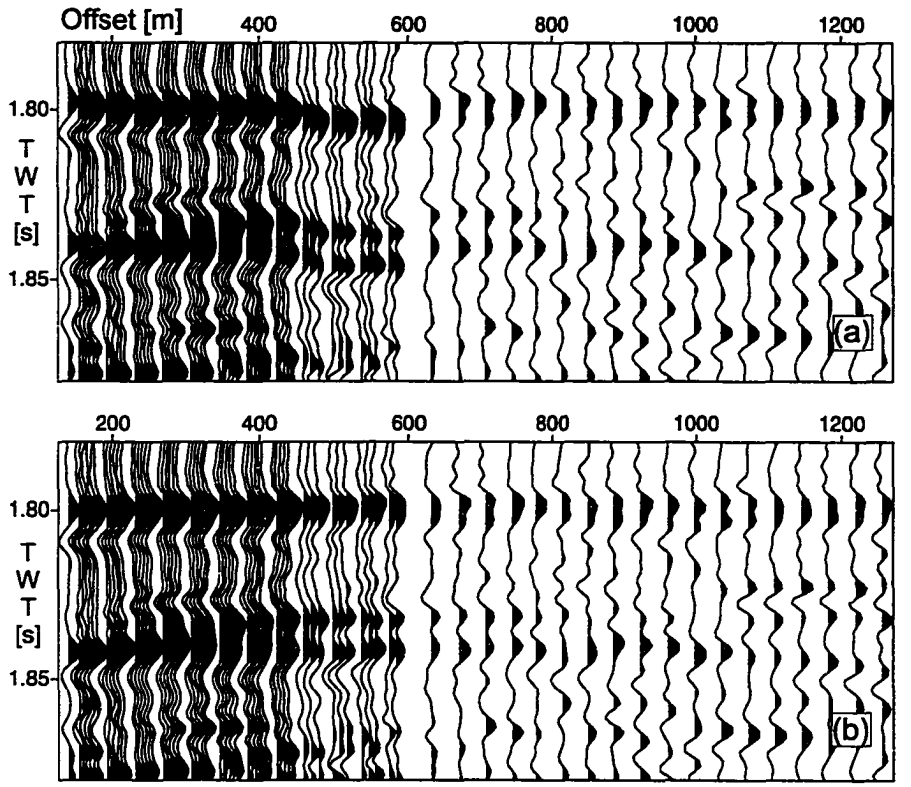

Figure 4.9 Comparison of a CMP (a) before and (b) after applying trim statics (with AEL-based static shifts previously applied).

4.4.3 Velocity Analysis

Velocity analysis is needed for stacking the multichannel seismic data and for geological/lithology information. Velocity analysis was carried out by using the semblance technique. The semblance technique is based on performing NMO corrections for varying velocity profiles and calculating the stack-power of the NMO corrected CMP gather on a sample-by-sample basis. The semblance plot is typically visualized by a colour-coded contour plot of stack-power as a function of velocity and TWT. Velocities are picked manually from the semblance plot by the interpretor.

A Super CMP (SCMP) was created by summing six adjacent CMPs to increase the fold. Velocity analysis was carried out every 20th CMP. To optimize the semblance resolution, several additional processing steps were added: forward and inverse τ–p filter using an average velocity depth profile and automatic gain control (AGC). The τ–p filter generally increases the signal-to-noise ratio (Yilmaz, 1987). The τ–p filter performs hyperbolic velocity filtering. The data is transformed into the τ–p domain limited to a window about a specified velocity profile. This procedure is a muting operation in the τ–p domain and helps to reduce noise that does not correspond to hyperbolic events such as linear noise travelling along the array (Mitchell and Kelamis, 1990). The AGC helps to identify lower amplitude reflections. The improvement of using the τ–p filter and an AGC on the semblance is illustrated in Figure 4.10.

The influence of different static corrections on the velocity spectrum was investigated by comparing the semblance output for (a) the static correction based on the AEL, (b) a static correction based on a spline interpolation and (c) a constant depth correction for all hydrophone groups (Figure 4.11). Only by incorporating the estimated depth and offset correction based on the AEL was a clear velocity spectrum recovered. The effect of the AEL-based static correction on the velocity determination is examined in the next Section.

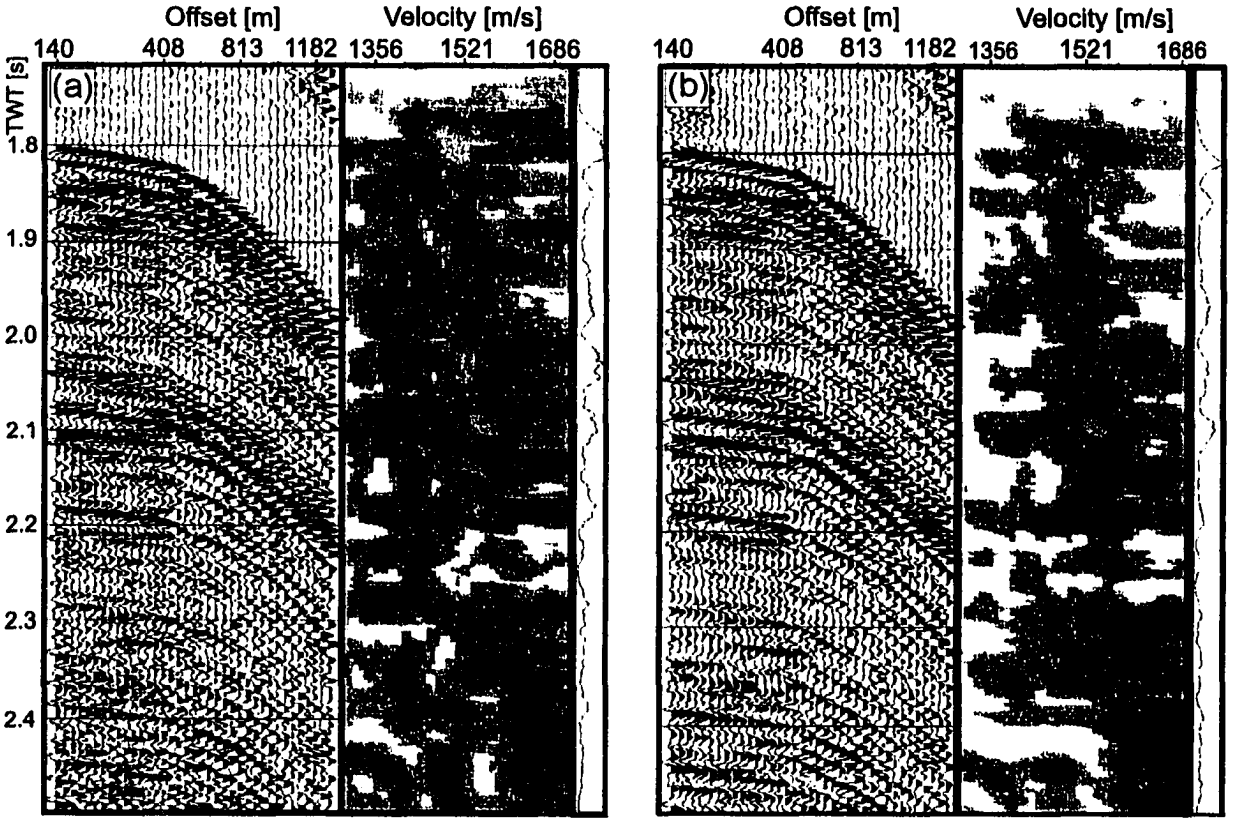

Figure 4.10 Semblance on SCMP (a) without and (b) with τ–p filter and AGC applied. Note the non-linear offset spacing in the SCMP (Screen frame grab from ITA system).

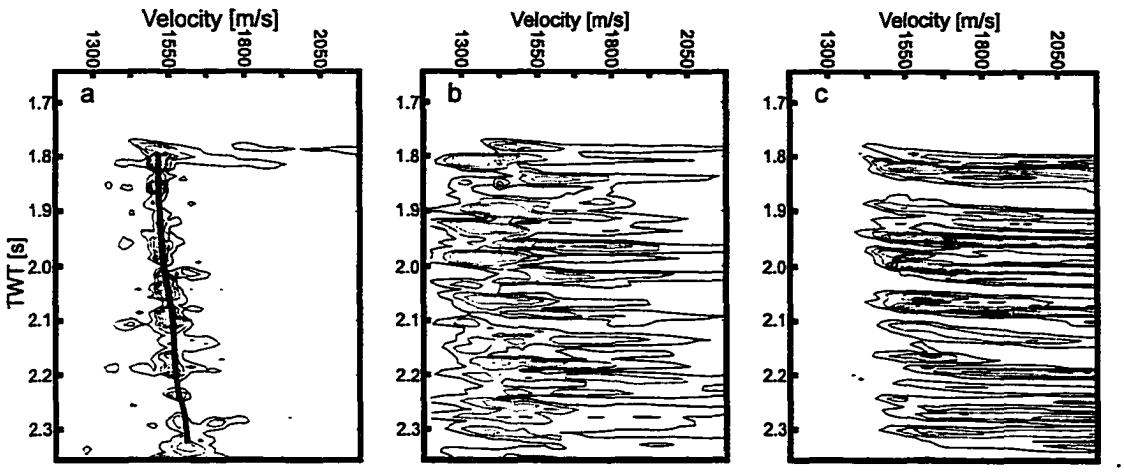

Figure 4.11 Seismic velocity spectra using (a) hydrophone positions determined by AEL inversion, (b) nominal hydrophone offsets and depths 15 m below the sea surface, and (c) hydrophone offsets and depths determined from cubic spline interpolation of depth-sensor measurements (from Dosso and Riedel, 2001).

Velocity Error Estimation

Interval velocities from conventional multichannel data have earlier been used successfully in detecting the presence of hydrate, as mentioned in the introduction. It is therefore important to investigate the uncertainty of the velocity determinations. Several methods can be used to estimate the error in interval velocity (e.g. Al-Chalabi, 1974). A good error estimate of the root-mean-square (RMS) velocity is needed. Critical parameters in interval velocity determination using the semblance technique are maximum offset, signal-to-noise (S/N) ratio and coherent noise such as multiples or ghosts.

There are several systematic errors to the semblance technique, such as a pure two-dimensional treatment of a three-dimensional velocity field and an assumption of a hyperbolic move-out. However, in these data these assumptions (or systematic errors) are negligible compared to random errors due to picking RMS velocities from the velocity spectrum.

In this data set, the maximum offset is 1240 m, which is approximately the water depth. From Figure 4.6 it can be seen that significant moveout is available for RMS velocity discrimination. However, the moveout is strongly influenced by the irregular shape of the array and the receiver ghost. The array shape was determined prior to velocity analysis as described above, restoring the 'correct' move-out hyperbola. Residual moveout deviations were corrected by using trim-statics. In total the error introduced to the velocity analysis due to the array shape is believed to be less than a few percent (about $\pm$ 50 m/s).

The ghost could not be suppressed completely in the pre-stack domain. The waveform of the ghost is opposite to its primary reflection. As seen in Figure 4.5, several deeper reflectors interfere with the ghost reflection. Those deeper reflections however, have the same positive reflection polarity as the seafloor and these reflections destructively interfere with the seafloor ghost. The semblance technique is based on determining the NMO that maximizes the stack power. The destructive interference of the ghost with regular reflectors, however, partially decreases the stack power. The result is a smearing of the RMS velocity contours. Only strong primary reflectors with large reflection amplitude can be identified in a semblance plot. Reflectors with small reflection amplitude (usually including the BSR) are more vulnerable for ghost interference and could not be detected. The result is a coarse RMS and interval velocity profile with sometimes only one or two reflectors in addition to the seafloor reflection.

Estimating the error in RMS and interval velocity is difficult due to the complicated ghost interference. One way is investigating the variation of the interval velocity of a particular reflection along a seismic line assuming its interval velocity does not change. A prominent reflector on inline 27 at a depth of about 100 ms TWT bsf was chosen for this analysis (Figure 4.12). No shallower reflectors were strong enough for velocity analysis. With the exception of one CMP on a dipping section, the RMS and interval velocities are consistent with only small variation. The mean RMS velocity

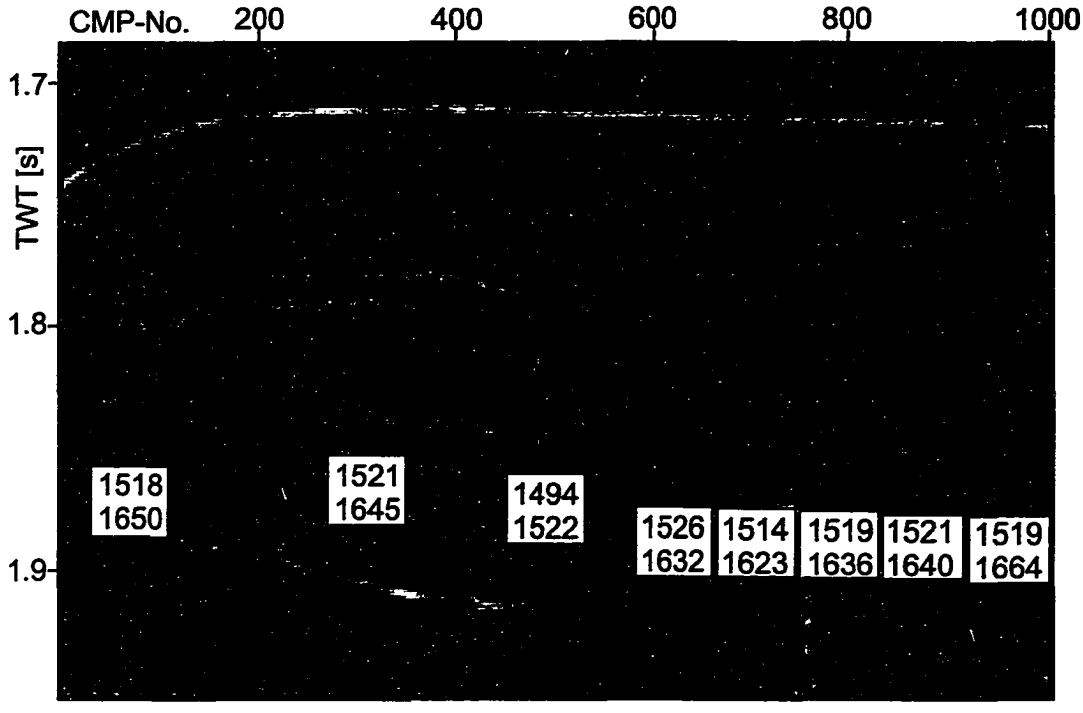

Figure 4.12 Section of stacked COAMS inline 27. RMS and interval velocities of horizon at about 100 ms TWT at selected CMPs are indicated. The mean RMS velocity is 1517 ± 10 m/s and the mean interval velocity is 1626 ± 45 m/s.

is 1517 ± 10 m/s and the mean interval velocity of this horizon is 1626 ± 45 m/s. On average the standard deviation is less than 3% of the interval velocity.

However, this deviation might represent also true variations of the interval velocity along the layer. In order to investigate the accuracy of each individual interval velocity determination, one representative SCMP was used to estimate the picking accuracy of the RMS velocity. In Figure 4.13 the SCMP gather and corresponding velocity semblance spectra are shown (note non-uniform offset) for the maximum (1672 m/s) and minimum (1517 m/s) possible interval velocity for the horizon at about 100 ms TWT below the seafloor. The corresponding NMO-corrected gathers are shown in Figure 4.14. Both interval velocities produce almost identical move-out corrections. Picking of the RMS velocity is normally done by defining the RMS velocity that best

corrects for the moveout. In this case, the accuracy in RMS velocity determination results in an accurracy of ± 80 m/s or equivalently ± 5% for the corresponding interval velocity calculation (given the two given extrema of 1517 m/s and 1672 m/s).

This analysis showed that the error in determining the interval velocity is relatively large. Combining errors due to the shape of the array and uncertainty in the RMS velocity determination probably do not exceed 10%. However, due to the strong ghost interference, no detailed interval velocity profile especially above and below the BSR could be obtained. Although a ± 10% (about 150 m/s) error in the interval velocity profile is reasonable for many velocity applications, it is not good enough for quantitative determination of hydrate concentrations.

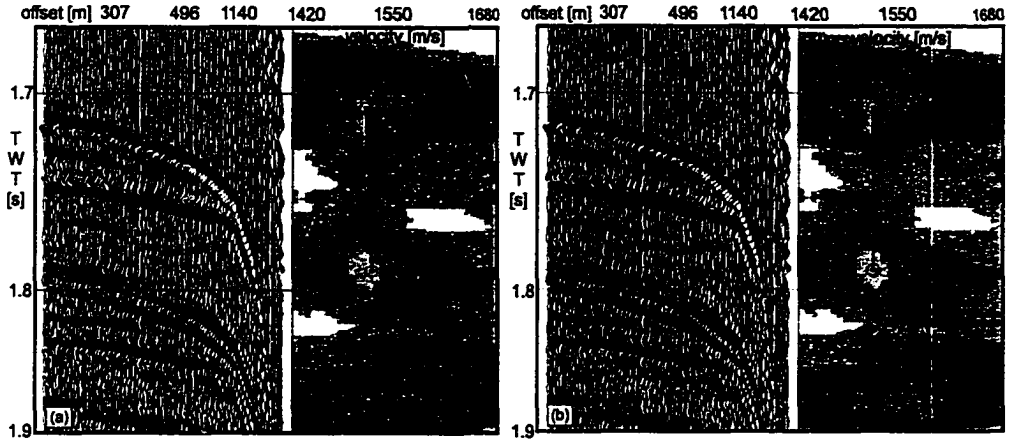

Figure 4.13 SCMP gathers and corresponding velocity spectra and semblance plot for (a) a maximum possible interval velocity of 1672 m/s and (b) a minimum possible velocity of 1517 m/s for the layer at 100 ms TWT bsf. (Note non-uniform offset).

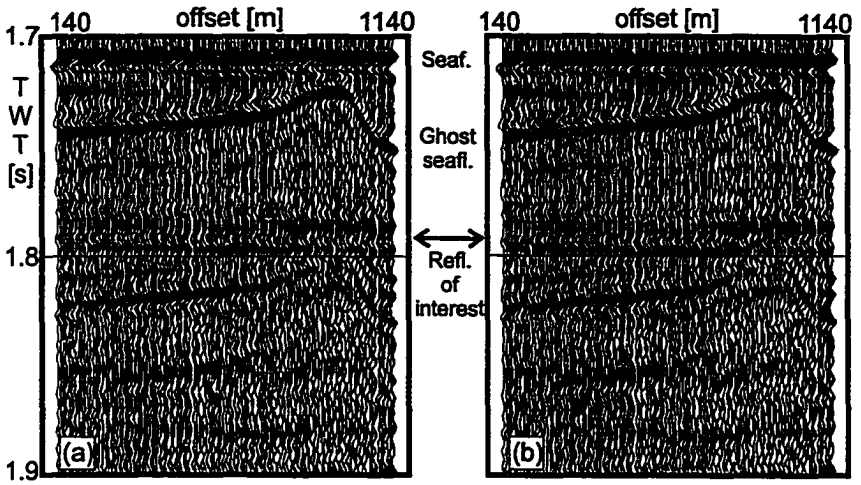

Figure 4.14 Corresponding NMO corrected SCMP gathers for (a) maximum possible and (b) minimum possible interval velocity of the layer at 100 ms TWT bsf.

4.4.4 Interval Velocities and Hydrate Concentration

As outlined above, interval velocity determination from the multichannel COAMS data by using the semblance technique yield relatively large uncertainties. The semblance technique itself is based on manually picking RMS velocities from a velocity spectrum. The picking accuracy is a function of the sharpness of the RMS velocity contours. As shown before, the error associated with picking the RMS velocity results in an error in the interval velocity of the order of 2–5%. This corresponds to an interval velocity error of about 50–100 m/s, depending on the velocity value itself. In addition to this more random component of velocity determination, there is an apparent systematic error to the absolute values of the interval velocities obtained.

Comparing velocities from the ODP sonic log, interval velocities from the multichannel 1989 data and the DTAGS data shows that the velocities from the COAMS survey are too large, especially at shallower depths less than 100 m below the seafloor (Figure 4.15). The DTAGS velocities themselves are relatively low (below 1500 m/s) for the upper 100 m of sediment compared to the ODP log. At greater depths from

100 m bsf to the BSR depth, COAMS interval velocities agree well with previous observations. Interval velocities are around 1650–1850 m/s (with a few outliers as large as 2100 m/s).

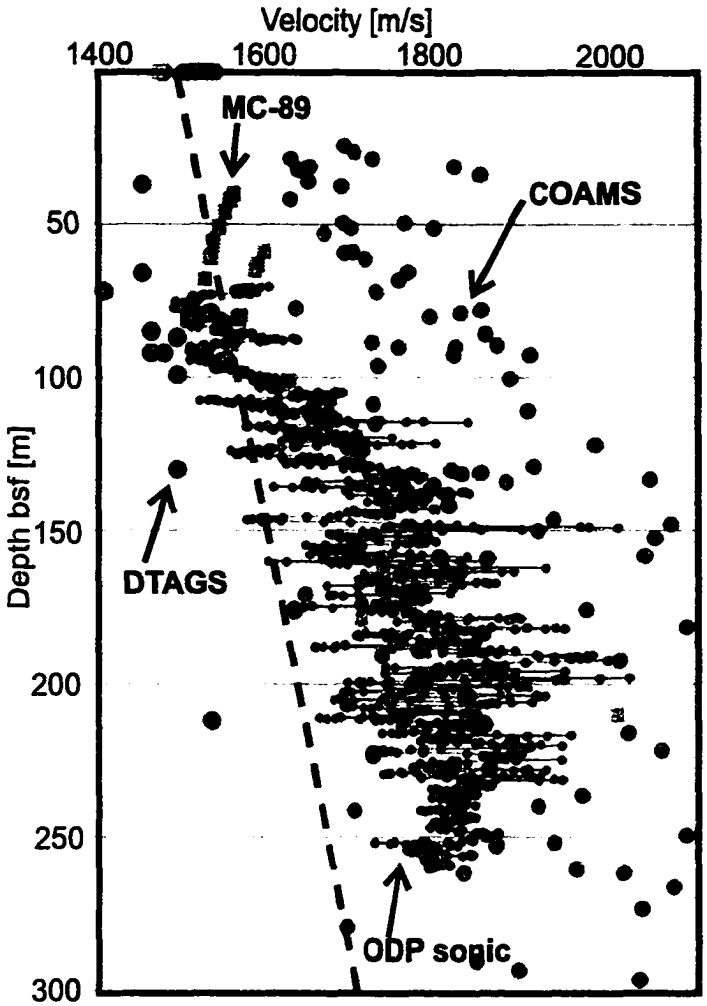

Figure 4.15 Comparison of interval velocities derived from MC-89, DTAGS, and COAMS inline 40. In addition the ODP sonic log 889A is shown.

It is unclear, whether the shallow larger interval velocities are real or not. If the COAMS interval velocities are systematically too high, values at greater depth should also be larger than the ODP sonic log and MC-89 data. Since this is not the case,

the interval velocity values obtained have to be treated with caution.

Using the method based on porosity reduction by Yuan *et al.* (1996) to convert seismic P-wave velocity to hydrate concentration, the shallow high interval velocities would represent hydrate concentrations of more than 10% of the pore space. In the ODP core, the presence of hydrate was inferred based on the occurrence of soupy layers and pore fluid freshening as effect of hydrate dissociation. Soupy layers and low pore fluid salinity associated with hydrate were detected in units II and III only, i.e. deeper than 100 m. The interval velocities obtained from the COAMS-99 survey could therefore not be used to estimate hydrate concentration to useful accuracy.

In order to do a complete 3-D hydrate reservoir evaluation, seismic interval velocities should be estimated with an accuracy of less than 5% (relatively and absolutely). The velocity effect of hydrate is relatively small (about 200 m/s). This requires high quality data. The COAMS system is not able to achieve this accuracy in it's present state. If the array would be balanced at a relatively shallow and constant depth of less than about 5 m below the sea-surface, the ghost would not affect the RMS velocity spectrum and a more detailed interval velocity profile could be achieved. Also no artificial correction for receiver offset and depth has to be carried out. However, the relatively short offset of maximum 1200 m will always limit the accuracy of interval velocity calculations.

4.4.5 Stacking

Due to, the complicated shape of the COAMS array, the relatively high noise level, and the small airgun size, the amplitudes of arrivals on the far offset traces were small and the signal to noise ratio was very low. Therefore stacking was limited to the first 64 channels. Including larger offsets generally reduced the quality of the stacked section. The stacking process over the selected offset range included forward and inverse τ–p filtering to maximize the signal to noise ratio and an additional

automatic trim static correction with the corresponding velocity-depth profile.

4.5 Post-stack Processing

4.5.1 Crossline Static

The seismic lines were acquired over six days with different weather, waves and tidal conditions. The expected vertical shifts due to different tidal conditions are less than 2–3 m. Topographic changes of the order of more than a few meters are expected over the COAMS survey 100 m line spacing interval and no flattening/smoothing was therefore applied. Crossline static is however a strong problem in the single channel seismic data with 25 m line spacing (see Section 4.8).

4.5.2 2-D Migration

The main 3-D grid covers an area with strong topographic variation. Migration has to perform well on different topographic features in the same way. All available migration techniques that allow incorporation of 2-D velocity profiles in the ITA/Insight system have been tested on inline 2 (large topographic changes) and inline 27 (small changes but blank zones and strong lateral velocity changes):

- Frequency-Space (FX) migration,
- Finite-Difference (FD) migration,
- Regular phase shift migration,
- Fast phase shift migration.

The FX-migration performs time and/or depth migration in the frequency-space domain using finite-difference approximations to the one-way acoustic (no S-wave) wave equation. Downward continuation is performed in the FX domain through

application of convolutional operators along the x-direction. Prior to migration a 2-D velocity grid has to be calculated, which allows the incorporation of vertical and lateral velocity changes. The finite-difference migration performs downward-continuation using the two-way wave equation. This migration module also requires a 2-D velocity grid. The phase-shift migration modules in ITA/Insight are based on Gazdag's one-way wave equation migration method (Gazdag, 1978). The fast phase-shift migration uses the same parameters as the regular phase-shift migration, but provides a more efficient way of migrating the data, which results in a smaller computation time.

Phase-shift migration performed the best on average, defined by visual comparison of the migrated sections. The fast phase-shift migration was used to minimize computation time, which was a critical parameter for migrating the 48 lines. The migration of all 48 lines took about 10 days continuous processing on an Ultra-5 SUN-sparc station. The criterion for comparison was based on the removal of diffractions. Figure 4.16 shows the stacked section of inline 27 and should be compared to Figure 4.17 which shows the migrated section using the fast phase-shift migration technique. Each inline was migrated with the same control parameters defined in Appendix D. Especially around the area of blank zones, the diffraction removal was not complete. This is most likely the result of the simplified, smoothed velocity function and 3-D side-diffractions.

4.5.3 Ghost-removal

The predictive deconvolution in the pre-stack shotgathers was not successful in completely suppressing the ghost, probably due to the offset-varying arrival time and waveform of the ghost. Therefore post-stack predictive deconvolution was applied after stacking and again after migration (parameters as defined in Section 4.4.1).

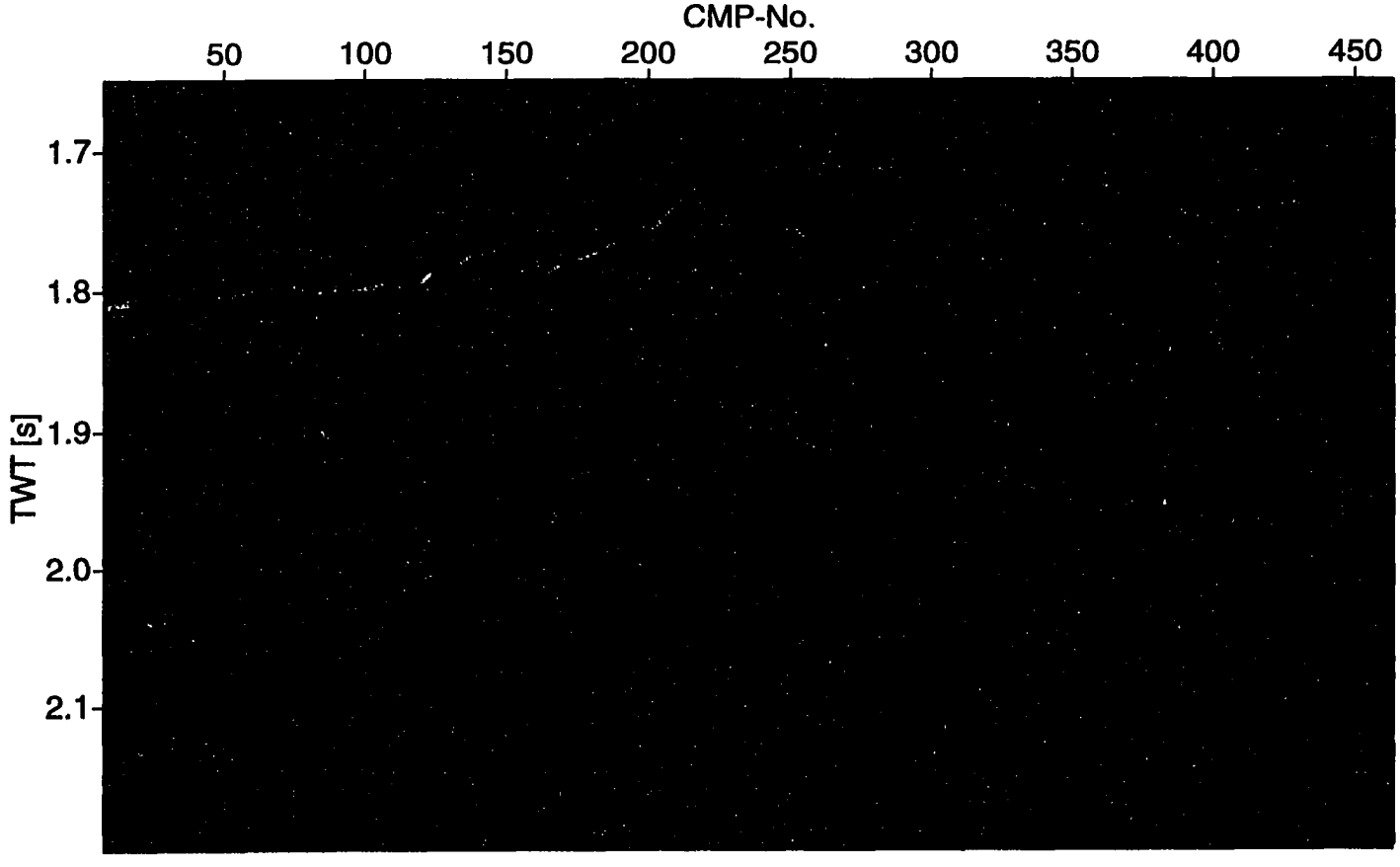

Figure 4.16 Stacked section of inline 27.

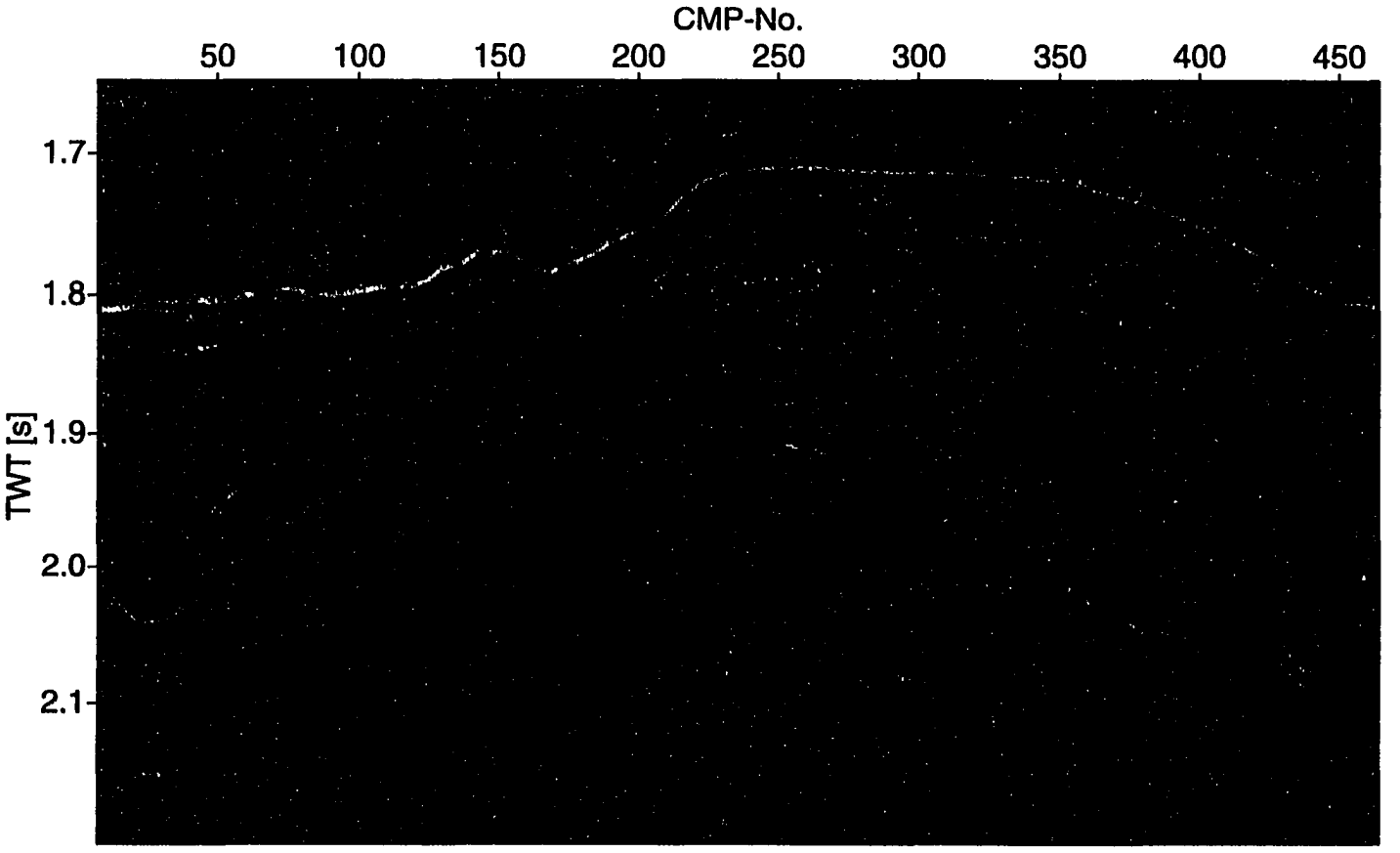

Figure 4.17 Migrated section of COAMS inline 27 (fast phase-shift) without post-stack deconvolution.

The suppression of the ghost was not uniform over the entire data set. No correlation of BSR occurrence (same waveform as a ghost, i.e. opposite reflection polarity) and successful ghost-removal was found. In Figure 4.17 the migrated section of inline 27 is shown before and in Figure 4.18 after applying the post-stack predictive deconvolution. Overall the ghost was reduced by about 50%.

4.6 2.5-D Migration

Prior to applying a complete 3-D migration of the entire data set, a 2.5-D migration was performed on selected crosslines of the final data cube. For all eight crossing lines the corresponding crosslines were selected from the 3-D data cube. Prior to migration a crossline interpolation was performed from 100 m spacing down to 50 m spacing using the *seismic-unix* tool *suinterp*. Each individual crossline was then migrated using the same fast phase-shift migration technique as being used on the inline direction. In general the migration resulted in poor results on all of the crosslines mainly due to the coarse spatial sampling. In Figure 4.19 two representative crosslines are shown before and after migration. Especially around steep topographic changes, the migration resulted in strong diffractions (smiles). Another effect of the migration is a loss of energy on inline 1–3 at the western edge and inline 38–40 at the eastern edge of the data cube. This however, is an expected effect of the migration procedure. Increasing the crossline interpolation was not successful and resulted in artificial results especially around the steep topography. In general no satisfactory result could be obtained from 2.5-D migration using the available frequency range.

One way of overcoming that problem might be using lower frequencies to avoid the spatial aliasing. Using only data over a frequency range up to 40 Hz is hampered by the fact that frequencies below 20 Hz had to be filtered out due to the strong flow noise generated at the bulk-heads of the array. Therefore only a frequency range

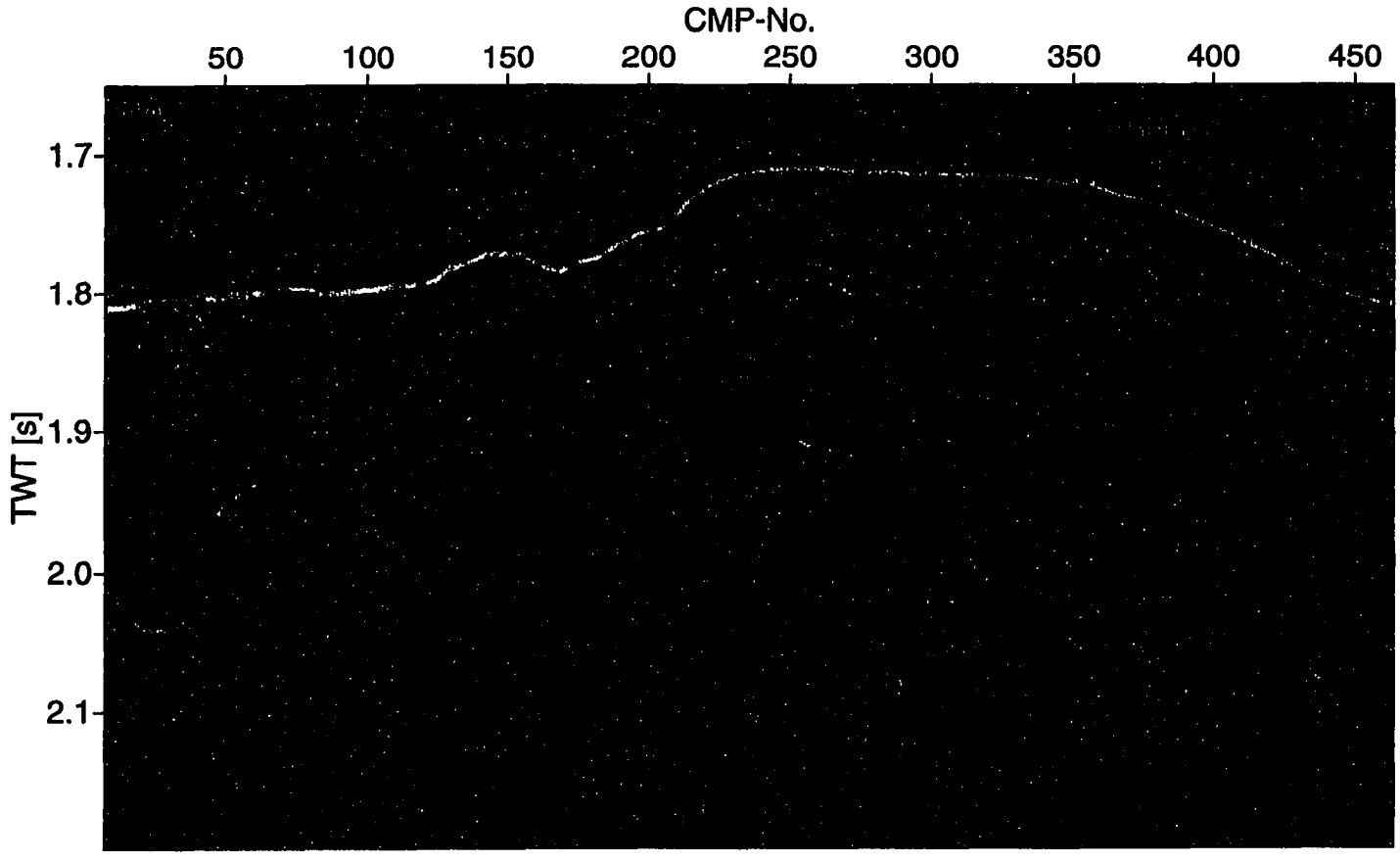

Figure 4.18 Migrated section of COAMS inline 27 (fast phase-shift) with post-stack deconvolution applied.

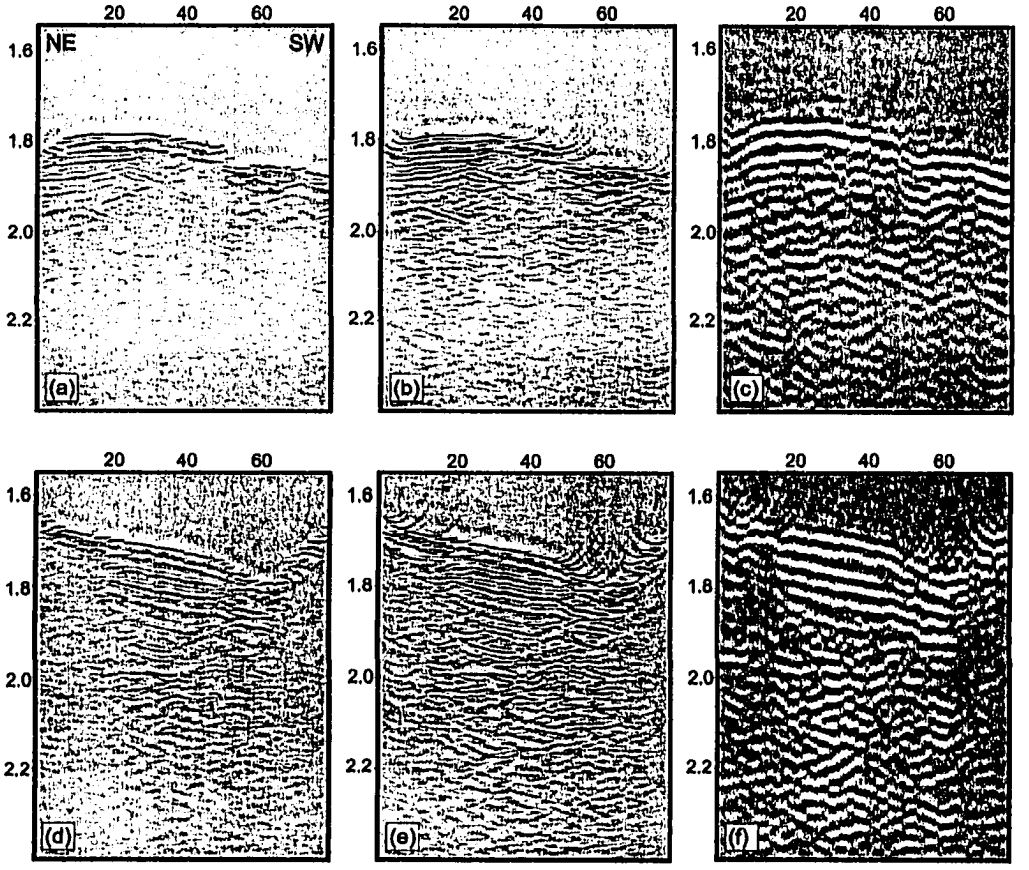

Figure 4.19 2.5-D migration results from COAMS crossline 205 and 615. (a) line 205 original 2-D migrated section , (b) 2.5-D migration, (c) 2.5-D migration with low frequencies, (d) line 615 original migrated section, (e) 2.5-D migration, and (f) 2.5-D migration with low frequencies.

of 20–40 Hz was available for this migration, which resulted in an almost mono-frequency, ringing seismic section. For comparison the migration results of crossline 205 and 615 using the low-frequency limit are also shown in Figure 4.19.

The two small single channel seismic grids acquired around the vent field do not suffer from spatial aliasing problems. Using equation 3.1 with an angle of 6° and a velocity of 1650 m/s, the maximum frequency is about 150 Hz. However, the data cubes are relatively small and the 2.5-D migration gave a poor result, especially around the edges of the data sets. The 1999 Teledyne data set is 3500 × 750 m wide and the 2000 data set is only 2000 × 500 m wide. Because of the failure of the 2.5-D migration, no full 3-D migration was performed. It was concluded that the full 3-D migration will have the same spatial aliasing problems as the 2.5-D migration and the migration process reduces the useful area.

4.7 3-D Binning Procedure

In order to use the main grid lines in a 3-D interpretation, the data must be binned into a regular spaced grid. The COAMS array is a nested array of several sections with different hydrophone spacings and together with the irregular shot point distance, CMP coverage varied strongly between lines. From the available data a cube containing 1000 CMPs for each of the 40 inlines was created by summing adjacent CMPs along each 2-D migrated line. The final CMP distance was 9.8 m. The final grid consists of 9.8 m × 100 m bins.

4.8 Single Channel Processing for the Teledyne Array

The objective of processing the single-channel seismic data is to increase the single-to-noise ratio and to suppress the source bubble pulse. The processing sequence for

the single channel array includes, after correction for trigger time delay, bandpass filtering and predictive deconvolution as defined in the sequence used for the COAMS array. Using a generalized velocity-depth function the single channel data was migrated using phase shift migration. No 2.5-D or 3-D migration was performed. The data sets were too small as indicated earlier and the migration results were not useful for interpretation. Therefore the individual 2-D migrated sections were binned into a regular spaced cube. Due to the variable shot point spacing during the 1999 experiment, the data cube over the vent field contains only 109 crosslines over 3500 m. To increase the data density a trace interpolation was performed to decrease the processed CMP distance to 15.5 m. The two single channel seismic data sets had to be corrected for crossline statics. The crossline static correction was done by defining a smoothed seafloor bathymetry and calculating the trace shift needed to project the actual trace onto the smoothed bathymetry. Striations are especially prominent at the start of each line. The ship speed was decreased during each turn and the Teledyne array sank to a greater depth. After the turn and corresponding speed-up, the array equilibrated to the new towing conditions and floated at a shallower depth. The corresponding TWT difference is about 2–4 ms.

Chapter 5

Regional Seismic Analyses

5.1 Introduction

A major objective of this thesis is to define the regional tectonic setting associated with the formation of gas hydrates and the geologic structures that control fluid flow and the formation of blank zones. Previous seismic analyses concentrated mainly on seafloor and BSR reflection amplitude studies as outlined in Chapter 2 without a detailed geological interpretation of what controls the formation of hydrates.

The COAMS 3-D high resolution seismic survey provides information about the tectonic setting around ODP site 889/890. However, interpretation of the seismic data is hampered by the ghost, which limited the vertical resolution and gave only a coarse velocity-depth function. Whenever possible, the COAMS seismic data were compared to the coincident higher-resolution single-channel (SC) seismic lines. SC seismic lines were not acquired over all of the main grid, so no single channel 3-D data cube was generated.

For 3-D display and analyses the 40 multichannel seismic lines were merged into a regular-spaced data cube. Adjacent CMPs along each line were stacked and placed in the center of the bin. Each seismic inline of the cube consists of 1000 CMP's spaced at 9.8 m. 3-D interpretation and visualization was carried out using the *Kingdom-Suite* software by Seismic Micro-Technology. From the 3-D data cube several horizons (such as the seafloor or the BSR) were selected to create amplitude and or bathymetric maps. The visualization software also allowed video animations of timeslices or 3-D perspective views. These videos and perspective views are available from the interactive CD-ROM attached to this thesis.

The new analyses allow a tectonic interpretation and characterization of related sediment deformation and reflection characteristics (amplitude reduction). Several types of amplitude reduction were identified from the seismic data: (a) fault-related, narrow blank zones, (b) broad-scale amplitude reduction associated with folding and low-level deformation, and (c) broad-scale amplitude loss due to the deformation and layer destruction during accretion. The two broad-scale types of amplitude reduction are discussed in this chapter and the fault-related blank zones are the focus of Chapter 6.

In this chapter, the main focus is on the COAMS 3-D data analyses to characterize (a) topography and (b) related seafloor reflection coefficients (especially to resolve the enigma of an area with high reflection coefficients), (c) seismostratigraphic characterization to define the boundary between accreted and slope sediments, (d) distribution and reflection strength of the BSR, and (e) regional heat flow estimated from the BSR depth.

5.1.1 Methodology of Reflection Coefficient Calculations

Seafloor reflection amplitudes were converted to reflection coefficients using the method of Warner (1990). Over a representative region the amplitude ratio of the seafloor water bottom multiple (A_{mult}) to the seafloor primary reflection (A_{prim}) is calculated. Using a spherical divergence correction proportional to travel time and assuming perfect seasurface reflection, the seafloor reflection coefficient (R_{seaf}) is given by:

$$R_{seaf} = 2 \cdot \frac{A_{mult}}{A_{prim}} \tag{5.1}$$

Since an amplitude correction for spherical divergence was carried out in the main processing sequence and amplitudes were picked from the migrated zero-offset seismic sections, the divergence factor of 2 was not included. Warner suggested to calibrate the conversion method over the flattest area to avoid effects of topography. No really

flat part that is also not affected by other local disturbances (such as blank zones) can be found in the area of the 3-D seismic data. The conversion factor was defined in the SW corner where there is an almost undisturbed sedimentation pattern. However, there is a gentle dip of the strata to the SW. To ensure that this method gives reliable results, density and velocity determined from piston cores acquired in 2000 were also used to calculate seafloor reflection coefficients (Novosel *et al.*, 2000). The cores were taken in the area of the uplifted sediment block. P-wave velocity varied between 1490 and 1510 m/s and densities were usually between 1.5 and 1.6 g/cm^3 in the upper few meters of the cores. The seafloor reflection coefficients determined with the Warner method in that area are about 0.2–0.25, in very good agreement with the values obtained from the piston cores (0.19–0.22), and no significant offset was observed between reflection coefficients determined from both methods. Seawater density was assumed to be 1.03 g/cm^3 and seawater P-wave velocity was set to 1485 m/s.

BSR and seafloor reflections were defined from the migrated seismic lines of the 3-D cube within the visualization software *Kingdom suite*. The seafloor reflection coefficient (R_{seaf}) was determined from the peak of the wavelet, which has a single peak-trough waveform, and the BSR amplitude was determined from the corresponding trough. BSR amplitudes were converted into reflection coefficients by trace-by-trace amplitude scaling and applying a correction factor for transmission loss at the seafloor (1-R^2_{seaf}). No further transmission losses were included into the conversion procedure, i.e. the calculated BSR reflection coefficients are conservative estimates.

5.2 COAMS-99 studies

5.2.1 Bathymetry

The seafloor reflection was used to generate a detailed bathymetric map of the area of investigation (Figure 5.1). Steep topographic changes were not completely imaged by the 2-D migration, especially around the prominent topographic highs, and bathymetry was therefore defined by interpolation. The resolution of the COAMS bathymetry data set is less compared to the earlier Hydrosweep bathymetry data (Figure 2.2 in Chapter 2).

The topography is mainly characterized by the two prominent topographic highs, which rise by about 200 m above the adjacent seafloor. In addition, several lineaments can be identified, which are interpreted as the surface expression of fault planes. There are two distinct lineaments in the SE part of the area. The east-most lineament is related to the eastern topographic high and can be traced for several kilometers to the south (compare to Figure 2.2 in Chapter 2). The second lineament follows approximately an east-west trend and can be traced up to crossline position 600 on inline 10. These two lineaments mark the boundary of an uplifted sediment block, in which several blank zones have been observed (Chapter 6). At the northern edge of the uplifted sediment block, the seafloor drops by about 45 m (crossline position 450, inlines 22–40), but the drop is not associated with a clear linear structure.

The NW corner of the area is dominated by the large mound structure, with a complicated surface expression (crossline 100, inlines 7–15). To both sides of the mound structure, which rises by about 80 m above the adjacent seafloor, deep troughs are possible slide or slump scars (compare to Figure 2.2 in Chapter 2). The complicated structures resulted in multiple diffractions often from out-of-plane arrivals. Topography was defined in comparison to the multibeam bathymetry available in the area. Often no coherent reflection phase could be used in defining the seafloor and the corresponding reflection coefficient was set to 0. From the seismic data available, this

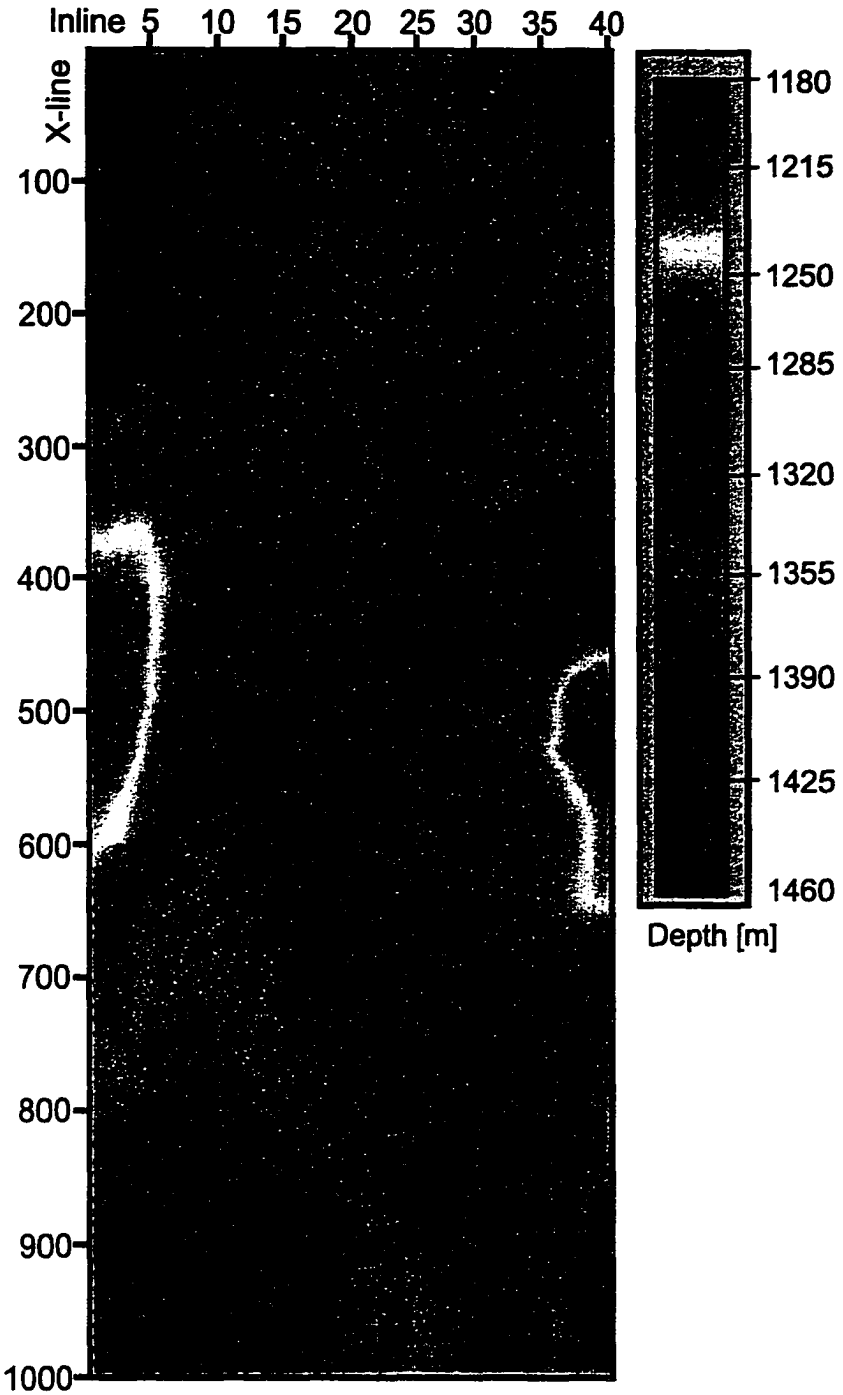

Figure 5.1 Color-coded bathymetry defined from COAMS 3-D seismic data. Depth is given in meters converted from seismic TWT using a constant sound speed of 1490 m/s in the water.

area was interpreted as typical mud/carbonate mound structure and seafloor video observation with ROPOS in May 2001 confirmed massive carbonate formations. A detailed analysis of the seismic data available over the mound structure and additional constraints from seafloor video observations are given in Chapter 6.

5.2.2 Seafloor Reflection Coefficients

Seafloor reflection coefficients are an important indicator of seafloor composition, especially the presence of carbonate pavements. Seafloor coefficients ranged mainly from 0.1 to 0.35, with local extrema as high as 0.75. In general, five distinct regions with different reflection coefficient characteristics were identified (Figure 5.2 and Figure 5.3);

1. Around the topographic highs (less than 0.15)
2. At the mound structure in the NW corner (less than 0.15)
3. The uplifted sediment block (0.15–0.3)
4. The SW corner where conversion factor was calculated (about 0.2 and less)
5. The NE corner at ODP site 889/890 (0.2–0.4)

The first region with very low reflection coefficients (less than 0.15) is around the two topographic highs. However, these low reflection coefficients may not be representative of the existing sediment properties, since the steep relief results in defocussing effects. At the foot of each topographic high very large reflection coefficients were observed, possibly due to the effect of focusing the seismic energy. Similar very low reflection amplitudes were observed over the large mound structure in the NW corner (region 2). Again, these values may not be very representative (compare to Chapter 6) of the real seafloor properties.

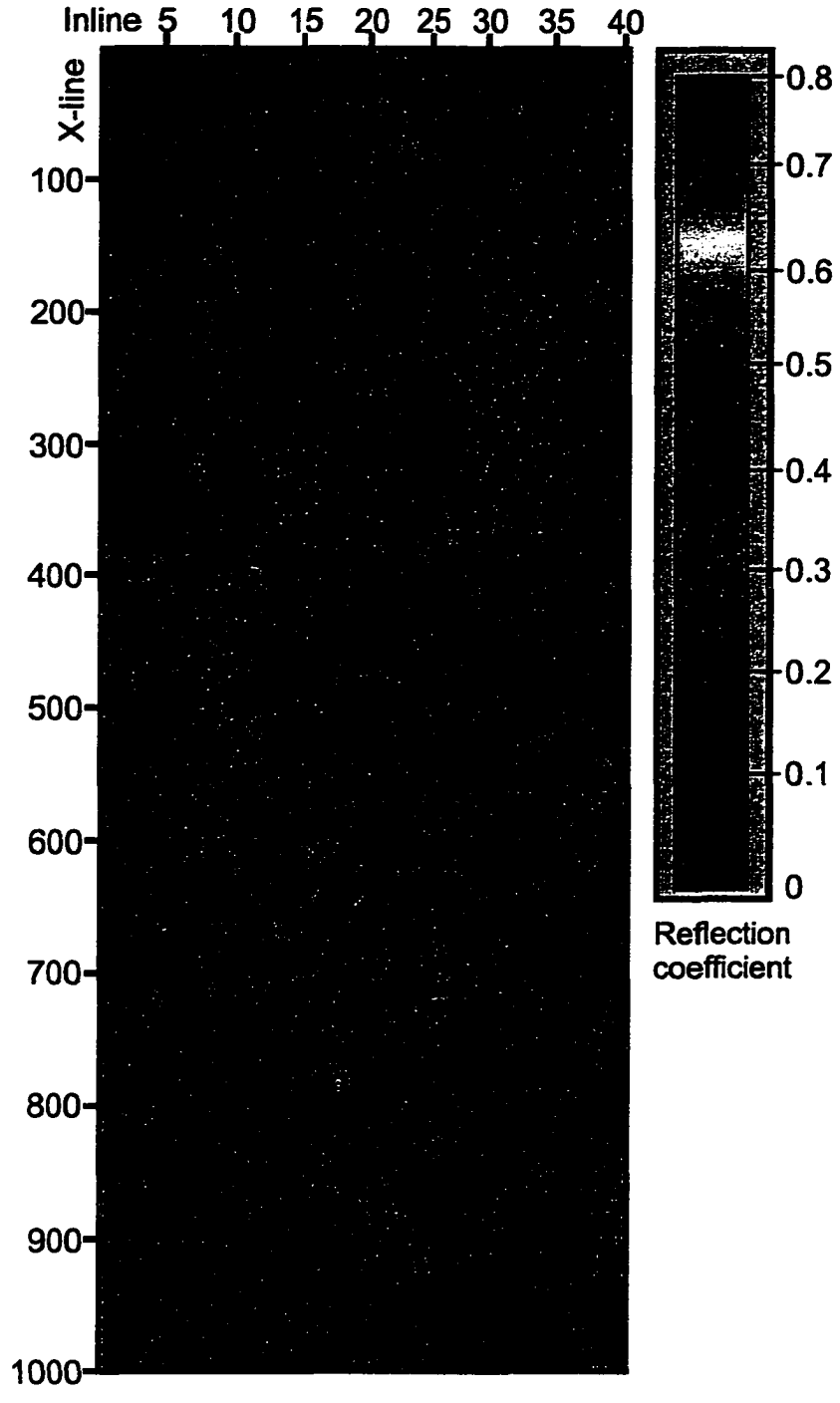

Figure 5.2 Seafloor reflection coefficients defined from COAMS migrated zero-offset sections using Warner's method (1990). Five distinct regions with different reflection characteristics were defined (see text for explanation). Note the linear low amplitude traces associated with the blank zone vent-field on inlines 20–35 and crosslines 400–550.

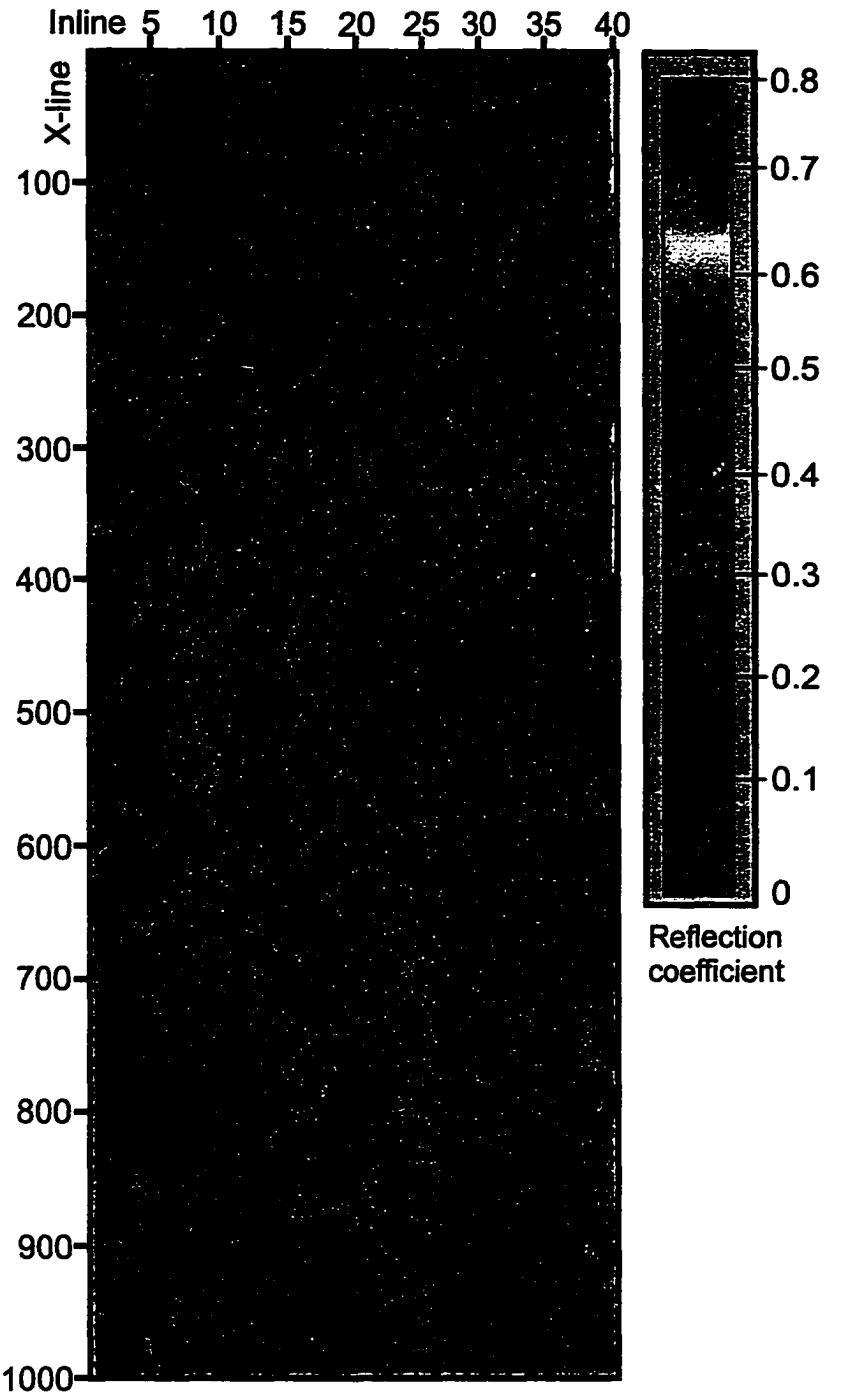

Figure 5.3 Seafloor reflection coefficient defined from COAMS migrated zero-offset sections using Warner's method (1990) and bathymetry from COAMS in TWT [sec]. Note the traces of large reflection coefficients following steep changes in the relief.

Relatively low values of less than 0.2 were observed in the SW corner, an area with an almost undisturbed sedimentation pattern. This area is sharply truncated to an area with moderate reflection coefficients of the uplifted sediment block by a lineament of very large reflection coefficients. The trace of larger values follows exactly the steep topographic change associated with the uplift of the sediment block (Figure 5.3). These larger values are probably a focusing effect. A 3-D perspective view of this step in seafloor topography associated with large reflection coefficients is shown in Figure 5.4 and a 3-D animated video is available from the interactive CD-ROM.

The uplifted sediment block is characterized by moderate reflection coefficients varying between 0.15 to 0.3. Three zones of reduced seafloor reflection coefficients can be observed, showing the trace of three blank zones (crosslines 400-550, inlines 20-35). An almost circular area of very low reflection coefficients marks the area of the main blank zone (No. 1). The reflection coefficients were affected by steep topographic ridges at the edges of the blank zone resulting in defocussing of the seismic energy. A detailed analysis of the reflection amplitudes associated with the blank zones is given in Chapter 6.

5.2.3 Area With High Reflection Coefficients

The last distinct area with relatively high reflection coefficients up to 0.4 was observed in the area around ODP Site 889. This area was mapped earlier as a highly reflective zone in a single channel seismic study in 1993 (Fink and Spence, 1999). Their reflection coefficients are on average 0.35 in this area and are very similar to the results from the COAMS data. Reflection coefficients were also observed to be frequency dependent. Modeling a 2 m thick carbonate pavement for a 30 Hz and 75 Hz seismic signal (Ricker wavelet) best explained the observed trends.

In the following, new seismic data from 3.5 kHz, DTAGS and the 3-D COAMS

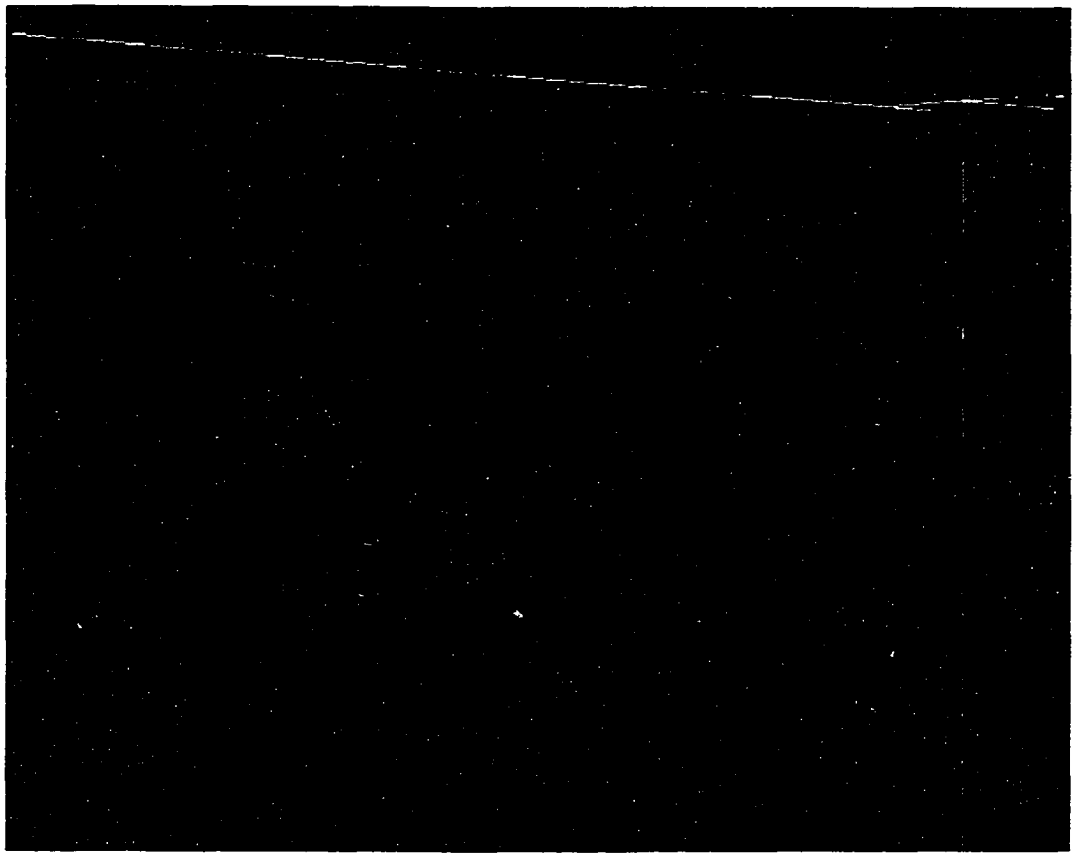

Figure 5.4 3-D perspective view of the step in seafloor topography associated with a trace of high reflection coefficients. View is to the NW from about 100 m above the seafloor. The main ridges of accreted sediment are to the left (west) and right (east) of the observer. In the background the top of the ridge structure is seen.

surveys are shown, allowing a more detailed interpretation of the observed reflection amplitudes. Observations of DTAGS data were done on unpublished sections processed by W. Wood, NRL (not shown). The part of DTAGS line BC-03 covering the vent field is shown in Chapter 6, Figure 6.6. Results from investigating color prints of the line BC-03 (inline 27 from COAMS 3-D) are presented. His processing included careful source waveform estimation and cross-correlation, which allowed for reliable amplitude and phase information.

What Causes the Frequency Dependent Reflection Coefficients?

A second shallow layer appears occasionally in the COAMS data that has an apparent opposite reflection polarity compared to the seafloor. This second reflector can be identified on inlines 23–40 and on crossline positions up to 350 (see e.g. Figure 5.5 and 5.6). On the DTAGS line BC-03 a second coherent reflector at a depth of about 10–20 m bsf can be identified that has an opposite reflection polarity compared to the seafloor reflection. The second layer in the COAMS inline 27 matches the deepest location (about 20 m) in the DTAGS record. For the COAMS data, there is no strong correlation between the occurrence of the second layer and seafloor reflection amplitudes. On inline 30 for example, the depth of the second layer is constant, but the reflection coefficients increase. Thus it seems that the seafloor reflection coefficients are not influenced by the negative polarity reflector in the ~100 Hz COAMS data. In the study by Fink and Spence, a frequency dependent reflection coefficient was modeled as a 2 m thick carbonate pavement. From the new data shown here, it can be seen that this is not a general realistic model. The low frequency signal of 30 Hz (about 50 m wavelength) is influenced by the second negative polarity reflector but the higher frequencies do not sample this depth. A simple two layer model with a second negative impedance-contrast layer was modeled for frequencies at 30, 75 and 100 Hz. Parameters used in the modeling are summarized in Table 5.1.

	P-wave velocity [m/s]	S-wave velocity [m/s]	Density [g/cm^3]
Layer 1	1550	450	1.55
Layer 2	1520	450	1.4

Table 5.1 Parameter values for modeling a negative impedance-contrast effect.

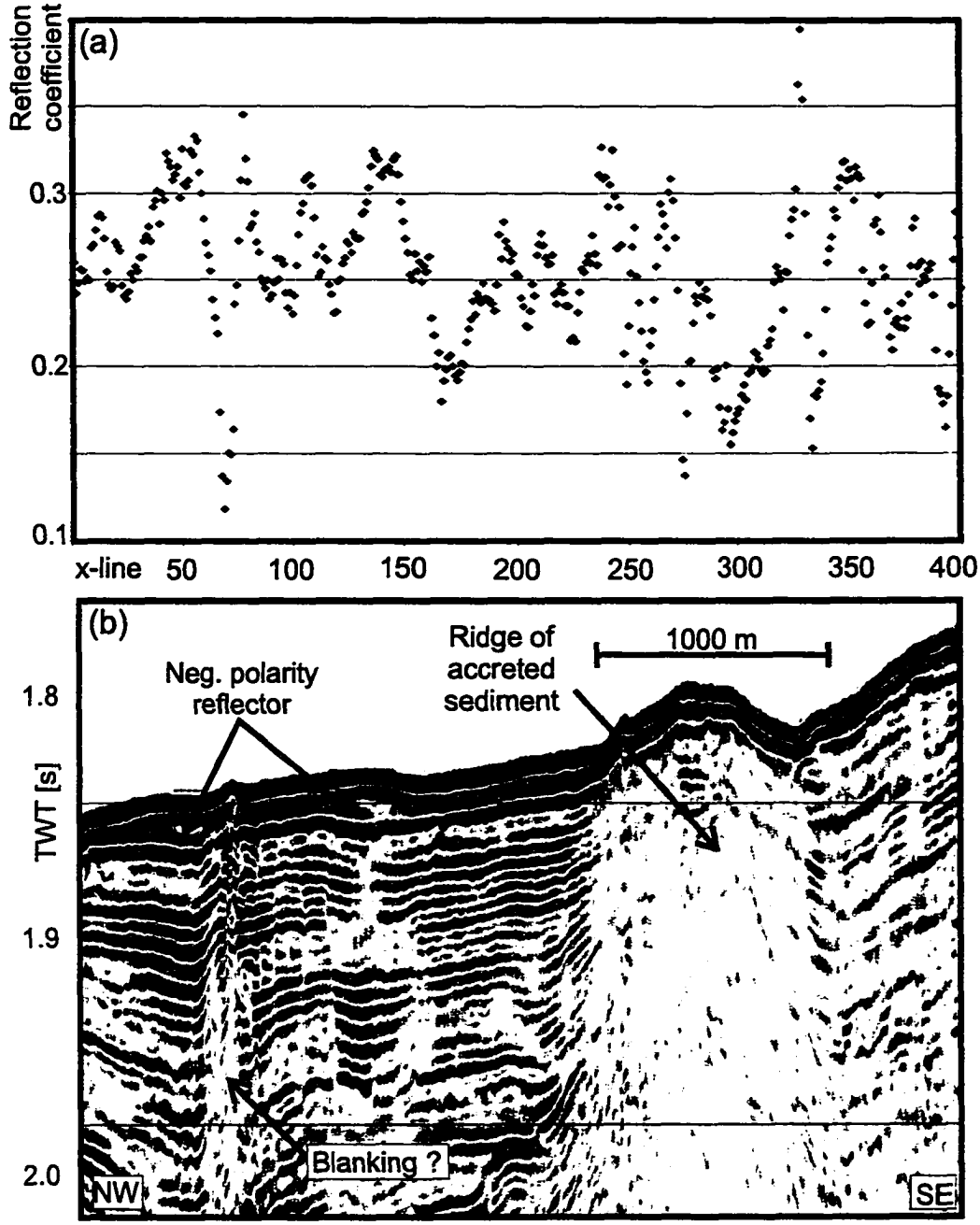

Figure 5.5 Comparison of (a) reflection coefficients and (b) migrated seismic section of COAMS inline 27.

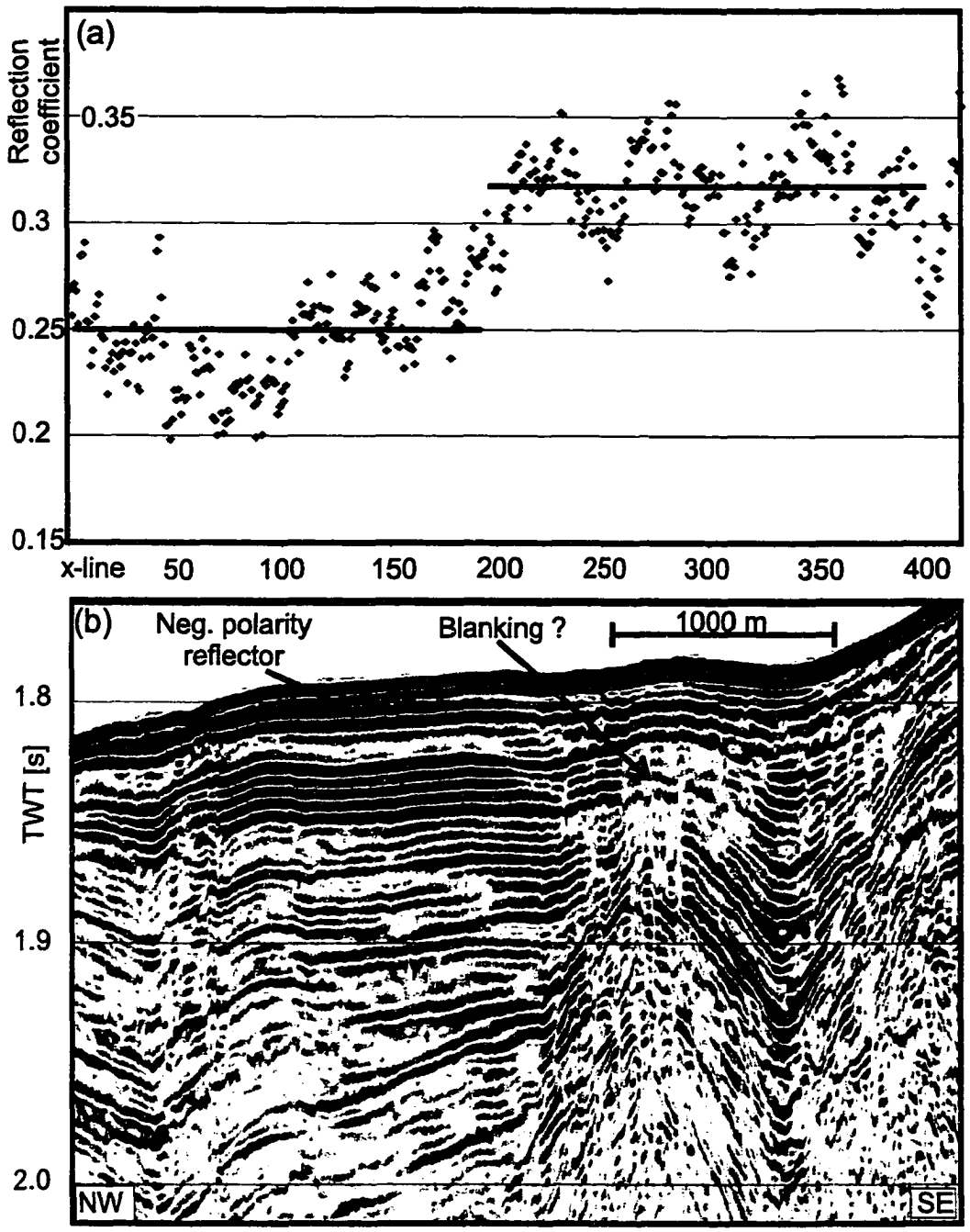

Figure 5.6 Comparison of (a) reflection coefficients and (b) migrated seismic section of COAMS inline 30. Note the zone of increased reflectivity.

Over the observed depth range of the second layer of 10–20 m, the 30 Hz signal is always influenced by this layer and shows a reduction in reflection amplitude by about 20% compared to the 75 and 100 Hz signals that are unaffected by the second layer. A similar difference was observed by Fink and Spence. Reflection coefficients calculated from the 75 Hz seismic signals were about 25% larger than the values obtained from the 30 Hz record. It can be concluded that the observed frequency dependence is mainly an effect of interference with a negative impedance-contrast layer at about 20 m bsf and not the effect of a 2 m thick carbonate pavement.

	30 Hz	75 Hz	100 Hz
2 m	0.79	0.98	1.04
5 m	0.81	1.04	1.02
10 m	0.83	1.0	1.0
20 m	0.84	1.0	1.0

Table 5.2 Computed ratios of frequency dependent reflection amplitude to normal reflectivity without second layer. Depths of second layer are 2, 5, 10 and 20 m, frequencies used were centered at 30, 75, and 100 Hz.)

Carbonate Pavement, Erosion or Sand Layers?

The 3.5 kHz data in general show less penetration in the area of high reflection coefficients, compared to the uplifted sediment block (Figure 5.7). However, a detailed analysis of the high reflectivity zone shows that the area is partially covered by a thin, 1–1.5 m thick layer that appears to be almost transparent (Figures 5.8, 5.9). This layer was previously identified by Davis *et al.* (1990) and perhaps represents the most recent Holocene sedimentation. The area where this layer is lost in the 3.5 kHz record marks the onset of the increased seafloor reflection coefficients. Thus this may indicate recent erosion and the seafloor is formed by older, more consolidated

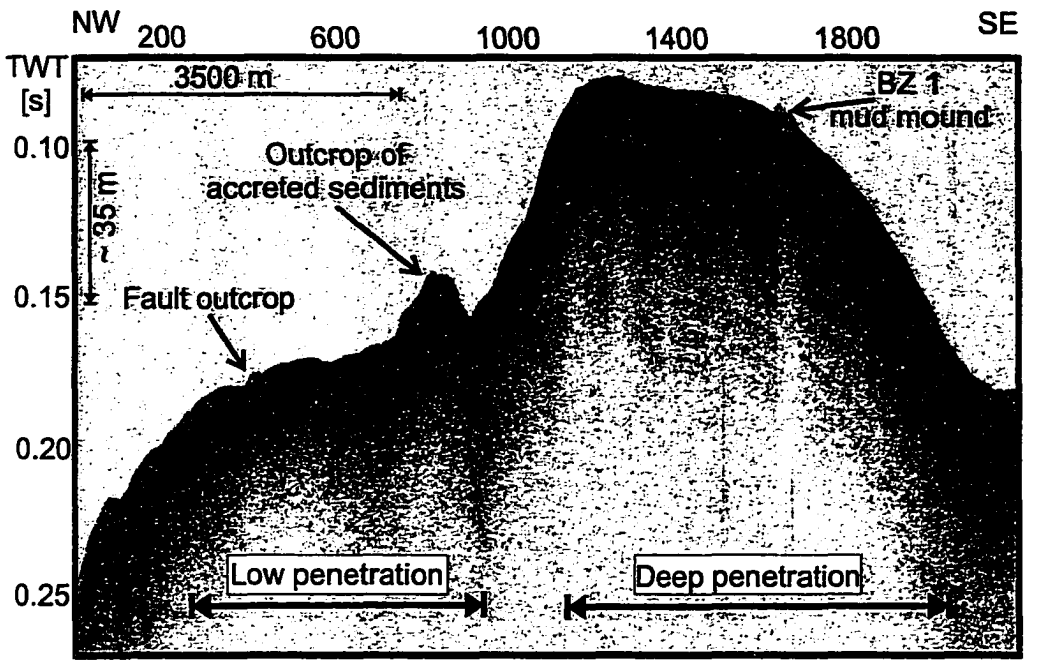

Figure 5.7 3.5 kHz subbottom profiler seismic section from inline 27. Note different penetration depth over the uplifted sediment block compared to NW part of line.

sediment.

The COAMS multichannel seismic data are not able to resolve the uppermost thin veneer as a separate reflector, but local lower seafloor reflection coefficients match with the location of the semi-transparent layer and therefore seem to reflect the occurrence of a relatively soft material (Figure 5.5). The reflection coefficients along COAMS inline 27 vary significantly but do not have a general increased zone, as observed on other inlines (compare to Figure 5.6).

As observed in the 3.5 kHz data, the area of higher reflection coefficients is not covered by the thin transparent layer. In the region of high amplitudes the reflection coefficients along COAMS inline 30 are on average 0.325. This reflection coefficient is equivalent to a seafloor impedance of about 3000 $g \cdot m/s \cdot cm^3$ using a water velocity of 1485 m/s and density of 1.03 g/cm^3. For typical seafloor sediment densities ranging

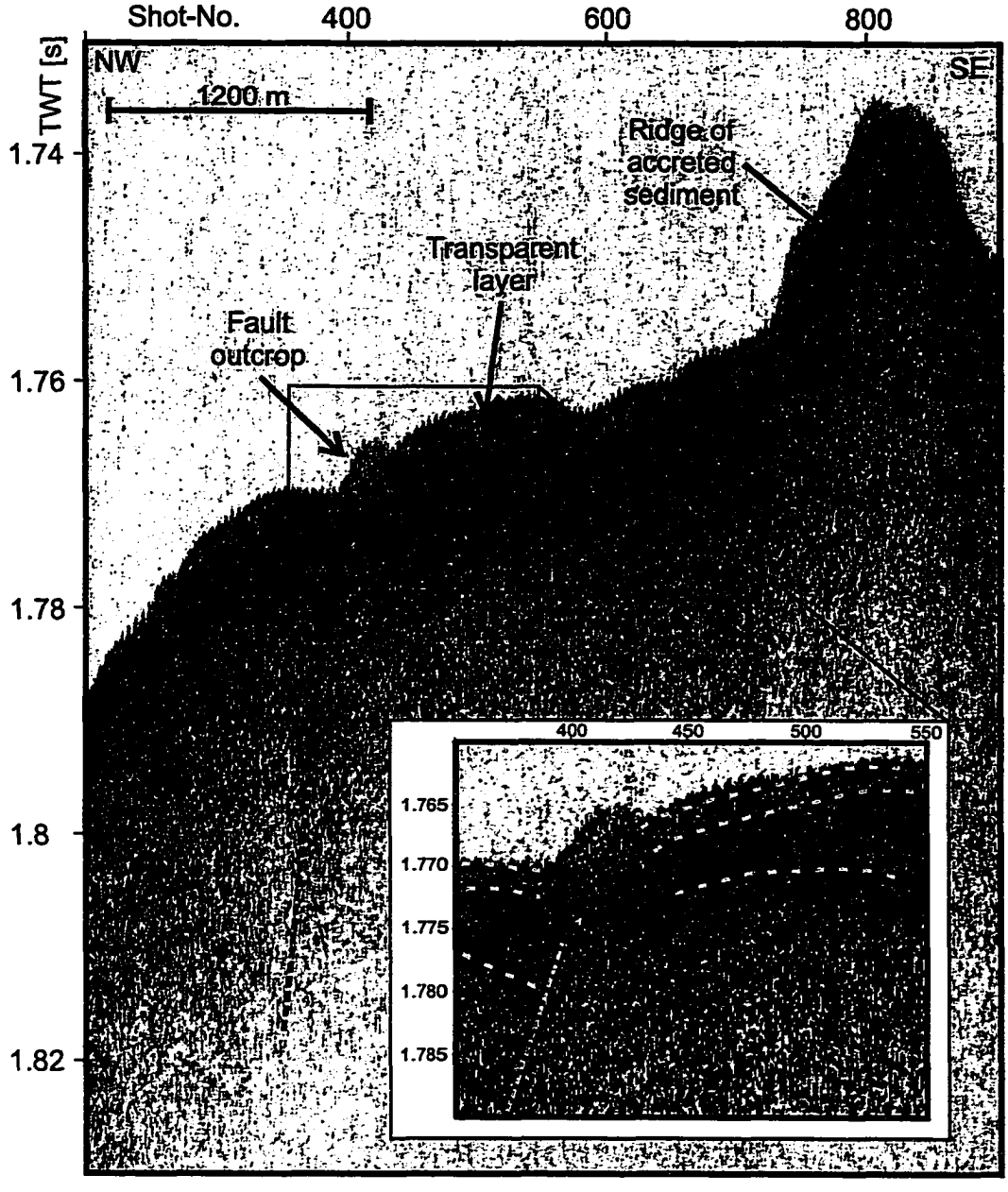

Figure 5.8 Detailed section of 3.5 kHz seismic section of inline 27 at area with high reflection coefficients. Penetration is on average only about 20 m bsf. A thin, about 1 m thick almost transparent layer is observed.

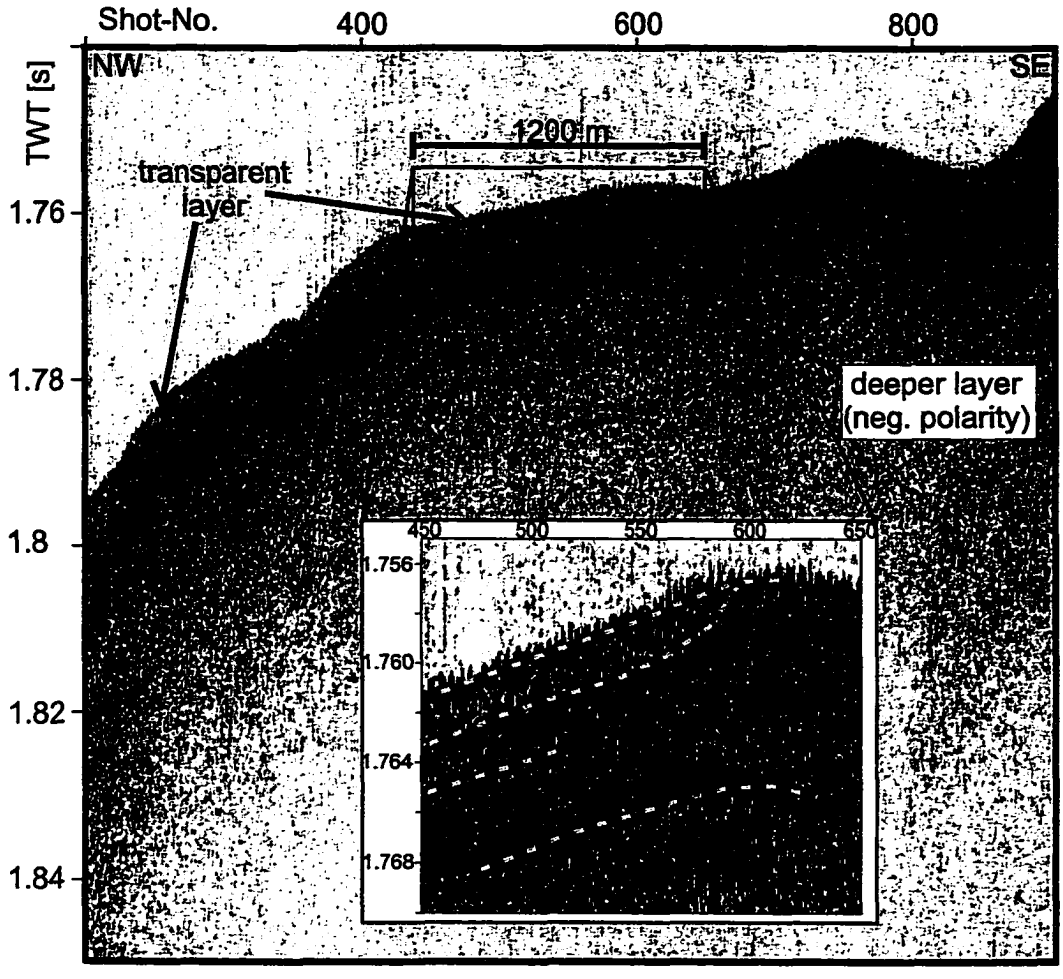

Figure 5.9 Detailed section of 3.5 kHz seismic section of inline 30 at area with high reflection coefficients. Penetration is on average only about 20 m bsf. A thin, about 1 m thick almost transparent layer is observed together with deeper reflectors.

from 1.4 to 1.8 g/cm^3, the corresponding P-wave velocity ranges from 1640 to 2100 m/s. These high velocities are normally observed at greater depth of around 100 m or more. A previously suggested explanation was a carbonate pavement. Using a typical density for solid carbonate of 2.3 g/cm^3, the calculated impedance corresponds to a velocity of 1280 m/s, which is far too low to be consistent with a solid carbonate pavement.

Using densities of 1.6–1.7 g/cm^3 and corresponding velocities from 1740–1840, the best model for the seafloor sediment that can explain the observed reflection coefficient is either a fine sand, i.e. an exposed turbidite layer with the upper most Holocene sediments eroded, or a carbonate-cemented sediment. The range of possible values for both models is in good agreement with values quoted for these kind of sediments (e.g. Hamilton, 1980).

Conclusion

The main result of the new studies is that the observed frequency dependence is not the effect of a 2 m thick carbonate pavement but is probably the result of interference of the seafloor reflection with a shallow negative impedance-contrast reflector. This negative impedance-contrast reflector was clearly mapped in the DTAGS data and can partially be identified in the COAMS data. The increased seafloor reflection amplitudes cannot be the effect of a solid thick carbonate pavement. However, there is evidence of erosion in that area suggesting that the higher reflection coefficients can be the result of exposed higher reflective material (turbidite sand layer).

5.2.4 Boundary Between Accreted and Slope Sediments

The boundary between accreted and slope sediments is the most prominent seismostratigraphic feature. It can be used to define the tectonic setting and related thrust faulting, which control the formation of hydrate and fluid/gas flow. In the following section a background description and definition of the two different types of sediment in the area of investigation is given and results from the COAMS-99 survey are described.

Sediments in the area around ODP Site 889/890 have two different origins. The accreted sediments were deposited as turbidites on the deep sea floor of the Cascadia basin and have been undergoing a long history of deformation. They have lost all coherent reflectivity and appear as seismically transparent areas. The other sediment type is formed by deposition in slope basins, mainly composed of turbidite sequences of continental debris and hemipelagic drape. These sediments are characterized by strong coherent layered reflectivity. Generally the slope sediments are found in basins between uplifted ridges of accreted sediments. Continuing uplift of the ridges relative to the basins has produced thinned and locally deformed sequences over the ridges between thicker, less deformed sedimentary sequences in the axes of the basins (Westbrook *et al.*, 1994). The boundary between the sediment types usually is a gradual transition. In the COAMS 3-D grid the boundary could be defined reasonably well from the seismic amplitude section in comparison with the instantaneous amplitude (envelope) section. The envelope seismic section enhances the contrast between sections with and without coherent reflectivity. The boundary between sediment types was defined from visual comparison of the seismic sections in the inline and crossline directions. The picking avoided complicated structure and represents a *smoothed estimate* of the boundary. The largest problem in defining the boundary was the receiver ghost as discussed above.

ODP Results and Seismostratigraphy

The ODP core and log data provide the primary calibration of seismic data. An interpretation of conventional low frequency seismic line 89-08 (frequencies around 30 Hz) and comparison to ODP drilling results is shown in Figure 5.10. Inline 38 from the higher frequency ~100 Hz COAMS data in close vicinity to ODP Site 889A is shown in Figure 5.11 in comparison to the lithostratigraphic interpretation from the ODP Site (Westbrook *et al.*, 1994). The distinction between incoherent accreted and bedded slope basin sediments is much clearer in this higher frequency data. The ODP core and log analyses showed three major units within the uppermost 400 m. Section I was divided into sub-units IA and IB. Unit IA from the seafloor to 87 m bsf comprises mostly clayey silts and silty clays with interbedded thin sand layers. The sediments are also poorly indurated. This unit is characterized by subhorizontal to shallowly dipping beds with little deformation and is interpreted to represent little deformed slope basin turbidites and pelagics. The age is from Holocene to early Pleistocene to about 450,000 years.

Section IB is also mainly silty clay but with less abundant sand layers. The sediments show moderate to steeply westward dipping beds. It was interpreted that the sediments in subunit IB represent a series of sediment gravity-flow deposits caused by tectonic uplift of the deformation front. Thus subunit IB may represent a transition between the abyssal plain sedimentation of units II and III to the subsequent deposition of subunit IA, which represents slope basin type sedimentation.

Units II and III consist of mainly clayey silt with a low abundance of sand layers. Sediments are also more indurated by compaction and slight cementation. Units II and III are distinguished on the basis of a significant increase in glaucony in unit III but no other compositional or structural differences were observed. Structurally units II and III show pervasively fractured silts with variable dip, inclined bedding, sheared fractures and stratal disruption. These units were interpreted as typical abyssal plain

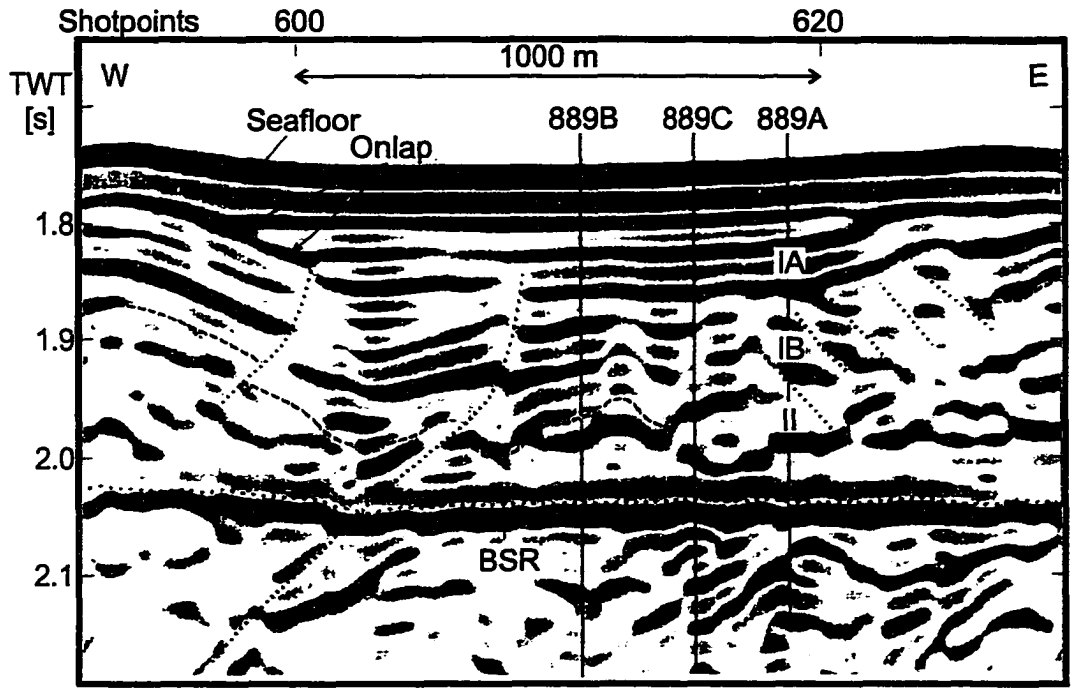

Figure 5.10 Detail of migrated line 89-08 in vicinity to ODP site 889. Units IA, IB and II as determined from Site 889A are superimposed with tectonic interpretation of faults. The dashed line marks contact between the unit I and II. Polarity convention of seismic: Black is positive, gray is negative (from Westbrook *et al.*, 1994).

sediments that were heavily deformed and fractured during the accretion process.

Seismic sections show that subunit IB is seismically incoherent. The boundary between accreted and slope sediments was placed at about a depth of 90 m (TWT of 1.88 s). The sediments of subunit IB have a different history and slightly different composition compared to the accreted sediments. However, seismically there is no difference between subunit IB-type of sediments and the deeper accreted sediments.

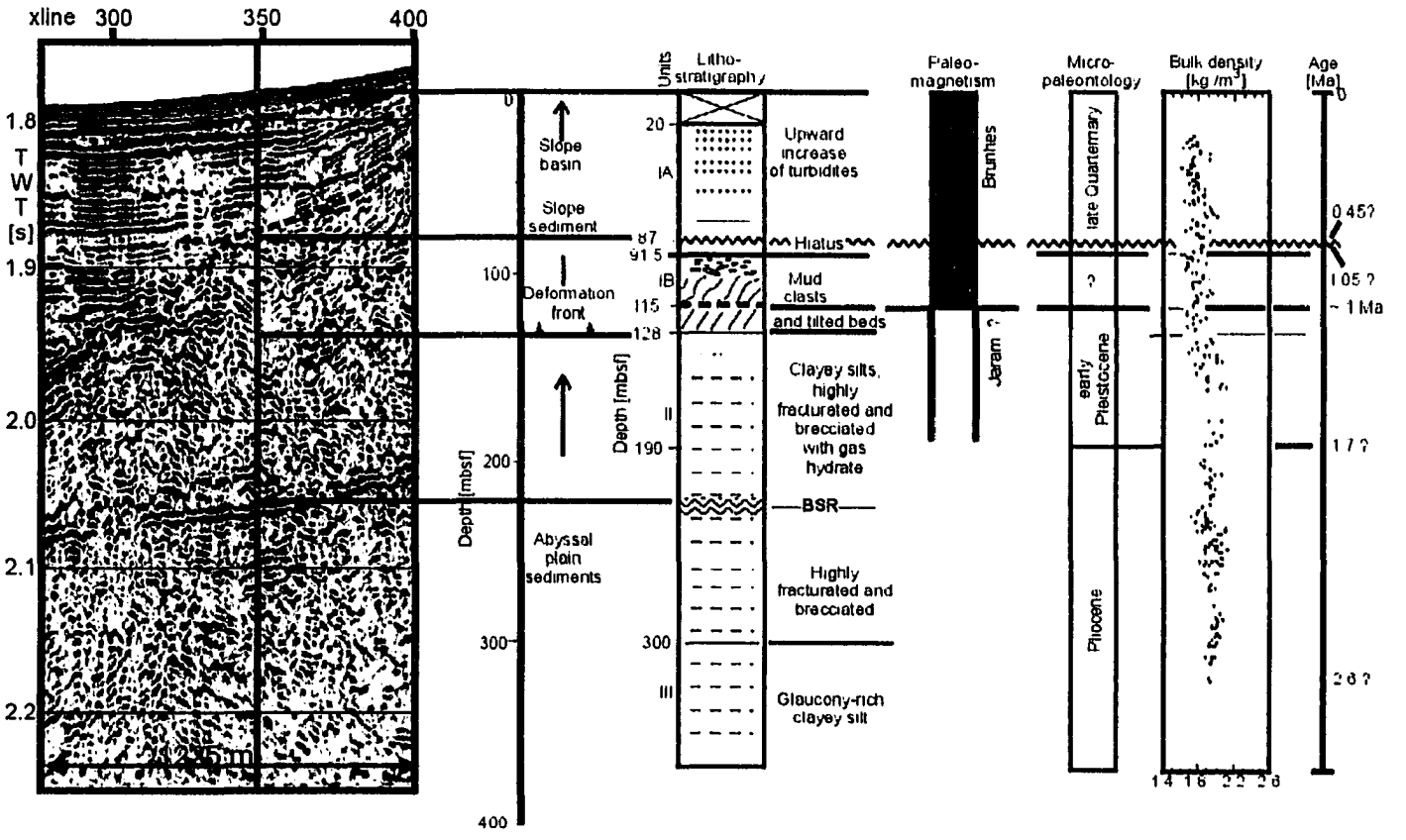

Figure 5.11 Seismostratigraphy and interpretation from ODP Site 889A (after Westbrook *et al.*, 1994). The part of inline 38 around ODP Site 889A is shown for comparison. Black is positive polarity.

Results From COAMS-99

Ridges of accreted sediment and thrust faults

In this section new results from the COAMS-99 seismic data are presented, extending the previous tectonic interpretation of the area around ODP Site 889/890 and relating the formation of ridges of accreted sediments to regional seismic amplitude reduction.

The two prominent topographic highs are almost entirely composed of accreted sediments. They do not show any internal coherent reflectivity as seen on line 40 crossing the eastern main ridge (Figure 5.12). However, the bottom-simulating reflector (BSR) is generally well developed within these sediments as it is in most accreted sediment sections. To both sides of the accreted ridges deep basins developed, filled with slope sediments in which no clear BSR can be seen. From the multibeam bathymerty (Figure 2.2 in Chapter 2) it can be seen that the two highs are relatively small, about 6 km elongated ridges. Both ridges are mainly oriented in a SE-NW direction, but show different curvatures. The eastern ridge bends towards the west, whereas the western ridge turns to the east. This indicates a different orientation of the underlying faults. As shown in Figure 5.13 the southwestern margin of the slope basin is an eastward facing fault scarp outcrop. This fault appears to be westward dipping based on the asymmetry of the sediment deformation and the uplift of the ridge. The eastern main ridge lies most likely at an eastward dipping thrust, based on the sediment structure to both sides of the ridge. Line XL-06 best visualizes the prominent main ridges of accreted sediment (Figure 5.13). The eastern ridge was uplifted by about 200 m relative to the deep basin of slope sediments that developed to the east of the site. Following the arguments of Westbrook *et al.* (1994), the area around the ODP Site 889/890 is located on a plateau of the accretionary prism that is thrust up along an eastward dipping fault that outcrops at the base of the steeply dipping slope to the west of the ODP Site (Figure 5.14).

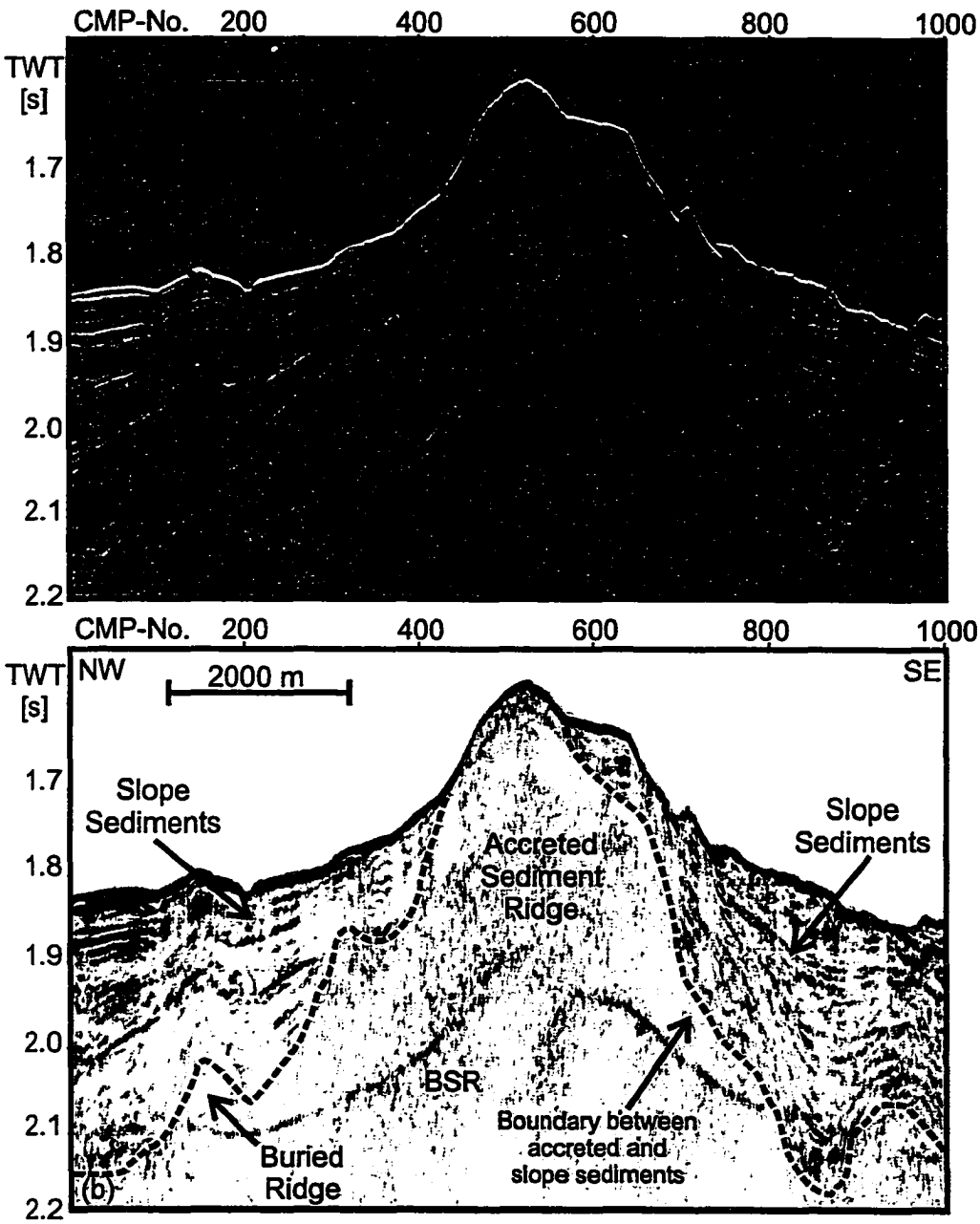

Figure 5.12 (a) Seismic amplitude (variable area) and (b) envelope section of COAMS inline 40 showing main ridge of accreted sediments in the east.

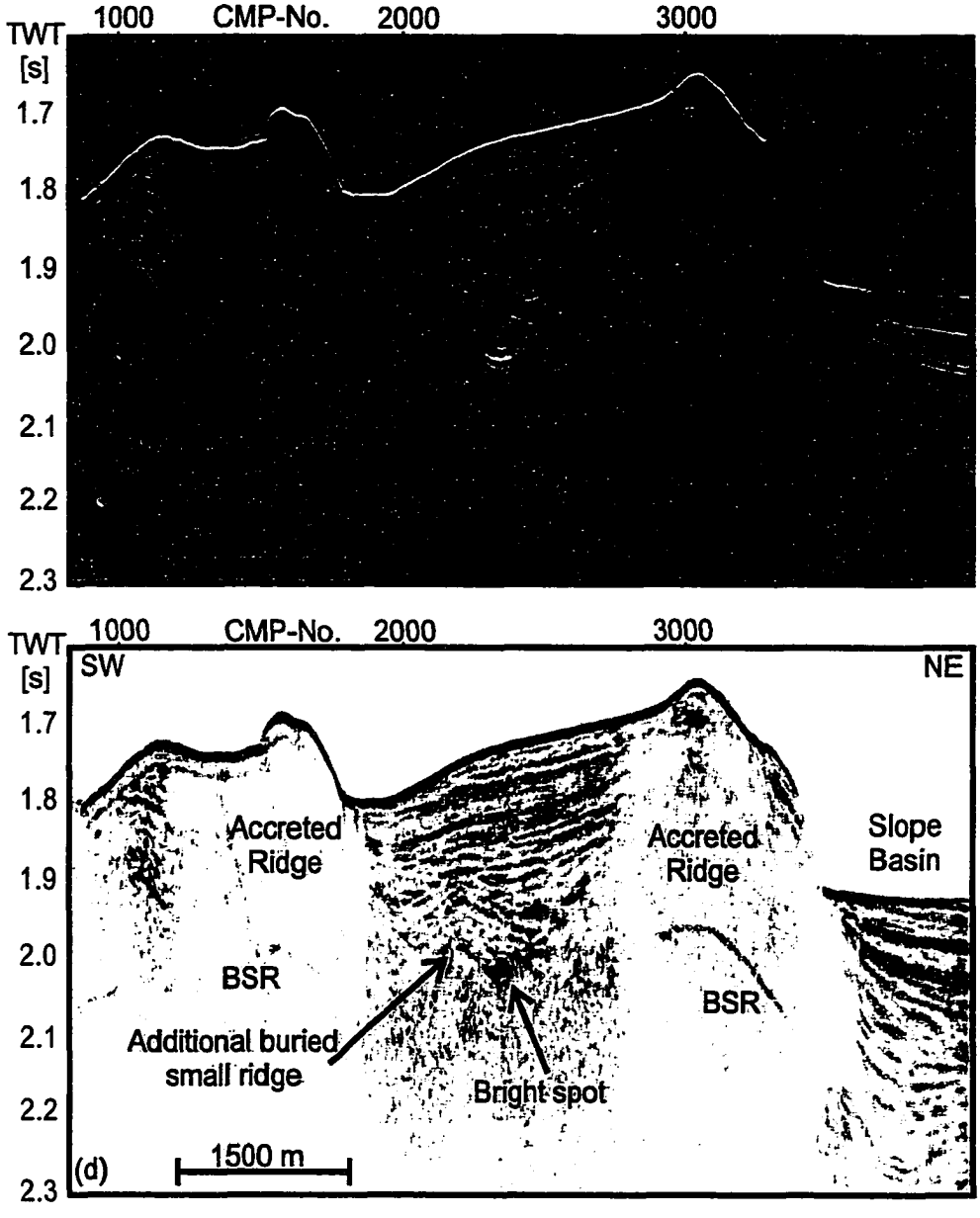

Figure 5.13 (a) Seismic amplitude section (variable area) and (b) envelope section of COAMS line XL-06. Note the bright spot developed below the sediment filled trough between the two main ridges of accreted sediment close to the additional small ridge.

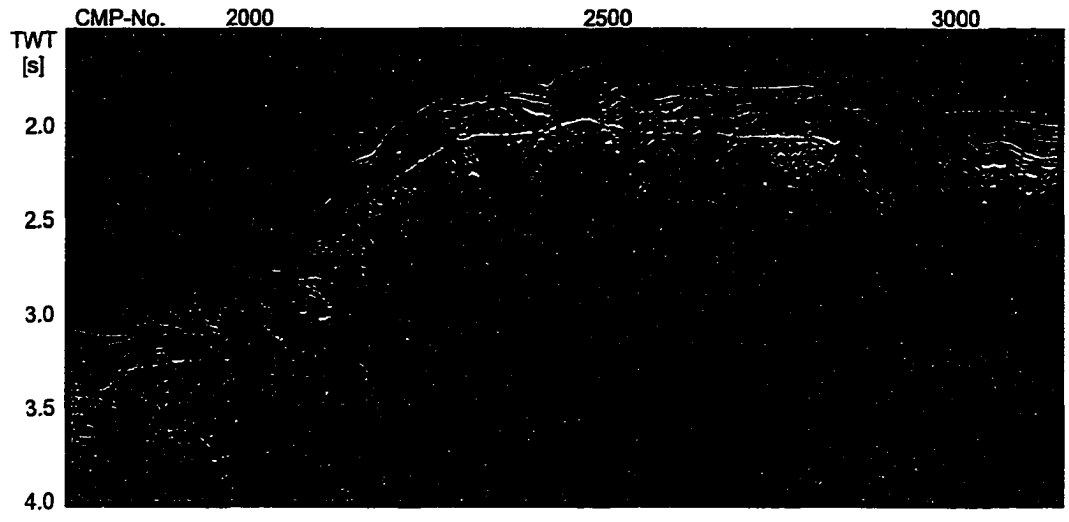

Figure 5.14 Large scale tectonic interpretation of the area around ODP Site 889/890 from migrated line 89-08.

Several smaller ridges of accreted sediments were also identified. Figure 5.15 (COAMS inline 15) shows a cross section through two of these ridges. At crossline position 280 in the NW part of the line a ridge extends to the seafloor, whereas at crossline position 700–800 another ridge is seen buried below 150 ms TWT of slope sediments. This ridge can also be seen on the line XL-06 (Figure 5.13). Deformation of the slope sediments above the buried small ridge is limited to a zone of about 100 ms TWT. Shallower sediments show less deformation until they are completely decoupled from the ridge.

The extent of these smaller ridges can best be seen in Figure 5.16. The relief of the boundary between the two sediment types is characterized by the alternating sequence of uplifted ridges and deeper basins. The small ridge in the NW part of the area shows an apparent east-west trend and is steeply dipping to the north. It extends to the seafloor and forms a dome approximately one kilometer in diameter (crosslines 200-300, inlines 22–30). The east-west trend is also evident from time slices of seismic and instantaneous amplitude (Figure 5.17). The regions with slope

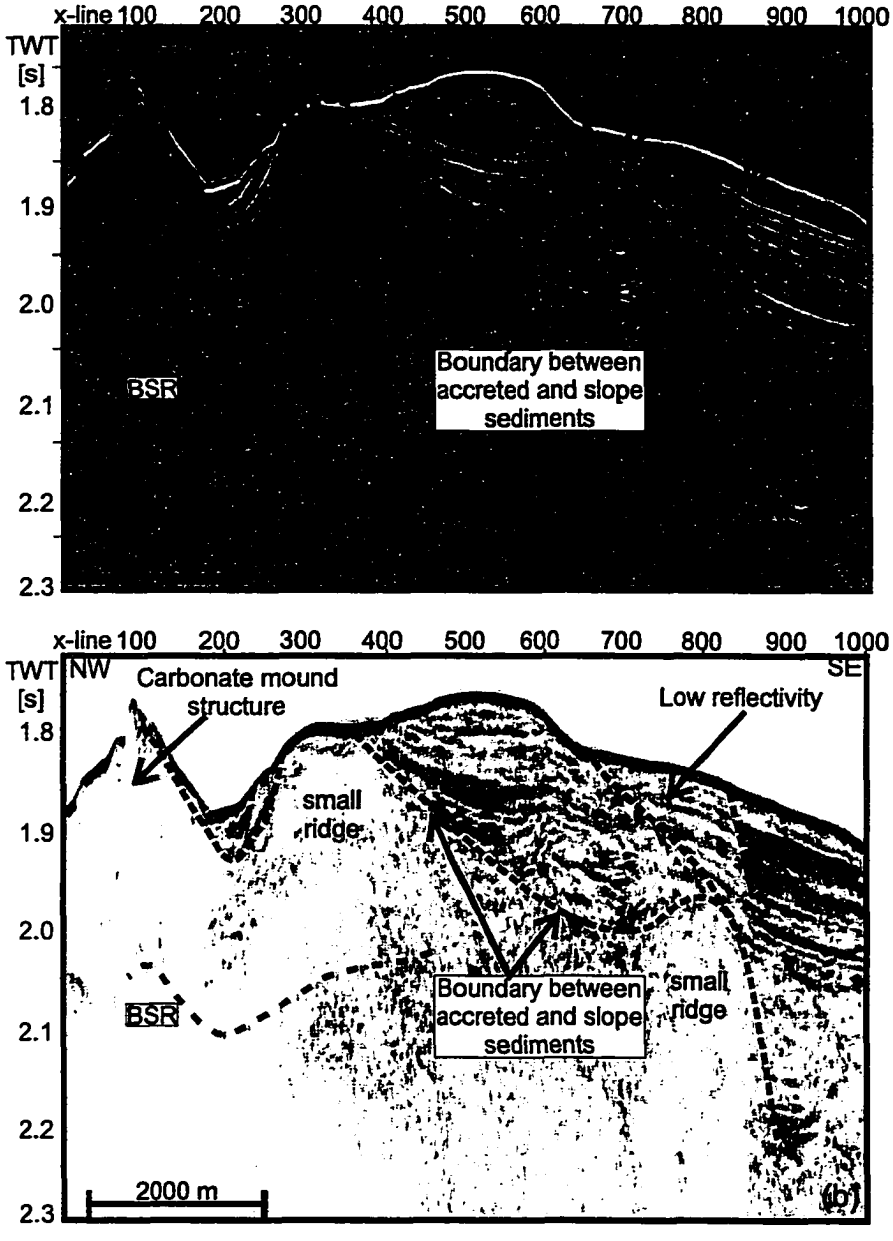

Figure 5.15 (a) Section of seismic amplitude and (b) section of instantaneous amplitude (envelope) from COAMS inline 15 showing boundary between accreted and slope sediments.

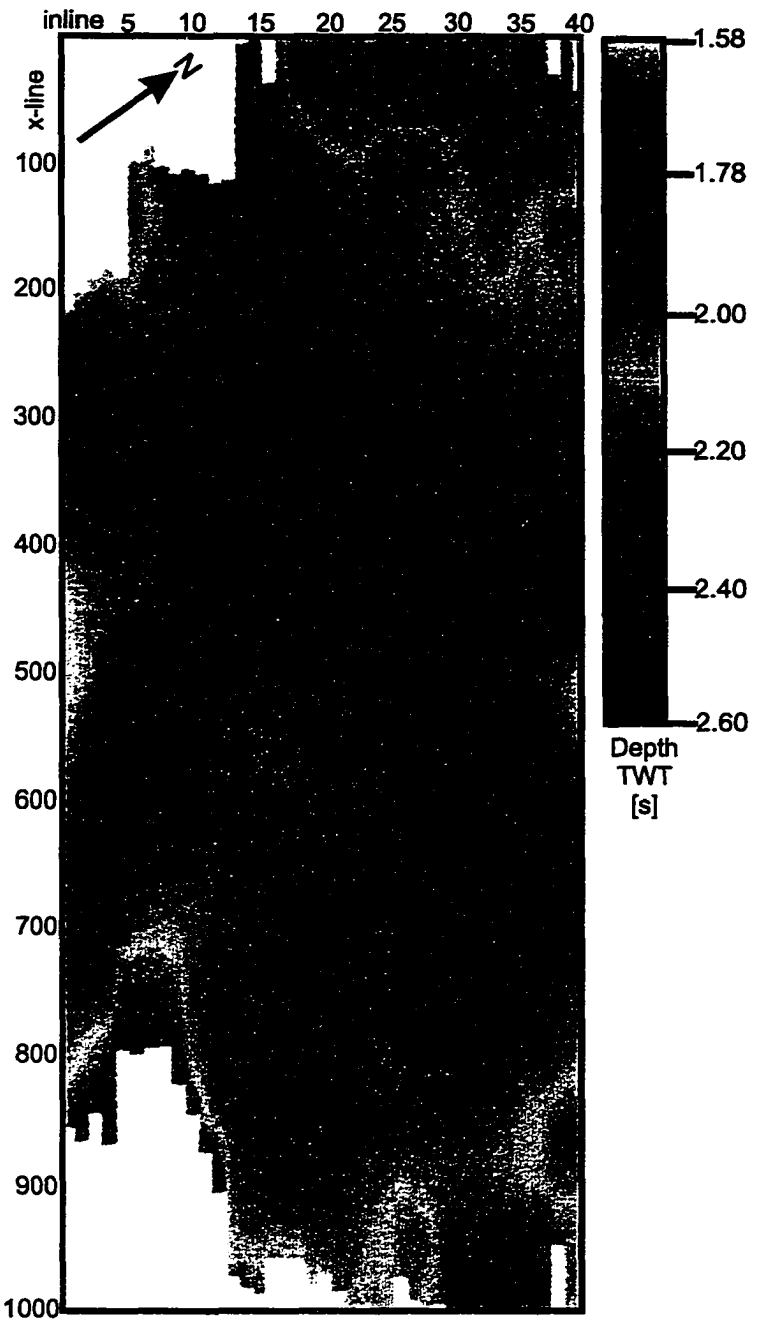

Figure 5.16 Color-coded map of the depth of the boundary between accreted and slope sediments.

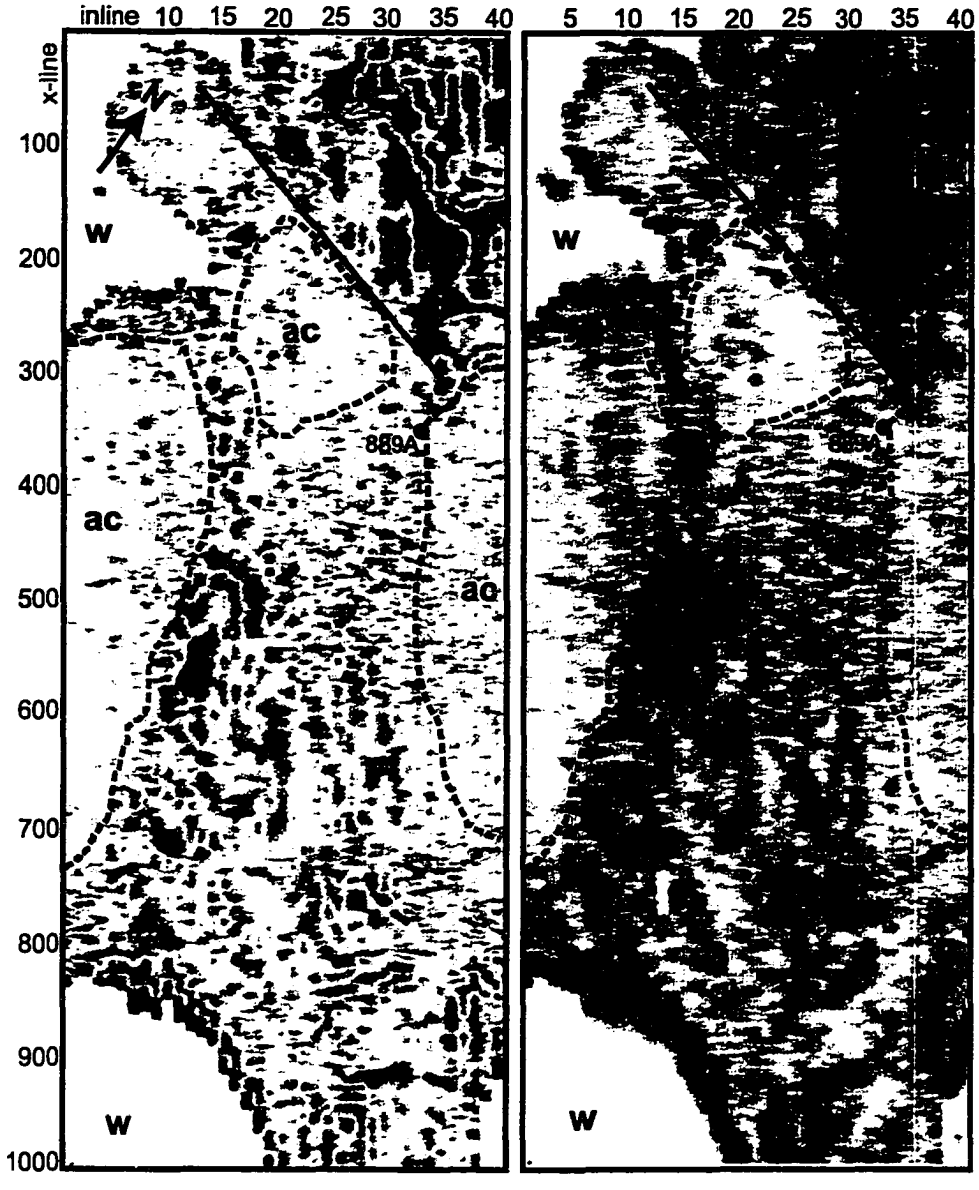

Figure 5.17 Timeslices of seismic and instantaneous amplitude from the COAMS 3-D cube at 1.852 s TWT. Zones of accreted material (ac) are easily distinguishable from regions of slope sediments that exhibit stronger coherent reflectivity. Note the east-west trend of the accreted ridge in the NE corner of the area. Parts labeled with *w* are within water.

sediments to the north of the ridge show strong reflectivity sharply truncated to zones of the accreted material. From the outcropping dome to the SW, the accreted sediments are progressively covered by slope sediments and form another ridge visible at crosslines 650–900 on inlines 12–25. The sediments above the SW-dipping ramp show strong faulting between crosslines 350–500 associated with blank zones.

A complicated ridge structure entirely composed of accreted sediment is visible in the NW corner of the main 3-D grid (see also Figure 5.15). This ridge is about 1.5 km in diameter and shows an uplift of about 80 m compared to the surrounding sediments. The seafloor is characterized by a series of diffractions and generally no deeper coherent reflectivity can be seen. However, a clear BSR is developed below the feature.

Different types of regional reflection-amplitude reduction

Several types of regional reflection-amplitude reduction were defined from the seismic data: (a) associated with accreted sediment, and (b) associated with layered slope sediments and an early stage of deformation. The blank zones associated with faults are the focus of Chapter 6.

The most obvious regional reflection-amplitude reduction is associated with the accreted sediment that lack coherent reflectivity. This type of amplitude-loss is due to the accretion process and the destruction of the original layered reflectivity. This process can result in a higher permeability of the accreted sediments, which allows for stronger upward fluid migration. This can explain why the BSR is generally much better developed within the ridges of accreted sediment compared to the basins of layered slope sediments.

In addition to the two main ridges of accreted sediments, several similar but smaller ridges were identified in the seismic data. These smaller ridges are buried below slope sediments that often show strong local deformation and associated amplitude reduction. This amplitude reduction is related to the uplift of the underlying

accreted ridge and the deformed slope sediments are in a gradational transition to the type of completely accreted sediment. However, there is also a type of amplitude reduction in the layered sediment that are almost undisturbed. A representative example of this kind of amplitude reduction is shown in Figure 5.15. A series of folds or gliding planes is developed in the sedimentary sequence near the uplifted ridges of accreted material. The folds or gliding planes separate blocks of slope sediments that exhibit different reflection characteristics. The sediments just above the ridge have reduced reflectivity sharply truncated at a block of stronger reflectivity. The amplitude reduction affects the entire sediment block from the seafloor down to the top of accreted sediments but layering is still preserved. All sediment layers are continuous across the boundary indicating no structural/geological difference between the two blocks. Thus the change in reflectivity is not due to a change in the internal sediment properties such as grain size and mineral composition that can create a change in reflection strength. A possible explanation is a fluid flow related increase in porosity and permeability that reduce the impedance contrast and increase the attenuation within the sediment (Zühlsdorff *et al.*, 1999). If these layers have increased porosity and permeability they are also prone to contain relatively more hydrate than the surrounding sediment. Thus, an original increase in porosity is counteracted with porosity reduction due to hydrate. However, the higher hydrate concentrations themselves can contribute to amplitude reduction by decreasing the impedance contrast (Lee *et al.*, 1993; Lee and Dillon, 2000) and an increase of attenuation (Guerin and Goldberg, 1999).

5.3 Combination With Regional Seismic Studies SC-93 and MC-96

Prior to the COAMS-99 seismic study, two regional parallel 2-D multi- and single channel seismic studies were carried out in the area of the ODP Site 889/890. A single channel seismic study (SC-93) was performed on a 200 m spaced grid parallel to the COAMS-99 main seismic survey grid (Fink and Spence, 1999). This survey mainly covered the area from about 2 km west of the ODP site into the broad slope basin east of the site. The multi-channel seismic study carried out in 1996 consists of 400 m spaced grid lines perpendicular to the SC-93 and COAMS-99 grid lines (Mi, 1996). This survey is the west-ward expansion of the SC-93 study area. The two surveys partially overlap by about 1000 m. Survey lines for both studies are shown in Figure 2.4 in Chapter 2. From both surveys regular spaced grids were generated for use in the 3-D visualization software *Kingdom Suite*. The primary goal of this study is the comparison of seafloor reflection coefficient studies, generating a combined bathymetric map and broad-scale tectonic interpretation.

5.3.1 Combined Bathymetry and Seafloor Reflection Coefficients

Combining the three different regional grids required binning of each survey into a regular grid. The COAMS-99 and SC-93 study had comparable navigation accuracy and data from the SC-93 survey had generally good quality. The seismic data quality of the MC-96 data set is relatively poor. In addition to the poor quality, the data covers the main slope region, with a drop in water depth of more than 1000 m. Almost no seismic imaging was possible over the slope region. Bathymetry was mainly obtained by interpolation and comparison to the multibeam-bathymetry available for the area.

To make all surveys comparable, migrated sections had to be used. Data from the MC-96 area were recovered from a CD-ROM containing the final time-migrated sections. However, these migrated sections did not contain correct header information

(such as navigation). The only navigation information available from this survey were rough estimates of start and end point of the individual lines. The grid was set to a 30 m spacing between adjacent CMP's and 400 m between inlines. One inline within the grid was missing in the data record (inline 96-18) and an empty line was inserted to ensure regular data coverage.

Only raw data for the SC-93 data set could be recovered from an exabyte tape. Seismic processing done for these lines followed the same steps and parameters as outlined by Fink (1995). Final migration using the fast phase-shift time-migration technique was carried out using a generalized velocity-depth function from previous multichannel seismic velocity studies (Yuan *et al.*, 1996).

The primary problem in merging the different grids was the vertical shift between the surveys. No information of trigger time delays or streamer depths was available for the surveys from 1993 and 1996. The lines from the SC-93 and MC-96 surveys that overlapped with the COAMS-99 grid were therefore shifted individually until a reasonable fit between the different topographies was achieved. These shifts varied between individual lines and no consistent mismatch of an entire survey was observed. Especially around the eastern topographic high a considerable mismatch between the SC-93 and COAMS-99 survey was observed that could not be completely removed. A possible explanation of these differences in depth and x-y position is the artificial gridding superimposed on the SC-93 data assuming a straight line. A similar problem occurred at the western topographic high. The MC-96 data were acquired with a recording delay of 1.5 seconds to ensure full coverage of the entire steep slope region. Over the top of the western ridge, this recording delay caused clipping of the topography that was shallower than 1.5 seconds. The COAMS-99 data set did not cover this region, resulting in a small gap in the total bathymetry.

Figure 5.18 shows the combined topography of all seismic data sets together with a representation of the seafloor reflection coefficients.

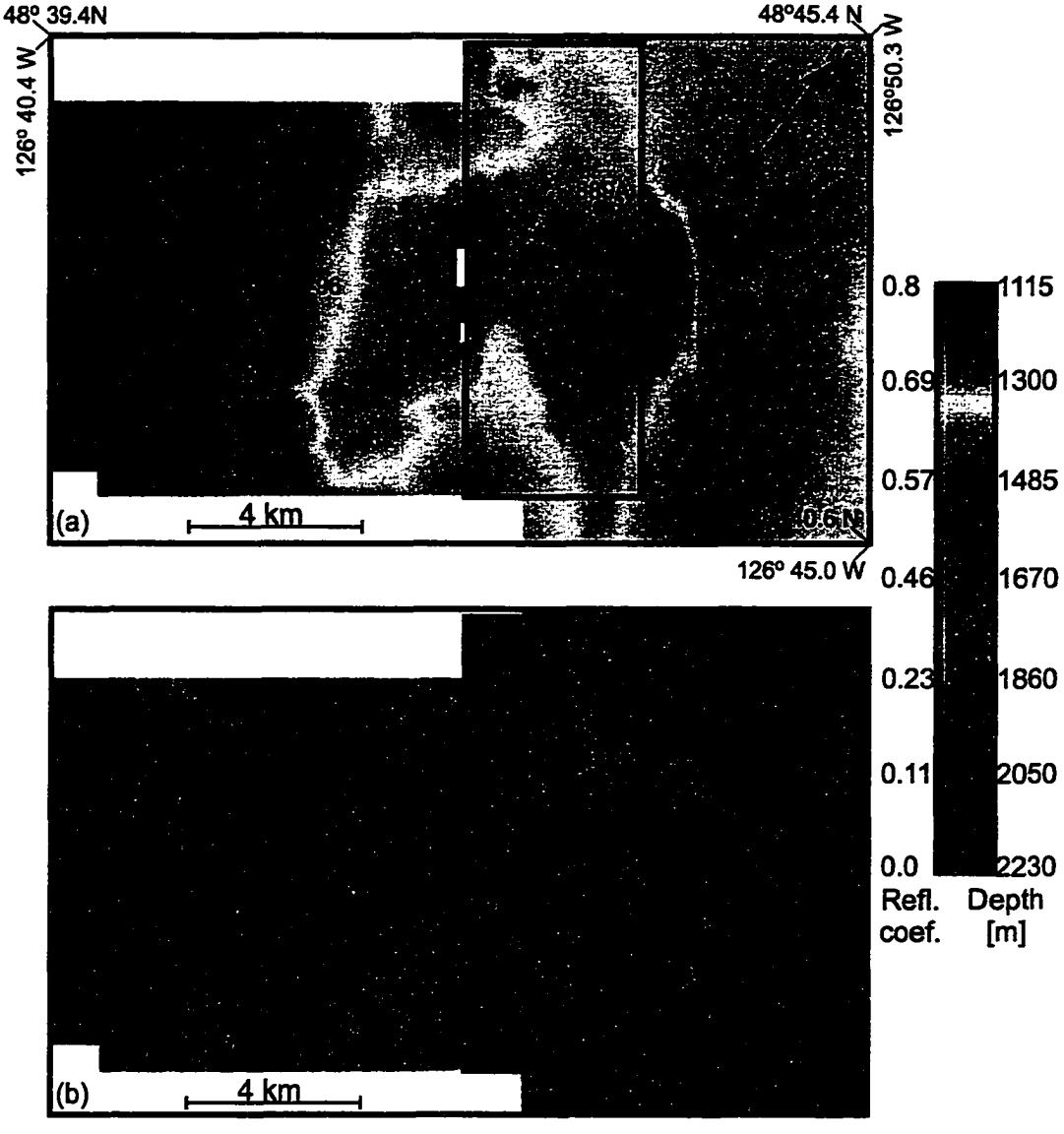

Figure 5.18 (a) Combined bathymetry and (b) seafloor reflection coefficients from all regional grids in area around ODP Site 889/890 (MC-96, COAMS-99, SC-99 from west to east).

Reflection coefficients of the SC-93 and MC-96 data were determined by an amplitude balancing between the surveys with the COAMS-99 data as reference. The reflection coefficients of the COAMS-99 data were determined using Warner's method (see section 5.2.2). The SC-93 and COAMS-99 data were in very good agreement especially in showing the same region of increased reflection coefficients around the ODP Site 889. However, the MC-96 data did not show any similarity with the COAMS-99 study in the overlapping area. Possible explanations for the mismatch include: (a) different seismic processing sequences, (b) different line direction and related interpolation in the crossline direction, and (c) amplitude calibration problems with the solid multichannel streamer used in 1996.

5.3.2 Boundary Between Accreted and Slope Sediments

The data quality of the SC-93 data allowed the identification of the boundary between accreted and slope sediments. The 200 m line spacing resulted in a relatively coarse observation but large-scale features are still visible (Figure 5.19). Major problems in defining the boundary in the SC-93 data were varying amplitudes among the individual lines and a line direction almost parallel to the main westward dipping thrust fault. The outcrop of the thrust fault lies directly at the foot of the ridge but the deeper root of this thrust could not be imaged. In general, the eastern basin is characterized by a series of accreted ridges covered by slope sediments with strong internal deformation. A striking feature of the basin is the almost flat seafloor (Figure 5.18) indicating relatively slow uplift of the accreted ridges.

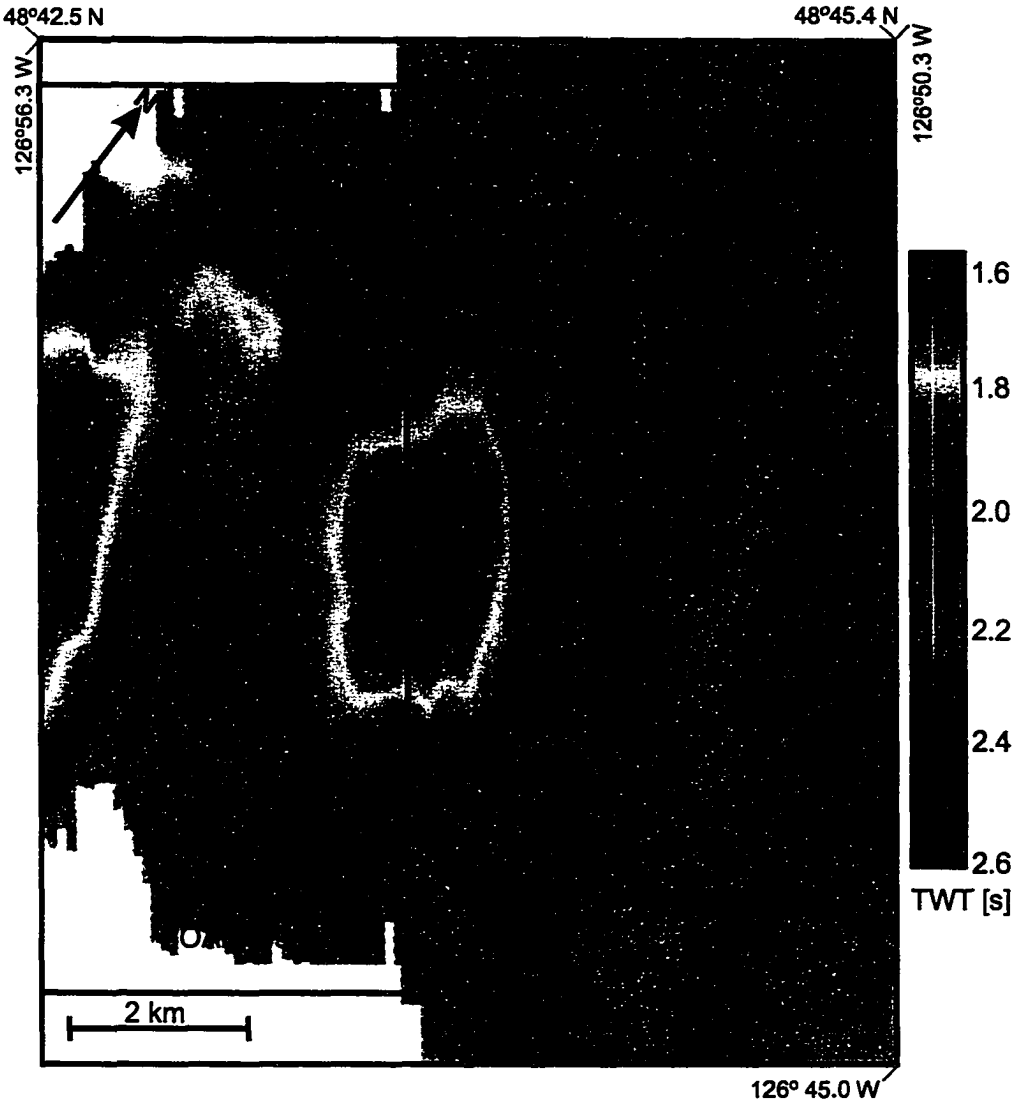

Figure 5.19 Combined topography of the boundary between accreted and slope sediments.

5.4 COAMS-99 BSR Studies

5.4.1 Distribution

A characteristic feature of an area with hydrate occurrence is the bottom simulating reflector (BSR). It is believed to mark the base of the gas hydrate stability zone, below which free gas perhaps can occur. Mapping the distribution and seismic reflection characteristics of a BSR is an important tool in imaging regional variations in hydrate concentration, free gas accumulations and heat flow patterns. The BSR occurrence and reflection coefficient is controlled by (a) the amount of hydrate in the overlying sediments, (b) the amount of free gas below the BSR and (c) the thickness of the gradient transition layer (Chapman *et al.*, 2001).

The distribution and reflection amplitudes of the BSR over the area of investigation are irregular. The BSR is clearly visible within sections of accreted sediment especially below the prominent topographic highs but it is almost absent in basins filled with slope sediments (Figure 5.12 and 5.13). One explanation is that the BSR is masked in the well layered sediments. However, where the sediments do not follow the seafloor, a BSR should cross-cut these layers. This is generally not observed in the large eastern slope basin. However, in the smaller basins within the area of the 3-D seismic study a BSR is observed in the basins. As an example a part of line XL-01 is shown in Figure 5.20 illustrating a clear BSR in the slope sediment section.

It was speculated that the well layered sediments inhibit vertical fluid/gas migration and BSR formation (Zühlsdorff *et al.*, 2000). However, hydrate in those no-BSR areas was inferred from remote electrical sounding (Yuan and Edwards, 2000). Since no BSR is observed, this either indicates very low hydrate concentrations or the absence of free gas below the base of hydrate stability (see Chapter 7 for further analyses).

Figure 5.21 illustrates where a BSR was observed in the area of the 3-D seismic study. No interpolation was carried out to fill in areas without a BSR. The BSR is

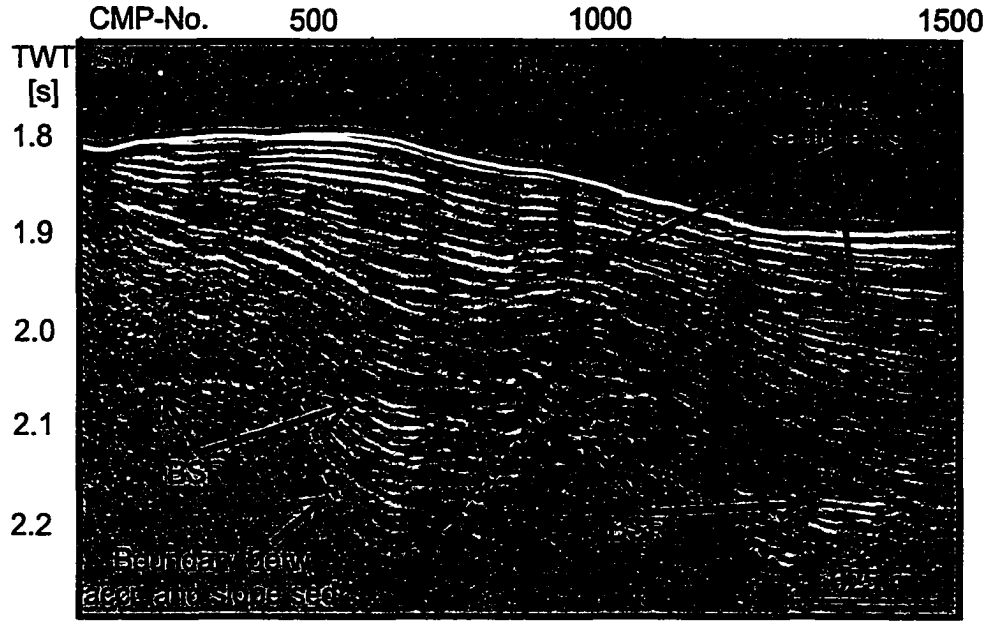

Figure 5.20 Part of COAMS line XL-01 showing a well developed BSR in slope basin sediments.

generally continuous below the topographic highs and in areas of smaller ridges of accreted sediment.

There is no clear BSR below the uplifted sediment block, although the BSR would occur within accreted sediment. The reflectivity below the expected BSR depth is generally increased compared to outside of the uplifted block and at one location within the uplifted block there is a BSR bright spot (see below). The uplifted sediment block hosts several blank zones that have been interpreted as methane cold seeps along faults that act as conduits for upward migrating fluids and gas (see Chapter 6). Increased methane flux inside the largest blank zone was inferred from geochemical analyses of pore waters (C. Solem, personal communication 2001) and within the center of this zone massive hydrate was recovered, which is an indication of increased methane supply. It can be speculated that the lack of a BSR is related to the methane seeps, i.e. the free gas that normally would accumulate at the base of the hydrate

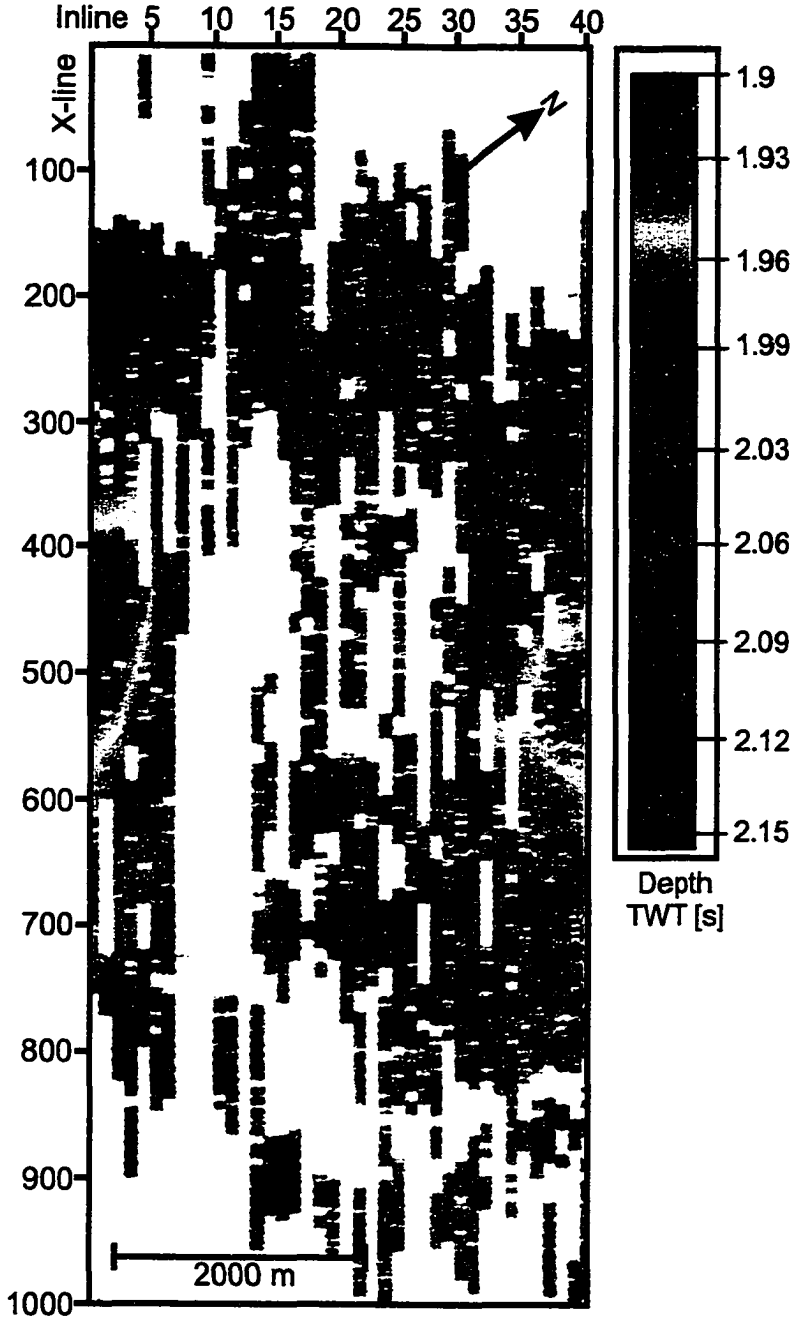

Figure 5.21 BSR distribution around ODP Site 889A. Shown are raw picks in TWT [s].

stability field can escape through the faults/conduits. However, another contrary explanation can be an increase in BSR thickness following the BSR thin bed model by Chapman *et al.* (2001). The BSR vertical incidence reflection coefficient is strongly affected by the thickness of the velocity gradient layer. For the COAMS center frequency of 100 Hz, the BSR is strongly attenuated for thicknesses larger than about 8 m (see Figure 2.5 in Chapter 2). Thus the observed missing BSR can be the effect of a thicker gradient layer. This thicker layer can be the direct effect of the sediment block uplift since the BSR had to move upwards through the sediments dissociating the hydrate. However, this is in contrast to von Huene and Pecher (1999) who argue that dissociated hydrates produced by uplift leave free gas behind and thus a strong BSR. This may be true for low seismic frequencies only.

5.4.2 BSR Vertical Incidence Reflection Coefficient

The BSR reflection coefficient provides a simple mapping tool for hydrate and/or gas concentration above and below the BSR. However, it is still unclear how much of the reflection coefficient variation is due to hydrate or free gas concentrations.

In general, the BSR reflection coefficients are relatively low, on average -0.05 (Figure 5.22). Higher values of about -0.1 were observed below the eastern main ridge indicating a larger velocity contrast at the BSR. This increased BSR reflectivity can reflect higher hydrate concentrations in the accreted sediments above or larger free gas concentrations below the BSR. In general the BSR is more prominent in the accreted sediments, which may reflect the higher permeability of the sediments and higher potential for gas hydrate formation and fluid/gas migration.

Several local BSR bright spots are seen with reflection coefficients as large as -0.3, such as close to blank zone 1 (Figure 5.22). It appears as an oval that follows roughly an east-west trend. It was traced on inlines 20–28 and crosslines 575–795 and covers an area of about 1 km^2. This bright spot was also imaged on crossing lines XL-06 and

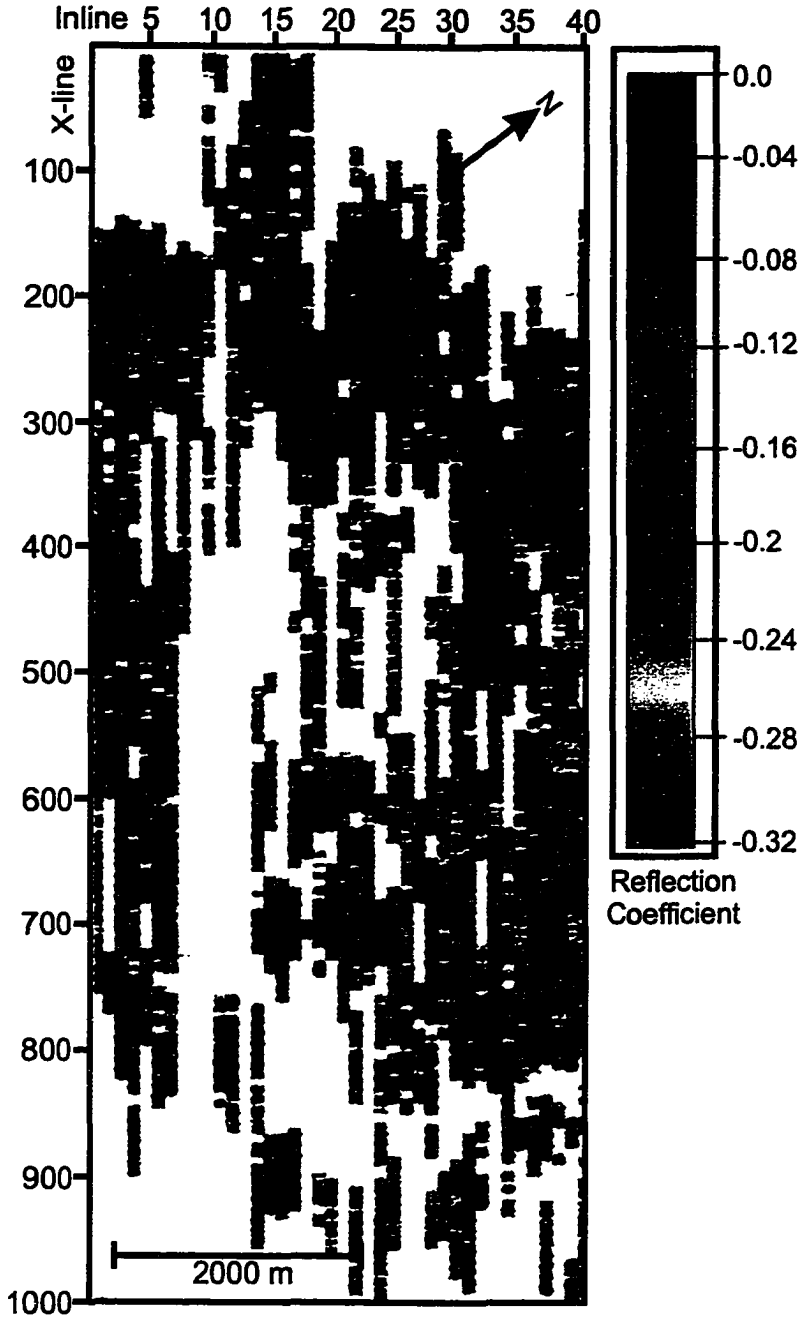

Figure 5.22 BSR reflection coefficients from COAMS data around ODP Site 889A. Note the prominent bright spot on inlines 20–28 and crosslines 575–795.

XL-07 (e.g. Figure 5.13). The local increase of reflection amplitude can again be an indication of larger gas or higher hydrate concentrations due to increased fluid/gas migration. Higher reflection amplitudes are also observed within the slope sediments 50 ms TWT above and below the BSR bright spot. The bright spot follows the axis of a small slope basin with steeply dipping ridges of accreted sediments to the east and west. Thus, the increased amplitudes can also be a focusing effect of the seismic energy, equivalent to what was seen for seafloor reflection coefficients at the foot of the topographic highs.

In the study by Fink and Spence (1999), BSR reflection coefficients were converted into hydrate concentrations by tying the observed reflection coefficients with the well log response at ODP site 889. Additional constraints from the full wave form inversion (Yuan *et al.*, 1999) and vertical seismic profiling (VSP) (MacKay *et al.*, 1994) were used in their approach. With the over-simplifying assumption that the seismic velocity of 1515 m/s below the BSR does not change over the entire area and that the density does not change across the BSR interface (which is a reasonable assumption), hydrate concentrations were determined using the technique of Yuan *et al.* (1996). Hydrate increases the seismic velocity, and the difference with respect to a reference profile will give a measure of the amount of hydrate formed. A reference velocity of 1625 m/s for non-hydrate/gas sediments at the depth of the BSR yields mean hydrate concentrations from 5–10% with local maxima as large as 20%.

The BSR shows a frequency dependent response (Chapman *et al.*, 2001) due to a velocity gradient layer that creates tuning effects. Thus a simple conversion of vertical incidence reflection coefficient into hydrate concentration as described above may not be the best approach. Depending on the frequency used, different hydrate concentrations would result. Scaling the vertical incidence reflection coefficient to the well-log and VSP response, which showed a reflection coefficient of about -0.09, partially overcomes this problem, but it assumes that the thickness of the thin layer is constant. The reflection coefficients from the COAMS 3-D experiment around the

ODP site 889A are on average -0.06, i.e. 30% lower than what would be expected from the well-log and VSP response. This reduction is in good agreement with the modeling results for a ~5 m thin-bed BSR (Chapman *et al.*, 2001). A rough scaling of the calculated reflection coefficients can be achieved following a similar procedure as outlined by Fink and Spence (1999). If the BSR is only the effect of hydrate above the BSR (i.e. no gas below), an average reflection coefficient of -0.1 corresponds to a velocity of 1990 m/s using the reference velocity of 1625 m/s for no-gas/hydrate sediments. This velocity is equivalent to a hydrate concentration of about 35% of the pore space. Assuming that the BSR is the effect of free gas below only (i.e. no hydrate above), the average reflection coefficient of -0.1 corresponds to a velocity of 1330 m/s in the gas-bearing sediment, which is equivalent to about 1–2% free gas.

No simple conversion of BSR vertical incidence reflection coefficients into hydrate concentration above or free gas concentration below the interface was carried out for the entire area. Hydrate concentrations can better be estimated from multichannel velocity analyses or careful full waveform inversion as described by Yuan *et al.* (1999). In Chapter 7, the amplitude-versus offset (AVO) response of the BSR, which may help to better constrain hydrate/gas concentrations above and below the interface, is described.

5.4.3 Heat Flow Derived From BSR Depth

The BSR closely approximates the base of the hydrate stability field, and due to the strong temperature influence on hydrate stability, the BSR marks an isotherm. Thus BSR-depth variation is an indicator for local variation in heat flow, which can be the result of fluid flow or thrust faulting. A simple conductive model, adapted from Ganguly *et al.* (2000), was used to convert observed BSR travel times into heat flow. Results from the regional 3-D grid and seismic line XL-06 are shown. These heat flow estimates are compared to in situ heat flow probe measurements carried out

during the piston coring cruise in July/August 2000.

Methodology of Heat Flow Calculations

Travel times of the seafloor (t_{seaf}) and BSR (t_{bsr}) were determined from the migrated sections of the 3-D cube and converted into BSR-depth (D_{bsr}) by using a simplified velocity function (V_p) from previous multichannel seismic studies (Yuan *et al.*, 1996).

$$\Delta t = t_{seaf} - t_{bsr} \tag{5.2}$$

$$V_p = 1511 + 521 \cdot \Delta t - 93 \cdot (\Delta t)^2 \tag{5.3}$$

$$D_{bsr} = 0.5 \cdot V_p \cdot \Delta t \tag{5.4}$$

The simplified velocity function does not take the velocity increase due to hydrate into account. But the estimated heat flow is not very sensitive to velocity, since a change in BSR depth results also in a change in BSR temperature without changing the temperature gradient significantly. A change in velocity of about 180 m/s at a typical BSR depth of 200 m bsf results in heat flow values that differ by only 2–3% (Ganguly *et al.*, 2000).

Hydrostatic pressure was assumed at the BSR depth and was calculated by using a water density of 1030 kg/m^3. However there is a controversy over which pressure model is correct: hydrostatic or lithostatic. Previous estimates of heat flow from BSR depth were done using the hydrostatic pressure approach (Davis *et al.*, 1990; Hyndman *et al.*, 1993), but logging-while-drilling data from the Barbados accretionary prism suggest nearly lithostatic pressures at BSR depth (Moore *et al.*, 1998). The study by Ganguly *et al.* (2000) used lithostatic pressure. Heat flow estimated using the lithostatic pressure model tend to be 8–12% larger (Ganguly *et al.*, 2000). In general, the values obtained from the hydrostatic pressure model for the area of the 3-D seismic study were closer to the observed values from the in situ measurements,

which is therefore the preferred model:

$$P = \rho \cdot 9.81 \cdot (wd + D_{bsr})/1000000, \tag{5.5}$$

where P is pressure in MPa and wd is water depth in m.

Temperature at the BSR (T_{bsr}) was estimated from the phase boundary in the hydrate stability field for the pressure calculated. Equation 5.6 is adapted from Bouriak *et al.* (1999):

$$\begin{aligned} K &= 0.0400782^2 + 4 \cdot 0.00035 \cdot (log(P) - 0.4683776), \\ T_{bsr} &= (-0.0400782 + \sqrt{(K)})/(2 \cdot 0.00035). \end{aligned} \tag{5.6}$$

The last parameter needed is thermal conductivity (k). An empirical expression for thermal conductivity versus depth was given by Davis *et al.* (1990):

$$k = 1.07 + 5.86 \cdot 10^{-04} \cdot D_{bsr} - (D_{bsr}^2 \cdot 3.24 \cdot 10^{-07}), \tag{5.7}$$

with k in W/m°C, and D_{bsr} in m. This relation is also in good agreement with new measurements carried out during the July/August 2000 cruise (see Table 6.2 in Chapter 6).

Heat flow (H) can now be calculated assuming a linear temperature gradient and a simple conductive heat transport relation:

$$H = k\frac{T_{bsr} - T_{seaf}}{D_{bsr}}. \tag{5.8}$$

Seafloor temperature values were taken from a generalized temperature-versus depth profile from Davis *et al.* (1990) for the main 3-D grid and were on average in good agreement with in situ bottom water temperatures observed during the July/August cruise. The accuracy of estimating absolute heat flow from BSR depth using the method by Ganguly *et al.* (2000) is about 20%, but the relative accuracy between individual estimates is about 5–10%.

5.4.4 Heat Flow Pattern

The BSR-depth was determined from an interpolated and smoothed BSR surface. Heat flow values were obtained from the interpolated BSR reflector. Wherever possible, gaps between individual BSR occurrences were removed. Figure 5.23 shows a map of the smoothed BSR topography and Figure 5.24 is a map showing the heat flow pattern over the area of the 3-D seismic survey. The heat flow varies only by about 30 mW/m^2 over the entire area. The lowest values were observed below the topographic highs, a phenomenon that was also observed by Ganguly *et al.* (2000). This deepening of the BSR and associated low heat flow values are displayed in Figure 5.25. The area of the uplifted sediment block also shows relatively low heat flow values, which equivalently can be an effect of the exposed topography. The highest heat flow values are observed close to the giant carbonate ridge in the NW corner. These heat flow values may not be very representative due to imaging problems related to the complicated seafloor structure.

Significant differences between the in situ heat flow measurements and the estimates based on BSR depth were observed (Lewis, 2000). Heat flow values along seismic line XL-06 are consistently higher from the BSR estimates compared to the heat probe data (Figure 5.26). Probe heat flow values as low as 35 mW/m^2 were measured below the eastern topographic high, which is about 30 mW/m^2 less than the BSR estimate. Within the sediment-filled trough between the main ridges, the difference between measured and estimated values is only about 10 mW/m^2.

A possible explanation for this difference can be the fact, that there was a bottom water temperature transient propagating into the sediment changing the temperature gradient with depth. The bottom five sensors of the heat probe were taken to calculate average heat flow during the measurements only. Therefore heat flow values are always smaller than the *true* values (Lewis, 2000). Given the accuracy of the BSR-to-heat-flow conversion of about 20%, measurements and estimates are thus in general

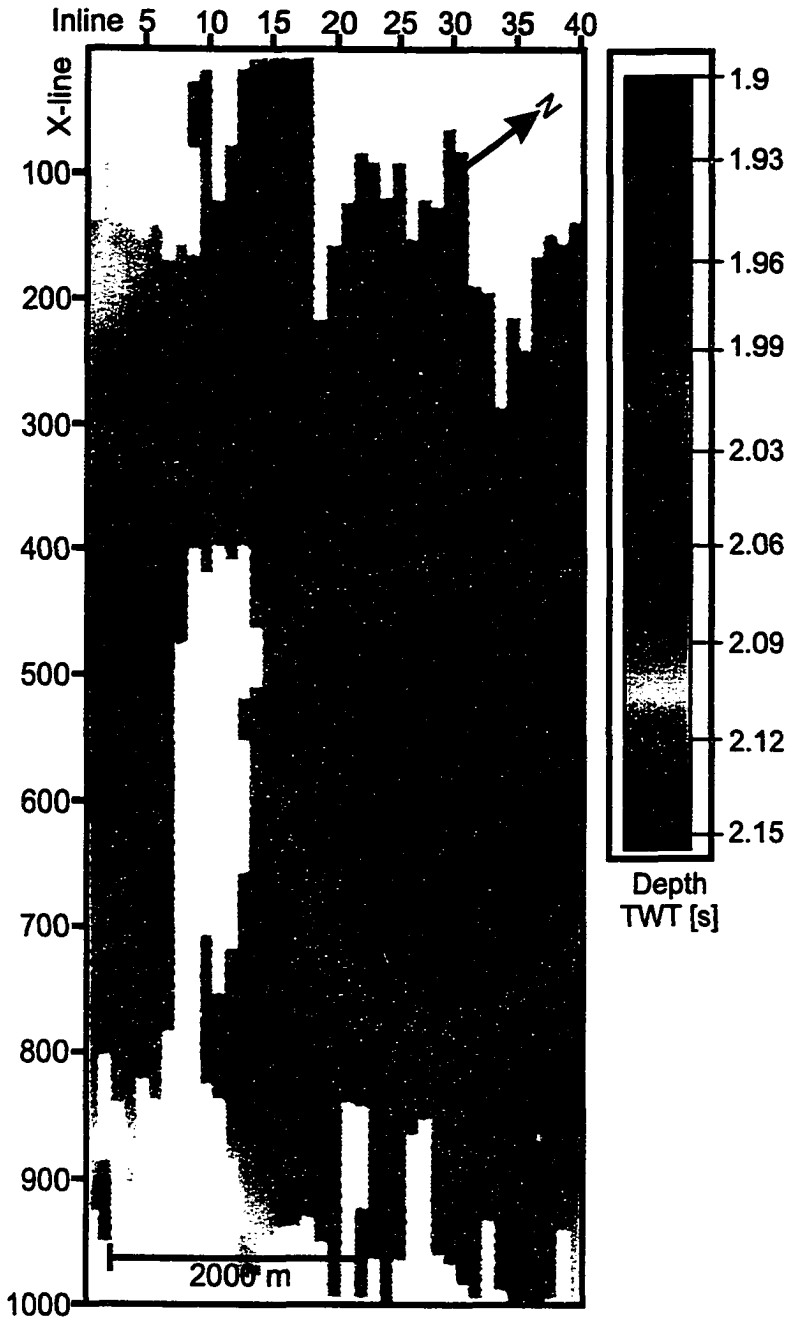

Figure 5.23 Map with interpolated and smoothed BSR topography. Depth is given in seconds TWT.

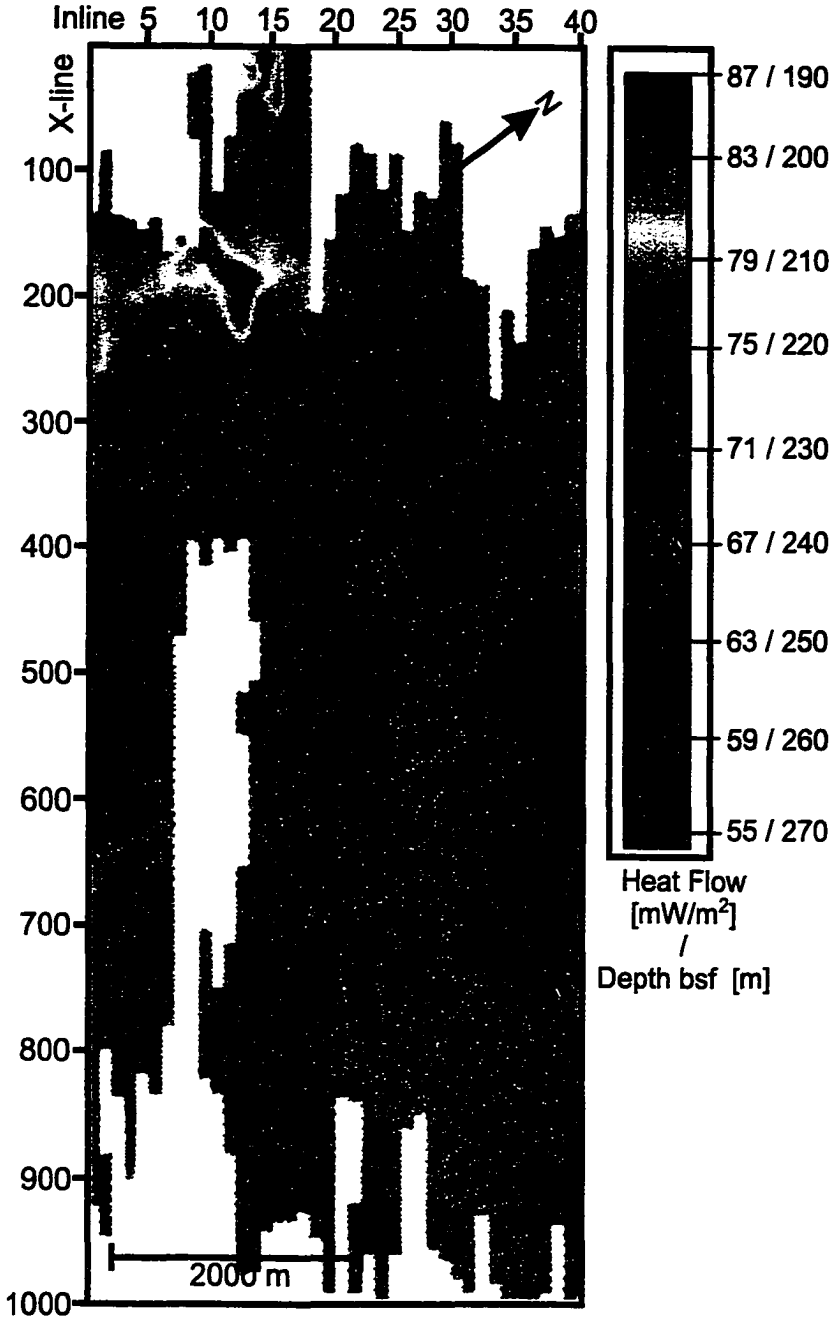

Figure 5.24 Heat flow (in mW/m^2) and depth of BSR (in m bsf) determined from interpolated BSR following method by Ganguly *et al.* (2000).

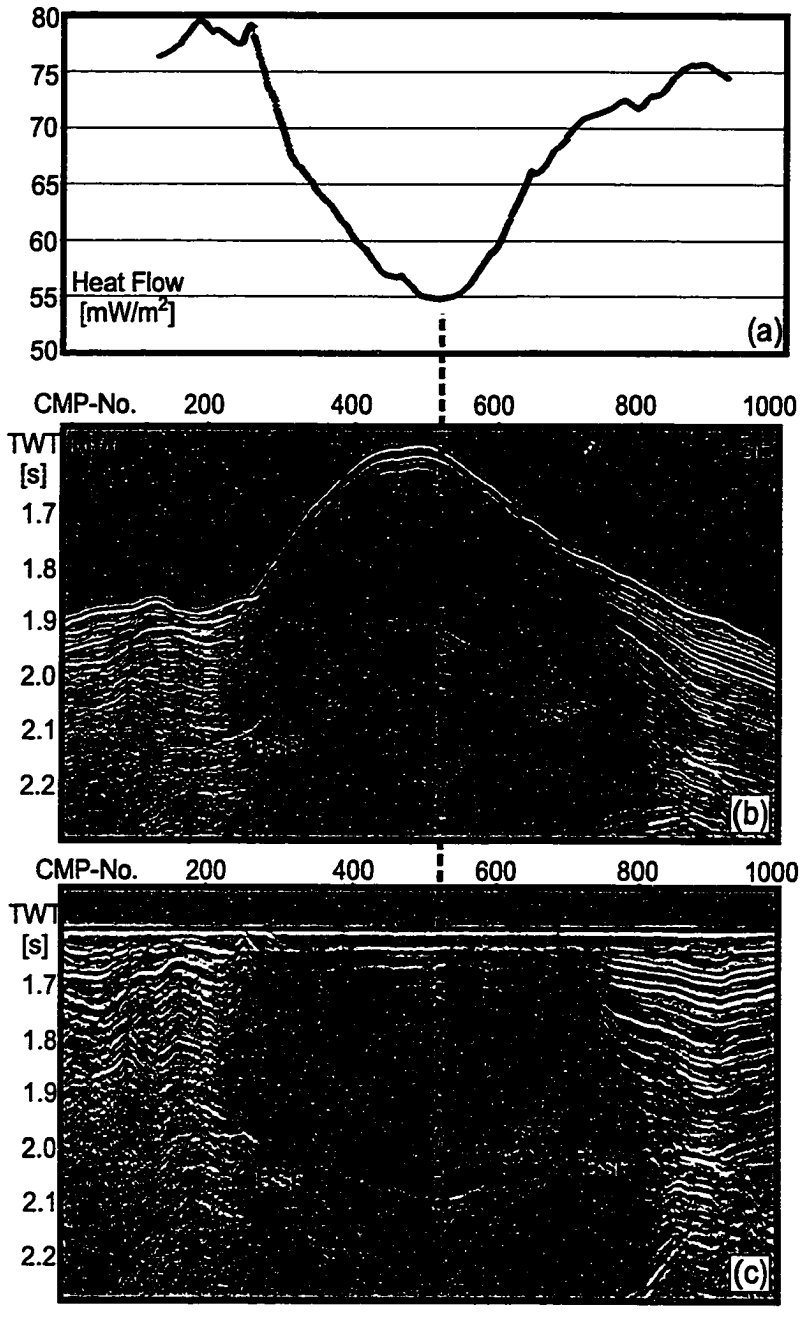

Figure 5.25 (a) Calculated heat flow values, (b) original seismic section, and (c) seismic section flattened to seafloor of COAMS inline 02 of main 3-D grid. Note the deepening of the BSR towards the center of the accreted ridge.

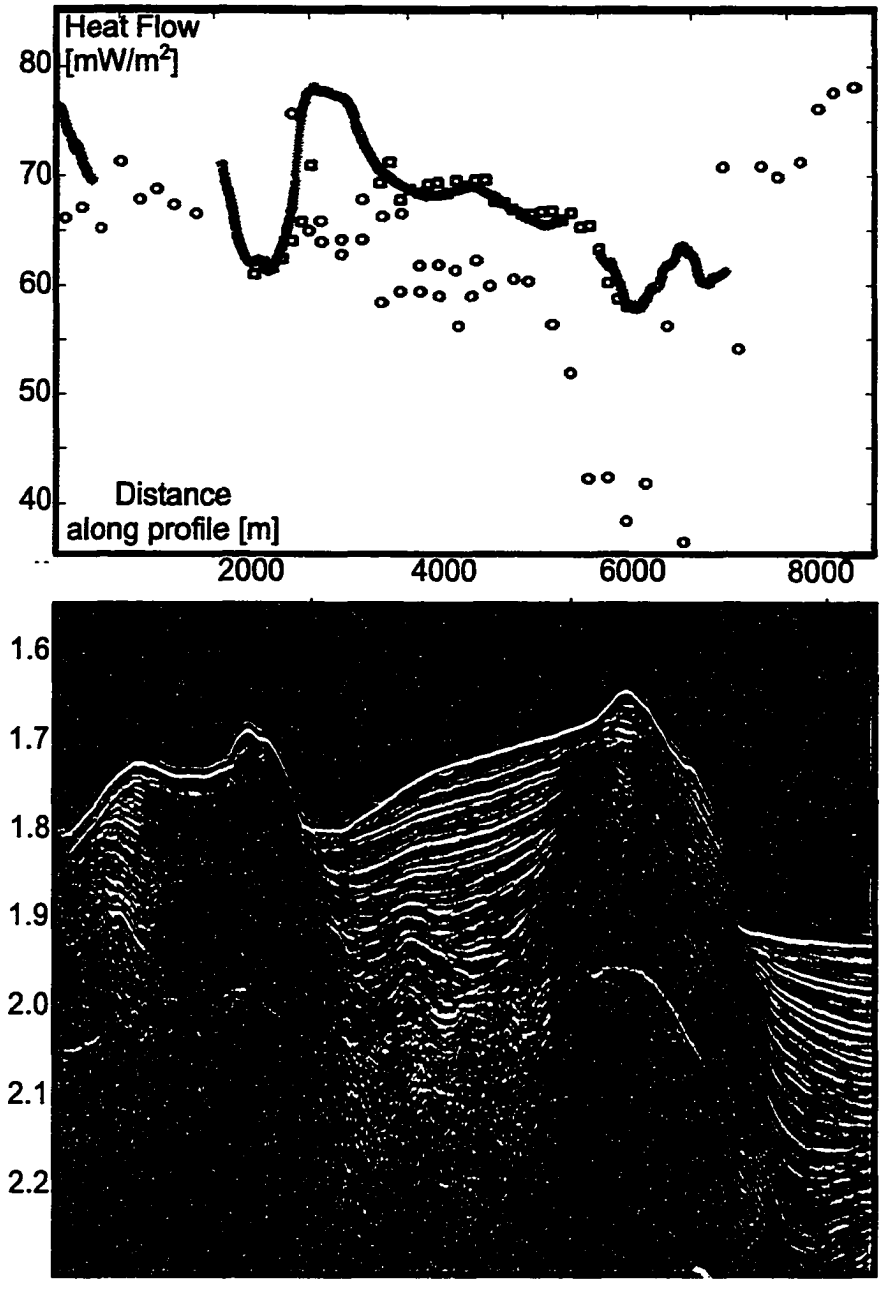

Figure 5.26 Heat flow from BSR depth estimates and from in situ measurements along COAMS line XL-06. Red crosses are from line XL-06, black squares are estimates from main grid and blue circles are the heat probe measurements (Measurements were carried out by T. Lewis, P. Flueck and J.K. Hong).

agreement. Heat flow measurements were carried out further along seismic line XL-06 to the east. Heat flow values stay as high as 70 mW/m^2. The observed heat flow signal, i.e. very low values below the ridge (also may be an effect of the topography) and larger values behind the ridge, is consistent with the presence of a thrust and local fluid discharge (Figure 5.27). The thrust at this ridge was interpreted to be westward dipping. Thrusting alone would result in low values below the ridge only and fluid flow along a channel without any deformation would result in a local heat flow high above the outcrop of the channel. There are not enough measurements taken around the western topographic high due to a very hard seafloor sediment, which did not allow for probe penetration. However, BSR derived heat flow values suggest a similar mechanism at this ridge, but the difference is not as pronounced ($\Delta H = 15$ mW/m^2) as at the eastern ridge ($\Delta H = 40$ mW/m^2).

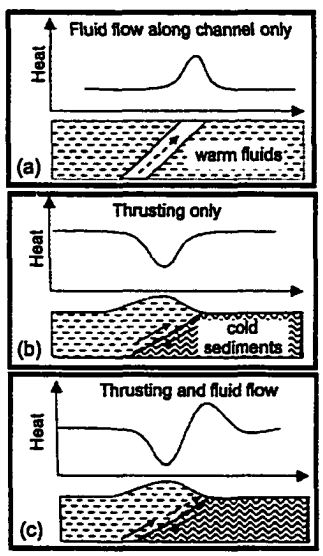

Figure 5.27 Simplified heat flow response to (a) fluid flow along a channel/conduit, (b) thrusting, and (c) a combination of thrusting and fluid flow. The observed heat flow pattern along seismic line XL-06 suggest thrusting and fluid flow for both major accreted ridges. (From Ganguly *et al.*, 2000).

Chapter 6

Seismic Blank Zones - Active Cold-Vents?

6.1 Introduction

Sub-vertical zones of reduced seismic reflection amplitude have been observed using different seismic recording systems and source frequencies. They were first recognized during a deep towed multichannel DTAGS cruise (Deep-Tow Acoustics-Geophysics System) in 1997 (Chapman *et al.*, 2001). However, careful reinterpretation of the single-channel seismic data from 1993 over the same area showed the same structures but they have been overlooked at the time of first interpretation.

This chapter describes the seismic character of these blank zones based mainly on the new 2-D and 3-D seismic data acquired in 1999 and 2000. Seismic interpretation is complemented by heat flow measurements, piston coring, pore-fluid geochemistry and seafloor video observations with the unmanned submersible ROPOS. Several mechanisms for the origin of blank zones are discussed favoring the formation of hydrate due to focussed fluid/methane flow in fault planes as the most likely source of amplitude reduction. Typical cold-vent related surface expressions such as carbonate formations and clam fields are additional evidence for the fluid/methane flow related origin of the blank zones.

There are four prominent blank zones within a small area of approximately 3 km^2 size. These zones are all located within the uplifted sediment block described in the previous chapter. They are labeled 1–4 in all following data examples. The blank zones are a few 100 m across and amplitude reduction seems to be restricted to the upper slope-sediment section above the BSR. However, deeper accreted sediments lack coherent reflectivity and amplitude reduction cannot be distinguished from the

generally chaotic low reflectivity of the sediments at these depths.

This vent field was investigated as part of the 3-D seismic reflection survey in 1999. Based on this survey, piston-coring was carried out in July 2000 and 26 cores were acquired over the vent field. These cores provide information about physical properties and chemical state of the shallow sediments inside and outside of the vent area. Massive gas hydrate was recovered in four piston cores at blank zone 1. This blank zone has an almost circular structure 400 m in diameter and shows a several meter high surface expression of reduced reflectivity. On selected cores geochemical analyses of the pore fluids were carried out in co-operation with M. Kastner and C. Solem from Scripps Institute of Oceanography. Pore fluid alkalinity gradients obtained were converted to sulfate gradients, from which the amount of methane and related fluid flux were calculated (Borowski *et al.*, 1996). During the July 2000 survey, a second high-resolution single channel 3-D survey was carried out over the most prominent blank zone with the same airgun and streamer configuration as used in 1999. However, shot spacing was reduced to 12 m to increase horizontal resolution. A set of 21 northeast-southwest oriented lines spaced at 25 m covered the entire blank zone. The seismic investigations were complemented by heat flow measurements over the vent area in July 2000 by T. Lewis. In cooperation with the Marine Geophysics group from the University Bremen, Germany, additional high resolution seismic data were acquired over the main blank zone. From their study the *Parasound* 4 kHz seismic data are shown (courtesy of V. Spiess and L. Zühlsdorff). The most prominent blank zone was also the target of seafloor sampling and video observation surveys with the unmanned submersible ROPOS in September 2000 and May 2001.

Seismic amplitude reduction is not restricted to the vent field alone. Fault-related amplitude-loss was also observed at two other locations within the area of the main 3-D seismic grid from 1999. These locations are more isolated and amplitude reduction extends through a thick column of slope sediments to depths below the BSR. These locations have similar seismic character as the vent field blank zones. One of these

blank zones shows a several meter high surface expression of low reflectivity similar to blank zone 1 at the vent field.

Based on the seismic character and topographic expression, an area associated with the outcrop of a thrust fault was the target of a detailed seafloor video observation with ROPOS in May 2001. This area is seismically characterized by a ridge of accreted sediments with a steep relief. The video observation showed evidence of wide-spread fluid/methane venting such as carbonate formations, clam fields and tube worms.

From the seismic data and video observations, a general conclusion can be drawn that amplitude reduction associated with fluid/methane flow along faults is a common feature and is expected at other tectonically similar areas. Typical surface expressions are carbonate formations and cold-vent related biota. Another typical surface expression can be mud volcanos as the result of strong fluid flow. These mud volcanos are characterized by low seafloor reflection coefficients probably due to high porosities (fluid rich) and/or a general chaotic reflectivity due to the reworked nature of the sediment.

6.2 Seismic Observations at the Vent Field

The seismic data from different systems are described below in order of decreasing frequency and increasing depth penetration.

6.2.1 12 kHz Echosounder

12 kHz data were obtained using the CCGS J.P. Tully standard echosounder with color amplitude display (see Chapter 3 for details). This frequency penetrates only a few meters into the sediment and the system has a relatively wide beam resulting in poor spatial resolution. However, the data provide useful information

about the nature of the seafloor. Data were mainly acquired around blank zone 1. The topography around blank zone 1 along inline 27 is characterized by two mounds, approximately 5 m in height, separated by a small depression of about 1 m depth (Figure 6.1). Reflection strength over the blank zone is decreased (green colours) compared to the area outside of the mound area. The color code used for echo-strength is defined in Chapter 3, Section 3.3.5. Additional data were acquired in the perpendicular direction as part of the 3-D grid from July 2000 (Figure 6.2). On these lines, the topography shows a triple mound structure separated by two smaller depressions. Height of these mounds is approximately 2–5 m. The same reflection strength pattern as seen on inline 27 is observed on these lines, i.e. lower reflectivity material in the upper 5–10 m (green colours) underlain by some higher reflective material (red colours). To both sides of the blank zone, the seafloor reflection strength is increased.

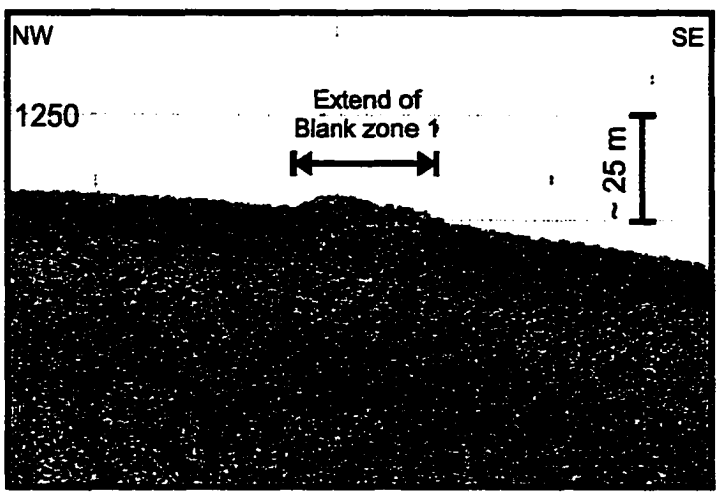

Figure 6.1 Part of 12 kHz echosounder recording from inline 27. Center of blank zone 1 shows a double mound structure with reduced reflection strength.

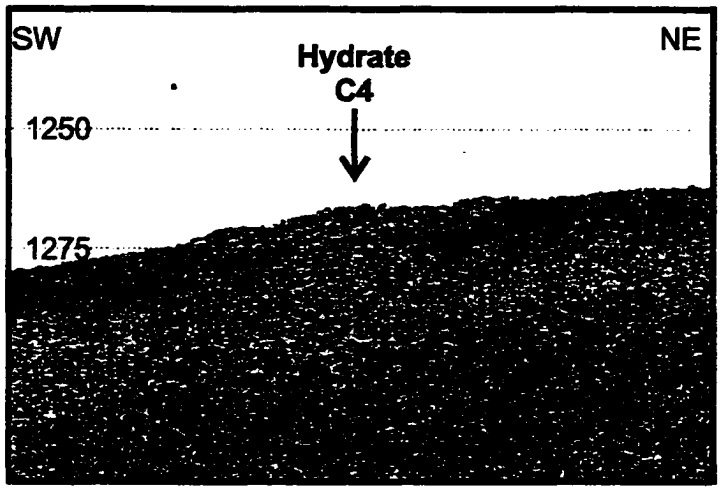

Figure 6.2 12 kHz echosounder recording from inline 14 of the July 2000 3-D grid. This line is almost perpendicular to inline 27. Center of blank zone 1 shows a triple mound structure with reduced reflection strength, similar to the observations on inline 27.

6.2.2 Parasound (4 kHz) and 3.5 kHz Subbottom Profiler

The Sonne Parasound system is a 4 kHz narrow beam subbottom profiler that provides sediment structure data to depths of a few tens of meters. The foot-print of the beam is about 7% of the water depth. Water depth at blank zone 1 varies between 1260 m and 1280 m, i.e. the footprint of the Parasound system is approximately 90 m. Around the vent area the depth penetration is about 60 m. The Parasound line acquired along MC inline 27 shows four blank zones (Figure 6.3) located within a sediment block that was uplifted by about 45 m.

Blank zone 1 has a distinct surface expression (as seen on the 12 kHz echosounder data), whereas blank zones 2–4 have no equivalent surface expression. A prominent high amplitude layer at 6–8 m bsf is an apparent upward barrier for blank zones 2 and 4. Blank zone 3 extends to the seafloor but has little seafloor topographic expression. In general, sedimentation in the SE part of the area is dominated by a series of thin seafloor-parallel layers. The NW end of the area shows some indication of faulting,

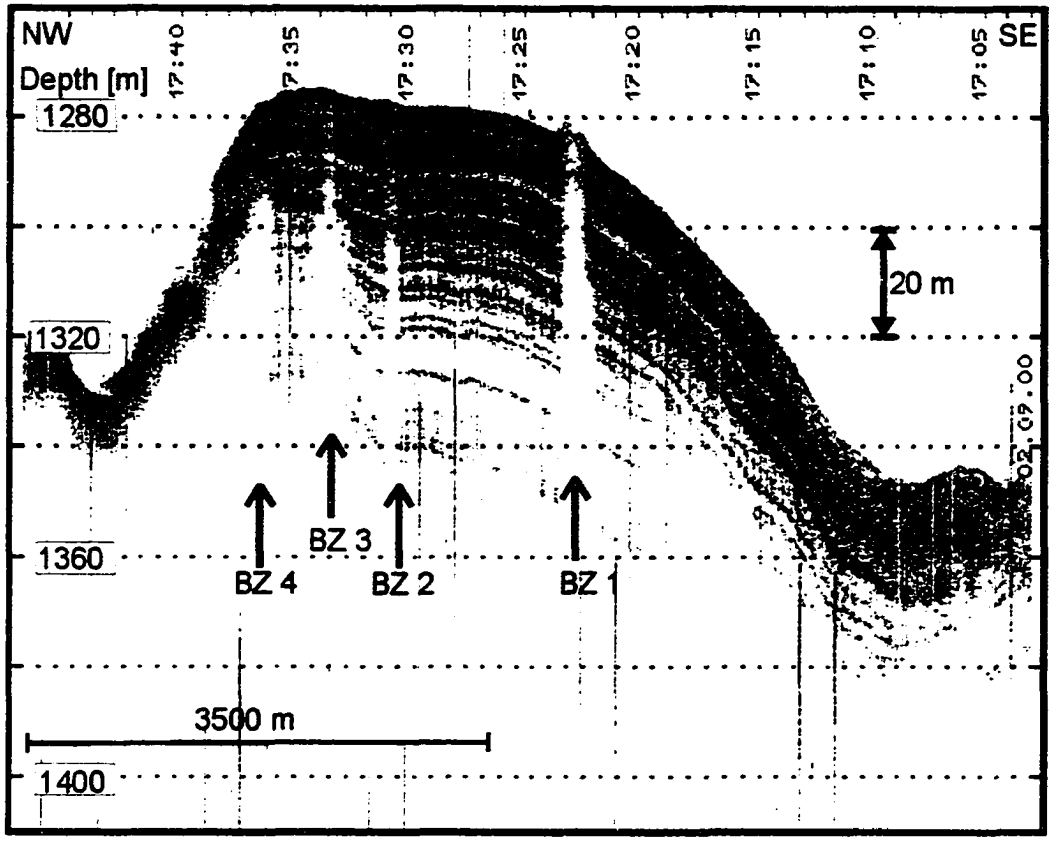

Figure 6.3 Parasound (4kHz) recording from inline 27 (courtesy of V. Spiess and L. Zühlsdorff).

associated with the occurrence of blank zones 2 and 3. Blank zone 4 is located at the edge of the vent field area, close to a steep 45 m drop in topography.

Reflectivity is lost completely within blank zones 1, 3 and 4, whereas amplitude-loss increases with depth at zone 2. Blank zones 1 and 2 are characterized by a sharp boundary at the NW side and their widths increase towards the SE. Blank zones 3 and 4 do not have sharp boundaries and the width of the zones increases with depth. The top of blank zone 2 shows some reflector upward doming, especially around the high amplitude layer. A small topographic mound (less than 2 m in height) is also observed on top of this zone. The asymmetric shape of the blank zones may indicate

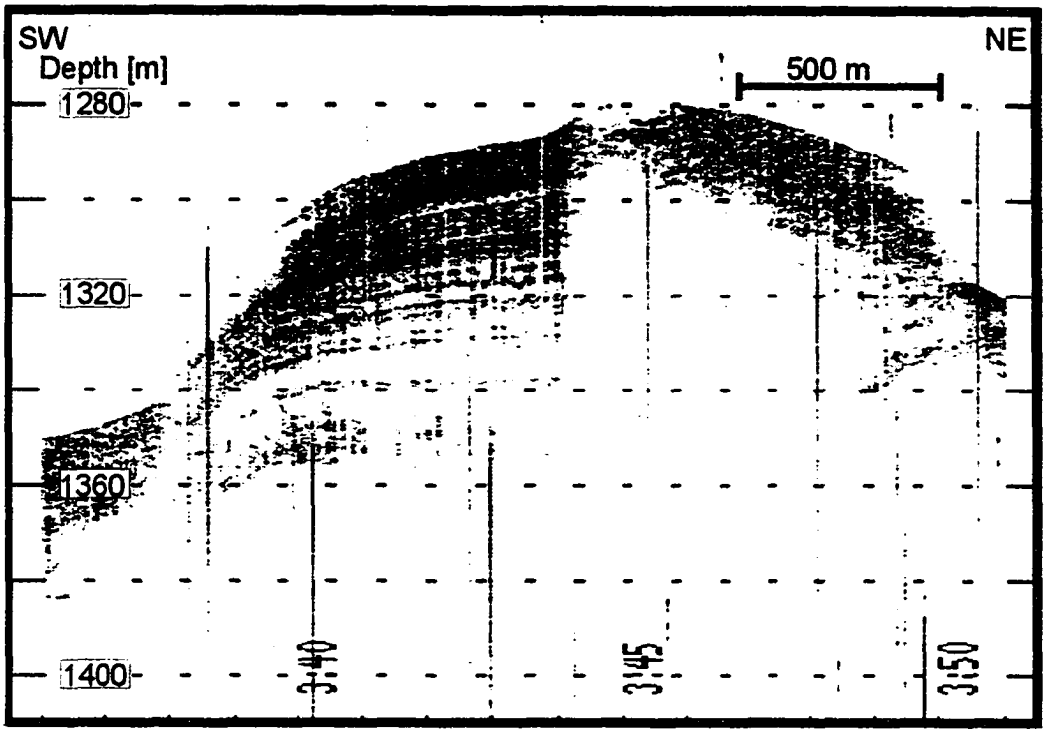

Figure 6.4 Parasound (4kHz) recording across the center of blank zone 1 (approximately along line 14 from July 2000 3-D grid) (courtesy of V. Spiess and L. Zühlsdorff).

the tilt of the underlying fault.

The line acquired in the perpendicular direction (Figure 6.4) crosses the center of blank zone 1 through the uplifted sediment block. Blank zone 1 is sharply truncated in the SW, but is more diffuse on the NE side. The reflectivity pattern shows thin seafloor-parallel layers on the SW part of the uplifted sediment block, whereas no coherent reflectivity can be seen on the NE side.

The 3.5 kHz subbottom profiler on the CCGS J. P. Tully gave a high-resolution image of the uppermost 30–40 m of the sediment column (Figure 6.5). No data processing was applied and the amplitude envelope was used for plotting. The system has a broad beam (30°) and has therefore poorer spatial resolution than the Parasound system. The 3.5 kHz subbottom profiler data are equivalent to the Parasound data,

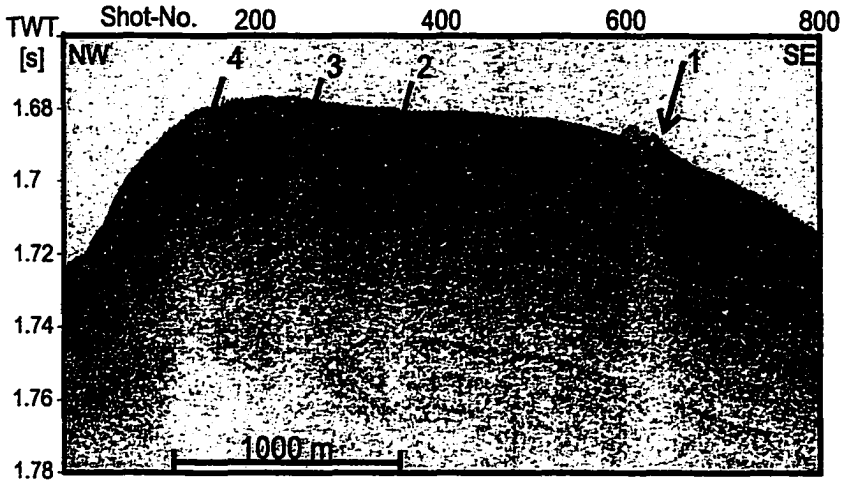

Figure 6.5 3.5 kHz recording across the vent field (along inline 27).

but with less data quality and depth penetration.

6.2.3 DTAGS

The DTAGS system provides 250–650 Hz high resolution data with penetration to several hundred meters. The largest blank zone (No. 1) in the DTAGS record also penetrates to the seafloor (Figure 6.6). In this data it has a dimension of about 250 m at the seafloor and widens to about 300 m at 170 ms TWT (140 m) bsf (Figure 6.6). The seismic line shown in this figure does not cross the blank zone on a diameter. The surface expression of blank zone 1 is similar to a pockmark with a depression in the middle. Several other small-scale (20–40 m wide) blank zones are also visible that stop at deeper layers. The prominent high amplitude reflector at about 10 ms TWT (6–8 m) bsf is again an apparent upward barrier for blank zone 2. Blank zones 3 and 4 cross this layer partially. All blank zones with the exception of zone 1 are asymmetric as observed in the Parasound data. The SE sides widen with depth, whereas the NW flanks appear as sharp vertical boundary. The flanks of the blank zones show an apparent increase in seismic reflectivity and small-scale diffractions in

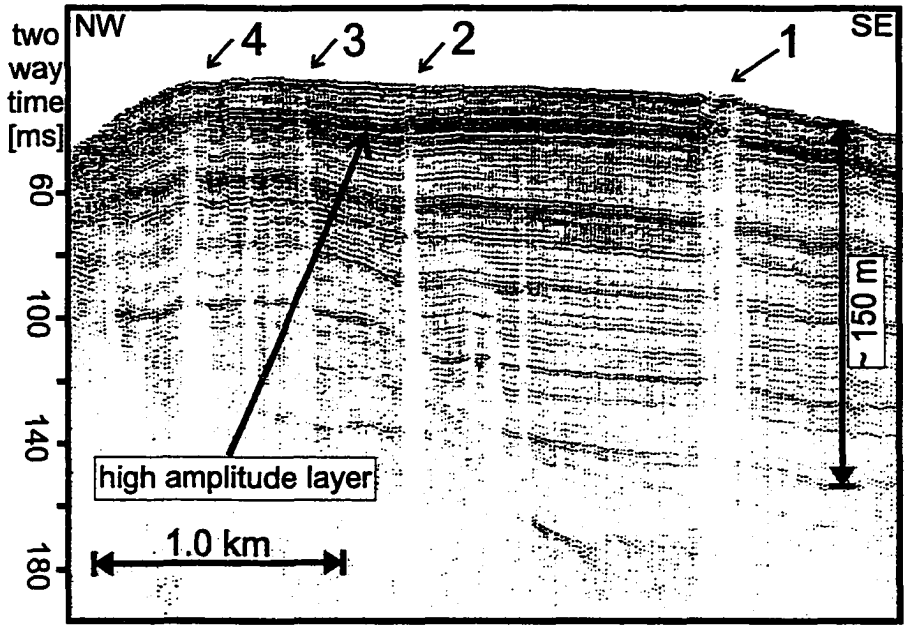

Figure 6.6 DTAGS line BC-03 (equivalent to inline 27). Stack of first five near offset traces from geophysical sub-array (reduced traveltime).

case of blank zone 3.

6.2.4 COAMS

Six parallel multichannel seismic inlines from the main 3-D grid cover the area where blank zones are observed. As an example, inline MC-27 and line MC-X7 intersect near blank zone 1 (Figure 6.7). This zone shows a strong diffraction hyperbola on inline 27, whereas no similar feature is observed in the perpendicular direction. On both lines, a BSR is enhanced around blank zone 1. The increase in BSR amplitude is asymmetric and localized over a section of about 400 m wide to the NW side of the blank zone. The crossing line MC-X7 also indicates enhanced reflection amplitudes of sediment layers about 80 ms TWT above and below the BSR.

All sediment layers in the uppermost 250 ms TWT throughout blank zone 1 are pulled up by about 5–10 ms suggesting either higher velocities, real deformation or

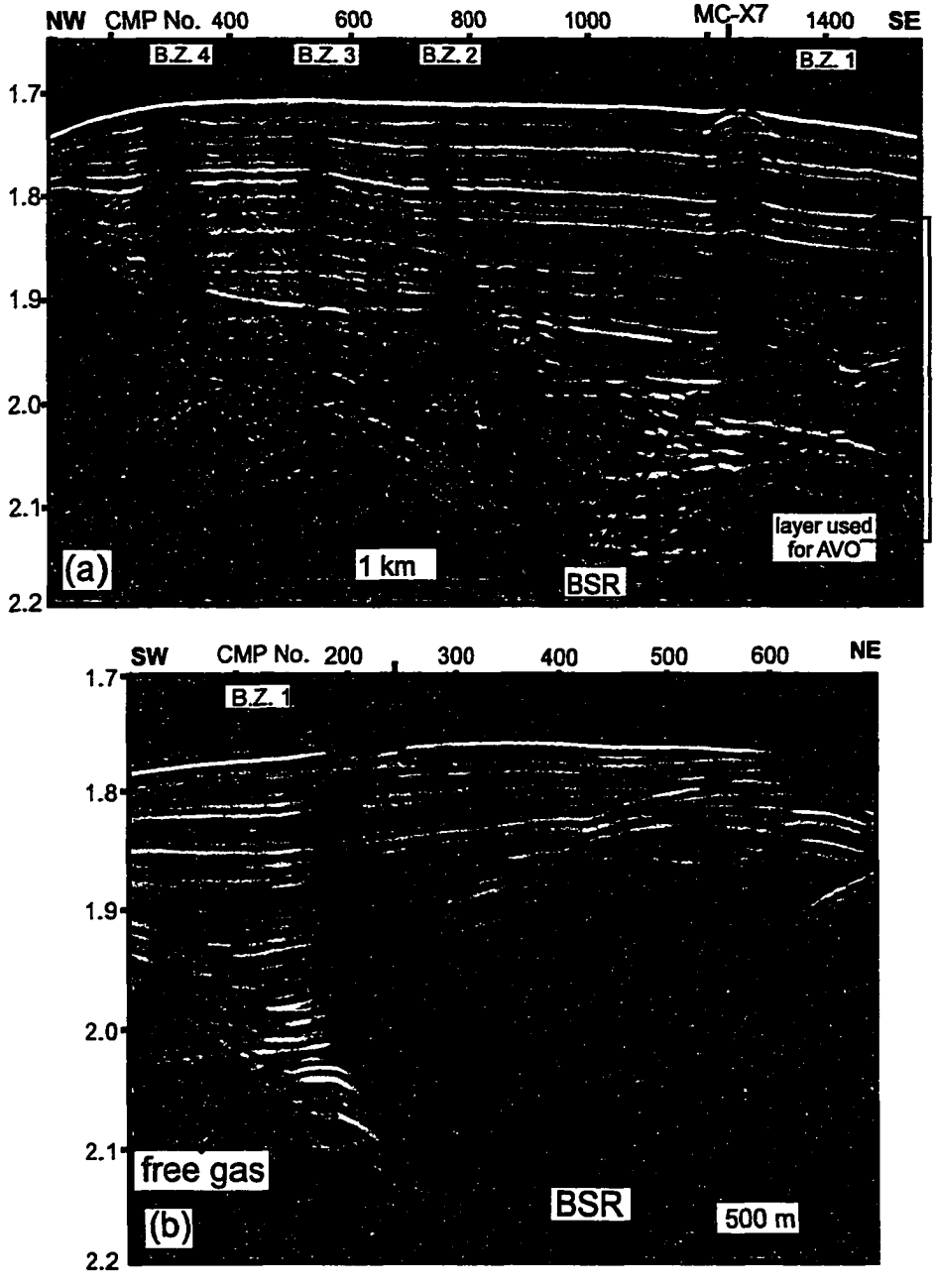

Figure 6.7 (a) COAMS inline 27 from main 3-D grid and (b) COAMS XL-07, 64-channel stack (maximum offset about 460 m), unmigrated. Note the column of increased seismic reflection amplitude.

seafloor topographic effects. Amplitude reduction is more prominent below 1.8 s TWT. Between 2.0 and 2.1 s TWT strong deeper reflectivity is observed directly below the blank zone.

In contrast to the DTAGS data, most of the sedimentary layers can be traced through the blank zones 2–4 in the lower frequency COAMS data. This is also evident in the unstacked seismic data. In Figure 6.8 two SCMP (Super Common Mid Point) gathers about 300 m apart from outside and inside blank zone 4 are shown after NMO correction. The layers have reduced vertical incidence amplitudes inside of the blank zone, but can be seen on the far offset traces. Amplitude reduction is not uniform for all layers. The prominent reflector at around 1.96 s TWT that is visible on the outside SCMP, is difficult to identify on the SCMP inside the blank zone. However, layers above and below are clearly visible.

A characteristic difference relative to all other data sets is the occurrence of diffractions at the boundaries of the blank zones. This can be the effect of the dense hydrophone spacing and related detailed sub-surface imaging with a CMP distance of about 2.5 m. A coarser spatial sampling would reduce the number of data points imaging the diffraction hyperbola, which is therefore less pronounced and more difficult to distinguish from the regular reflectivity. Often only the one arm of the diffraction hyperbola that extends away from the blank zone is visible. There is also a prominent diffraction visible at the seafloor just above blank zone 3. There is no clear diffraction at the seafloor above blank zone 2 and 4. However, their boundaries show diffractions through the entire sediment column. Migration of this line was difficult and not all diffractions were removed completely (compare with Figure 4.17 in Chapter 4) indicating either off-line diffracted energy, that could not be migrated with a 2-D migration scheme, or a strong lateral varying velocity-profile that could not be resolved with the COAMS system. The multichannel seismic velocity analyses indicated no significant change in P-wave velocity across the ventfield (Figure 4.12), but the accuracy of the velocity analysis of $\pm$ 150 m/s is not sufficient to distinguish

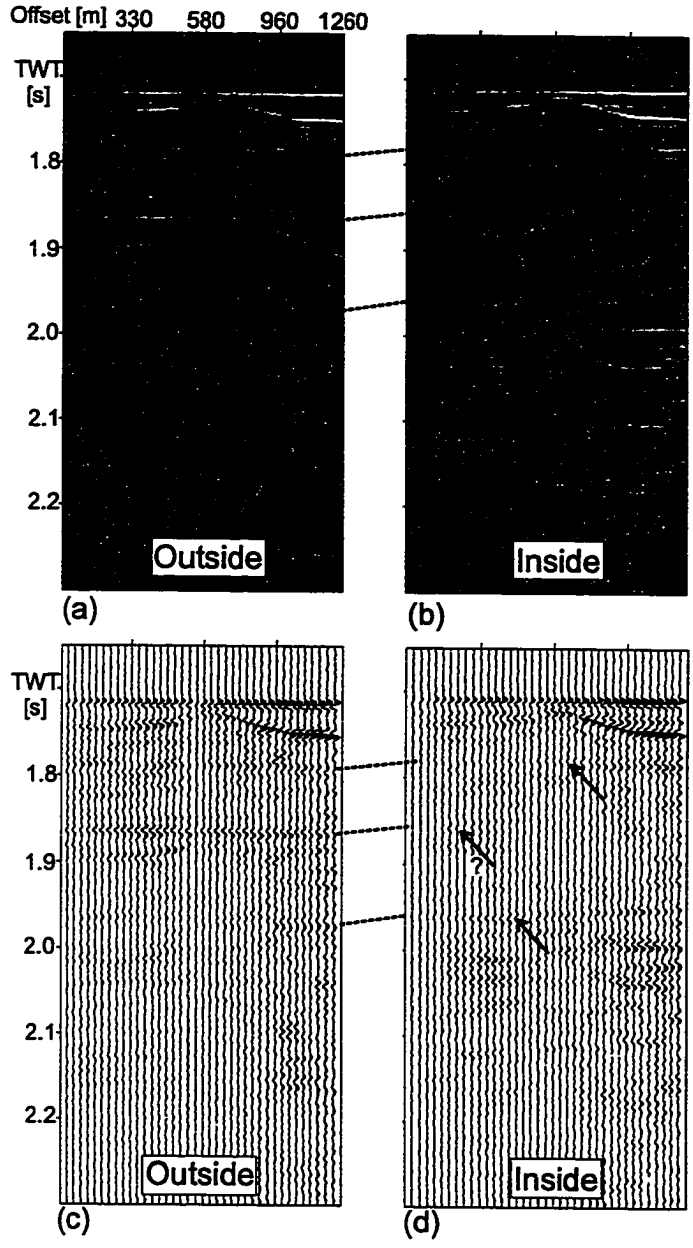

Figure 6.8 Example of two NMO corrected SCMP gathers for an area outside (a,c) and inside blank zone 4 (b,d). For comparison, the wiggle and variable area plots are shown. Several layers can be seen inside the blank zone, but especially their vertical incidence amplitude is reduced. Amplitude reduction is not uniform for all layers.

those changes unless they are very large.

6.2.5 Teledyne Single Channel Data

The 1999 single channel survey covered the area shown in Figure 3.2. This survey gave detailed 3-D structure of the vent field. Two representative lines of the 1999 single channel 3-D seismic data set are shown in Figure 6.9. Sedimentation in the southern half of the area is almost parallel to the seafloor without any indication of near-surface faulting. The sedimentation is interrupted only by blank zone 1, which penetrates the entire sediment column. The northern part of the area shows evidence of near surface folding and faulting associated with the occurrence of blank zones 2–4. Wherever the tilt of the sediment layers changes in this area, blank zones occur. All of these blank zones appear as chimneys penetrating through the whole sediment column. On most of the lines, significant deeper coherent reflectivity is observed below the blank zones. Within the data resolution the chimneys extend up to the seafloor. In this data set the high amplitude layer at 10 ms TWT bsf is not resolved due to a receiver ghost, which follows the primary reflections at 6–8 ms and merges with the reflection of interest. Blank zones 2–4 are irregular in shape (Figure 6.10), usually sharply truncated on the NW side but showing an irregular surface increasing and decreasing in width at the SE side.

Blank zone 1 shows characteristics that are different from the other zones. In the unmigrated sections it shows a strong diffraction hyperbola (Figure 6.9b) probably a result of the seafloor topography, visible in the 3.5 and 4 kHz subbottom profiler data. Deeper layers (e.g. at 1.8–1.9 ms TWT on line SC-18) are again pulled up by about 5–10 ms TWT.

The BSR, which can be identified in this area where it crosscuts the sedimentary reflectors on some of the lines, marks the top of a high reflectivity zone. On most of the other lines, no single BSR reflection can be identified, but below the expected

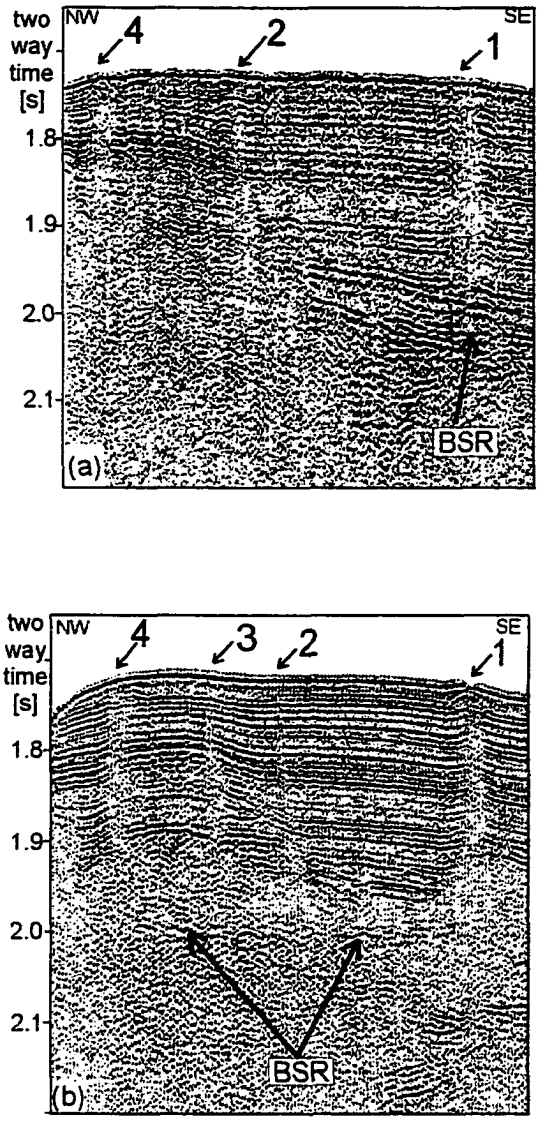

Figure 6.9 Examples of unmigrated single channel seismic data (Teledyne) of (a) line SC-12 and (b) line SC-18. Blank zone 1 shows a strong diffraction hyperbola in the center of the zone and a pull up of about 5–10 ms TWT of deeper sediment layers.

depth of the BSR an increase of mostly chaotic reflectivity is observed.

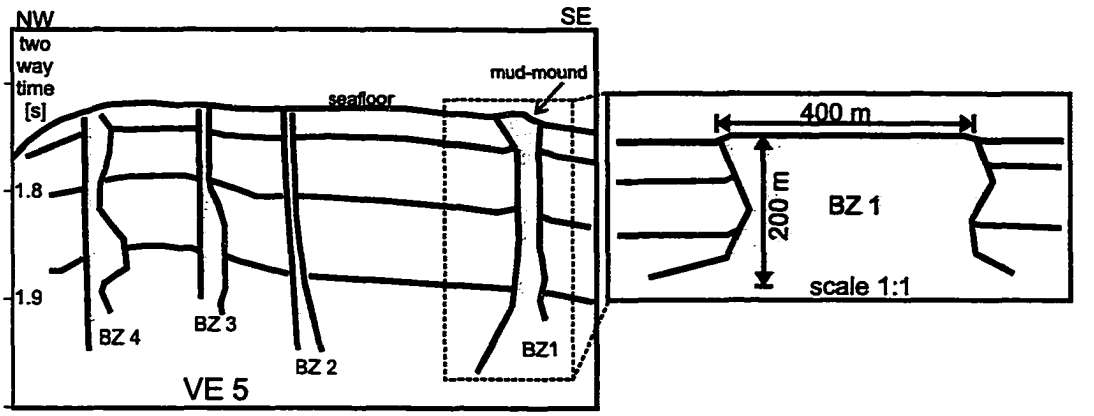

Figure 6.10 Linedrawing of blank zones from Teledyne line SC-18. Blank zones 2–4 have a sharply truncated boundary at the NW side compared to a irregular shape at the SE side. In the left panel the vertical exaggeration is 5 and blank zones appear as chimneys. However, in a 1:1 scale they are more rectangular.

3-D Analysis of the 1999 SC Data

The 31 lines of closely spaced single channel seismic data from the 1999 survey have been used to generate a 3-D data cube. The single channel data were acquired during varying weather conditions yielding strong static shifts (striations) among the individual lines. To remove the crossline statics, the data were flattened to the seafloor and a lateral coherency filter was used to remove residual swell. After swell removal the data were shifted back onto the smoothed bathymetry as defined from the seismic data and the regional bathymetry data. From this data cube, amplitude time and horizon slices were created to (a) define the spatial extent of the blank zones and (b) to define the detailed sediment structure and nature of deformation within the area.

In the southeast part of the 3-D area, the sediments generally follow the seafloor topography (Figure 6.11) and have a slight SSW dip. The slices of seismic amplitude were generated at 1.79 s and 1.802 s respectively (Figure 6.11b,d). A regular pattern

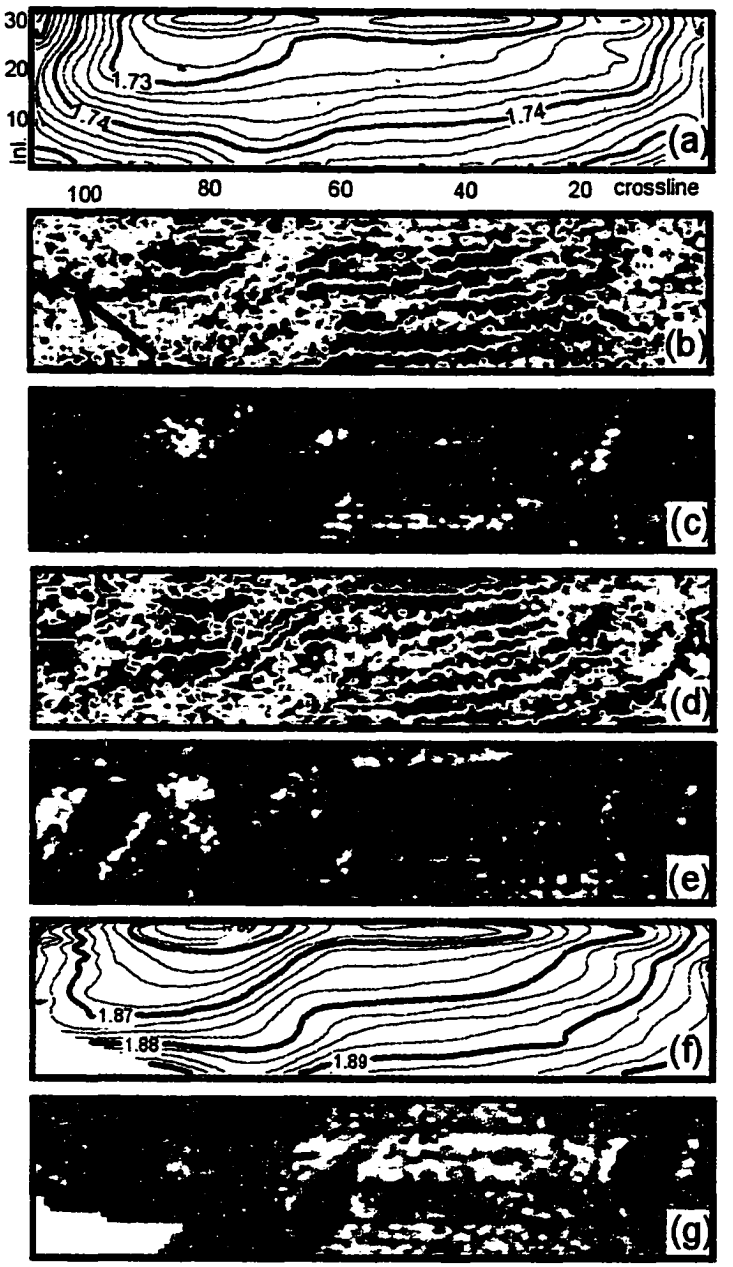

Figure 6.11 3-D analysis of 1999 single channel seismic data. Seafloor topography in TWT [s] (a) is shown for reference. Time slices of (b) seismic amplitude and (c) instantaneous amplitude at 1.79 s TWT, time slices of (d) seismic amplitude and (e) instantaneous amplitude at 1.802 s TWT, horizon topography (f) and horizon amplitude (g) (see Fig. 6a for selected horizon). Blue colors indicate positive, red colors indicate negative seismic amplitude on (b) and (d). Dark shaded regions on (c), (e), and (g) represent lower amplitudes.

of color (amplitude) change indicates the dip of the reflectors. In the southeast corner of the slices, sedimentation is interrupted by blank zone 1 and only chaotic reflectivity is observed. The dip of the layers changes abruptly at around crossline position 65–70. The sediments appear to be curved towards the west. Between crosslines 75–85, the sediments form a plateau, before they steeply dip towards the northeast at crossline position 90. The spatial extent of the blank zones can best be visualized using slices of instantaneous amplitude, i.e. the envelope of the seismic trace (Figure 6.11c,e). Blank zone 1 in the southeast corner is almost circular and has a diameter of about 400 m. The inner low reflectivity zone (dark shaded color) is surrounded by a high-amplitude ring, up to 40 m wide. Blank zones 2–4 are more linear features and appear to follow an east-west trend. They are also surrounded by high amplitude rims, but these rims are not always well developed.

To test whether the high amplitude rims are artificially generated by the timeslice technique, one selected horizon slice was generated (Figure 6.11f,g). This horizon slice confirms the high amplitude rims as well as the east-west trend of the blank zones 2–4. The topography of this horizon is almost identical to the seafloor with the same steep increase in dip around crossline positions 65.

3-D Analysis of the 2000 SC Data

The SC data in 2000 were acquired using similar acquisition parameters as used in 1999. However, shot-point distance was decreased to 12 m. Data processing was similar as outlined earlier. During the cruise in July 2000, massive hydrate was recovered in piston cores around blank zone 1 at depths of 3–8 m below the seafloor (see Section 6.4.1) so the near-seafloor seismic data was examined in detail. The top of the hydrate was mapped as a shallow reflector around the center of the blank zone. The depth of the reflector corresponded well to the depth of the hydrate recovery at the four piston core sites. The hydrate forms a cap, which dips away from the center of the vent (Figure 6.12).

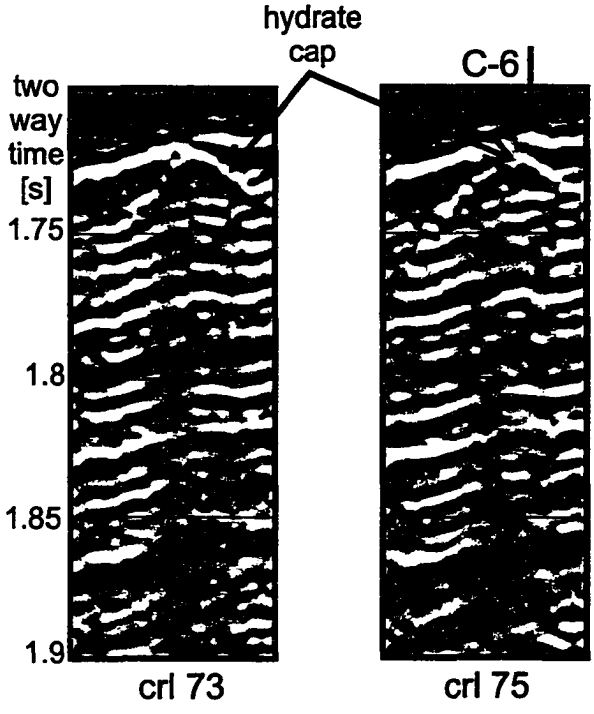

Figure 6.12 Crosslines from the 2000 single channel seismic data showing hydrate cap reflector at blank zone 1 (mud/carbonate mound). Note reduced seismic amplitudes below center of the vent.

Below the hydrate cap the amplitude of the seismic data is reduced, probably an effect of increased transmission loss at the high reflectivity cap. The hydrate cap reflector has an irregular top surface. Slices from the unprocessed seismic data show clear patches of increased reflectivity near the surface (Figure 6.13a, b). Around these patches diffraction halos develop, that form a complicated interference pattern (Figure 6.13c). These diffraction halos form a more uniform, single-circle pattern at greater depth, that locally enhanced the reflection amplitude of regular reflectors (Figure 6.13d). Reduced seismic amplitudes at greater depths (Figure 6.13e) are exactly limited to the zones where high amplitude patches have been seen near the seafloor. The waveform of the seismic signal (close to a Ricker wavelet) is visible in

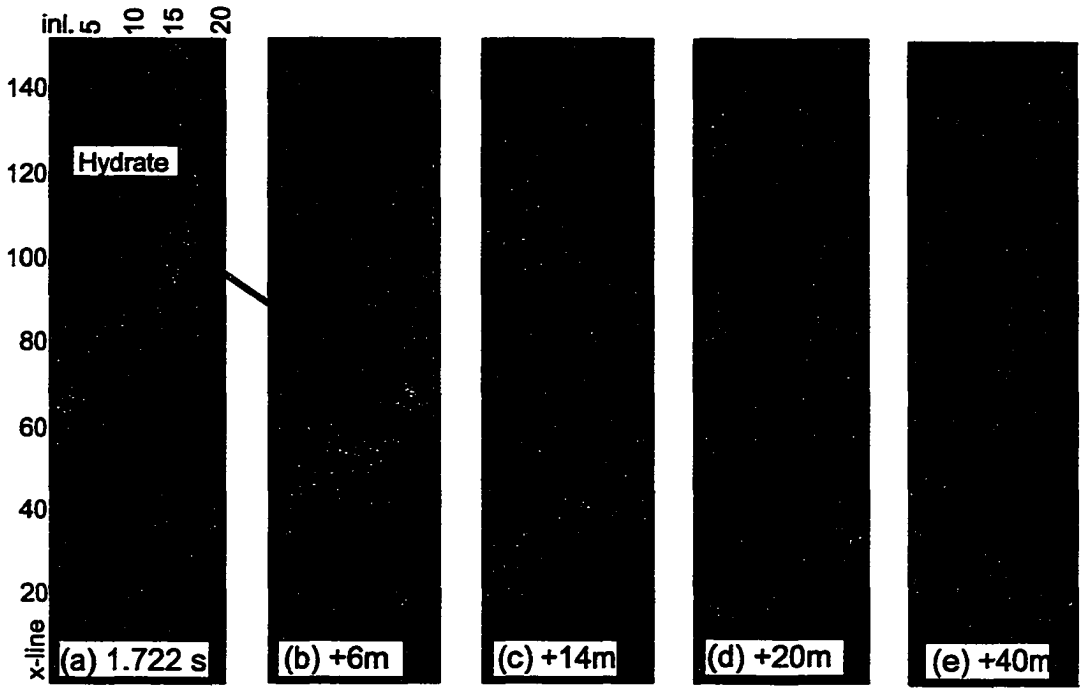

Figure 6.13 Slices of instantaneous amplitude from unprocessed 2000 3-D data. Several high amplitude patches are visible near the seafloor (a, b), which result in diffraction halos that expand around them (c). At greater depth the different diffractions interfere to a single-circular pattern (d,e). Blanking visible on the slice 35 m (e) below the first slice, is limited to three zones exactly below the high amplitude patches seen in slice (b). Slices were taken at (a) 1.722, (b) 1.723, (c) 1.74, (d) 1.75, (e) 1.766, and (f) 1.774 s TWT. Corresponding depth below first slice was calculated using a constant velocity of 1550 m/s.

these time slices, forming the triple ring pattern of the individual diffraction halos (Figure 6.13d). After processing and migration of the data, these structures were lost.

Seafloor reflection coefficients are reduced to less than 0.1 in the area below the hydrate cap reflector (Figure 6.14). This observation is in good agreement with the observation from the 12 kHz and 3.5 kHz echosounders that showed lower reflective

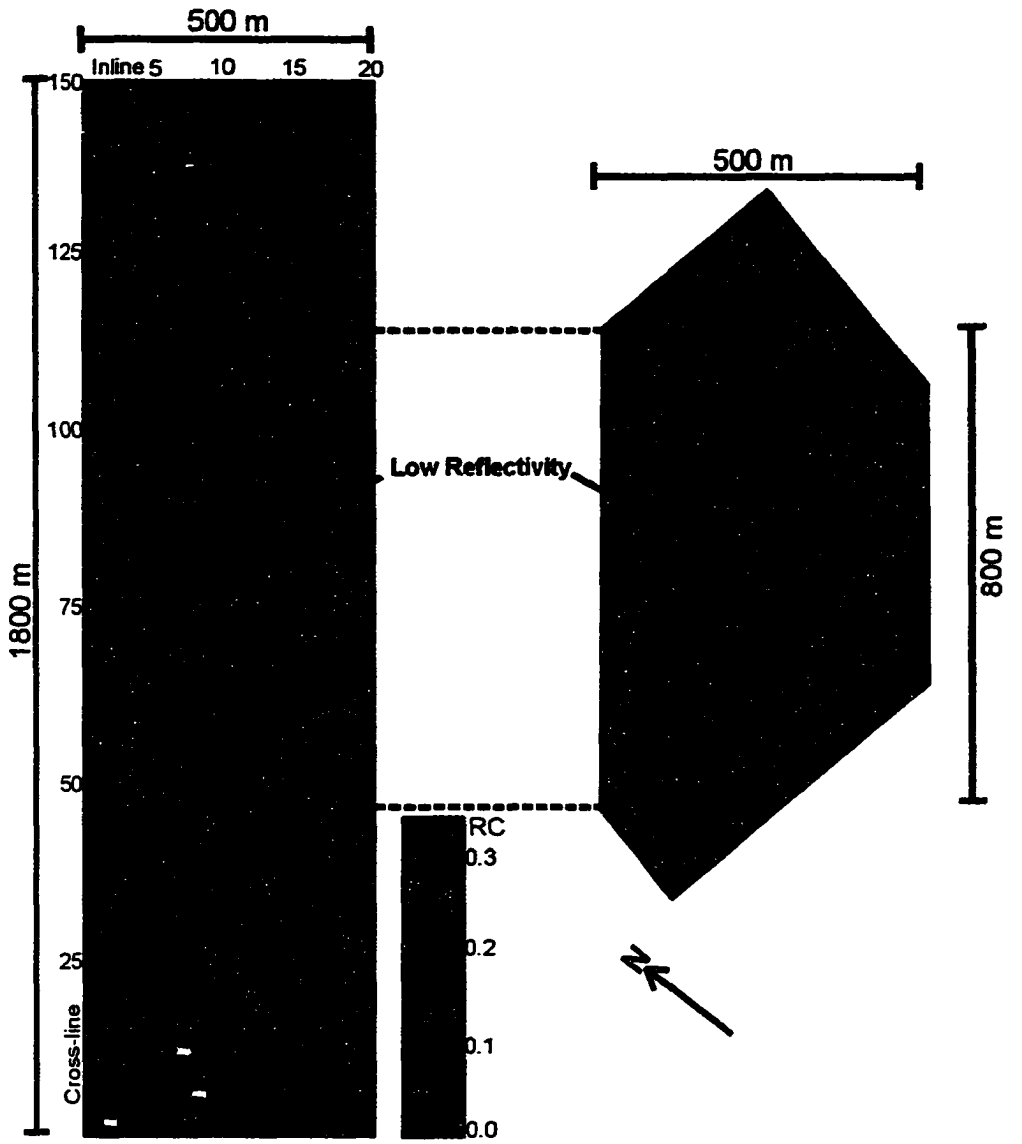

Figure 6.14 Seafloor reflection coefficient around blank zone 1 with core locations. The reflection coefficients are reduced below the hydrate cap.

material in the center of the blank zone. The seafloor reflection coefficient around this center zone is relatively homogeneous with values around 0.2–0.25.

Several single spots of higher reflectivity were observed but they most likely represent variations in the output strength of the seismic source. Reflection coefficients

were calculated using Warner's method (Warner 1990) with an average conversion factor. No point-by-point conversion factor was estimated, since the multiple reflection was not recorded on all traces consistently. There is no evidence of strong reflectivity corresponding to the observed carbonates around the piston cores site C-4. However, the carbonates are formed around smaller outcrops or were found as small chunks embedded in the seafloor and their total distribution is unknown so far. These small outcropping carbonates may not influence the reflection strength, especially given the footprint of the seismic source of about 100 m at the water depth of 1300 m at this site.

Blanking extends over even a larger region than just where the hydrate cap was mapped. In a horizon slice at a depth of about 30 m bsf, a high amplitude rim is observed around the center part of the vent only (Figure 6.15).

Time slices of instantaneous amplitude instead show a partially closed ring of higher amplitudes around the entire blank zone (Figure 6.15b,c). A 3-D perspective view of the blank zone is shown on Figure 6.16. A seismic inline and crossline is shown in addition to the time slice at 1.754 s TWT of instantaneous amplitude showing the high amplitude ring. The amplitude reduction is mainly visible just below the occurrence of the hydrate cap reflector.

In contrast to the single channel seismic data acquired in the perpendicular direction in 1999, this data set shows no indication of pull up. Most of the sediments follow the general seafloor topography or were completely disrupted such that no coherent reflectivity was observed. There is no clear evidence for near-surface faulting similar to that seen at blank zones 2–4 in the 1999 data set.

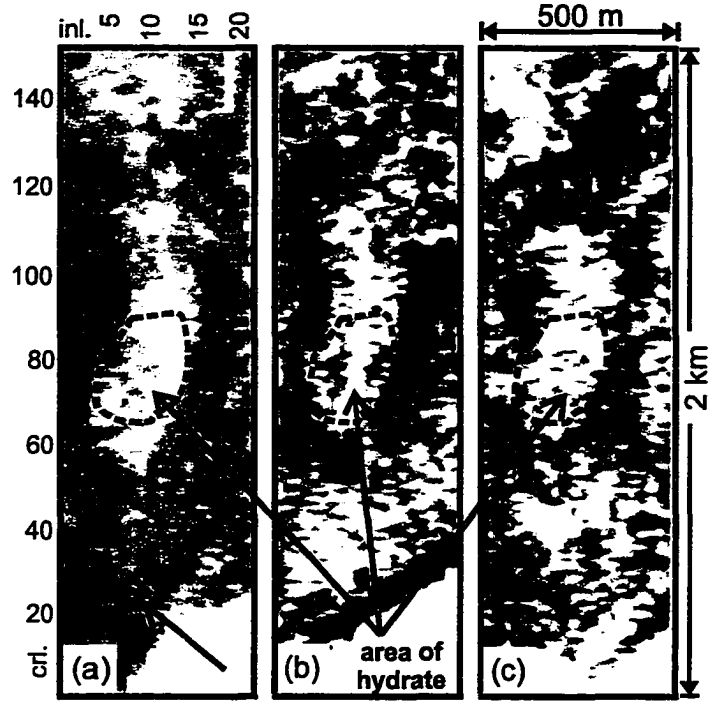

Figure 6.15 3-D analysis of 2000 single channel seismic data. (a) horizon amplitude slice (30 m bsf) showing amplitude reduction and surrounding high amplitude rims. (b) time slice of instantaneous amplitude at 1.754 s TWT and (c) at 1.79 s TWT showing high amplitude ring structure. Location of hydrate cap reflector is indicated by dashed circle.

6.3 Frequency Dependence of Amplitude Reduction

Blanking was observed over a wide frequency range in different seismic acquisition systems: (a) 3.5 kHz subbottom profiler, (b) vertical incidence DTAGS (250–650 Hz), (c) vertical incidence airgun (Teledyne, 20–180 Hz), and (d) multichannel airgun (COAMS, 20–180 Hz). From visual comparison it is evident that the amplitude loss seems to be more pronounced at higher frequencies. This observation is important for the discussion of different mechanisms that can produce seismic amplitude reduction (see Section 6.12).

Quantifying this observation is difficult since the different seismic sources have

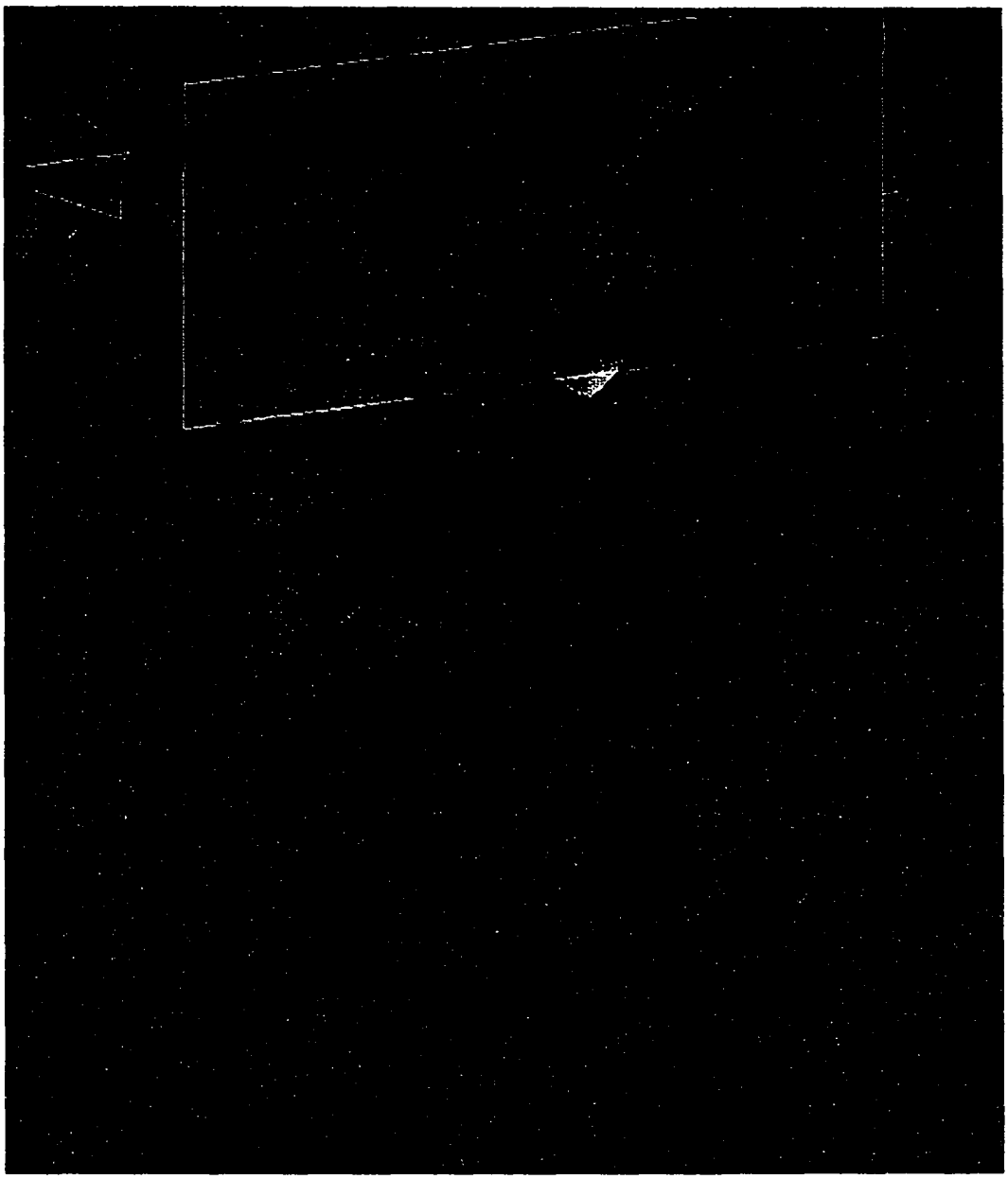

Figure 6.16 3-D perspective view of blank zone 1 from July 2000 3-D seismic data. The seismic lines shown are inline 14 and crossline 80. In addition to the seismic lines a time slice at 1.754 s TWT of instantaneous amplitude with the high amplitude ring is shown. The top of the hydrate cap reflector is added as horizon. A video of this perspective is available on the interactive CD-Rom.

different penetration depths. In order to estimate the amount of amplitude loss over the frequency range used, the RMS amplitude in representative data examples was calculated at a sub-seafloor depth of about 20 ms TWT over a time window of 14 ms. The amount of amplitude reduction shown in Figure 6.17 was calculated by dividing the average amplitude inside a blank zone by the average amplitude outside the blank zone. For this calculation only blank zones 2–4 were used. Amplitudes in the 3.5 kHz subbottom profiler were variable, resulting in an amplitude reduction varying from 75% to almost 100%. For intermediate frequency vertical incidence DTAGS data, amplitude reduction ranged from 50% to 100%. However, amplitudes of the DTAGS data were unstable, since the original source sweep was not recorded and a synthetic sweep was used in the crosscorrelation. Amplitude reduction in the lower frequency airgun data was observed to be dependent on the angle of incidence. The vertical incidence Teledyne data show higher amplitude reduction (45% - 65%) than the stacked multichannel COAMS data (25% - 50%).

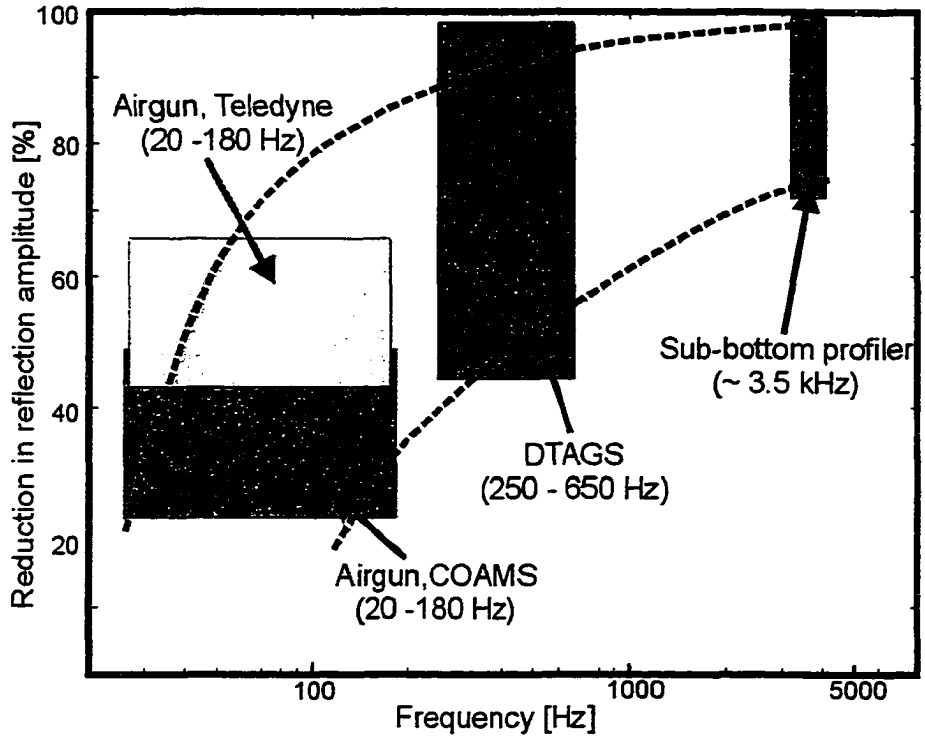

Figure 6.17 Frequency dependent amount of amplitude reduction from MC and SC seismic airgun, DTAGS and 3.5 kHz seismic data.

6.4 Piston Coring at Blank Zones 1 and 4

Based on the preliminary 3-D analyses from the 1999 3-D seismic data, an extensive piston coring program was carried out in July/August 2000 to further investigate the nature of the blank zones (Novosel *et al.*, 2000). In total 26 cores (on average 7-8 m long) were recovered over the main vent field along major seismic lines and at sites outside known vent occurrences in that area. At blank zone one, 15 piston cores were taken (Figure 6.18); four of them contained hydrate (C-4, C-6, C-18, and C-20). Hydrate samples were preserved in liquid nitrogen for analyses of the gas and isotopic composition. Six piston cores were recovered over blank zone 4 (Figure 6.18).

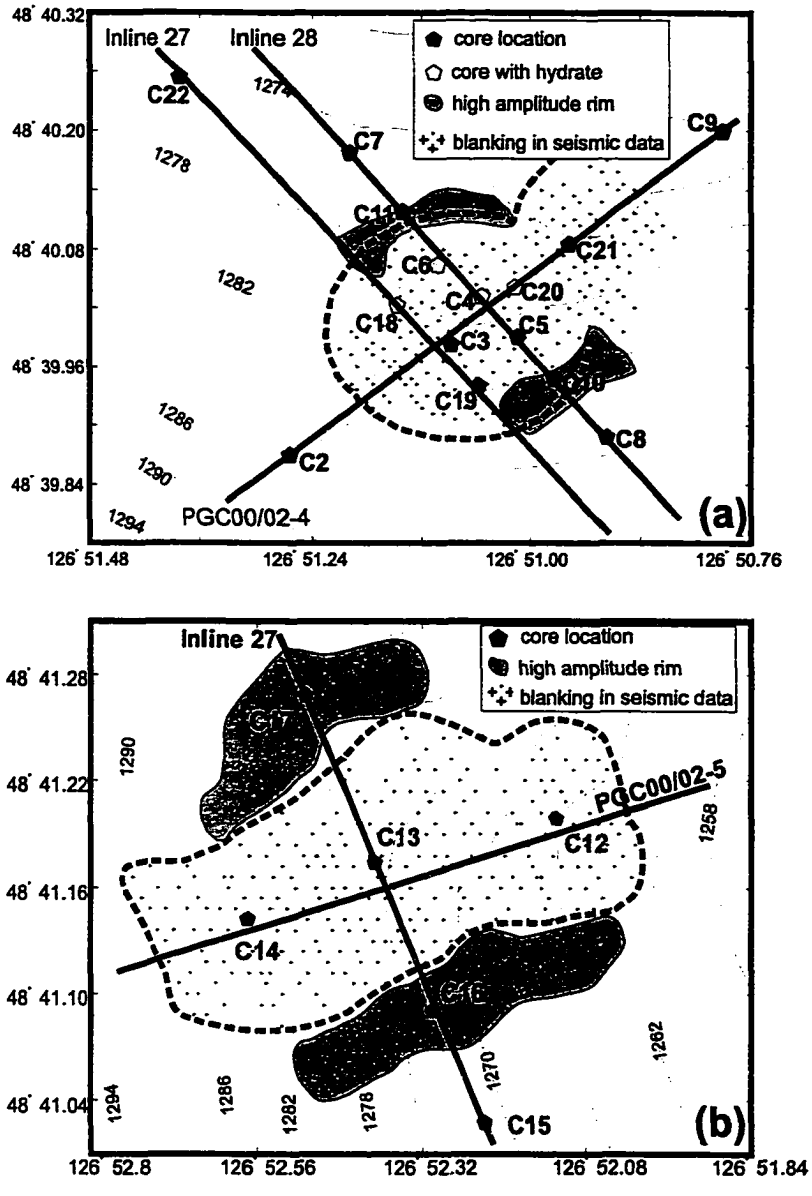

Figure 6.18 Location of core sites around blank zone 1 and 4. Seismic key lines are indicated, as well as extent of seismic amplitude reduction and the high amplitude ring.

Physical properties were measured onboard a few hours after core recovery to allow thermal equilibration of the core sections. On the full core sections, magnetic susceptibility and thermal conductivity were measured. After splitting the core sections, electrical resistivity, seismic P-wave velocity and shear strength were measured. Finally, samples were collected from the split cores for density determination.

First preliminary data analyses carried out by I. Novosel indicate no major difference in the physical properties (P-wave velocity, density and shear strength) between the cores C-3 and C-5 taken inside of blank zone 1 compared to the cores C-7, C-8, and C-9 taken outside of the blank zone. Density of the uppermost 1 m of sediment recovered varied typically between 1.4 and 1.6 g/cm^3 and was on average 1.5 g/cm^3. Density slightly increased with depth. P-wave velocity was almost uniform over the core length and was on average 1500 m/s. If shear strength could be measured, it generally increased linearly with depth starting from about 20 kPa at the seafloor to 80 kPa at a depth of about 6–7 m.

Cores C-3, C-5 and C-9 were all located on a seafloor with similar reflection coefficient (Figure 6.14). Even if an uncertainty for the positioning of the core site of several 10's of meters is assumed, core sites C-3 and C-5 fall outside the area of low reflection coefficients. The cores C-4, C-6, and C-20 perhaps indicate differences in physical properties, but the cores contained hydrate and most of the sediment was lost.

6.4.1 Hydrate Recovery

Massive hydrate was recovered at four piston core sites around blank zone 1 at depths of 3–8 m below the seafloor (Figure 6.18). Hydrate was usually found at the bottom of the cores or in the core catcher and may have stopped deeper core penetration. Thus the total thickness of the hydrate occurrence was not determined. The top of the hydrate was mapped in the single channel seismic data from 2000 and

the depth of hydrate recovery matches the depth of the hydrate cap reflector.

Hydrate samples varied between 2 and 15 cm in size (Figure 6.19). At position C-20 the recovered sample was composed entirely of hydrate with no embedded sediments (Figure 6.19b). Several samples were preserved in liquid nitrogen for additional geochemical analyses. Gas hydrate samples recovered from core 6 have an isotopic $\delta^{13}C$ signature of -70.4, indicative of biogenic methane as primary methane source (Claypool and Kvenvolden, 1983).

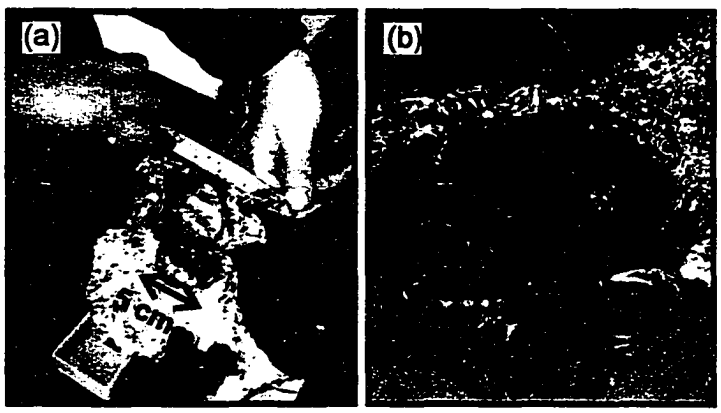

Figure 6.19 Hydrate samples recovered from piston cores at C-4 (a) and C-20 (b).

6.5 Carbonates Occurrences

Around the four core sites of hydrate recovery at blank zone 1, widespread carbonates were found on the seafloor during an unmanned submersible dive using the ROV ROPOS. Carbonates occurred either as several centimeter thick pavements or as disseminated chunks embedded in the seafloor sediments. Most of the carbonate pavements are associated with steep ridges approximately 2–3 m high. Figure 6.20a shows an overview of an area with massive carbonate pavement, approximately 10–20 cm thick. The carbonate pavement visible in Figure 6.20a covers an area of about 25

m^2. It is not known if this pavement is lying on of the seafloor, or if the carbonates penetrate deeper into the sediments.

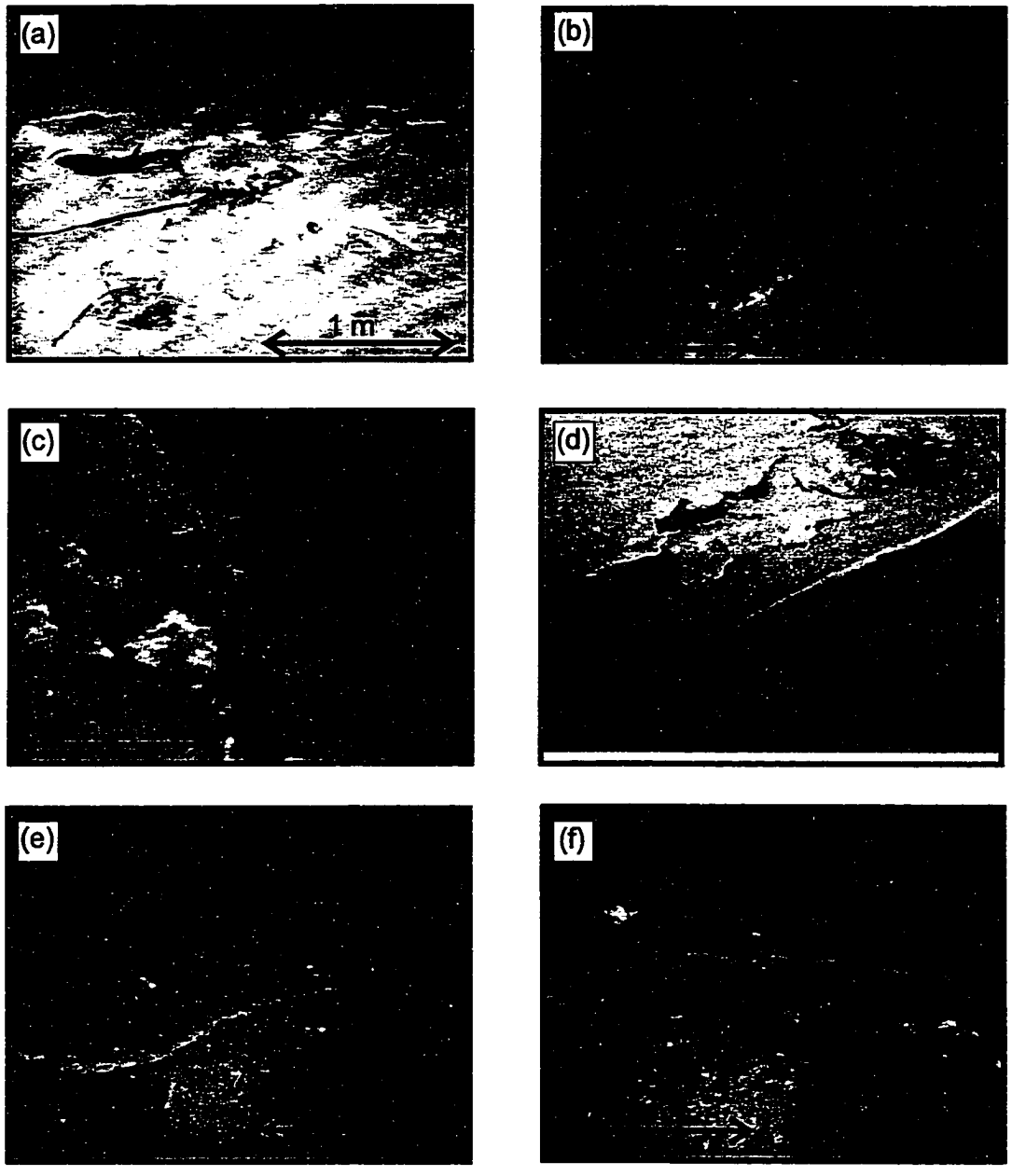

Figure 6.20 Examples of carbonate formations around blank zone 1 (a–d) and blank zone 3 (e,f). Approximate scale is given.

Figure 6.20b shows a top-view of a carbonate ridge, nearby the carbonate outcrop shown in the previous figure. This figure clearly shows that the carbonates outcrop along multiple lineaments. The outcropping carbonate sheets are about 3–5 cm thick. It is again not known how far these sheets continue into the deeper sediment. Along one of these lineaments, the carbonate outcrop was investigated more closely (Figure 6.20c). In the background a *solemya riedi* (*acharax*) clam shell is visible. These clams are indicative of high sulphide environments and normally live several centimeters deep in the sediment. Figure 6.20d shows a closeup of the sampled carbonate sheet. The surface of this rock is smooth and does not show any indication of burrowing, most likely indicating a young stage of carbonate formation.

Carbonates also occur as disseminated chunks embedded in the sediment without being associated with a larger ridge structure. Several chunks were collected during the ROPOS dive. These rocks show a completely different texture. They have a rough surface and burrows on the side facing the seafloor sediments. These rocks most likely are older and have been altered by biological activity. Another distinct character of the embedded chunks is their yellowish-brown color, whereas the rocks sampled at the mound/ridge structures are more grayish-blue. These rocks also have a different isotopic composition (Table 6.1). The $\delta^{13}C_{PDB}$ values of samples 575-039 and 575-144 indicate a strong methane source typical for cold-seep related carbonates, whereas the other two samples probably show a mixing of carbon sources (Bohrmann *et al.*, 1998).

During a subsequent cruise with ROPOS in May 2001, an active part of the vent was found. At a carbonate mound of about 1.5 m height living colonies of clams (*vesicomyids*) were found indicating active methane venting and related sulphide emissions (Figure 6.21a). The clams form small-scale colonies which are aligned around the ridge probably following cracks/fissures in the carbonate mound along which methane preferentially seeps out. Figure 6.21b is a close-up of one of the colonies, about 30 cm in diameter, showing the clams, worms and bacterial mats.

Sample ID	$\delta^{18}O_{PDB}$	$\delta^{13}C_{PDB}$	
575 - 039	5.81	-46.52	(see Figure 6.20a)
575 - 050	7.46	-33.29	
575 - 063	7.41	-28.62	
575 - 144	5.77	-47.31	(see Figure 6.20c,d)

Table 6.1 Isotopic composition ($\delta^{18}O_{PDB}$ and $\delta^{13}C_{PDB}$) of selected carbonate rocks sampled around blank zone 1. Measurements were done by Wendi Abdi, G.G. Hatch Isotope Laboratories, University of Ottawa.

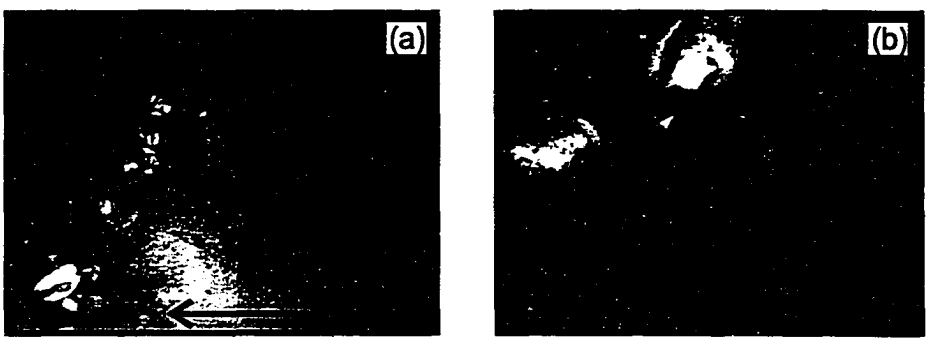

Figure 6.21 Examples of the observed active part of the vent (blank zone 1) close to piston core site C-4. Clams (*vesicomyids*) form small colonies about 40 cm in diameter along cracks of the carbonate ridge. The colonies contain clams, worms and bacterial mats.

Bottom video observations were also carried out on a transect connecting blank zones 1 and 4 along the DTAGS line BC-03 (also inline 27 in COAMS 3-D data) in the May 2001 ROPOS cruise. Following the line, widespread carbonates were observed around blank zone 3. Several centimeter thick crusts were found at several locations around this zone (Figure 6.20e and 6.20f). The carbonates appear to be formed almost parallel to the seafloor. Most of these carbonates were covered by mud and the total

topography changed by only about 1 m over the search area. No surface evidence of carbonates were found at blank zones 2 and 4. However, the transect covers only a small area of about 3–4 m in width. Carbonates may be present at locations outside of this zone or were covered with mud and were therefore not detectable with a video observation.

6.6 Heat Flow

During the cruise PGC00-02 in July 2000, extensive heat flow measurements were carried out. The analyses are not yet complete (Lewis, 2000) but initial results are shown here. A 3 m Lister-type probe was used and the bottom five sensors were used to calculate the heat flow values. Single-site measurements were carried out at blank zone 1 and 4 close to the piston core sites. In addition to these single-site measurements, a profile across the vent field along seismic inline 27 was measured (Figure 6.22). Heat flow values obtained appear quite uniform across blank zone 1 and across the entire vent area (Figure 6.23). However, with the current station spacing we are not able to rule out any possible heat flow anomaly that may occur on a smaller spatial scale. Values ranged from about 55 mW/m^2 to 69 mW/m^2 (Table 6.2). Bottom water temperatures were also quite uniform across the vent area and were on average 3.2 °C. An uncertainty in the heat flow values was estimated from the repeated measurements at piston core site C-4. Assuming that the heat flow does not change over the area over which the measurements were taken (approximately 100 m^2 in diameter), the 4 individual measurements yield a very low standard deviation of approximately 2 mW/m^2, approximately the measurement uncertainty.

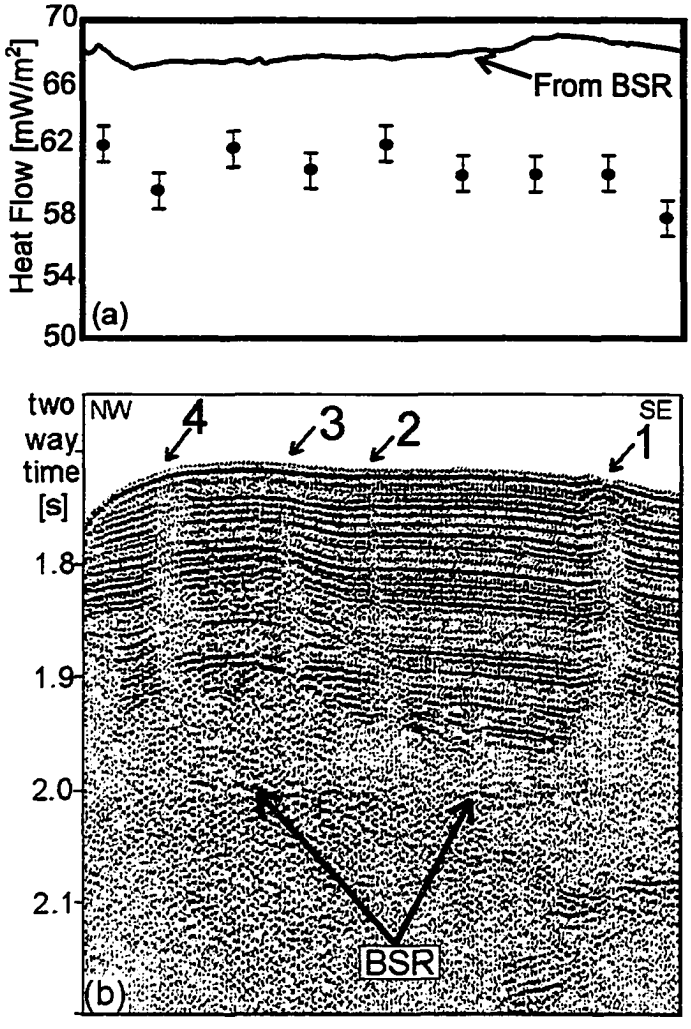

Figure 6.22 Heat flow (in mW/m^2) profile across the vent field and comparison to SC seismic inline 27. Error bars on heat flow values are estimated as 2 mW/m^2 from repeated measurements at piston core site C4. In general heat flow appears to be quite uniform across the vent field.

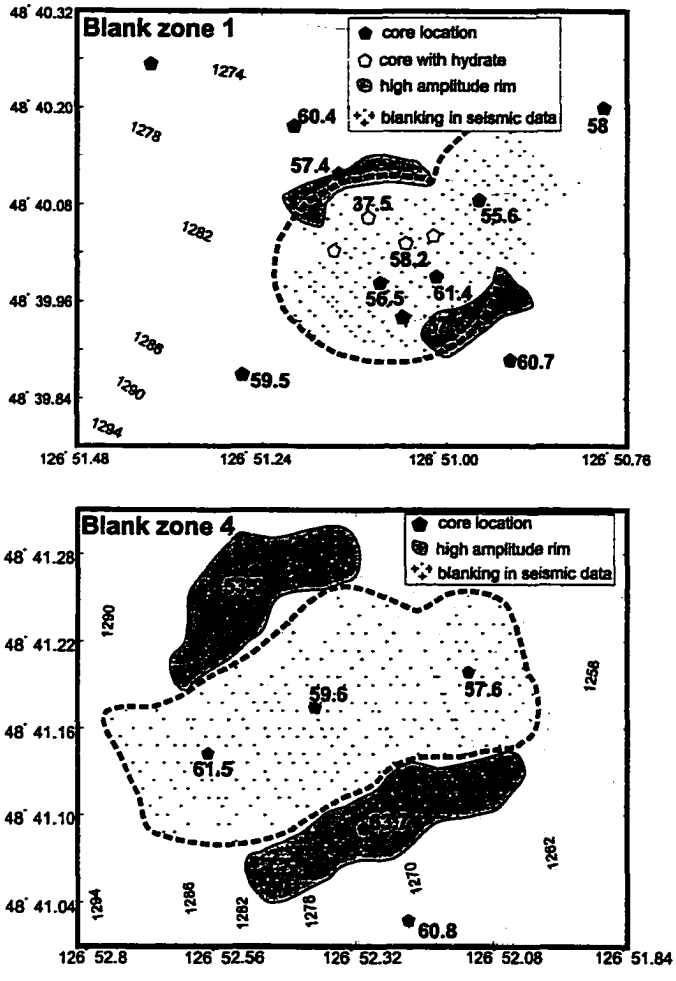

Figure 6.23 Heat flow measurements at core positions at blank zone 1 and 4. Compare to Figure 6.19 for core-sites and key seismic lines.

Station Number	Core Site	Heat flow (mW/m^2)	Water Depth (m)	BWT (°C)	Conductivity (W/m K)
Blank Zone 1					
002	C-2	59.5	1280	3.26	1.113
003	C-3	56.5	1275	3.23	1.085
004a	C-4	58.0	1272	3.15	1.098
004b	C-4	55.8	1272	3.23	1.077
004c	C-4	61.5	1272	3.38	1.085
004d	C-4	57.4	1272	3.16	1.058
005	C-5	61.4	1274	3.2	1.087
006	C-6	37.5	1267	3.15	1.082
007	C-7	60.4	1268	3.2	1.067
008	C-8	60.7	1280	3.24	1.070
009	C-9	58.0	1267	3.18	1.054
010	C-10	57.6	1276	3.16	1.101
011	C-11	57.4	1268	3.15	1.070
014	C-21	55.6	1267	3.16	1.045
Blank Zone 4					
015	C-15	60.8	1265	3.16	1.070
016	C-16	63.7	1260	3.29	1.072
017	C-13	59.6	1265	3.27	1.090
018	C-17	53.9	1275	3.23	1.060
021	C-12	57.6	1255	3.16	1.053
022	C-14	61.5	1280	3.11	1.080

Table 6.2 Measured heat flow values, bottom water temperatures (BWT) and thermal conductivities around core sites at blank zone 1 and 4.

6.7 Geochemistry From Piston Cores

The amount of methane flux (and related fluid transport) can be inferred from sulfate concentration profiles in the upper 10–20 m of sediment. Anaerobic oxidation of methane causes sulfate depletion by consuming one mol of methane for each mol of sulfate:

$$SO_4^{2-} + CH_4 \rightleftharpoons HS^- + HCO_3^- + H_2O$$

The depletion of sulfate and methane in the reaction zone yields steep concentration gradients, and diffusion brings in sulfate and methane at equal rates. The supply of methane cannot easily be maintained without fluid flow from below. Measuring the sulfate concentration therefore provides a measure of fluid flow rates from below. Typically the depth of no sulfate (*dns*) can be used as a chemical marker horizon. The shallower the *dns*, the more methane is being supplied.

At 11 piston cores around blank zones 1 and 4 (Figure 6.18), geochemical analyses of the pore fluids were performed by C. Solem (personal communication, 2001) onboard a few hours after core recovery. The bottom 5 cm of each core section was used for pore fluid extraction. The alkalinities of the pore fluid were determined using the Gran method (Gieskes and Rogers *et al.*, 1973). The resulting sulfate gradients were then used to determine methane flux (Borowski *et al.*, 1996). The alkalinity gradients and the corresponding *dns* were calculated following the method by Gieskes and Rogers (1973). The corresponding amount of estimated methane flux is illustrated in Figure 6.24. At most of the core sites the *dns* lies at about 4–5 m bsf. The core site C-22 is outside the main vent area and shows a *dns* of approximately 8.5 m, which is almost twice as deep as the observation around the vent area. This may indicate a general increase of methane supply at the blank zone 1 and 4. However, core locations C-9 and C-2 are both outside of blank zone 1, but also have a relatively shallow *dns*, equivalent to the core locations inside of a blank zone.

The amount of fluid flow associated with the methane flux can be calculated

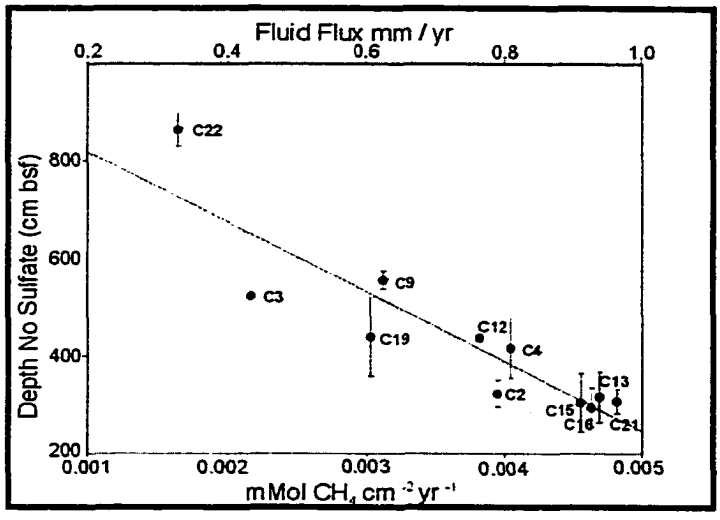

Figure 6.24 Extrapolated depth of no sulphate and corresponding methane flux at 11 piston core sites at blank zones 1 and 4. Sites C-2, C-9 and C-22 are outside of the blank zones. Corresponding fluid flux was estimated using a methane solubility of 0.001 mol fraction. Analyses were carried out by C. Solem, Scripps.

assuming full methane saturation of the fluid migrating upward. For the temperature and pressure conditions at blank zone 1, the methane solubility is about 0.001 mol fraction (Claypool and Kaplan, 1974). Thus, the maximum calculated methane flux of 0.005 mmol CH_4 cm^{-2} yr^{-1} corresponds to a fluid flux of about 1 mm/yr. This relatively small amount of fluid flux can be an average over a longer time scale with fluid flow being strongly episodic.

There is however evidence of increased methane concentrations in the water column (Figure 6.25). Concentrations above core site C-4 at blank zone one are increased by almost an order of magnitude relative to background ocean methane-concentrations. The measured concentrations of about 20 nmol/L within the first 100 m above the vent are relatively small compared to Hydrate Ridge (> 400 nmol/L, Suess *et al.*, 1999) but larger than vents at the Aleutian subduction zone (4–5 nmol/L, Suess *et al.*, 1998).

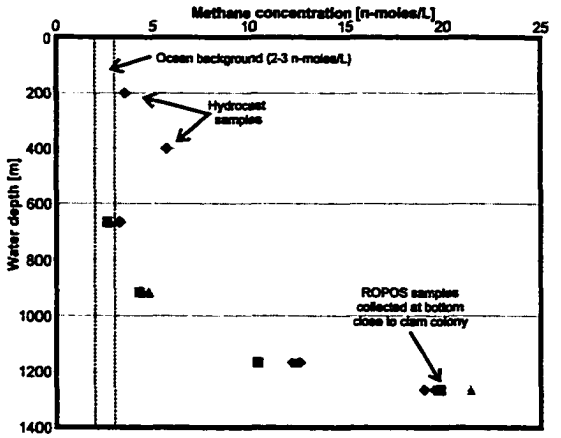

Figure 6.25 Methane concentration in the water column above core site C-4 (1280 m water depth) at blank zone 1. Ocean-background concentration are about 2–3 nmol/L methane. Upper two water samples were taken by single-bottle hydrocasts, other samples were acquired with ROPOS during ascent. Shown are results from several runs with 250 and 165 ccm water samples. Analyses were carried out by C. Solem, Scripps.

6.8 Other Fault-Related Blanking

Two additional locations were identified from the COAMS multichannel seismic data that showed fault-related amplitude loss. The reduced seismic amplitudes at these sites extends even deeper than the expected BSR depths, which is different from the main vent field area. However, as stated earlier, the faults of the vent field could only be identified in the layered slope sediments and were lost in the underlying ridge of accreted sediment due to the low coherent reflectivity.

Within this section, the seismic character of the two new sites outside the main vent field is described. These occurrences are important observations and contribute towards a complete characterization of fluid flow and related indicators in the entire area of investigation.

The first region is a small area at the southern flank of the western ridge of accreted

sediments. A fault with reduced seismic amplitudes was observed on inlines 3–5 of the 1999 COAMS survey grid only. The amplitude loss is continuous even for depths below the expected BSR depth (Figure 6.26).

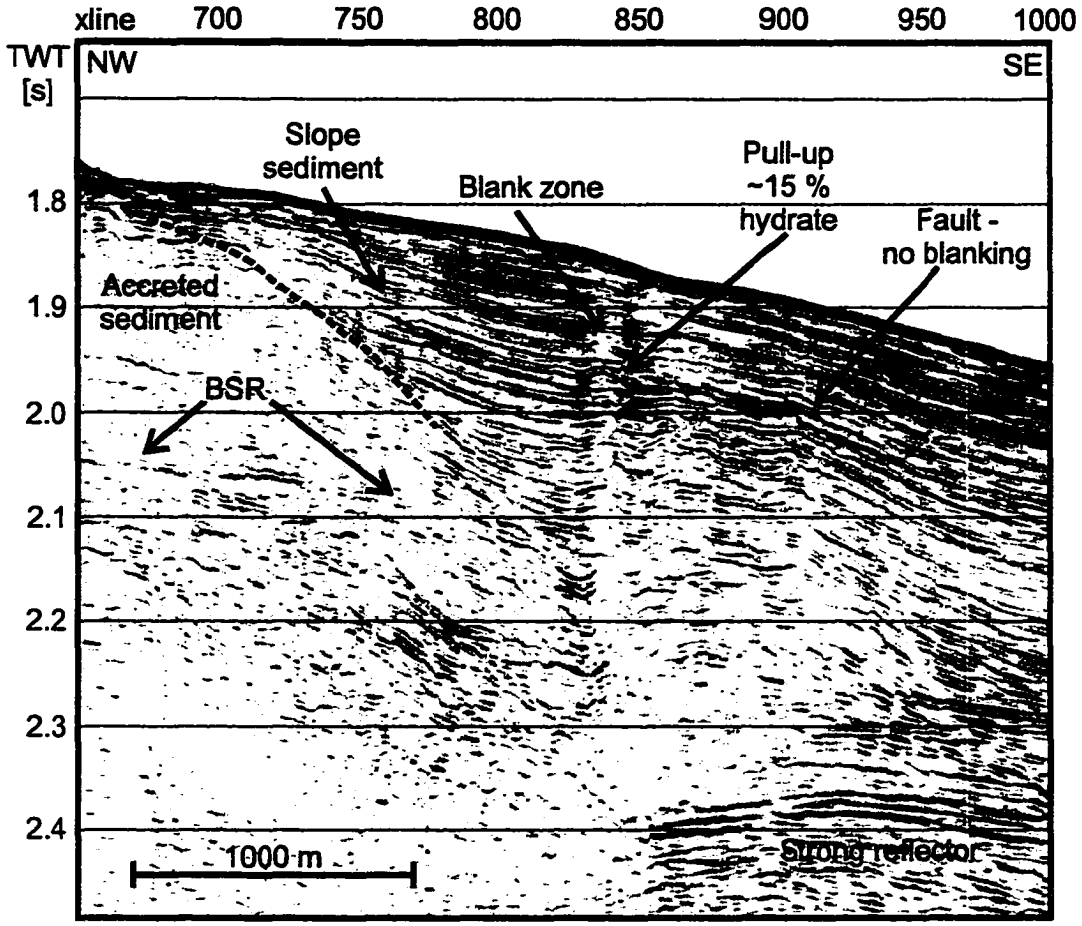

Figure 6.26 Blank zone from COAMS inline 5 at the SW flank of the western main ridge of accreted sediment. Note strong pull-up in the middle of the blank zone. This pull-up would be equivalent to about 15% of hydrate.

To both sides of the blank zones, the sediments show evidence of large-scale deformation and folding, probably due to uplift of deeper ridges of accreted sediment. This blank zone is characterized by a small-scale dome formed at about 100 ms TWT (~90 m) below the seafloor at around crossline position 835. This doming seems to

be unrelated to the local deformation and it is only limited to a few layers. Assuming a background interval velocity of 1550 m/s, the observed pull-up is equivalent to a depth-change of about 8–10 m. This pull-up can be converted to a velocity increase of 140 m/s, which is equivalent to a local hydrate concentration of about 15% using the porosity-reduction model by Yuan *et al.* (1996). This pull-up structure is different to the structure seen at blank zone 1 at the vent field, where the pull-up structure seems to be related to the topographic expression of the mud/carbonate mound. There is no seafloor expression above the pull-up structure at the blank zone of inlines 3–5. Amplitude reduction at this site can be seen above and below this pull-up structure, ruling out the occurrence of free gas as a source of amplitude reduction and related pull-up due to overpressuring of the sediments at least over the depth range of hydrate stability, which extend to about 240 ms TWT bsf. A second small nearby fault about 700 m to the SE of this blank zone (crossline position 910) does not show any evidence of amplitude reduction. The blank zone at this site may be related to a strong deep reflector that dips towards the NW. This reflector is truncated abruptly at the blank zone fault. It was identified on nearby inlines but its origin and relation to the overall tectonics could not be determined.

The second region was found about 3 km to the NW of the main vent field (Figure 6.27 and 5.5). The associated fault can be traced over several inlines and was observed over a total length of 2 km. However, seismic amplitudes within this fault are reduced only over a small part of the fault of approximately 200 m length between inline 27 and 28 (Figure 6.27). The fault cuts through a slope-sediment basin of up to 0.4 s TWT thickness and follows roughly a North trend as defined from timeslices of instaneous amplitude (Figure 6.28).

The seafloor around the fault outcrop itself is mainly composed of low reflectivity sediment and a small dome is formed (Figure 5.8 in Chapter 5) similar to the surface expression at blank zone 1 at the main vent field. The main blank zone separates sediment blocks on either side of the fault plane. The throw of the fault increases

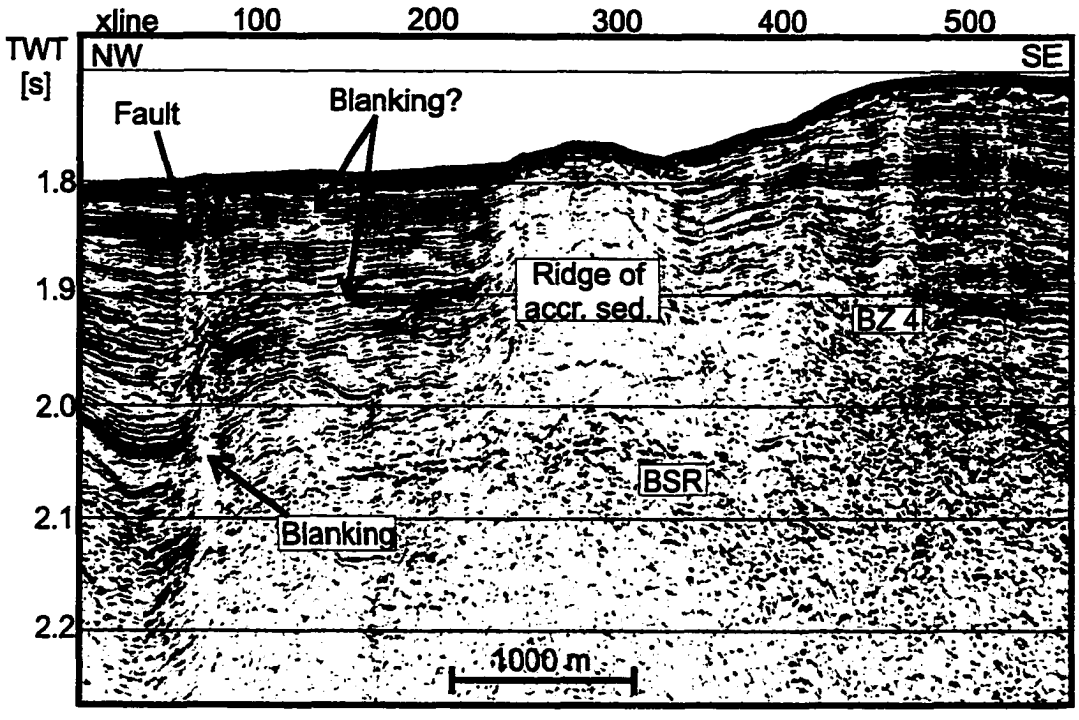

Figure 6.27 Part of COAMS inline 27 showing fault associated amplitude reduction at about 3 km NW of main vent field.

with depth from about 5 m at the seafloor to about 15 m at 180 m below the seafloor. However, the layers show evidence of being dragged so that the observed throw is probably divided into several smaller steps.

The main fault is split into a series of smaller faults towards the east that follow a parallel North trend. These smaller faults show also some evidence of amplitude reduction but are not directly connected to the BSR (Figure 6.29 or Figure 5.6 in Chapter 5). They mainly occur over the top of the uplifted ridge of accreted sediment. The area where these small faults occur is the region of increased seafloor reflection coefficients (Chapter 5, Section 5.2.3).

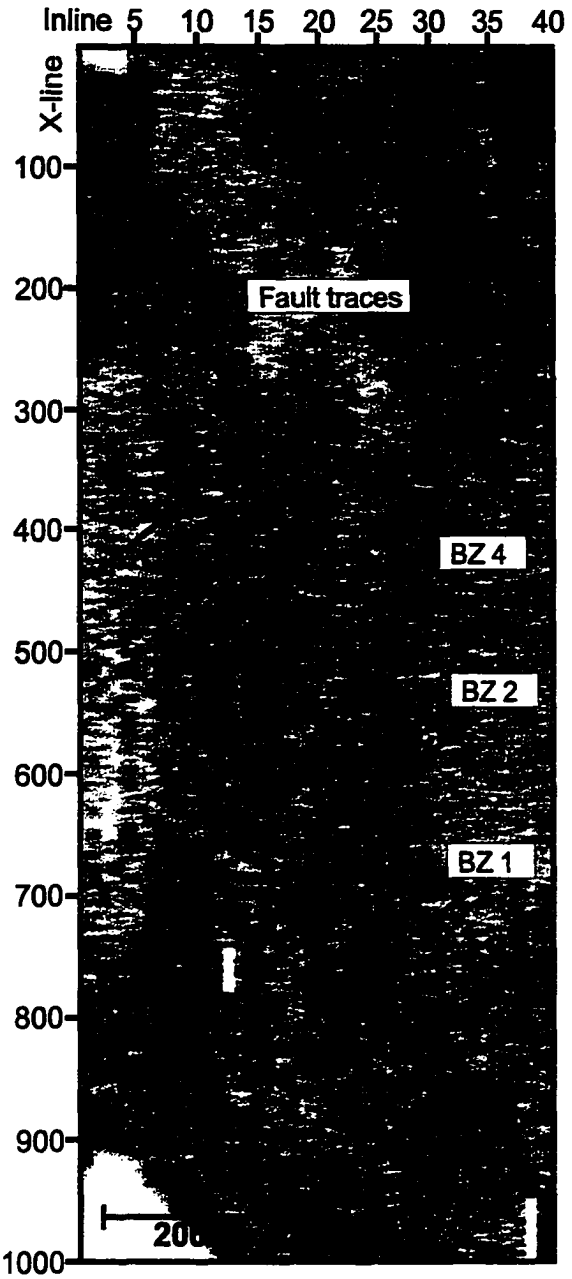

Figure 6.28 Timeslice of instantaneous amplitude at 1.89 s TWT. Several fault traces were identified associated with blank zones 1,2 and 4 of the main field and two new faults towards the NW of the vent field. High amplitudes are dark.

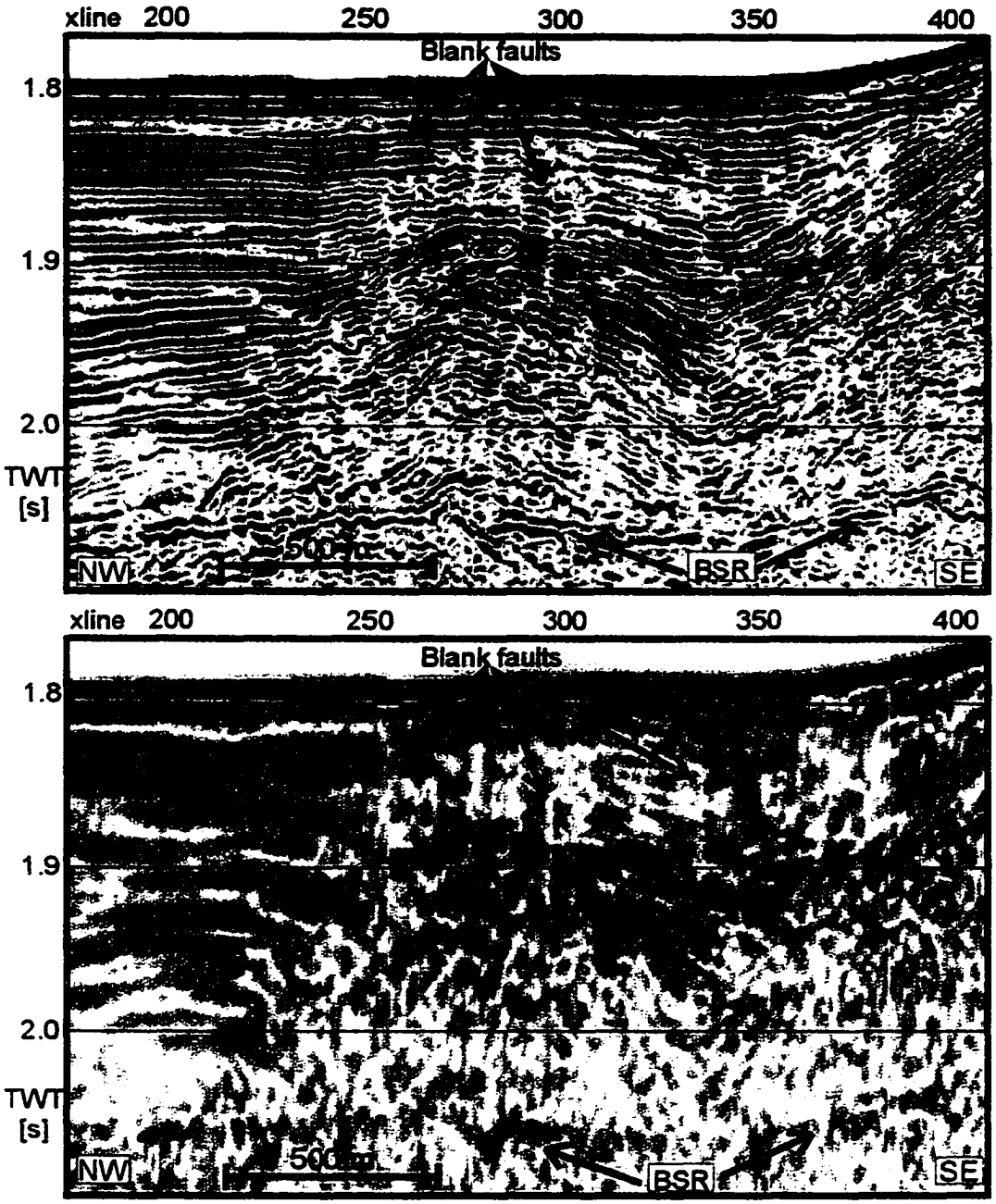

Figure 6.29 Example of small faults with reduced seismic amplitudes. The seismic section shown is from COAMS inline 31. Section (a) is seismic amplitude and section (b) is instantaneous amplitude.

6.9 Evidence of Wide-Spread Venting Associated With Thrust Faults

6.9.1 Introduction

The prominent ridge structure in the NW corner of the 3-D seismic area of investigation was the target of a detailed bottom-video survey with the unmanned submersible ROPOS in May 2001. It was selected based on the topographic relief, its proximity to a fault outcrop and chaotic seismic reflection pattern. The general goal of this study was to investigate fluid/methane flow related to large-scale faulting and to test if venting is limited to the area of the vent field only or if there are other locations with similar structures. Broadscale swath-bathymetry in that area indicates slumping around the mound structure (Figure 6.30). The detailed video observations showed typical vent-related carbonate formations and very high biological activity. Highlights of the video survey and detailed seismic structures are presented below.

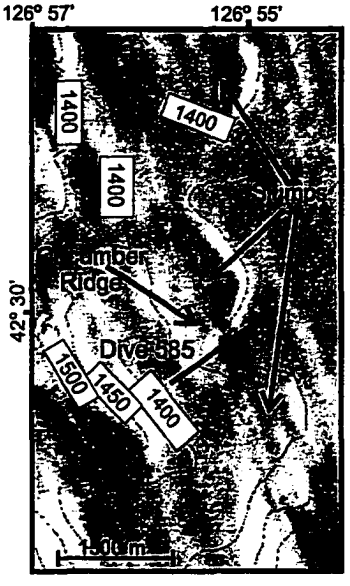

Figure 6.30 Detailed view of the swath bathymetry around the mound structure (Cucumber Ridge). The ridge is about 1.5 km in diameter. To the north and south of the ridge slope failures or slumps occurred.

6.9.2 Seismic Observations

The ridge structure is crossed in an NE-SW direction by COAMS multichannel seismic line XL-01 (Figure 6.31). This line shows an up to 0.2 s thick slope sediment cover in the NE part that is progressively thinned towards the ridge structure. The ridge itself does not have any internal seismic coherent reflectors, but is marked by the occurrence of a prominent BSR. The fault outcrop at around CMP position 1100 is about 80 m deeper than the top of the ridge. This change in topography occurs over a distance of about 500 m, which is equivalent to a slope angle of about 10 degrees. ROPOS dive 585 that followed approximately this line started at about 200 m east of the fault outcrop (CMP position 1150) and ended ontop of the ridge at around CMP 1450. The total length of this dive is about 700 m.

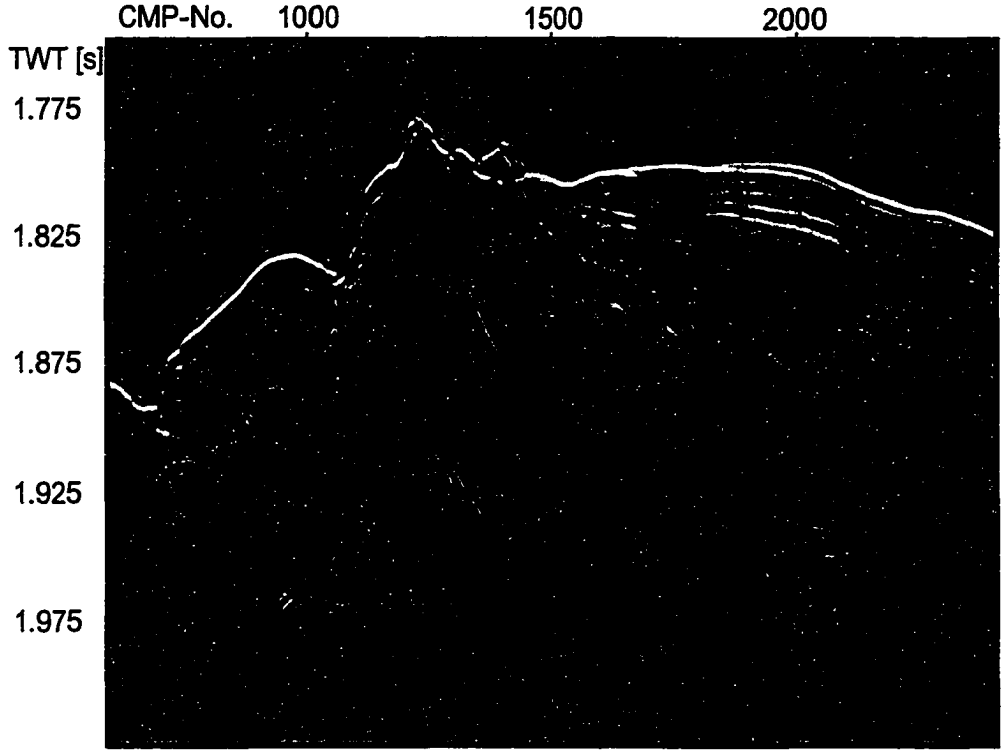

Figure 6.31 Migrated multichannel COAMS line XL-01 showing fault associated with the ridge structure.

The inlines of the COAMS 3-D seismic grid covered this ridge in a perpendicular direction. On these lines, no coherent seismic reflectivity was observed and detailed imaging of the structure was impossible due to abundant side diffractions (compare e.g. to Figure 5.15 of inline 15 in Chapter 5). Several lines of the 3-D grid were recorded on the 3.5 kHz subbottom profiler. These records show the complicated nature of that ridge structure (Figure 6.32). The records are dominated by overlapping diffraction that are partially out-of-plane arrivals. The structure itself shows several less steeply dipping patches of high reflectivity, as for example seen around shot number 380 on Figure 6.32.

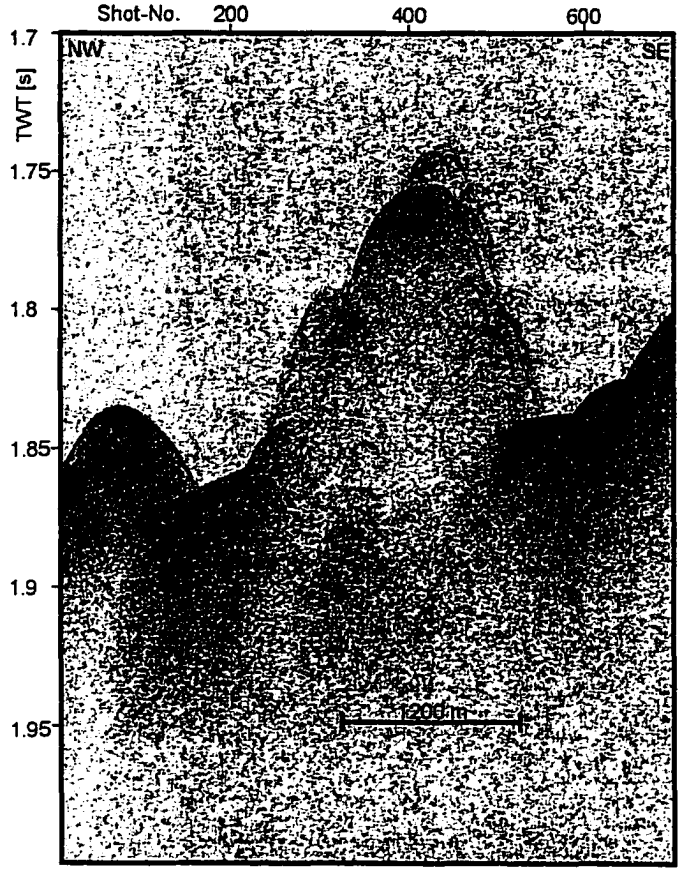

Figure 6.32 Part of inline 9 over ridge structure recorded on 3.5 kHz subbottom profiler.

During the ROPOS Dive 585 12 kHz echosounder data were collected along the transects. Several regions of increased seafloor reflectivity are visible related to local carbonate outcrops. Figure 6.33 shows parts of transect 5 about 100 m to the north parallel to COAMS line XL-01. Several carbonate samples were taken about half way along the part of the transect shown.

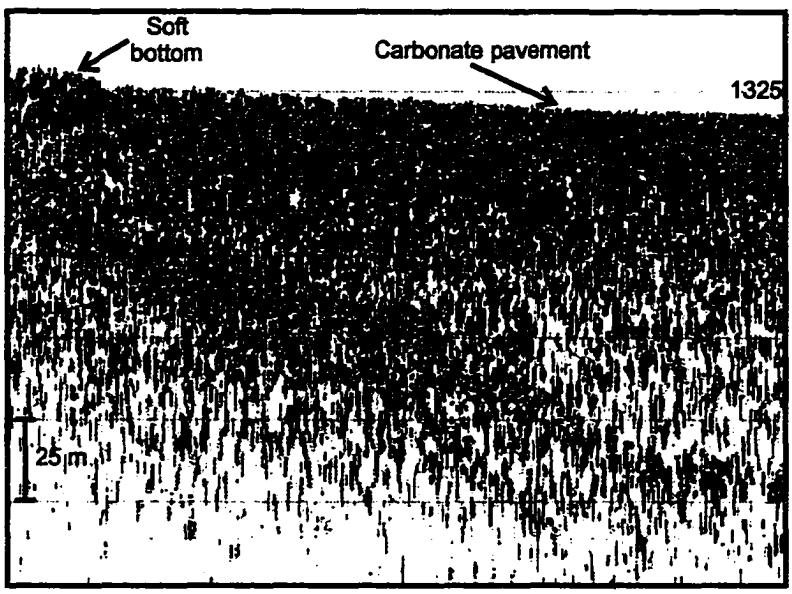

Figure 6.33 Detailed view of 12 kHz profile recorded during ROPOS dive 585. Increased seafloor reflectivity matches with observed carbonate formations on seafloor. Profile is approximately 500 m long.

6.9.3 ROPOS Observations

During the start of the dive 585 along line XL-01, the seafloor 100 m around CMP location 2000 was investigated. The seafloor was composed of very hard, highly consolidated sediment that could not be penetrated with push-cores. ROPOS's claws were used several times to probe the seafloor. Below a very thin cover of mud solid, carbonated seafloor was found. Several ridges, up to 2 m in height, were found close to the starting point of the line (Figure 6.34a, b). These ridges were composed of thick carbonate, covered with a variety of biota, such as corals and anemonies. In general, this area showed a character that was completely different from all other sites visited at around the blank zones.

In the following the ridge was further investigated by a total of six parallel lines of about 650-700 m in length mainly to the south-east of the seismic line XL-01. Along these transects several fields with clams (*vesicomyids*), tube worms (*vestimentiferan Lamellibrachia barhami*) and carbonate formations were found (Figure 6.34c, d). A preliminary investigation of the rocks showed that typically around clam/worm fields, the seafloor carbonates were relatively thin, soft and fragile. They have a characteristic bubble-fabric, which may indicate carbonate formation during a stage of active gas bubbling (Figure 6.34g). However, during the dives 585 and 586, no active gas seepage was observed. Two other types of carbonates were identified. One type of carbonate forms typically in isolated large chunks, having a dense, fine-scaled texture. The other type of rock identified is a coarse grained carbonate-cemented sand (Figure 6.34e,f).

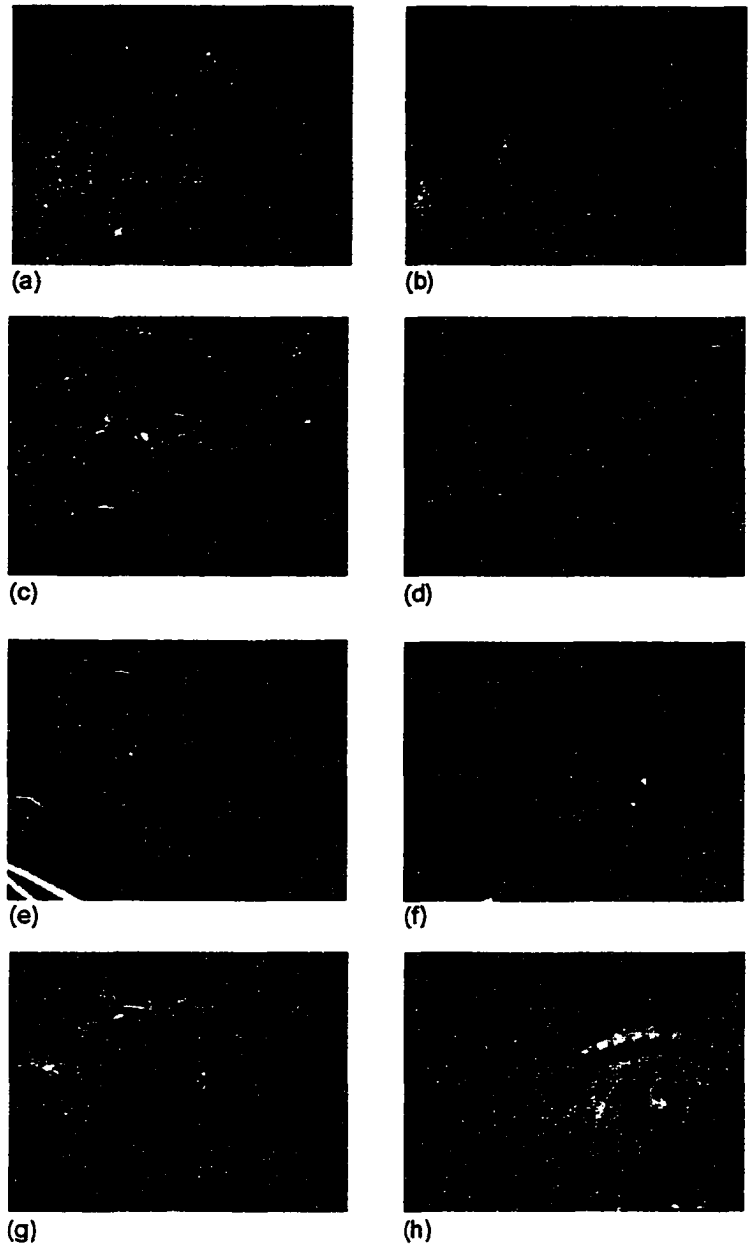

Figure 6.34 Images from bottom-video observation over the ridge structure. (a) Carbonate ridge found at around start of dive along line XL-01. This ridge is about 1.5 m high. (b) along line XL-01, carbonate formations were surrounded by abundant corrals, (c) and (d) examples of clam fields, tube worm bushels and carbonate formations, (e) partially carbonate-cemented, coarse-grained sandy sediment outcropping ontop of ridge, (f) coarse-grained rocks forming a 5 m wide half-circle, (g) close-up of very thin, fragile carbonates with bubble-fabric, (h) the famous sea-cucumber.

6.10 Amplitude-Versus-Offset (AVO) Analyses

In this section, the AVO technique is applied to COAMS multichannel data. The objective is to find a meaningful physical model that can explain the amplitude reduction. In the previous sections, seismic observations were done on vertical incidence single channel or stacked multichannel seismic data. However, AVO is a more powerful tool to further constrain the range of physical properties of the sediments since it is sensitive to S-wave as well as P-wave velocity. However, AVO is based on several assumptions, such as a single sharp interface between different strata. A typical approach to incorporate those effects is full-waveform modeling (e.g. Yuan *et al.*, 1996; Korenaga *et al.*, 1997). Full-waveform modeling and inversion was not considered for the multichannel COAMS data due to the complicated shape of the array during data acquisition and the strong directivity effects (see Chapter 3 and 4 for details). These effects strongly influence the waveform and are difficult to incorporate in a modeling/inversion approach.

In a first simple AVO approach, a purely elastic inversion is carried out to find a best-fit model for the sediments inside and outside a blank zone. However, a purely elastic treatment of the sediments is only an approximation. In a second approach, a viscoelastic modeling is carried out using the best-fit elastic model for the sediments outside the blank zone defined by the elastic inversion and additional P-wave attenuation.

To investigate the amplitude behaviour across a blank zone, an AVO analysis (Figure 6.35) was carried out for a horizon on COAMS inline MC-27 at a depth of about 100 ms TWT bsf (see Figure 6.7). RMS amplitudes were calculated for a window length of 10 ms, representing the length of the wavelet. Amplitudes were then corrected for streamer directivity. The airgun source amplitudes were assumed not to vary with angle and no source directivity correction was performed. The near offset was in general noisier than the far offset traces due to noise generated by the streamer

tow cable. Seismic amplitudes were normalized to a seafloor reflection coefficient of 0.2 for vertical incidence. This average reflection coefficient was obtained from the ratio of primary-to-multiple reflection amplitudes (Warner 1990) and from physical properties of piston-cores acquired in July 2000 (Novosel *et al.*, 2000). Due to the limited range of offsets with the COAMS array, the maximum angle of incidence at the reflector is about 30°.

Simple straight path ray tracing was used to determine the angle of incidence. AVO modeling was done for a simple two-layer model only and transmission loss at additional layers between the seafloor and the target horizon was assumed to be small and therefore neglected. Velocities determined from the multichannel NMO analysis were used as the basic constraints on the AVO modeling. Density and S-wave velocity were allowed to vary within reasonable bounds determined from Hamilton's relations (Hamilton, 1980) and the ODP downhole logs (Westbrook *et al.*, 1994) (Table 6.3).

AVO trends were modeled at three locations around blank zone 2:
(a) the area outside of the blank zone, (b) inside the blank zone, and (c) outside, but close to the left boundary with offsets extending into the blank zone. The AVO behavior is nearly symmetrical about the center of the blank zone and the results are shown from one side only. Locations (a) and (b) show a similar AVO behavior with amplitudes increasing with offset. However, the overall magnitude of the reflection coefficient is decreased inside the zone by about 50%. Location (c) shows a different AVO trend, i.e. a decrease of reflection coefficient with offset. At location (c) the vertical incidence reflection coefficient (0.1) is the same magnitude as that outside of the zone; that is, the vertical incidence rays are not affected by the blank zone. Rays that have to travel partially through the blank zone are reduced in amplitude, with the amount of amplitude reduction increasing with raypath length.

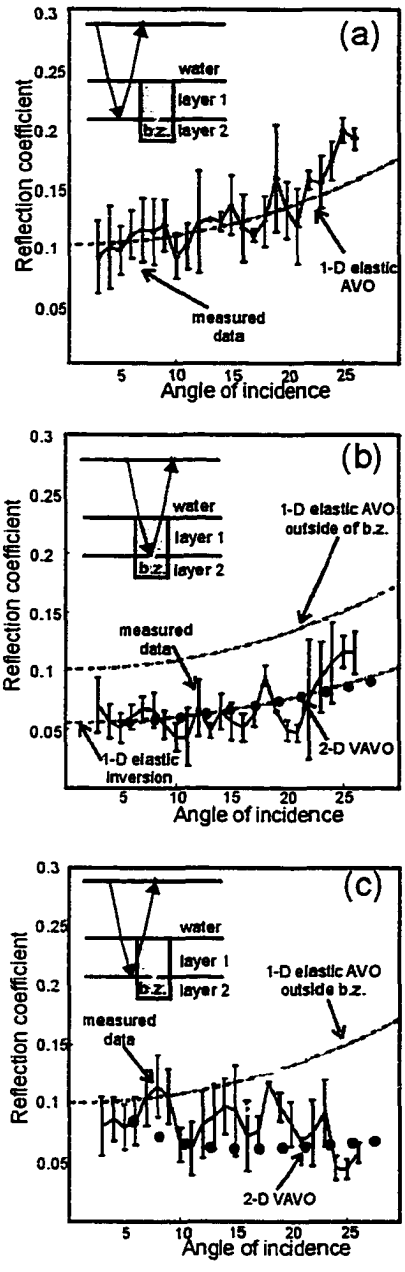

Figure 6.35 Amplitude versus offset (AVO) analysis around blank zone 2 at inline MC-27 from COAMS data. Measured reflection coefficient (averaged in 1° bins; errorbars represent standard deviation in the bin), inverted elastic 1-D AVO (dashed lines), and modeled 2-D viscoelastic AVO (VAVO) (solid black dots) are shown for (a) location outside blank zone 2, (b) inside the blank zone, and (c) outside at the left edge. Simplified sketches of the ray paths involved are shown.

	P-wave velocity (m/s)	**S-wave velocity** (m/s)	**V_p/V_s ratio**	**Density** (g/cm^3)
Layer 1				
Lower Limit	1550	10	1.9	1.4
Upper Limit	1650	800	165	1.8
Layer 2				
Lower Limit	1600	10	2	1.45
Upper Limit	1800	800	180	1.8

Table 6.3 Range limits for elastic AVO inversion.

6.10.1 Elastic 1-D Inversion

The objective of this inversion was to obtain a background model of elastic properties, that is consistent with the observed AVO trend. The inversion scheme used is a sequential-quadratic programming technique (Riedel and Theilen, 2001), i.e. an iterative linearized inversion procedure to find a constrained minimum misfit between observed and modeled AVO data. The forward model is based on the full Zoeppritz equation for two solid, elastic layers (Zoeppritz, 1919). The inversion was constrained to accept only those models that fall inside the predefined range of representative values (Table 6.3). The location outside the blank zone was used first to determine a reasonable set of physical properties for the two layers of interest since this location is not affected by attenuation due to the blank zone. The inverted values for P-wave velocity and density in both layers are reasonable and fall well within the expected range for the type of sediments in the area. The S-wave velocities are in contrast not very reliable. However, the best misfit to the observed AVO data could only be found if the S-wave velocity was allowed to decrease significantly. Constraining the

inversion to accept only an increase in S-wave velocity resulted in a misfit that was up to five times higher. An elastic 1-D AVO inversion was also performed at location (b) inside the blank zone. The same constraints as used at location (a) were applied to this inversion. The resulting P-wave velocities were similar to the values obtained outside the zone; however, to fit the observed lower level of reflection coefficients the density contrast was reduced to almost zero (Table 6.4).

	P-wave velocity velocity (m/s)	**S-wave velocity velocity** (m/s)	**Density** (g/cm^3)	V_p/V_s **ratio**
Outside blank zone				
Layer 1	1600	600	1.62	2.7
Layer 2	1780	100	1.77	17.8
Inside Blank zone				
Layer 1	1600	410	1.50	3.9
Layer 2	1745	10	1.53	174.5

Table 6.4 Elastic 1-D AVO inversion results inside and outside blank zone.

6.10.2 2-D Viscoelastic Modeling

In order to investigate the AVO behaviour for locations with rays partially traveling through the blank zone, a 2-D AVO modeling was carried out. Viscoelastic AVO modeling (VAVO) was used to determine the amount of attenuation needed to explain the observed amplitude decrease for rays traveling through the blank zone. The modeling was based on the ray tracing code HARORAY (Pignot and Chapman 1998), which includes attenuation loss along ray paths. The subsurface was parameterized into cells with varying physical properties. The properties obtained from

elastic 1-D inversion at location (a) outside the blank zone were used as background elastic properties. This assumption is based on the observation during NMO analyses that the P-wave velocity does not vary across the blank zone. Since density and S-wave velocity are both closely related to the P-wave velocity (Hamilton, 1980), these parameters cannot vary independently. For simplicity, only 11 representative angles were chosen for modeling.

To first achieve a reasonable fit to the observed vertical incidence reflection coefficient inside the blank zone, an attenuation coefficient α_p of 0.085 dB m^{-1} kHz^{-1} (Q = 200 for a P-wave velocity of 1650 m/s and frequency of 150 Hz) for the P-wave was found. This parameter was subsequently used to calculate the reflection coefficients for larger angle of incidence. The increase of reflection coefficient with angle of incidence predicted by the VAVO modeling is not as strong as for the elastic background AVO function defined from outside the blank zone. This is the result of a competing effect between larger attenuation loss at larger ray path length and increase of the reflection coefficient of the background AVO function. However, the VAVO modeling resulted in a similar fit to the observed data as the 1-D elastic inversion (Figure 6.35b).

Next, the location close to the boundary of the blank zone was modeled. At this location, only non-vertical rays (larger than 8°) travel through the blank zone. The vertical incidence reflection coefficient is the same as at location (a). The outside AVO function is plotted for reference (Figure 6.35c). For rays that pass through the blank zone, the modeled reflection coefficient is reduced. The attenuation coefficient of 0.085 dB m^{-1} kHz^{-1} (Q = 200) was not sufficient to explain this observed decrease. A fit to the data required an attenuation coefficient of 0.3 dB m^{-1} kHz^{-1} (Q = 55). This apparent mismatch between the attenuation can be explained with an additional attenuation loss for rays passing through the boundary of the blank zone. The boundary of the blank zone can be a relatively rough surface and the additional attenuation is due to scattering.

In general, the physical properties obtained from the elastic AVO inversion are reasonable, with the exception of S-wave velocity. Amplitude reduction inside the blank zone was achieved in this inversion by decreasing the density difference between the two layers modeled. However, the same amplitude reduction can be achieved by larger P-wave attenuation without changing the elastic properties. At this stage, no final conclusion can be drawn about which model is correct.

6.11 Seismic Modeling of Blanking and High Amplitude Rim

Within this section, several possible mechanisms for the loss in seismic amplitude are tested to determine if they reproduce the observed amplitude variation around blank zones seen in the single channel and stacked multichannel seismic data. The focus is especially on the high amplitude rim structures. Modeling was carried out with the software OUTRIDER by the company DigiRule. OUTRIDER is an industry-standard software package that allows for structural modeling of 2-D elastic (only) models. Due to software related limitations in the seismic sampling rate of minimum 1 ms, the possible frequency range was limited to 200 Hz.

The following three models have been tested based on the previously described observations: (a) density decrease as predicted from the 1-D elastic AVO modeling, (b) hydrate formation, and (c) surface carbonate formation. No attenuation can be included and the frequency limit of 200 Hz did not allow an investigation of the observed frequency dependent amplitude reduction.

The modeling procedure is based on wavefront modeling. Wavefront modeling in OUTRIDER creates a ray-traced zero offset synthetic seismic section. It works by scattering a dense series of diffractions along an interface and summing them into an output seismic file. The output seismic file (reflectivity series) then is convolved with a wavelet of choice. In this work a Ricker wavelet was used.

6.11.1 Amplitude Variations in MC and SC Airgun Seismic Data

Amplitudes of the horizon that was used in the previous AVO modeling study were extracted for inline 27 from the multichannel COAMS and single channel Teledyne data. These amplitudes must be compared to the seafloor amplitude variation. Strong variations in seafloor reflection amplitudes influence the amplitudes of the deeper layers. The amplitude of the seafloor in the multichannel seismic data shows only small-scale variations along the vent field. Seafloor amplitude is slightly reduced at the locations of blank zones 2–4 (Figure 6.36). At blank zone 1 the amplitudes are increased at the boundary of the zone with a distinct sharp drop to the inner part of the zone. The low amplitudes are most likely due to defocusing effects at steep topographic changes.

The amplitude variation of the sediment horizon is characterized by large-scale changes (Figure 6.36b). The best estimate of a raw background reflection amplitude can be achieved between CDPs 2300 and 2500, which is on average 180. Blank zone 1 is characterized by an asymmetric amplitude variation (Figure 6.37a). To both sides an amplitude increase of approximately 20% is observed. However, amplitudes drop by about 60% to the center of the blank zone. Blank zone 2 shows a symmetric amplitude variation with an increase of approximately 50% to both sides (Figure 6.37b). Amplitudes drop by about 60% to the center part of the zone. At blank zone 3 only the SE boundary shows a distinct amplitude increase by about 80% and the center part of this zone has amplitudes reduced by about 60%. The NW boundary has only an amplitude increase by about 10% (Figure 6.37c).

The amplitudes between blank zone 3 and 4 vary significantly but no clear blank zone can be identified in the seismic data. At blank zone 4, the amplitude variation is again asymmetric. At this blank zone, the NW side shows a strong amplitude increase by almost 100% of the background value. Amplitudes inside the zone are reduced by about 70% and stay fairly constant for about 100 m before the amplitudes increase

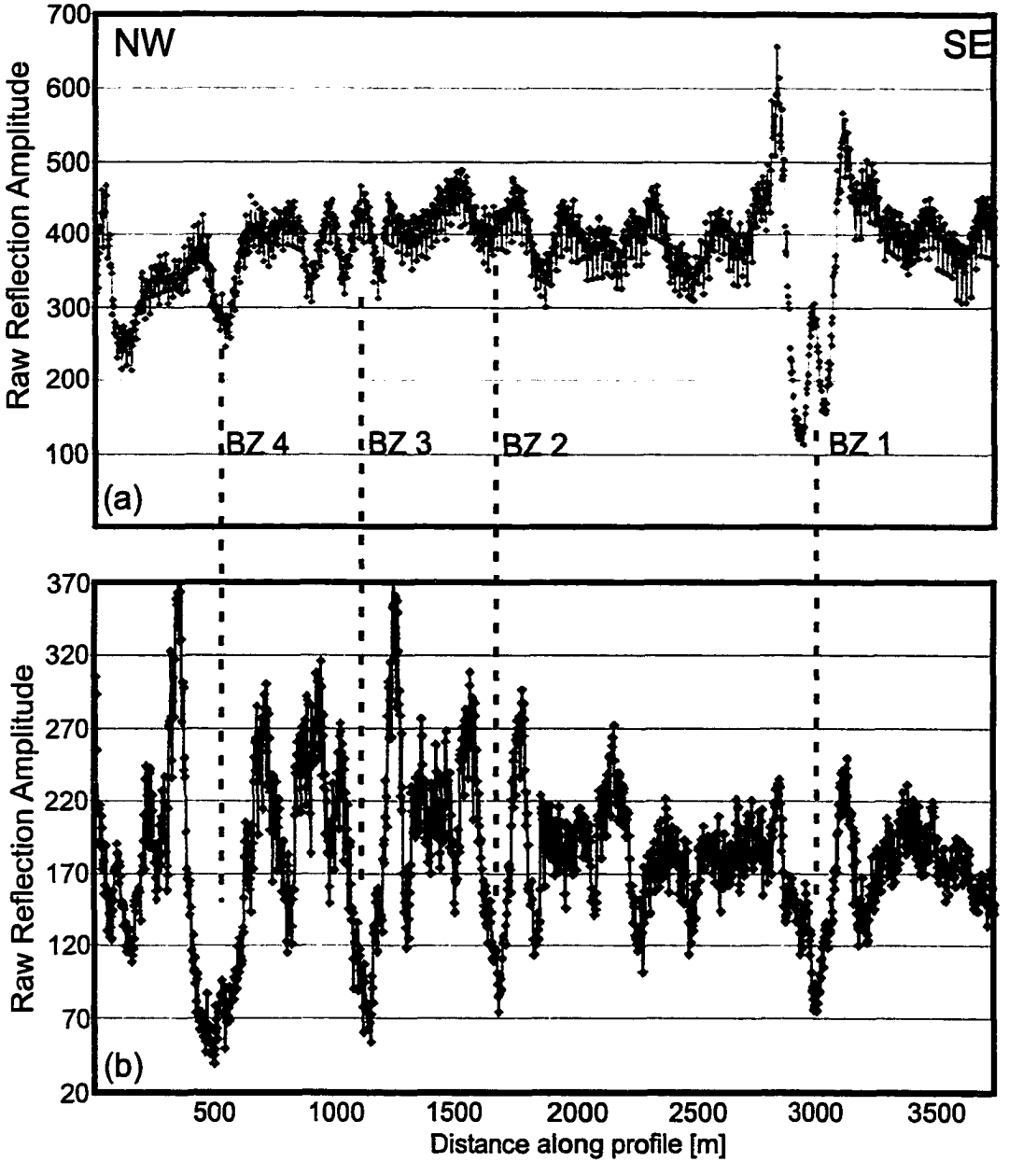

Figure 6.36 Observed amplitude variation over the vent field from 64-channel-stacked multichannel COAMS data. (a) raw seafloor amplitude, (b) raw amplitude of the AVO layer used in previous AVO analyses.

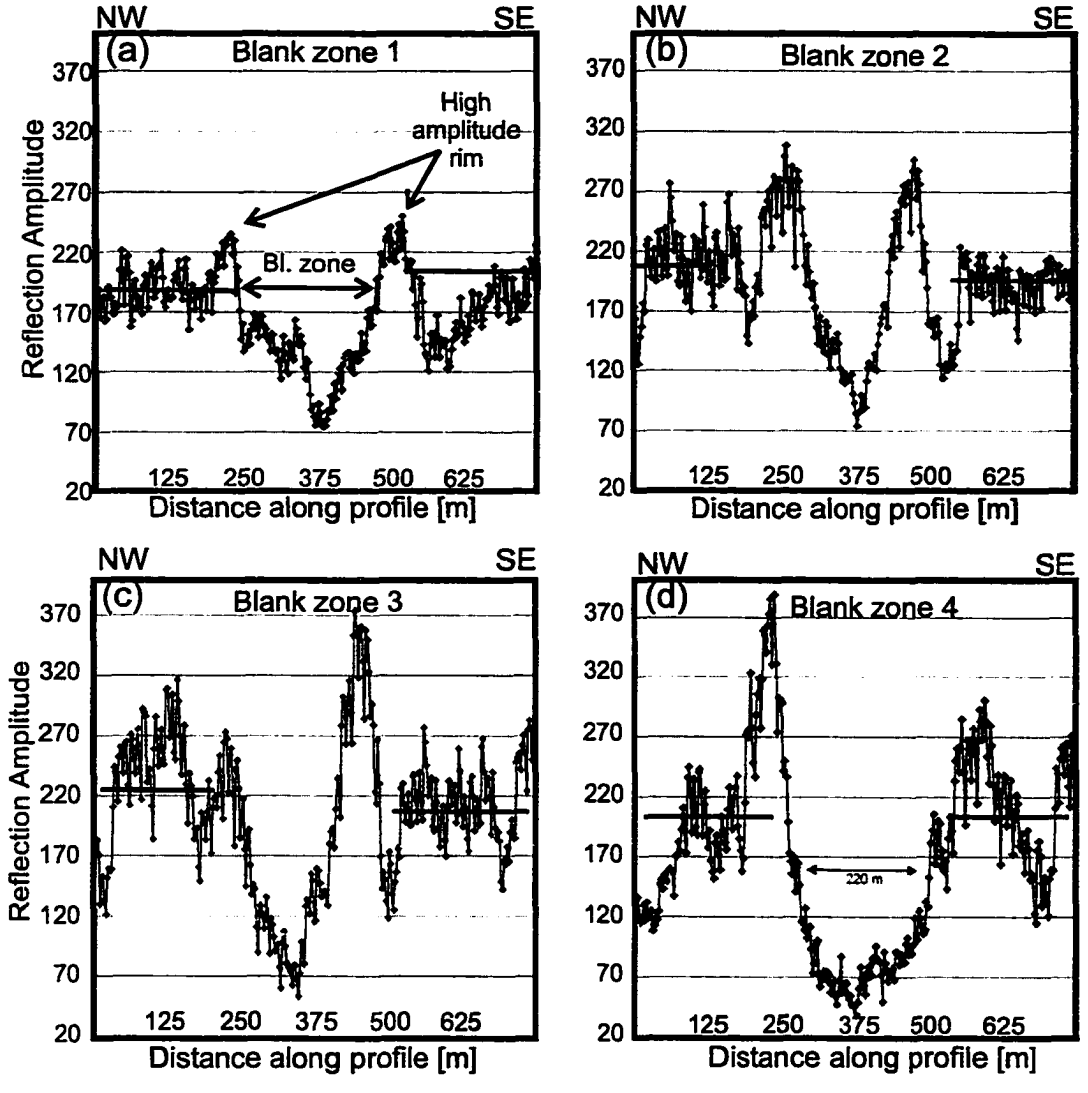

Figure 6.37 Detailed view of amplitude variations at (a) blank zone 1, (b) blank zone 2, (c) blank zone 3, (d) blank zone 4 from 64-channel-stacked multichannel COAMS data.

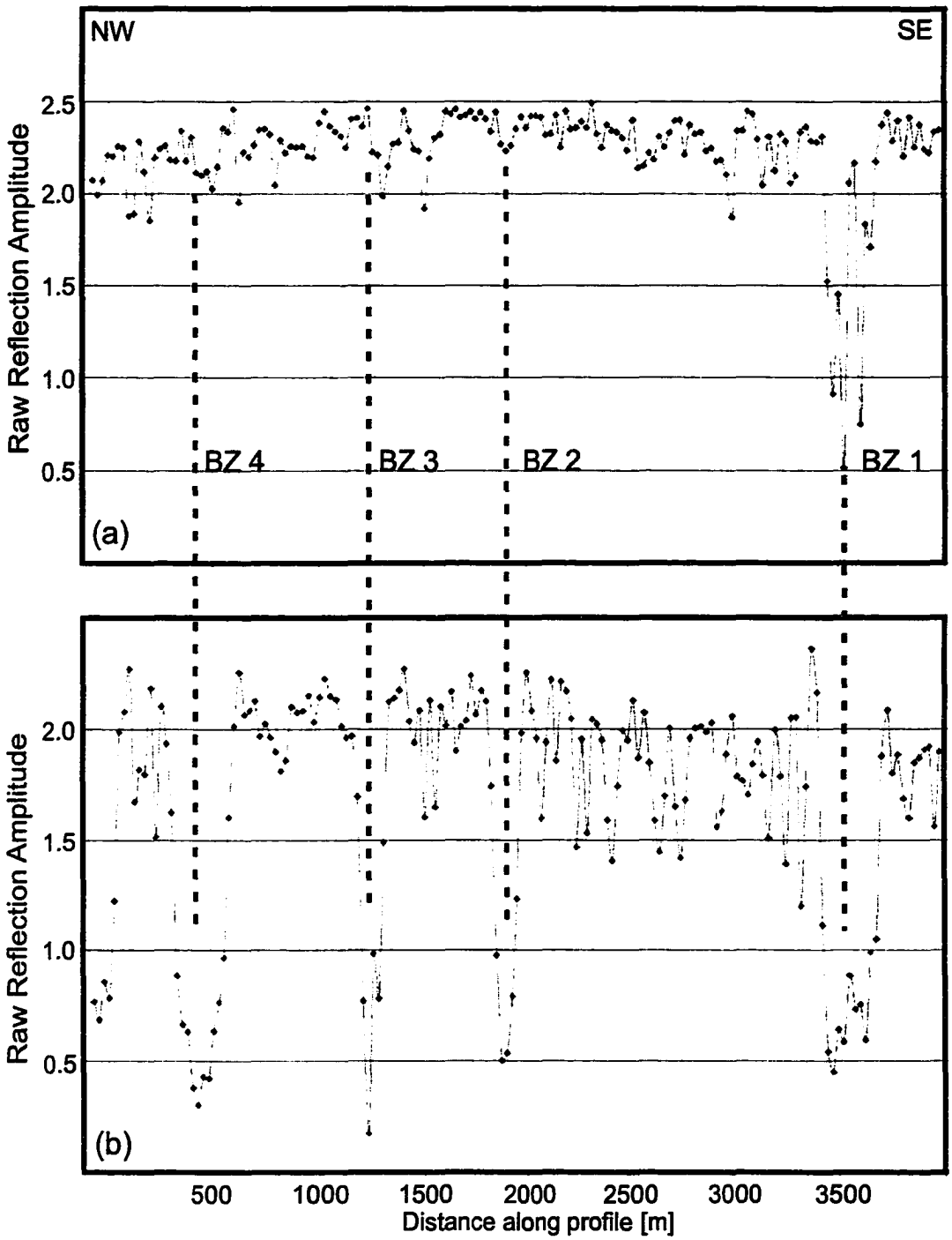

Figure 6.38 Observed amplitude variation over the vent field from single channel seismic data. (a) raw seafloor amplitude, (b) raw amplitude of AVO layer.

again towards the boundaries (Figure 6.37d). Amplitudes derived from the single channel Teledyne data do not have the same detailed structures as the COAMS data due to the approximately 10 times larger distance between individual data points (Figure 6.38).

All blank zones are surrounded by high amplitude rims; however, they sometimes consisted of one or two data points only. The high amplitude rim structures are especially visible in the 3-D visualizations. All blank zones show an amplitude drop of about 65–75% compared to an average reflection amplitude. Blank zone 1 shows an amplitude drop towards the center of the zone and an additional increase just at the center, most likely the effect of an interference of the side diffractions.

6.11.2 1-D AVO Model

Using the physical properties for the material inside and outside the blank zone generated by the 1-D elastic AVO inversion, a reasonable fit to the observed amplitude reduction in the lower frequency data was achieved (Figure 6.39).

The blank zone was modeled for a 100–400 m wide zone and seafloor-parallel sediment layers. Parameters used for this modeling are summarized in Table 6.4. The decrease in density results in the necessary drop in vertical incidence reflectivity of about 60%. The different seismic properties of the material inside versus outside the blank zone result in very weak diffractions (Figure 6.40). These diffractions partially interfere constructively with the reflectors just outside of the zone and a small increase of reflectivity at the boundary of the blank zone of about 2% is observed. However, the seismograms for these models do not show the diffractions as observed in the MC seismic data.

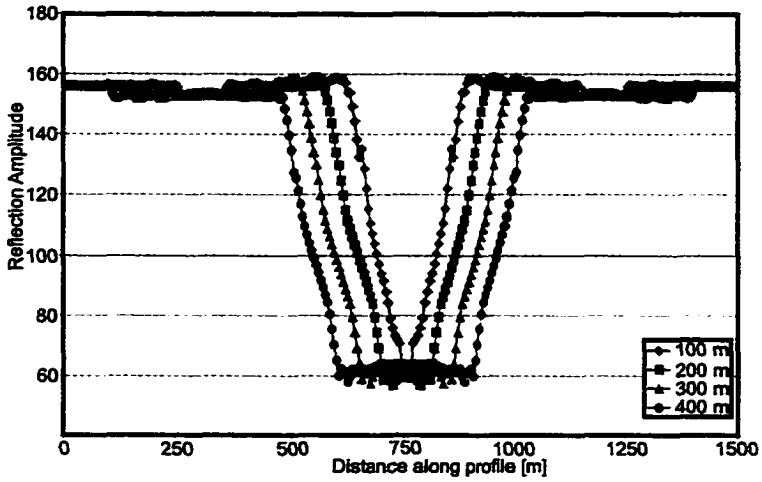

Figure 6.39 Modeling results for the 1-D AVO model (50 Hz). The blank zone was modeled as 100, 200, 300 and 400 m wide zone. Only a small amplitude increase is observed at the boundaries, but the amplitude reduction inside the zone is similar to the observations in the airgun data.

6.11.3 Surface Carbonates

During the video observations by ROPOS widespread carbonates were found around blank zones 1 and 3 (see Section 6.4.1). Seafloor carbonates could reduce acoustic energy penetration and thus contribute to the loss in seismic amplitude. A simplified representation of this carbonate cover was modeled assuming a uniform carbonate pavement of 1 m thickness and an additional surface elevation of 1m. Below this surface layer two additional layers were included in the model. The properties of this model are defined in Table 6.5. In general, the surface related transmission loss of the pavement is sufficient to reproduce the amount of seismic amplitude reduction observed in seismic data (Figure 6.41). On average the amplitude dropped by about 80% inside the blank zone. The surface elevation and the strong velocity contrast at the carbonate pavement resulted in strong diffractions, which interfere with the deeper reflections. These interferences occur at a large distance from the blank zone. At the boundary of the blank zone small amplitude diffractions occur, which do not

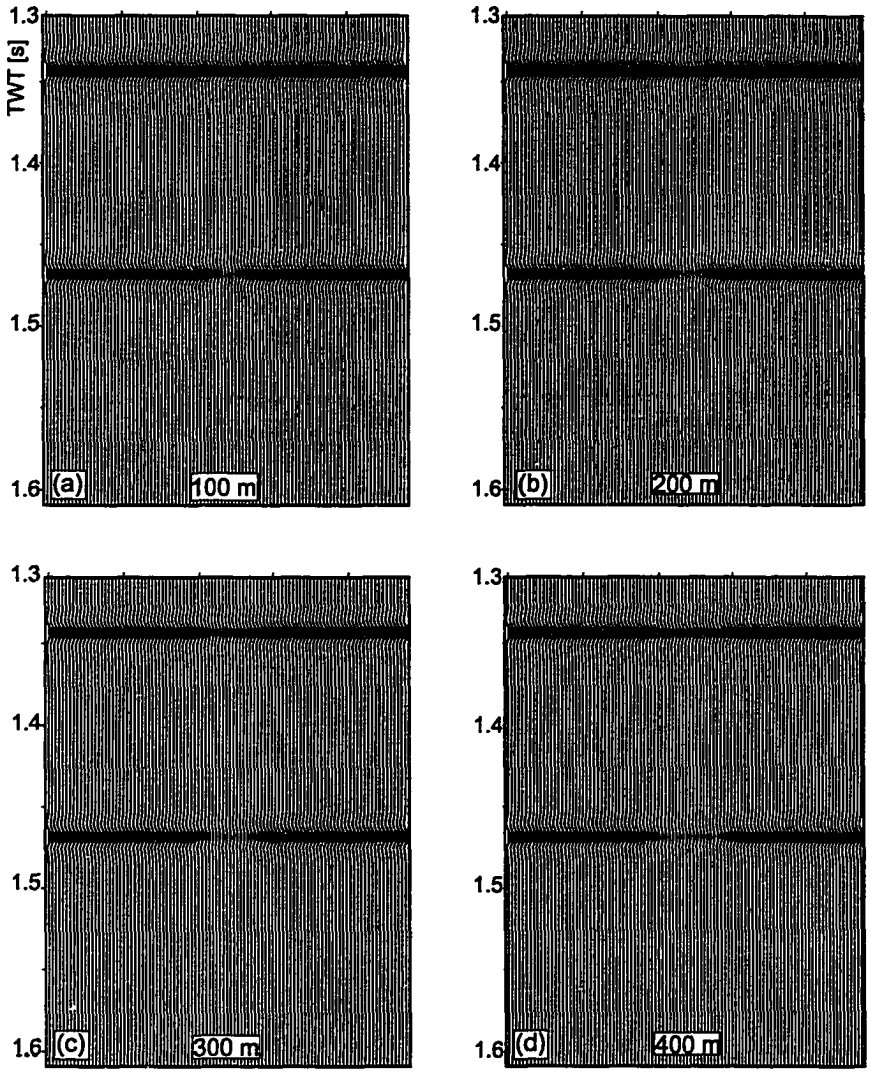

Figure 6.40 Synthetic seismograms for the 1-D AVO Model using a (a) 100 m, (b) 200 m, (c) 300 m, and (d) 400 m wide blank zone. No strong diffractions are observed. Amplitude were scaled with $time^{20}$ for plotting purposes.

significantly increase the reflection amplitude of the boundary. The layers cannot be traced through the blank zone (Figure 6.42). This environment was modeled for frequencies from 50–200 Hz. The higher the frequency, the higher the amplitude loss below the carbonate pavement. Amplitudes below the pavement using a 200 Hz signal

are reduced by almost 100%.

This modeling shows that a carbonate pavement can reduce seismic energy penetration, but at the same time, seafloor reflection coefficients are increased by a factor of 2.8. This kind of increase is not observed in the data (Figure 6.36 and 6.38). Also the 2-D VAVO study showed that the amplitude of rays that partially travel through the blank zone are reduced considerably, although they have not been in contact with any surface carbonate.

	P-wave velocity (m/s)	S-wave velocity (m/s)	Density (g/cm^3)	V_p/V_s
Carbonate	3000	900	2.28	3.3
Layer 1	1650	500	1.65	3.3
Layer 2	1750	530	1.75	3.3

Table 6.5 Modeling parameters for the Carbonate pavement. The pavement was modeled with a 1 m surface elevation.

6.11.4 Hydrate Formation

Intensified hydrate formation was suggested to explain widespread amplitude reduction observed at the Blake-Bahama Ridge at the U.S. Atlantic margin (Lee *et al.*, 1993; Lee and Dillon, 2000). It is thought that hydrate preferentially forms in higher porosity layers and the increase in seismic velocity reduces the impedance contrast with the lower porosity (originally higher velocity) layers. As a simplified representation of this model, two layers of originally 60% and 50% porosity were assumed to be filled with 10% and 5% hydrate respectively. Following the weighted equation by Lee *et al.* (1993) for hydrate-bearing sediments, seismic P- and S-wave velocities were defined (Table 6.6). Densities were estimated from ODP logs and were assumed to be unmodified by hydrate formation. This environment was modeled for a 50,

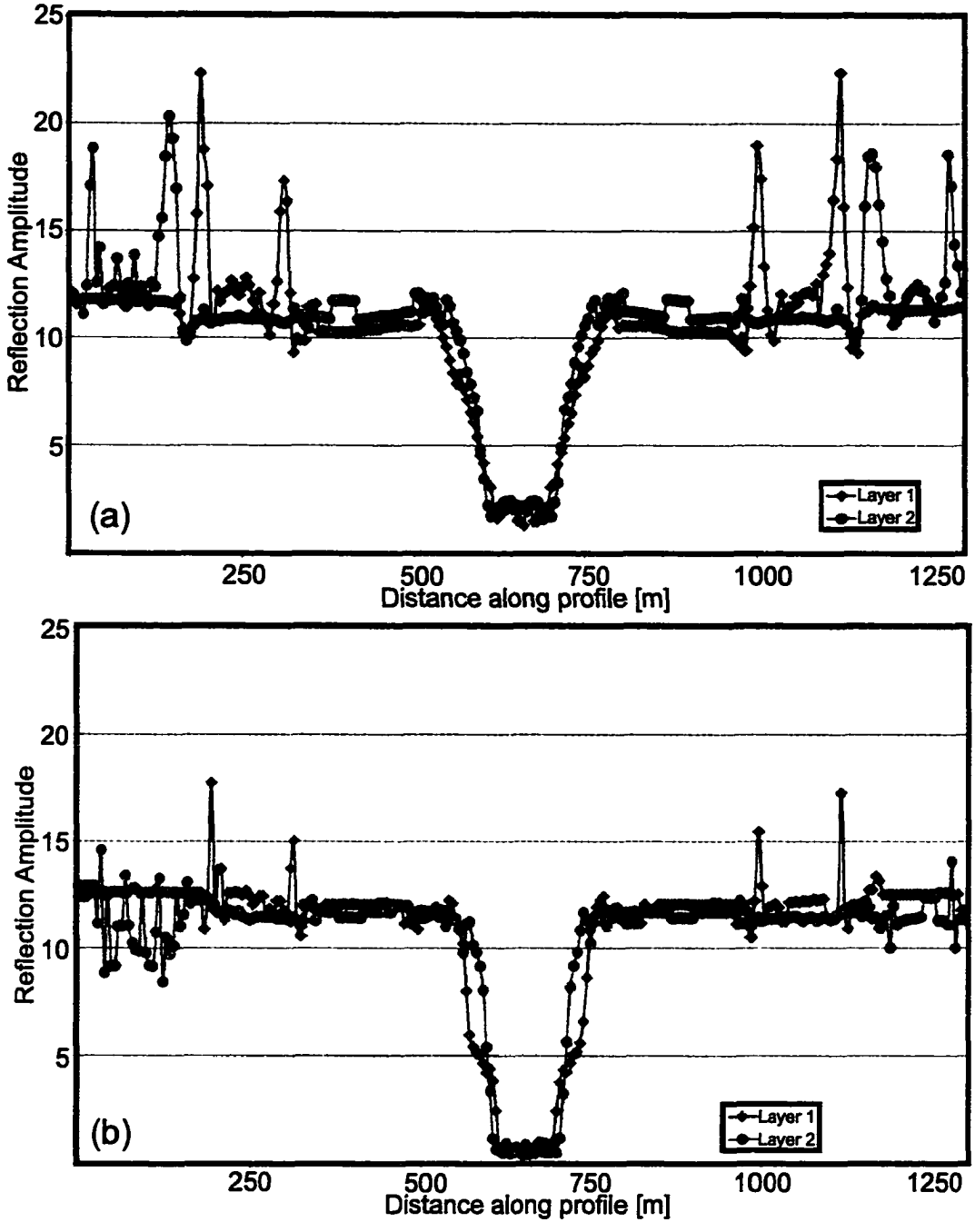

Figure 6.41 Modeling results for the carbonate pavement model using (a) 50 Hz and (b) 200 Hz seismic signals (Ricker wavelet). The amplitude loss inside the blank zone for the 200 Hz signal is slightly increased. No prominent amplitude build-up at the boundaries is observed.

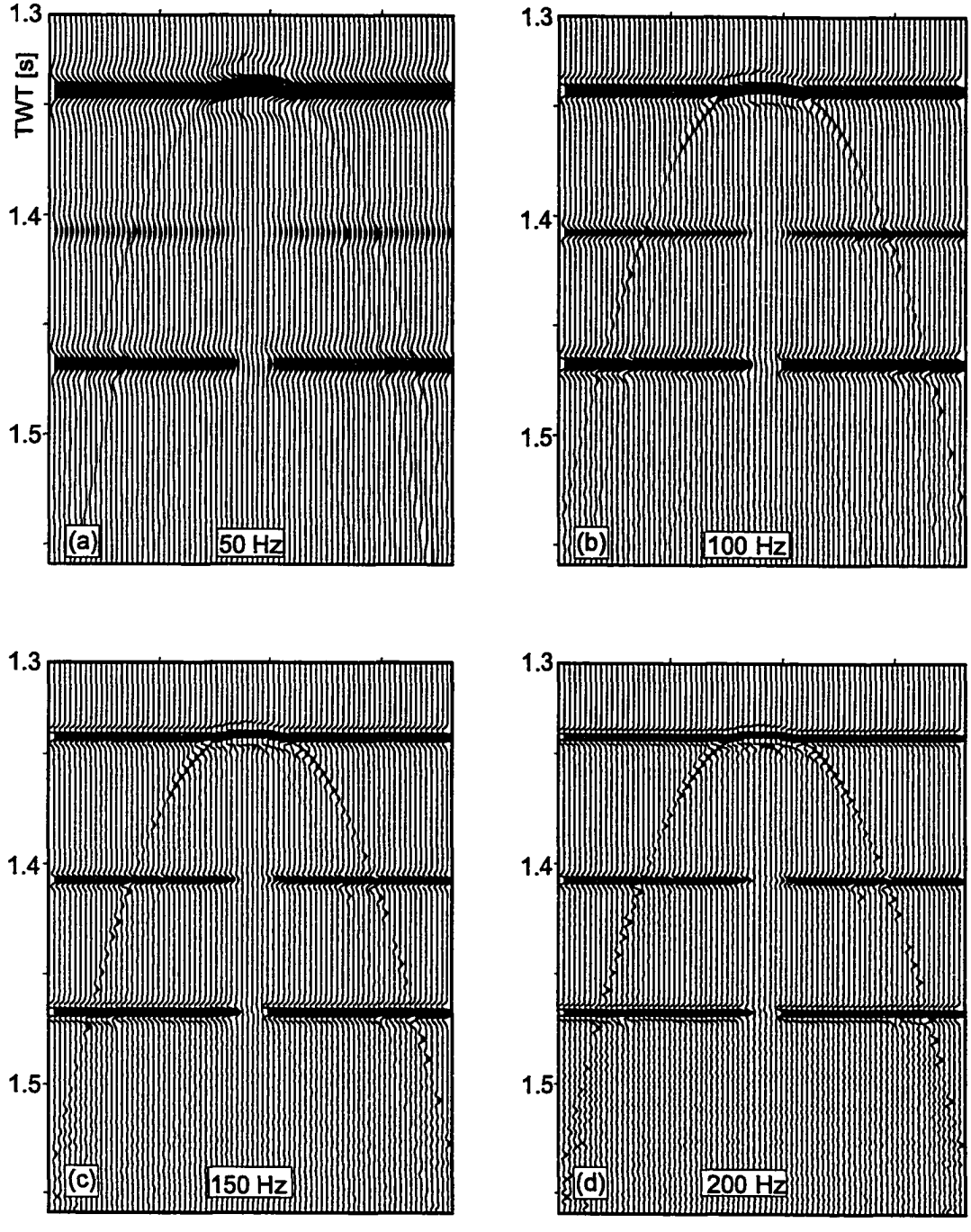

Figure 6.42 Synthetic seismograms for the carbonate pavement model using a (a) 50 Hz , 9b) 100 Hz, (c) 150 Hz, and (d) 200 Hz Ricker wavelet. Amplitude have been scaled with $time^{20}$ for plotting purposes.

100, 200 and 400 m wide blank zone. In general the reflection amplitude is increased at the boundaries by about 40% (Figure 6.43). The amplitudes inside the zone are reduced by about 75% but the center part of the blank zone is characterized by an increase of reflection amplitude. The wider the zone, the stronger the increase. For a 50 m wide zone, the amplitude variation is relatively similar to observations in the seismic data. The total blank zones always appear to be almost twice as wide as defined in the model based on the distance between the high amplitude rims. The corresponding seismograms show a pull-up of the layer inside the blank zone as result of the increased seismic velocities (Figure 6.44). For the 50 wide zone, this pull-up is reduced by the interference with the side-diffractions.

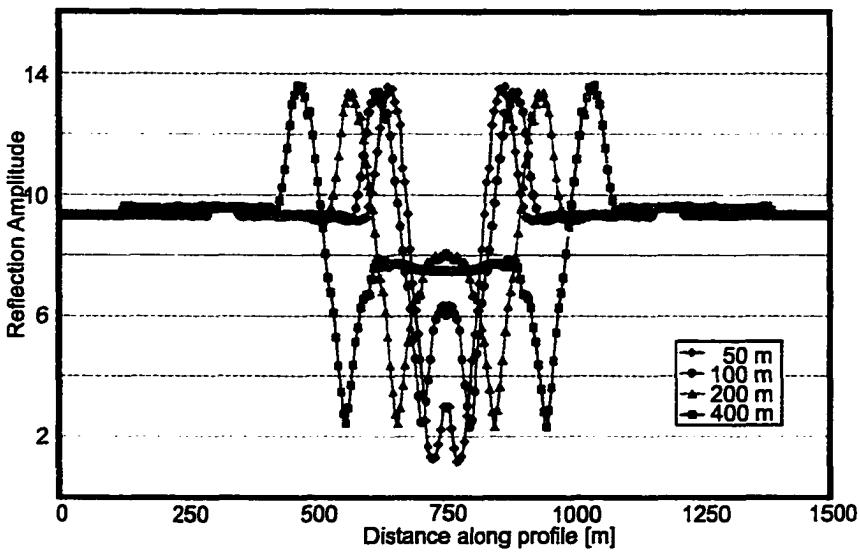

Figure 6.43 Modeling results for the hydrate-fill model for a 50, 100 and 200 wide blank zone (50 Hz). A prominent amplitude build-up at the boundaries is observed. Due to side-diffraction interference, the amplitude increases towards the center of the zone.

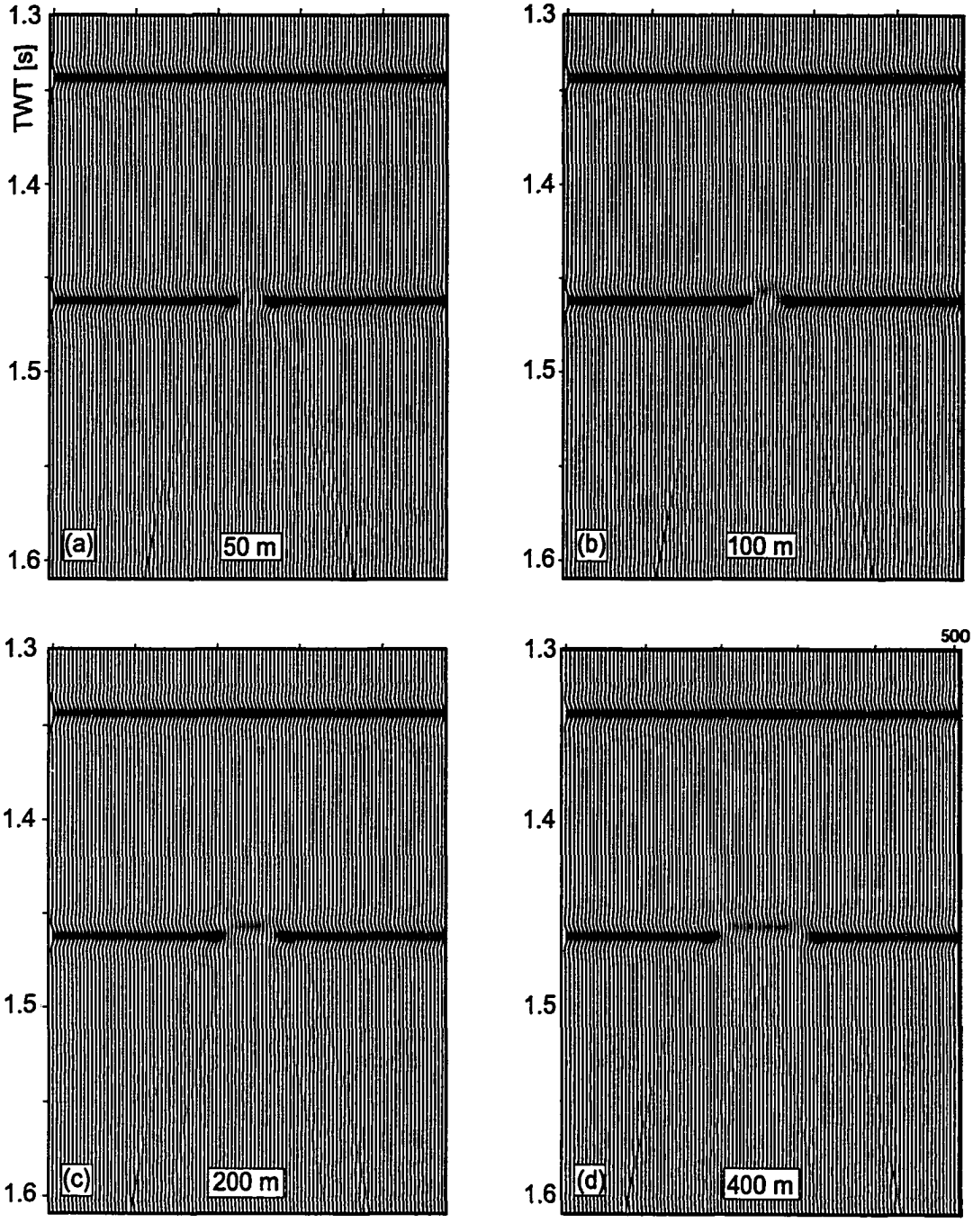

Figure 6.44 Synthetic seismograms for the hydrate fill model for (a) 50 m wide zone, (b) 100 m wide zone, (c) 200 m wide zone and (d) 400 m wide zone. Amplitude have been scaled with $time^{20}$ for plotting purposes.

	P-wave velocity (m/s)	S-wave velocity (m/s)	density (g/cm^3)
Layer 1 outside (60% por.)	1680	390	1.6
Layer 2 outside (50% por.)	1820	530	1.7
Layer 1 inside (+10% hydrate)	1760	480	1.6
Layer 2 inside (+5% hydrate)	1870	580	1.7

Table 6.6 Modeling parameters for the hydrate fill model. Values were calculated with the weighted equation by Lee *et al.* (1993).

6.11.5 Conclusions From Seismic Modeling

In general, the observed high amplitude rim structures are concluded to be the result of diffractions. These diffractions occur due to changing physical properties of the material inside the blank zone and enhance the reflection amplitude at the boundaries of the blank zone.

The reduction in seismic amplitude was modeled using the 1-D elastic AVO model, a carbonate pavement model and a hydrate formation model. The amount of amplitude reduction was reproduced by all models; however, significant amplitude build up at the boundaries of the zones was only modeled using the hydrate formation model. The reduced seismic amplitudes modeled with the 1-D AVO elastic properties is basically the result of a density decrease inside the blank zone. Both layers modeled have almost the same lower density, which results in an decrease of vertical incidence reflection coefficient. The loss in seismic amplitude in the carbonate pavement model is due to a strong transmission loss at the hard seafloor; however, no high amplitude rim is created and the associated strong seafloor reflection coefficients are generally not observed. Using the hydrate formation model, both an amplitude decrease in the center and a strong amplitude build-up at the boundaries was modeled. However, if

the zone is relatively wide, a pull-up of the layer modeled is observed and the amplitudes *recover* in the center part. In all models, the blank zone appears wider as defined in the model based on the distance between the high amplitude rims. In can be concluded that the observed high amplitude rims most likely are the result of a velocity change, probably related to intensified hydrate formation. Transmission loss at surface carbonate enhances the drop of reflection amplitude. The widths of the observed blank zones are most likely only half the distance between the high amplitude rims.

6.12 Possible Mechanisms of Blanking

Several possible mechanisms can be used to explain seismic amplitude reduction: (a) occurrence of free gas, (b) increased porosity, (c) destruction of sediment layers due to fluid flow, (d) surface related transmission loss and/or (e) formation of hydrate. These mechanisms do not incorporate viscoelastic attenuation, which might be a different possible mechanism to explain the reduced amplitudes (compare to the VAVO modeling in Section 6.10.2). However, no reliable estimate of attenuation could be found due to the loss of the seismic signals inside of the blank zones. In the following paragraphs each of the models (a) to (e) is discussed and compared to seismic and video observations, as well as the results from the seismic modeling.

6.12.1 Free Gas Model

Geochemical analyses of water samples taken during the ROPOS cruise in May 2001 above blank zone 1 indicated methane concentrations of about 8 times ocean-background values. Active gas bubbling at cold vents has also been observed at several locations on the Cascadia Margin offshore Oregon and other known cold-vent sites all around the Pacific and increased methane concentrations were also detected in water samples collected above several of these vent sites (e.g. Suess *et al.*, 1999). The presence of free gas in sediments is often associated with an almost complete loss of seismic energy through the entire sediment-column below the gas occurrence, especially at higher frequencies. The presence of free gas also reduces the P-wave velocity, which can result in an apparent push-down effect. These push-down effects have been observed e.g. in the Bering Sea basin and were referred to as *VAMPs* (Velocity-Amplitude Anomaly, Scholl and Cooper, 1978). The *VAMPs* are also often associated with high gas hydrate concentrations at shallow depths. A push-down effect can also be created by interfering side diffractions. Small apparent push-down effects are observed in the re-processed DTAGS data (Wood *et al.*, 2000)

only. However, no push-down effects were observed in the water-gun seismic data acquired by the Bremen group over the vent-field in September 2000 (Zühlsdorff, 2001, personal communications). The water-gun operates in a similar frequency range as the DTAGS system. The COAMS multichannel and occasionally the single channel seismic data showed that several layers could be traced through the blank zones, and no apparent push-down is observed in this lower frequency data. However, the amount of transmission loss and scattering at gas bubbles for seismic frequencies used in the DTAGS system where no layers could be traced through blank zones (250–650 Hz) may be larger than for the frequencies used in the airgun seismic data (20–180 Hz). Considerable coherent reflectivity is also observed in COAMS MC and SC seismic lines below the blank zones as well as partially in the re-processed DTAGS data. This would be difficult to explain if free gas is the only cause of seismic amplitude reduction.

Since the entire sediment column is well within the hydrate stability field, free gas should be transformed immediately into hydrate. Free gas can only be present in equilibrium if hydrate formation depleted all the available pore water in the sediments. If this were the case, the large concentrations of hydrate (i.e. 100% saturation) would be detectable with a large increase in P-wave velocity. A strong pull-up of sedimentary layers should be evident, if they can be traced through the zone. No such strong increase in P-wave velocity was observed, and the apparent pull up seen in some seismic data is more likely related to topography around blank zone 1 and related diffractions. This pull up was observed only for seismic lines crossing the vent in a NW-SE direction but not in the perpendicular direction.

An alternative model favoring the presence of free gas was suggested by Wood (2001, personal communication). If the blank zones were associated with active fluid venting along a fault, the upward migrating fluids are warmer than the surrounding sediments. The higher temperatures start to dissociate the hydrate and free gas is produced. The isotherms are bent upward following the geometry of the fault plane.

This mechanism would explain the widening of the blank zones with depth, but no strong heat flow anomaly was observed over the vent area.

A pronounced reduction in seismic amplitudes was observed at two sites outside the main vent field extending to depths deeper than the BSR. In those settings, the amplitude loss at below-BSR depths can be the effect of the upward migrating free gas that gets transformed into hydrate, once it reaches the hydrate stability field.

6.12.2 Porosity Increase Model

An alternative general explanation of the reduction of seismic energy and the increase of amplitude reduction with increasing frequency is an increase in porosity (Zühlsdorff *et al.*, 1999). However, an increase in porosity of about 25% as suggested by Zühlsdorff *et al.* to explain the amount of amplitude loss would significantly decrease the P-wave velocity. No such decrease was detected from the multichannel seismic velocity analysis or push-down effects. However, the accuracy of the velocity determination with the COAMS system is not high enough to allow for a unique determination.

Another problem is of how to generate these high porosities geologically or hydrologically. Deformation of the shallow sediments (mostly silty clays) does not result in brittle faulting. These sediments deform more plastically and the fault plane is rather a shear zone with increased permeabilities but reduced porosities (Arch and Maltmann, 1990). Upward migrating fluid flow however can locally increase the pore pressure and increase the porosity but a sufficient seal is needed to build up the pore pressures.

6.12.3 Fluid Migration and Mud Volcanos

Enhanced fluid migration can result in destruction of sediment layers and related lateral amplitude loss. An often-observed feature related to fluid/gas migration is the

formation of a diatrema (Brown 1990) and/or collapse structure (pockmarks). Other distinct surface expressions are mud volcanoes. At two locations a mound similar to a mud-volcano was observed. However, at this stage it is unclear if these features are related to fluid-flow related sediment expulsion. Also, several layers could be traced through the blank zone 1, which has a seafloor mound, indicating no strong sediment movement and layer destruction. There are no mound structures over blank zones 2–4, but these may have been eroded after the main fluid flow has stopped.

6.12.4 Surface Transmission Loss Model

During the video observation survey extensive carbonate occurrences were found around blank zone 1 and 3. Carbonates occurred either as complex mound structures, pavements or as disseminated chunks embedded in the sediments. The total thickness of the carbonates could not be determined from the video observations. However, the amount of carbonate found at the surface is an indicator of longterm activity and related fluid/gas expulsion of the blank zones/cold-vents.

The observed carbonate crusts result in increased transmission loss at the surface as shown in Section 6.11. The amount of amplitude loss observed can be entirely explained by the occurrence of surface carbonates. However, the synthetic modeling showed that transmission loss at the surface does not result in high amplitude build-ups at the boundaries, and corresponding increased seafloor reflection coefficients were not observed.

Carbonates have been observed only at blank zone 1 and 3 so far, and they also do not occur over the entire area below which low seismic amplitudes were observed. Surface related transmission loss at carbonates could therefore only result in local enhancement of seismic amplitude reduction.

6.12.5 Hydrate Formation Model

Widespread regional amplitude reduction on the Blake Ridge offshore the US Atlantic coast was interpreted as blanking effect (Lee *et al.*, 1993; Lee and Dillon, 2000). Blanking is thought to result from preferential hydrate formation in coarser (more porous) sediment layers. The initial lower seismic velocity of these layers is increased and the entire impedance contrast to the surrounding sediments with lower porosity is decreased. However, this mechanism was questioned by Holbrook *et al.* (1996). The amount of hydrate needed to explain the observed apparent amplitude loss is also significantly higher than the inferred hydrate concentrations on Blake Ridge.

The blank zones at the vent field offshore Vancouver Island are thought to represent faults acting as conduits for fluid/gas migration. Preliminary geochemical analyses indicated a larger methane flux at the piston core sites within the vent area compared to the reference core sites outside the vent-field. This extra supply of methane can result in an increase of hydrate formation along the fault. However, significant formation of massive hydrate throughout the entire blank zone or fault is unlikely since it would result in a strong velocity effect and pull-up as mentioned above. However, not the entire blank zone has to be filled with hydrate. Following the blanking hypothesis by Lee and Dillon (2000), hydrate preferentially forms in the more porous sediment layers. Several 5–10 cm thick sandy layers have been observed during ODP drilling (Westbrook *et al.*, 1994) and within the piston cores recovered in July/August 2000. It can be speculated that a series of those thin layers (lenses) filled with relatively more hydrate than the surrounding material results in an overall transmission loss and reduction in seismic amplitude. An example of such a hydrate layer/lens was observed as a cap-reflector at the mud mound. In a very recent study, Guerin and Goldberg (2001, unpublished) show that there is a strong positive correlation between hydrate saturation and P-wave attenuation. This would explain the

frequency dependence of amplitude reduction. The data from the Mallik 2L-38 research well also clearly showed that the hydrate was found in the porous sandy layers (Dallimore *et al.*, 1999).

There is an apparent problem, however, to explain the amplitude reduction at shallower depth with this kind of model. If the amplitude loss is the effect of larger hydrate formation inside the fault, how is it possible that free gas can reach the surface to produce the large amounts of hydrate? Free gas as the only mechanism was questioned due to the fact that the blank zones are well inside the hydrate stability field. There is also not enough organic carbon in the sediments to locally produce the high amounts of free gas. It can be speculated that gas is able to travel a fair distance into the hydrate stability field due to its buoyancy or it is carried by migrating fluids before being turned into hydrate (e.g. compare to the general hydrate formation model proposed by Minshull *et al.* (1994) discussed in Chapter 1). However, the maximum distance for gas to travel is strongly affected by the hydrogeological properties of the sediments in the fault plane, i.e. porosity and permeability. If a considerable increase of permeability inside the fault plane is assumed, free gas can reach the surface before being completely transformed to hydrate. However, once hydrate is formed in the fault plane it gets progressively plugged and porosity/permeability are reduced, inhibiting any further free gas movement. This would result in a self-sealing blank zone. The carbonate crusts seen above some of the blank zones are, however, an indicator of a long-term activity of the cold-vents, as a constant supply of methane is necessary to produce the carbonate pavements. One possible explanation is that fluid and related gas flow is highly episodic but very strong for a limited time to overcome the permeability barrier. As pointed out earlier, any fluid flow brings warmer fluids to shallower depths, and perhaps finally to the surface (Wood, 2001, personal communication). These higher temperatures can help to overcome the barrier and hydrates are locally dissociated and even more free gas is produced. But once the fluid flow has stopped, the hydrate starts to grow inside the fault plane consecutively

sealing it off again. The effect of this alternating forming and melting of hydrate perhaps also destroyed the originally layered nature of the sediments resulting in an additional lateral amplitude loss. The mechanism that triggers the episodic fluid flow may be related to the local tectonics and or earthquakes. From all available observations, there is no evidence of recent or ongoing strong fluid/gas flow and the cold vent is in a more quiet stage.

6.13 Tectonic Interpretation of the Vent Field Blank Zones

The blank zones of the vent field occur in an uplifted sediment block that is truncated by gliding planes. To both sides of the gliding planes, sediments have been dragged indicating the relative motion of the uplift. In general, uplift of the entire sediment block of the vent field destabilized the lowermost gas hydrates, because of the strong pressure effect on stability. The highest concentration of hydrate is found just above the BSR (Hyndman and Spence, 1992). If a sediment column is uplifted, the base of hydrate stability must move up through the sediment. Hydrate dissociation occurs, leaving free gas behind. However, no clear BSR reflection is generally observed below the vent-field. Beneath the center portion of the uplifted sediment block an increase in reflection amplitude is observed below the depth where the BSR is expected suggesting the presence of free gas. This gas cannot easily migrate upward through the very low permeability sediments containing gas hydrate and may follow faults acting as conduits.

The tectonic origin of the blank zones is not directly related to the two major thrust faults forming the topographic highs. Both fault systems do not follow the similar geographic trend and the blank zone faults are at high angle to the thrust faults. The eastern ridge was interpreted to be formed by a westward dipping thrust fault based on the observed asymmetry in sediment deformation (Westbrook *et al.*, 1994).

The western ridge appears to be formed at a similar, but eastward-dipping thrust fault. The western margin of the sediment-filled trough shows similar deformation features as seen in the eastern slope basin. Both ridges follow a southeast-northwest trend but the uplift is asymmetric. The eastern ridge appears to be uplifted by a larger amount than the western ridge.

In addition to these two major thrust faults and ridges, a third ridge was identified (Chapter 5) that perhaps is directly related to the formation of the blank zones. This third ridge outcrops at about 1000 m to the NW of the vent field and the top of the fault outcrop follows an east-west trend. From the location of the outcrop of the ridge, the top of the accreted sediments dips towards the south where it is progressively covered by slope sediments. Within these slope sediments the blank zones occur and they have an east-west trend similar to the ridge outcrop. It can be speculated that the blank zones, i.e. the faults they represent, are related to the fault that is associated with the uplift of the third ridge, although the blank zones occur in an uplifted block that apparently is decoupled from the motion along the ridge-fault. One possibility is that the blank zone faults were related in an earlier stage to the fault system in the northern part, but became progressively decoupled while the sediment block was uplifted as result of motion along the main westward dipping thrust fault. Another possibility is that the blank zone faults are still related to the northern fault system, and motion is active along both fault systems, the northern as well as the main westward dipping thrust system.

The shape of the blank zones is asymmetric, mainly with a sharp truncated NE side and a more diffuse SW boundary. This can be explained by the orientation of the underlying fault as illustrated in Figure 6.45. Amplitude reduction in this model is the effect of accumulated transmission loss at local hydrate lenses that form in the fault plane and may expand laterally into the layered sediments. If carbonates are also formed at the fault outcrop, the sharp truncation of the blank zone at the NE side is enhanced. Note that this model does not exclude the possibility that both

sides of the blank zones are diffuse.

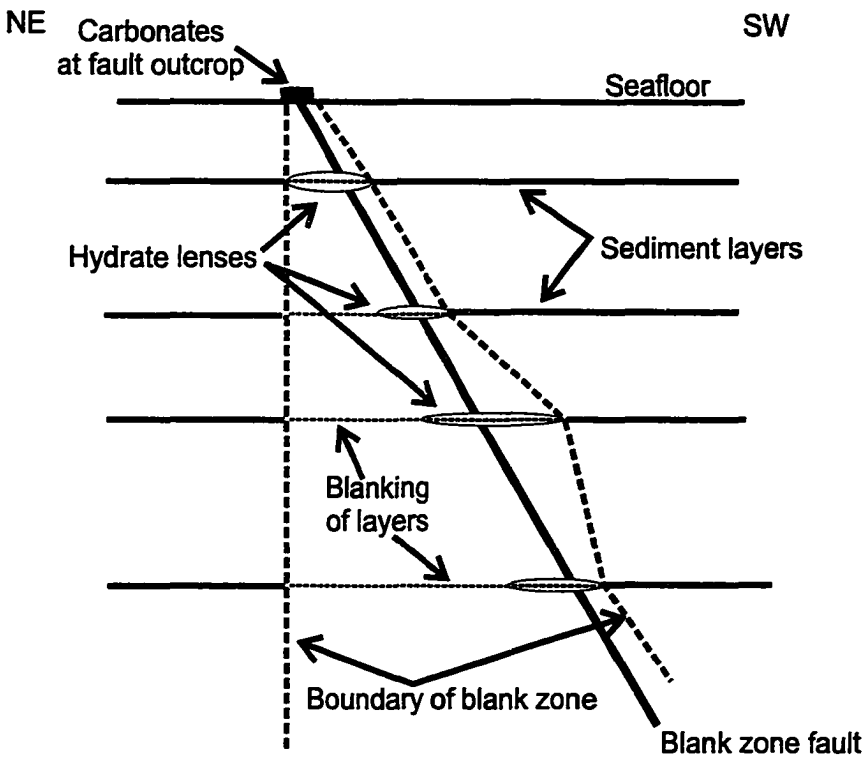

Figure 6.45 Simplified model of the blank zones 2–4 of the vent field. The dip of the fault allows for a more diffuse boundary at the side of the hanging wall of the blank zone fault. If carbonates are formed at the fault outcrop, the sharp truncation of the boundary is enhanced.

From all observations, blank zone 1 seems to be unrelated to any of the fault systems seen. This zone also is marked by a ring of increased seismic amplitude with a diameter of about 400 m, which can be traced to a depth of about 100 ms TWT bsf. The center of blank zone 1 coincides with the sites where massive hydrate was found. The hydrate forms a cap over the center, below which maximum amplitude reduction was observed. The unprocessed slice of instantaneous amplitude showed that the cap is not a uniform surface but has several high amplitude patches, which are interpreted

as local hydrate lenses. Diffraction halos develop around these lenses, which interfere with the regular surrounding sediment layers creating the high amplitude ring structure.

This blank zone is located between the main eastern ridge and a smaller buried ridge of accreted material. The smaller ridge has a different orientation than the eastern ridge, and they deviate from each other towards the north. Blank zone 1 occurs almost over the deepest part of the basin that developed between the two ridges and occurs at the location where both ridges are the closest to each other. Sediments within these two ridges are internally deformed, most likely resulting in squeezing out the pore fluids. These fluids have to migrate upward and would follow paths of least resistance. No prominent fault was identified and from the seismic sections seen, low amplitudes occur over a wide area indicating a relative diffuse upward fluid migration along a series of smaller faults and fractures. The surface expression, probably related to the most focussed fluid expulsion, is about 400 m in diameter, but low seismic amplitudes were observed in deeper sediments over an area twice as large as this (e.g. Figures 6.4 and 6.15). The video observation showed that the area of the surface expression is extremely heterogeneous. Carbonates were found at small ridges, typically several meters high, and carbonate mostly formed along lineaments/fractures, that were traced for several 10's of meters along the seafloor. Only at one small location, living colonies of typical cold-vent related biota were found, but at several places dead clam shells occurred typically washed into smaller depressions indicating earlier stages of activity. A typical observation at cold vents all around the Pacific margin is that venting switches between several places over time (Suess *et al.*, 1998; personal communication with Gerd Bohrmann, GEOMAR). Typically colonies of clams and tube worms form over the most active vent sites and die out very quickly once the methane supply is shut off. Clams, such as the type observed at blank zone 1, however, have the ability to move and follow the most active venting. There was no heat flow anomaly detected over the vent field and over

blank zone 1 in particular. The inferred methane flux from geochemical analyses is relatively low corresponding to a fluid flux of maximum 1 mm/yr. However, this value may be an average over several years or decades and fluid flow may be highly episodic. Venting can be related to local earthquakes triggering the fluid flow.

Chapter 7

Modeling of Elastic Properties of Hydrate-bearing Sediments and Amplitude-Versus-Offset (AVO) Modeling

7.1 Introduction

In this chapter a theory for calculating elastic properties of hydrate-bearing sediments is presented and applied to the sedimentological environment around the ODP Site 889/890. The theory is then used to carry out a comprehensive AVO analysis of the BSR. The AVO response is interpreted in terms of hydrate and free gas concentrations above and below the BSR. The theoretical results are qualitatively compared to multichannel seismic data from the 1989 and COAMS-99 surveys.

It has been speculated for a long time what is the effect of hydrate formation on the host sediment's shear properties. There are two possible end-member models: (a) hydrate forms in the pore space without sediment grain interaction (no S-wave velocity increase), and (b) hydrate cements the sediment grains (strong S-wave velocity increase).

Several theoretical studies predict the change in the elastic properties of hydrate-bearing sediments. Most previous approaches were based on the time-average equation of Wyllie *et al.* (1958), which predicts seismic velocities in a rigid, consolidated rock with only little fluid. This theory was related to hydrate studies by constructing two-phase and three-phase equations (e.g. Timur, 1968 or Wood *et al.*, 1994). However, these models are of limited use if e.g. the sediment is underconsolidated or if the rock contains considerable amounts of clay or organic material. Several modifications or correction factors were introduced to the time-average equation to overcome these problems (e.g. Castagna *et al.* 1985, or Tosaya and Nur, 1982). Another relevant

equation was developed by Wood (1941), which is applicable for high-porosity sediments with particles in suspension. There are only limited experimental observations of the influence of hydrate formation on the elastic wave velocities and it is difficult to know which equations best approximates the physical conditions of the hydrate occurrences. The Wood (1941) equation may be applicable, if the hydrate forms suspended in the pore space. Alternatively, the Wyllie *et al.* (1958) equation may be applicable if the hydrate cements the grain contacts. A comprehensive comparison of most of the known equations that relate hydrate concentrations to elastic wave velocities can be found in Lee *et al.* (1996).

An alternative approach to the time-average equations is the use of rock-physics models. Curtis (1992) e.g. used Biot's poroelastic theory (Stoll, 1977). This approach is difficult due to the lack of laboratory measurements of the modeling parameters in the Biot theory. In particular sediment permeability and viscosity but also empirical relations for structure factor and pore-size parameters are difficult to obtain. The formation of hydrate is at least qualitatively comparable to the formation of ice in permafrost. This analogy was used to formulate physical models for hydrate formation (e.g. Carcione and Tinivella, 2000). Their Biot-type three-phase modeling can incorporate a cementation effect, but it is valid only for granular sand-type sediments. It is also dependent on empirical estimates of pore-shape and average pore-radius, which in general are difficult to obtain especially in clay-rich marine sediments.

An elastic rock physics characterization for sediments with gas hydrates was developed by Dvorkin and Nur (1993) and used to qualitatively describe AVO effects of the BSR at the Blake Ridge (Ecker *et al.*, 1998). In this model gas hydrates can form either as inter-granular cement that stiffens the overall sediment matrix and increases S-wave velocity, or form as part of the pore fluid and not effect the shear properties of the sediment. However, this cementation model is only valid for low-porosity sediments having a sand-type granular structure. Therefore this model may not give a good representation for clay-rich marine sediments found at the Blake Ridge or at

the Cascadia margin. A model valid for clay-rich sediments was formulated thereafter (Helgerud, 2000). Hydrate is modeled either as part of the pore fluid or as part of the dry solid rock component without adding stiffness to the overall frame. Since this model has no cementation effect the shear wave velocity is not strongly affected by hydrate formation.

The model for typical marine sediments by Helgerud (2000) is used in the following modeling study for sediments around ODP Site 889/890. The cementation model by Dvorkin and Nur (1993) is used to explain qualitatively the effect of cementation and is used to predict AVO effects of hydrate-bearing sediments that have been stiffened by hydrate formation. The equations to calculate elastic properties of sediments containing free gas or hydrate (P-wave and S-wave velocity and density) for the two hydrate formation models by Helgerud (2000) and the cementation model is given in the Appendix E.

This modeling study provides a background shear wave velocity model for no-hydrate bearing sediments that can be compared to S-wave velocities in sediments that contain hydrates. There are no direct measurements of S-wave velocity in the area around ODP Site 889/890. S-wave velocities may be obtained from the Ocean Bottom Seismometer (OBS) experiment carried out as part of the COAMS-99 survey. Analyses of the OBS data is part of an ongoing research project.

The S-wave velocities predicted by the modeling are also used in an AVO study. AVO studies have been carried out by Hyndman and Spence (1992) and by Yuan *et al.* (1996) using the multichannel data from lines 89-08 and 89-10. This modeling is revisited and re-evaluated based on the results from the modeling of elastic properties. The AVO effect of the bottom-simulating reflector (BSR) is modeled using Shuey's two-term *Intercept-Gradient* (IG) approximation. In this approach a much simpler characterization of an AVO response is achieved that is applicable to a range in angle of incidence of less than 40°. Simple *rules-of-thumb* are developed to classify the AVO response of the BSR.

The last section in this chapter deals with the frequency dependent nature of the BSR. The earlier AVO modeling approaches are valid for low frequencies only, i.e. the BSR can be characterized as a simple interface. However, the BSR is more likely a thin layer of finite thickness with a strong P-wave velocity gradient. The frequency dependent effect of this gradient layer on the BSR AVO-response is modeled for the best-fit model obtained by Chapman *et al.* (2001).

7.2 Marine Sediments and Gas Hydrate Formation

7.2.1 Elastic Properties of Sediments at ODP Site 889/890

The modeling approach to characterize marine sediments used in this chapter follows the rock-physics model of Dvorkin *et al.* (1999a). This model relates the elastic properties of the sediments to porosity, mineralogy and effective pressure (depth). Input parameters involve the bulk and shear moduli of the individual mineral grain components, their volumetric fraction within the whole rock, and the porosity and depth at which the elastic properties are calculated.

The detailed mineralogy of sediments around ODP Site889/890 was taken from the ODP petrophysical smear slide analyses (Westbrook *et al.*, 1994). The sediments in the uppermost 100–150 m mainly contain pure clay or silty clay with intermittent thin sand layers. Deeper sediments are more fine grained but there are no significant differences in the mineralogy. A mixture of 85% clay and 15% quartz was used to represent this kind of sediment. This mineralogy is assumed to be homogeneously distributed over the entire depth modeled. No layering to represent the observed sand layers was implemented. Porosities were obtained from the density following standard ODP procedures as outlined in the explanatory notes of the ODP volume (Westbrook *et al.*, 1994). To simplify the modeling, the porosity data were smoothed to a linear decrease with depth from a porosity of 60% at 20 m bsf to 46.5% at 300

m bsf. These parameters were used first to calculate a no-hydrate/no-gas reference P-wave and S-wave velocity. Bulk and shear moduli and dry densities for the different minerals used as well as elastic properties of gas hydrate and free methane gas are summarized in Table 7.1.

Sediment Constituent	Bulk Modulus (GPa)	Shear Modulus (GPa)	Density (g/cm^3)
Clay	20.9	6.85	2.58
Quartz	36.6	45.0	2.65
Methane Hydrate	8.7	3.5	0.92
Methane gas	0.1245	0	0.25
Pore water	2.4	0	1.034

Table 7.1 Elastic properties of sediment solid phase components and pore fluid (from Helgerud, 2000).

7.2.2 Reference-Profile for P- and S-wave velocities

The calculated reference P-wave velocities are in very good agreement with the reference velocity profile estimated by Yuan *et al.* (1996). P-wave velocity at a depth of about 250 m bsf was about 1640 m/s in the Yuan-reference model. The rock-physics modeling with a smoothed porosity function yields a P-wave velocity of about 1650 m/s.

Calculated reference S-wave velocities increase with depth starting from a velocity of about 130 m/s just at the seafloor and reaching about 390 m/s at a depth of 250 m bsf. The velocity increase is not linear and follows a typical 'power-law' relation. These velocity are in good agreement with *standard* S-wave velocity depth profiles

(Hamilton, 1980).

7.2.3 Hydrate Formation in the Pore Space

The dry rock elastic properties are not changed if hydrate formation occurs only in the pore space. Thus, adding hydrate to the pore space increases the bulk modulus and decreases the density of the pore filling. The small change in bulk density increases the S-wave velocity by about 5 m/s over the entire depth modeled so this effect can be neglected.

The P-wave velocity is generally increased by the addition of hydrate. Figure 7.1 shows the effect of adding hydrate to the pore space. The amount added to the pore volume is a percentage of the total porosity, not of the whole rock. For comparison the modeled P-wave velocities, the ODP sonic log from Site 889A and the VSP results are shown. The effect of small amounts of free gas in the pore volume was also modeled. In general, the increase in P-wave velocity is relatively small, and the maximum observed P-wave velocities from the ODP sonic log would require a hydrate concentration of around 30–40%. The low VSP velocities of less than 1500 m/s below the BSR depth suggest the presence of free gas. Modeling 1–2% of free gas in the pore volume matches the observation of the VSP data. However, the sonic log did not sample the low velocities due to a drilling artifact. Modeling hydrate as a pure component of the pore volume slightly overestimates the hydrate concentration needed to explain the observations compared to results from previous seismic calculations (Yuan *et al.*, 1996). However, it seems in better agreement with results obtained from resistivity data (Hyndman *et al.*, 1999).

7.2.4 Hydrate Formation as Part of the Sediment Frame

In a second modeling approach, the hydrate formation is taken to occur in the sediment frame, i.e. the additional hydrate is treated as an independent part of the

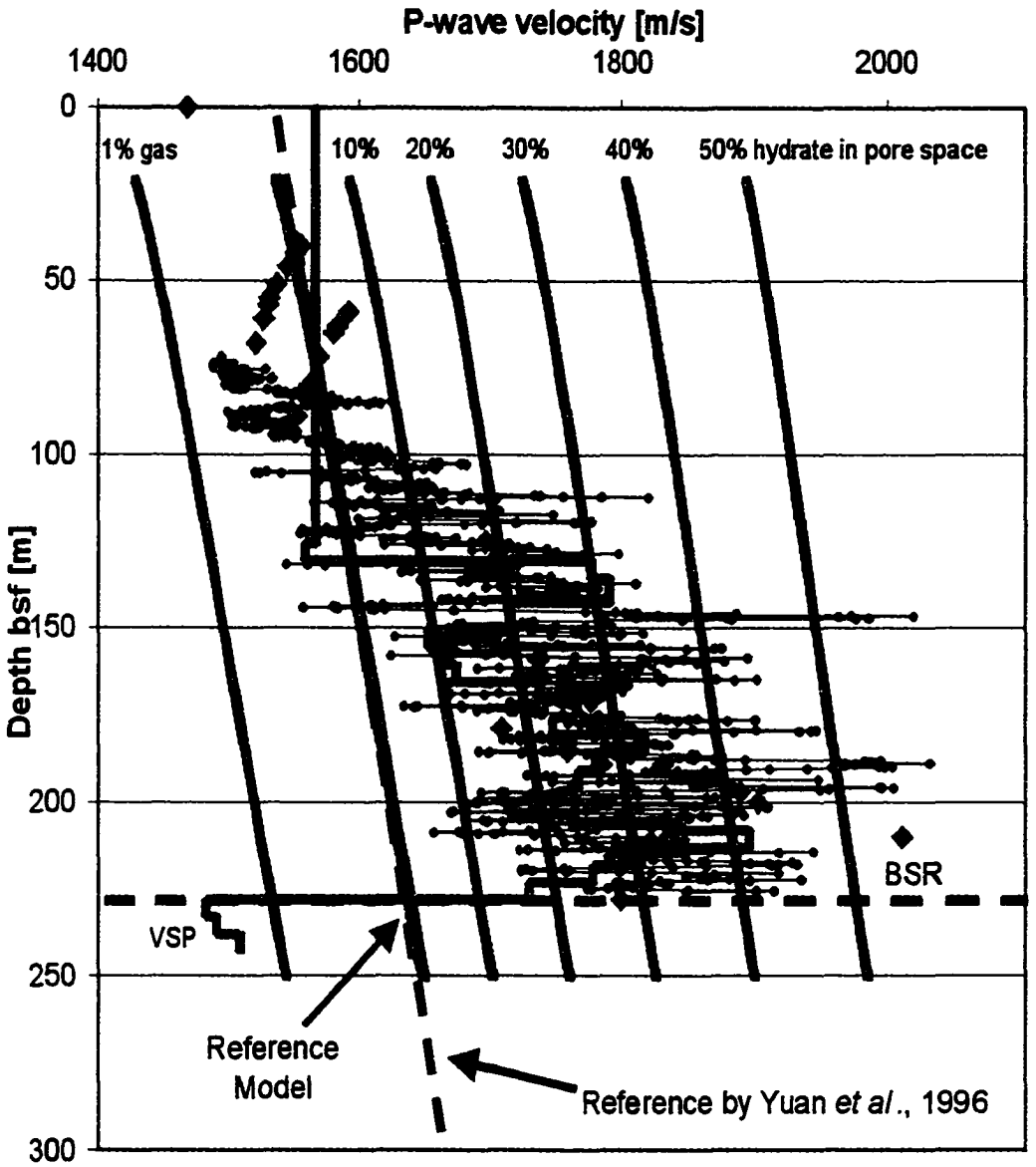

Figure 7.1 Modeling results of P-wave velocity for the 'hydrate in pore-space' model. For comparison, ODP sonic log, VSP data from MacKay *et al.*, (1994) and interval velocities (triangles) and reference model by Yuan *et al.* (1996) are shown.

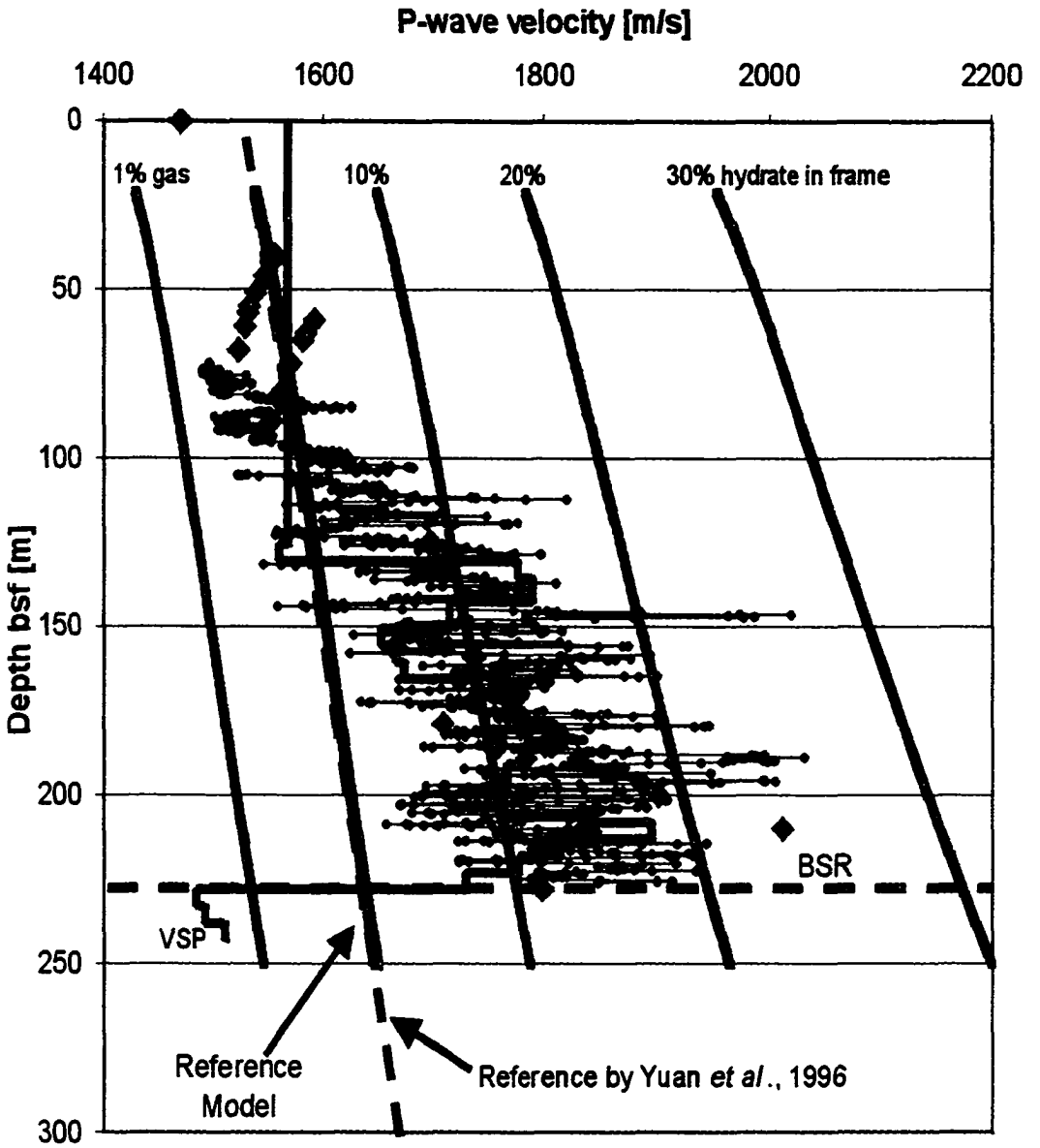

Figure 7.2 Modeling results of P-wave velocity for the 'hydrate in frame' model. For comparison, ODP sonic log, VSP data and interval velocities (triangles) and reference model by Yuan *et al.* (1996) are shown.

mineral assemblage. Figure 7.2 compares the resulting P-wave velocities for different hydrate concentrations with the ODP sonic and the VSP data. Also the results for 1–2% of free gas are added. This model explains the increased P-wave velocities as result of 10–20% hydrate, which is much less than what was predicted using the previous seismic analyses. Hydrate as part of the sediment frame also changes the dry shear modulus and therefore the S-wave velocity. Although no direct cementation is build into the model, the S-wave velocity is increased by about 25% to 465 m/s at a subbottom depth of 200 m and a hydrate concentration of about 30% (Figure 7.3). Thus any additional cementation that may take place increases the S-wave velocity even more.

7.2.5 Hydrate Formation as Grain Cement

The cementation model by Dvorkin and Nur (1993) is only valid for sediments with a granular structure such as sand. It is therefore not applicable to a marine environment with clay-rich high porosity sediments. The cementation model is used in this study to model general trends in the sediment elastic properties. These general trends are then used to predict the effect of cementation in a marine environment. In the original cementation model, porosities can vary between 30% and 40% and cement concentration should not exceed a few percent (Dvorkin and Nur, 1993). Recently this model was extended to a larger range of cementation concentrations (Dvorkin *et al.*, 1999a). However, this extension is not used in this modeling study. A simplified model with a layer composed of pure quartz grains having a original porosity of 40% was used to calculate P- and S-wave velocities for hydrate concentrations of up to 20% of the pore space. Small amounts of hydrate cement (less than 4%) sharply increased the velocities. However, with increasing cement concentrations, the velocity increase becomes more linear (Figure 7.4 and 7.5).

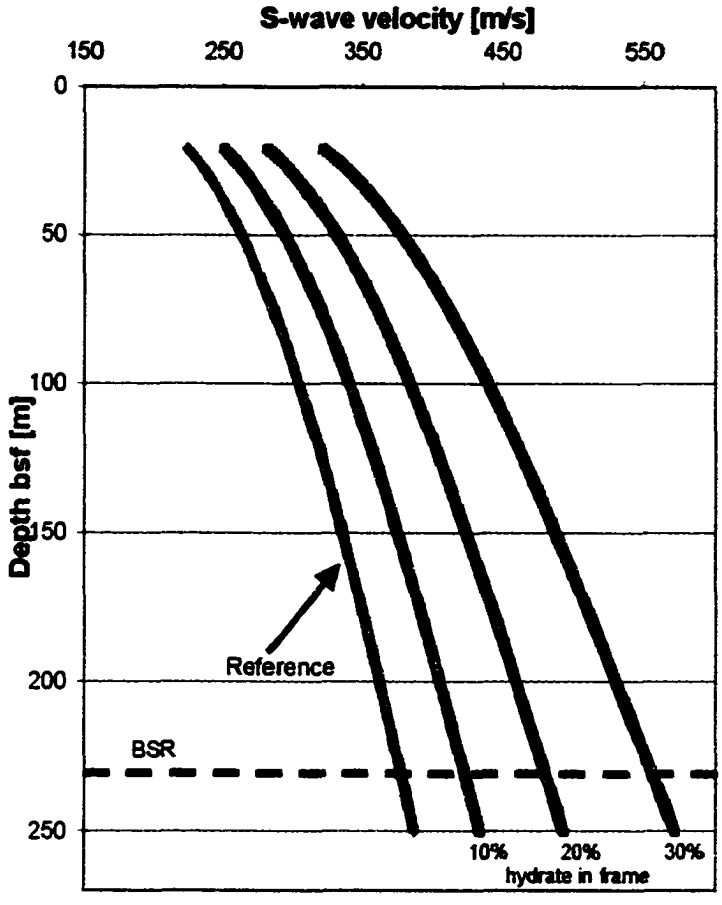

Figure 7.3 Modeling results of S-wave velocity for the 'hydrate in frame' model. Although no cementation is build into the model, the S-wave velocity is increased relatively to the reference velocity profile.

Cementation for a marine environment can be simplified by using the *hydrate-in-frame* model and additionally increasing the S-wave velocity proportional to the hydrate concentration. The rate of change in the S-wave velocity by cementation is of course not known, but general trends in the AVO behaviour of hydrate-bearing sediments and at the BSR can be observed that may help to further constrain the range of physical properties involved.

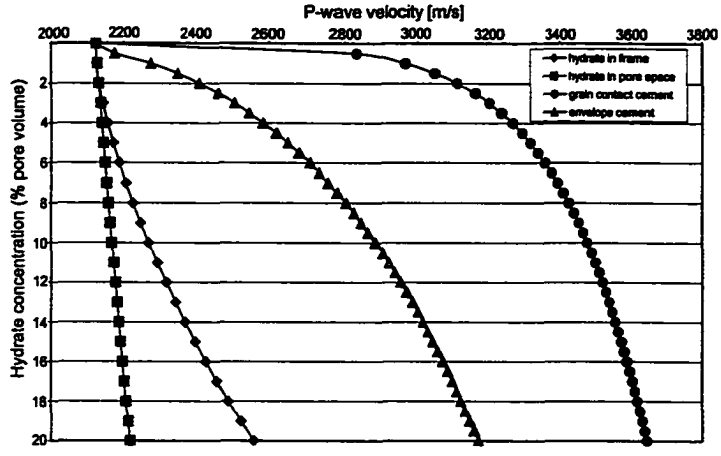

Figure 7.4 Modeling results of P-wave velocity for a pure quartz sand of 40 % porosity using the cementation model. Hydrate concentrations are 0–20% of the pore space.

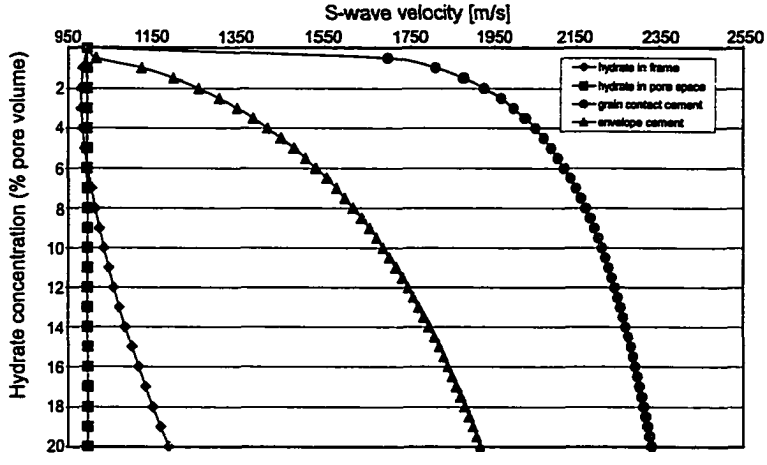

Figure 7.5 Modeling results of S-wave velocity for a pure quartz sand of 40 % porosity using the cementation model. Hydrate concentrations are 0–20% of the pore space.

7.3 General AVO and Crossplotting Theory

Amplitude-Versus-Offset (AVO) methods are based on measuring the reflection coefficient of acoustic or seismic waves at a particular interface as a function of the angle of incidence (referred to as the AVO function). The theory of AVO is based on the Zoeppritz equations (Zoeppritz, 1919) by which the AVO function can be calculated for given physical properties (i.e. P-wave and S-wave velocity and density). The AVO technique is an often-used method in hydrocarbon exploration to identify possible gas or oil occurrences. Based on a general knowledge about the background geology, oil/gas-charged reservoirs exhibit an anomalous AVO behaviour, that can be classified using a crossplotting technique (Castagna and Swan, 1997). The crossplotting technique is based on the simplified two-term *Intercept-Gradient* (IG) approximation of the general Zoeppritz equations (Shuey, 1985). In the following, the intercept-gradient crossplotting technique is adapted for marine sediments containing gas hydrate. The hydrate-bearing sediments take over the role of the background material, whereas the bottom-simulating reflector (BSR) forms the anomaly. In analogy to the *Rutherford-Williams* (1989) classification, the BSR is a class-III bright spot, with generally negative intercepts and gradients.

7.3.1 Shuey-Approximation and Intercept-Gradient Crossplotting

Zoeppritz (1919) formulated a set of equations that describe the amplitudes of reflected and transmitted elastic waves at a planar interface between two infinite elastic halfspaces. The influence of the individual physical properties of the two layers above and below the interface on the reflection coefficient is rather complex using the full Zoeppritz equations. Since most of the standard seismic reflection data sets are acquired over an offset range that correspond to the first 30–40° of angle of incidence, several approximation have been developed, which allow a simpler (and faster) computation of the reflection coefficient (e.g. Shuey, 1985; Aki and Richards,

1980). The most common form to calculate the reflection coefficient (R) as function of angle of incidence (θ) is the Intercept-Gradient formulation of Shuey's approximation (Castagna and Swan, 1997):

$$R(\theta) \approx \frac{1}{2}\left(\frac{\Delta V_p}{\langle V_p \rangle} + \frac{\Delta \rho}{\langle \rho \rangle}\right) + 2\frac{\langle V_s \rangle^2}{\langle V_p \rangle^2}\left(2\frac{\Delta V_s}{\langle V_s \rangle} + \frac{\Delta \rho}{\langle \rho \rangle}\right) \cdot sin^2(\theta) \tag{7.1}$$

With:

$\Delta V_p, \Delta V_s, \Delta \rho$	Difference in P-wave, S-wave velocity and density, respectively
$\langle V_p, V_s, \rho \rangle$	mean of P-wave, S-wave velocity and density, respectively.

Simplified, the reflection coefficient can be written as:

$$R(\theta) \approx I + Gsin^2(\theta) \tag{7.2}$$

with

$$I = \frac{1}{2}\left(\frac{\Delta V_p}{\langle V_p \rangle} + \frac{\Delta \rho}{\langle \rho \rangle}\right) (Intercept)$$

$$G = 2\frac{\langle V_s \rangle^2}{\langle V_p \rangle^2}\left(2\frac{\Delta V_s}{\langle V_s \rangle} + \frac{\Delta \rho}{\langle \rho \rangle}\right) (Gradient)$$

Intercept and gradient can be determined from pre-stack CDP gathers and used to either generate P-wave and pseudo S-wave reflectivity stacks (Smith and Gidlow, 1987) or crossplots (Castagna and Swan, 1997). The crossplotting technique is widely used to classify AVO responses based on the classification scheme by Rutherford and Williams (1989), who separated the IG-crossplot into four quadrants. In the case of a BSR, intercept and gradient are mainly negative and the BSR falls therefore into the third quadrant.

Generally, intercept and gradients are extracted from the CDP gathers and calibrated with a well log response. In the absence of a nearby well log the seismic data can be calibrated in a way that the near offset traces give the vertical incidence reflection coefficient obtained using e.g. Warner's method (1990).

7.4 AVO Modeling

7.4.1 Hydrate Replacement in Marine Sediments

A standard Intercept-Gradient AVO analysis carried out as in hydrocarbon exploration, is based on the detection of deviations that may be indicative of oil and/or gas from a background trend. In this AVO modeling study, the main anomaly of interest is the bottom-simulating reflector (BSR), which marks the base of the gas hydrate stability field. Before modeling the AVO effect of a BSR, the AVO effect of hydrate in the sediments above the BSR must be characterized. In this study an interface between a 60% and a 50% porosity layer is modeled. For this model the intercept, i.e. the vertical incidence reflection coefficient, is positive. Using (a) the hydrate formation models by Helgerud (2000) and (b) a modified cementation model, the effect of increased hydrate concentrations on the Intercept-Gradient crossplot is investigated. The Helgerud (2000) model predicts a reference P-wave and S-wave velocity that can be used to define a no-hydrate background trend for the sediment interface. Both P- and S-wave velocity increase with depth, but the P-wave velocity increase is almost linear whereas the S-wave velocity increase follows a power-law (see Figure 7.3). Since effective pressure, i.e. the depth of the interface, is built into the model, the calculated intercept and gradient change with depth. For a no-hydrate reference, the intercept increases only slightly with depth but the gradient changes sign, which is an expected effect of the increased compaction and therefore increased S-wave velocities of the sediments. The interface was modeled at 10, 50 and 100 m depth.

For the *hydrate-in-frame* model, additional hydrate increases intercept and gradient (Figure 7.6). In the crossplot, the effect of hydrate formation can be characterized by a replacement-vector that shifts the intercept/gradient towards the right, i.e. to more positive values. This linear shift is observed at all depths modeled. However, this model does not take any cementation into account that would produce higher S-wave

velocities. The effect of cementation was then modeled using the *hydrate-in-frame* model and increasing the S-wave velocity proportional to the hydrate concentration with no change in the P-wave velocity. For all depths, the cementation strongly decreases the gradient. This effect is especially evident at greater depth (e.g. 100 m bsf). Thus large negative AVO gradients may indicate hydrate that cemented the sediment grains.

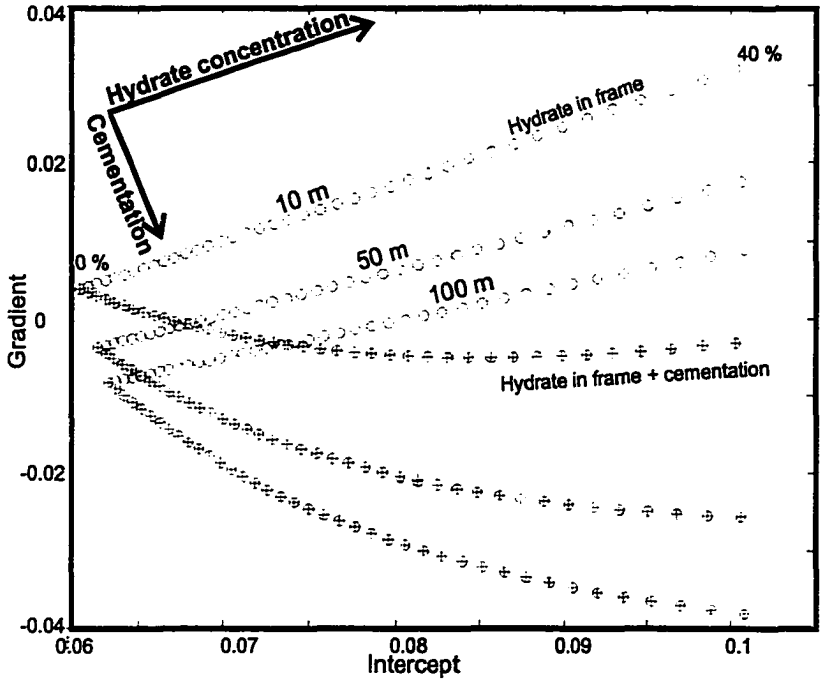

Figure 7.6 Crossplot of Intercept and Gradient for the *hydrate-in-frame* and additional cementation model for a two layer system. Layers have 60% and 50% porosity. Hydrate concentration increases from 0% to 40% of the pore volume. Interface between the layers was modeled at 10, 50 and 100 m depth. Increase in hydrate moves the IG to the right (open circles) but if additional cementation takes place, the gradient is reduced and changes to strongly negative values (crosses).

This modeling is based on adding equal amounts of hydrate to both layers. However, hydrate formation takes place preferentially in coarser, thus higher porosity

layers. The effect is a decrease in the impedance contrast, an effect that was used to explain blanking at the Blake Ridge (Lee *et al.*, 1993; Lee and Dillon, 2001). However, blanking at the Blake Ridge can be the effect of relatively homogeneous strata (Holbrook *et al.*, 1996). A decrease in impedance and gradient is observed if the *hydrate-in-pore-space* model by Helgerud (2000) is used, but the effect is very subtle (Figure 7.7).

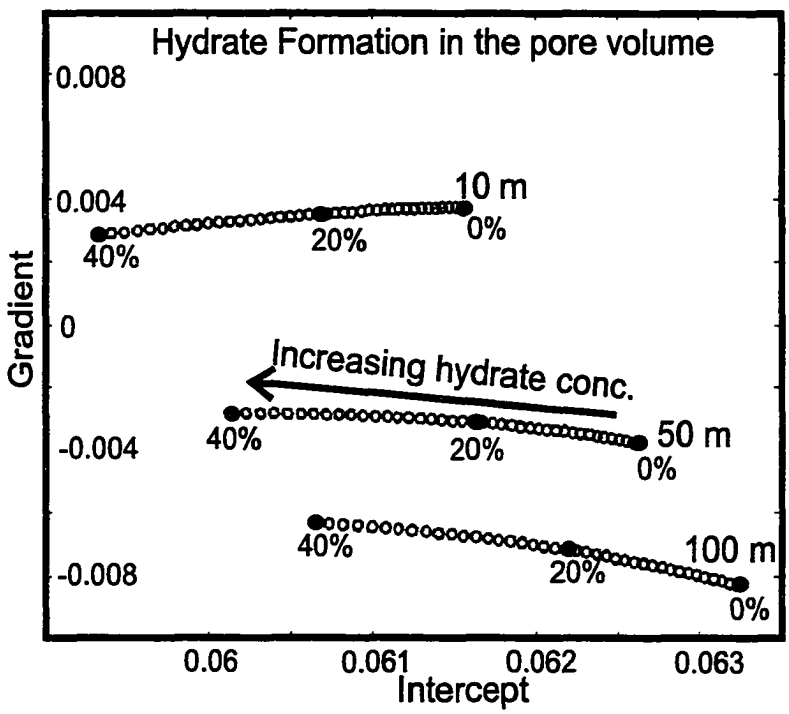

Figure 7.7 Crossplot of Intercept and Gradient for the *hydrate-in-pore-space* model for a two-layer system. Layers have 60% and 50% porosity. Hydrate concentration increases from 0% to 40% of the pore volume. Interface between the layers was modeled at 10, 50 and 100 m depth. A small change in gradient and intercept towards smaller values is observed.

7.4.2 Results From Line 89-08 and 89-10

The AVO intercept/gradient (IG) crossplotting technique was applied to data acquired in 1989 with a 3500 m long streamer and a tuned airgun array (Hyndman and Spence, 1992). The composite directivity attenuation D of the airgun array and the streamer was corrected by multiplying the data with an offset-dependent scalar $1/D$. The attenuation factor is based on directivity estimates by Hyndman and Spence (1992). The data was not calibrated to a well-log and no conversion to reflection coefficients was carried out. In general this calibration is not necessary, if general trends in the data are of major interest as in this study. The AVO processing was carried out with the software *AVO* by Hampson & Russell. The part of line 89-08 in the deep sea basin west of the deformation front was investigated to study a no-hydrate/no-gas IG crossplot. The sediment layers are mainly parallel to the seafloor and show a well defined AVO response (Figure 7.8).

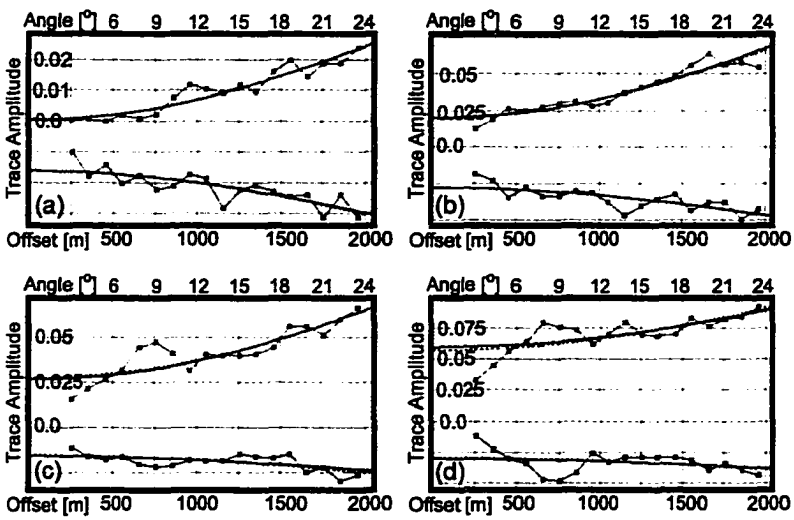

Figure 7.8 AVO trend of four layers from seismic line 89-08 in the deep sea basin. Layer depths [TWT] are (a) 3.6 s, (b) 3.85 s, (c) 4.25 s, and (d) 4.4 s. Shown are picked trace amplitudes of the peak (red) and trough (blue) of the wavelet and best fit curves. Compare with crossplot in Figure 7.8.

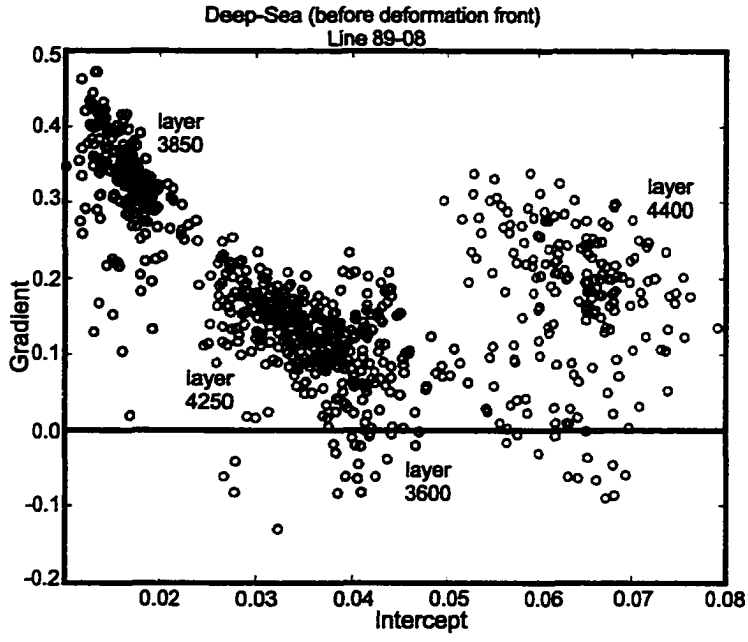

Figure 7.9 Crossplot of non-calibrated Intercept and Gradient of four layers in the deep sea basin west of the deformation front. All layers are clearly distinguished in the IG crossplot.

The amplitudes generally increase with offset over the range of angle of incidence extracted (maximum 24°). Within the IG crossplot the different layers are clearly distinguishable with some small overlap (Figure 7.9). All layers have a positive intercept and gradient. No clear pattern of negative gradients due to compaction of the deeper layers can be seen, indicating relatively low S-wave velocities (underconsolidated sediment) even at greater depth. The occasionaly observed negative gradients probably are due to residual moveout errors at some CDP's.

Parts of seismic Line 89-10 were used to define a IG crossplot for sediments that can contain gas hydrate. Multichannel seismic velocity analyses indicated the presence of about 10% hydrate in the sediments at a depth of 80–120 m bsf. The highest concentrations of up to 25% are observed just above the BSR. Two layers at around 100 m bsf show a positive intercept and gradient response (Figure 7.10 and Figure 7.11). There is no evidence for strong negative gradients within this data set suggesting that the hydrate that is present does not act as a inter-granular cement giving the sediment frame a stronger rigidity.

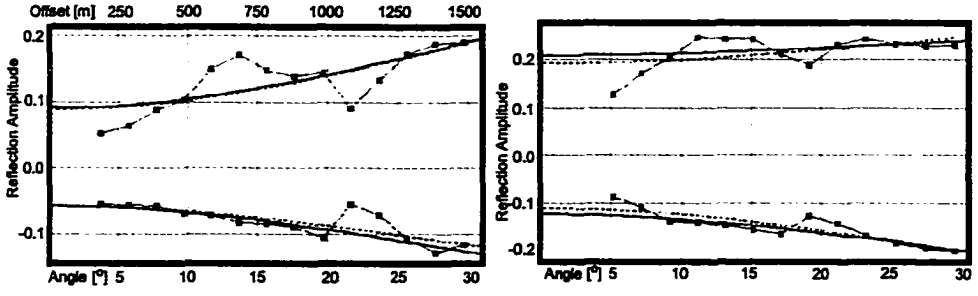

Figure 7.10 AVO trend of the two (hydrate-bearing) layers used in crossplot of Figure 7.10 from seismic line 89-10. Layer depths are 100 ms and 140 ms TWT bsf. Shown are picked trace amplitudes of the corresponding peak (red) and trough (blue) of the wavelet of the reflector and best fit curves (Frame grabs from Hampson & Russel AVO software).

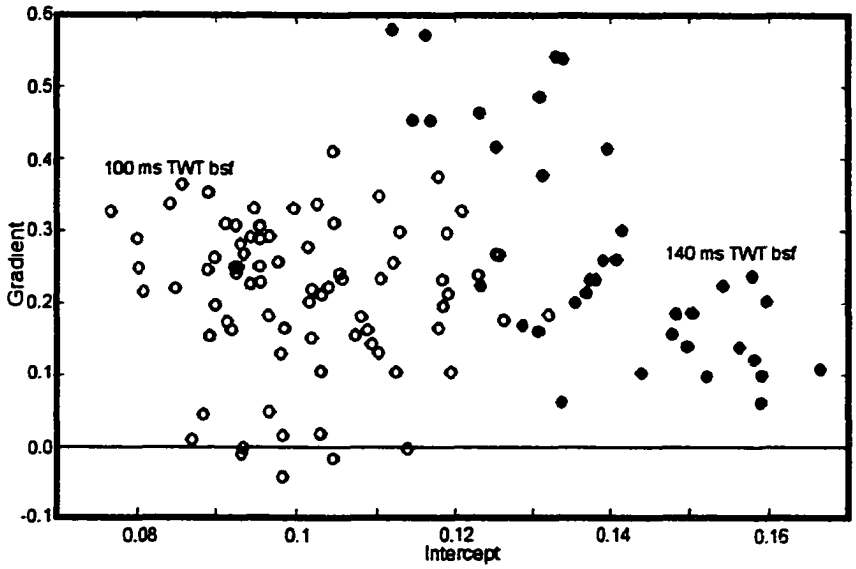

Figure 7.11 Crossplot of non-calibrated Intercept (I) and Gradient (G) of two (hydrate-bearing) layers of line 89-10. Layers are at around 80–100 m bsf. Both layers do not have strong negative gradients but contain about 10% hydrate.

7.4.3 BSR AVO-response

The BSR is mainly characterized by negative vertical incidence reflection coefficients that indicate a decrease in the impedance contrast. This decrease in the impedance contrast is mainly a P-wave velocity effect since the density is not expected to change significantly across the interface. A decrease in P-wave velocity can either be the effect of free gas below or gas hydrates above the interface or a combination of both. The AVO response is therefore ambiguous and without additional constraints from well logs or multichannel interval velocities, AVO cannot resolve the nature of the BSR. However, using the intercept-gradient classification, a simplified characterization of the BSR AVO response is possible. Also the IG crossplots may help to distinguish between an environment where the hydrate acts as grain cement or where the hydrate does not strengthen the sediment frame and the shear wave velocities are not significantly increased.

The rock-physics models by Helgerud (2000) are used to model general trends in an IG crossplot for the BSR response as function of free gas and hydrate concentration. Cementation was modeled using the *hydrate-in-frame* model and additionally increasing the S-wave velocity in the hydrate-bearing sediments proportional to the hydrate concentration. The modeling was done for a porosity of 50% in both layers at a common BSR depth for the area of 220 m.

BSR Crossplots: Hydrate, Gas and Cementation Vector

The *hydrate-in-pore* model predicts no increase of the S-wave velocity for hydrate formation, and thus there is no S-wave velocity contrast at the BSR. The BSR AVO response is therefore just affected by the P-wave velocity contrast, since density is not strongly affected by the presence of hydrate or small amounts of free gas in the sediments. Within the IG crossplot the effect of adding hydrate to the upper layer results in a linear shift towards larger intercepts and gradients (Figure 7.12). The same linear shift is observed for increasing gas concentrations in the lower medium. In general, not much difference is observed between the different models.

Using the *hydrate-in-frame* model changes the S-wave velocity in the upper medium, which results in strong changes in the IG crossplot (Figure 7.12). There are basically two trends observed within this model. Increasing the gas concentration in the lower medium strongly affects the gradient and intercept and shifts both to more negative values. However, increasing the hydrate concentrations has a larger effect on the intercept than on the gradient for a constant free gas concentration in the lower medium by shifting the intercept to the left, i.e. more negative values, whereas the gradient increase is relatively small.

A completely different behaviour of the IG crossplot is observed if the upper medium is modeled with the *hydrate-in-frame* model and additional cementation (Figure 7.13). The additional increase in the S-wave velocity shifts the gradient towards more positive numbers. For example the BSR is modeled as an effect of hydrate

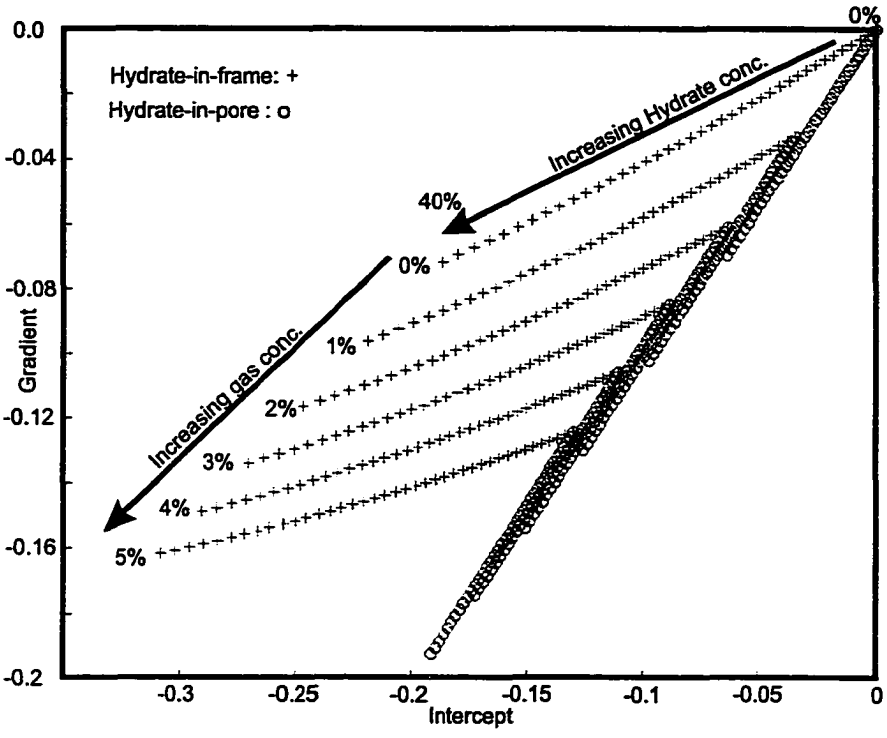

Figure 7.12 Crossplot of Intercept and Gradient for a BSR by using the *hydrate-in-frame* (crosses) and *hydrate-in-pore* model (open circles). Gas concentrations increase from 0–5%, whereas hydrate concentrations range from 0–40%. The *hydrate-in-pore* model predicts only a small range of possible intercepts and gradients due to the constant S-wave velocity across the BSR-interface.

above the interface only (no gas below), the gradient is always positive. The higher the hydrate concentration, the larger the intercept and the more positive the gradient. Two different realizations for the hydrate cementation have been modeled (with C_h as hydrate concentration): (a) weak cementation with $V_s' = V_s + C_h \cdot 5$ and (b) strong cementation with $V_s' = V_s + C_h \cdot 10$. In the weak cementation, the shear wave velocity for a sediment containing 20% hydrate would be 575 m/s, whereas strong cementation would results in 675 m/s. No cementation would result in a reference velocity of 475 m/s.

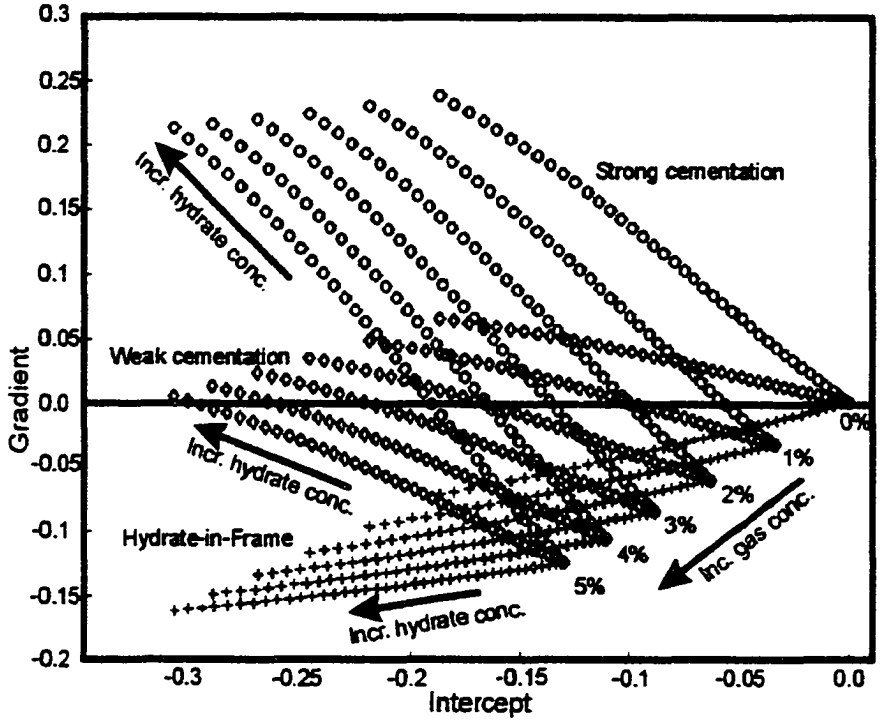

Figure 7.13 Crossplot of Intercept and Gradient for a BSR by using the *hydrate-in-frame* model (red) and two scenarios for additional cementation of the hydrate-bearing sediments above the BSR-interface (black: weak, blue: strong cementation). The effects of increasing gas and hydrate concentrations in the lower and upper layer were modeled respectively. Gas concentrations increase from 0–5%, whereas hydrate concentrations range from 0–40%.

Simplified, three different replacement vectors can be defined in terms of a BSR crossplot in analogy to the fluid-replacement vector defined by Castagna and Swan (1997): (a) the gas-vector, (b) the hydrate-vector, and (c) the cementation-vector. The gas-vector shifts the IG values towards more negative values and strongly influences intercept and gradient. The hydrate replacement-vector always shifts the IG towards more negative values without strongly effecting the gradient in the case of no cementation. The cementation vector shifts the gradient out of the third quadrant

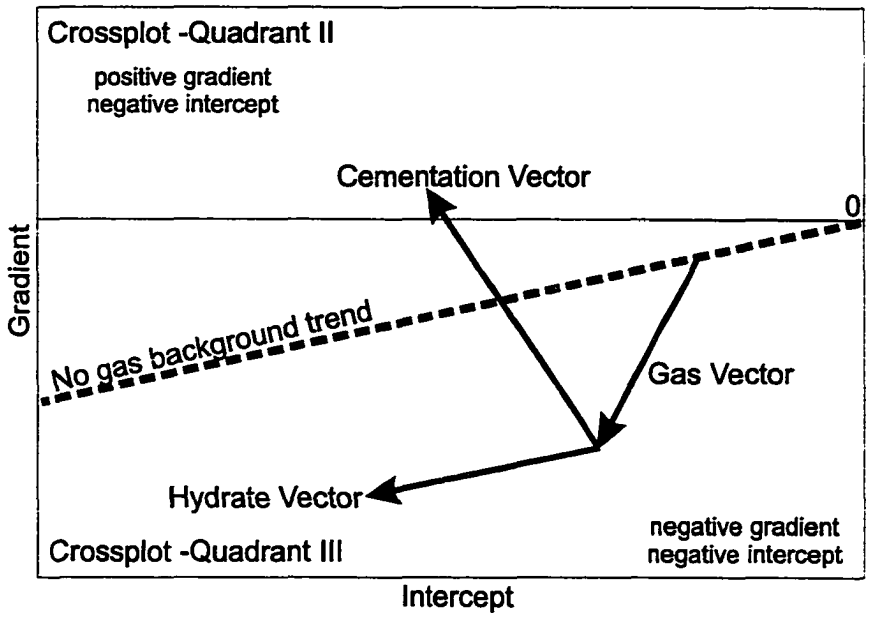

Figure 7.14 Simplified effects of increasing hydrate and gas concentrations plus cementation effects on a BSR Intercept-Gradient Crossplot.

towards more positive values (Figure 7.14).

In general the IG crossplot for the BSR may help to identify the presence of hydrate cementing the grains in the upper medium. Strong cementation results in a completely different gradient response of the BSR. However, if no or only weak cementation takes place, there is too much overlap between individual models to really distinguish between the individual effects of free gas below or just hydrate above or a mixture of both. But if constraints are available for the amount of hydrate in the sediments above the interface (for example multichannel seismic interval velocities or sonic logs), there is some possibility of distinguishing between the different models. However, small amounts of free gas less than 3–4% cannot be resolved.

7.4.4 Data Examples

The extracted intercept and gradient values from parts of the line 89-10 are all negative, suggesting that no strong cementation is taking place in the upper hydrated layer (Figure 7.15). However, the extracted gradient values after amplitude scaling using the Warner method were relatively large (greater than -0.3) for intercepts at about -0.1. The modeling was carried out for porosities of 50% in both layers, and thus the overall position of the two reference lines of no-gas/no-hydrate and data in between these limits will change for a different background medium.

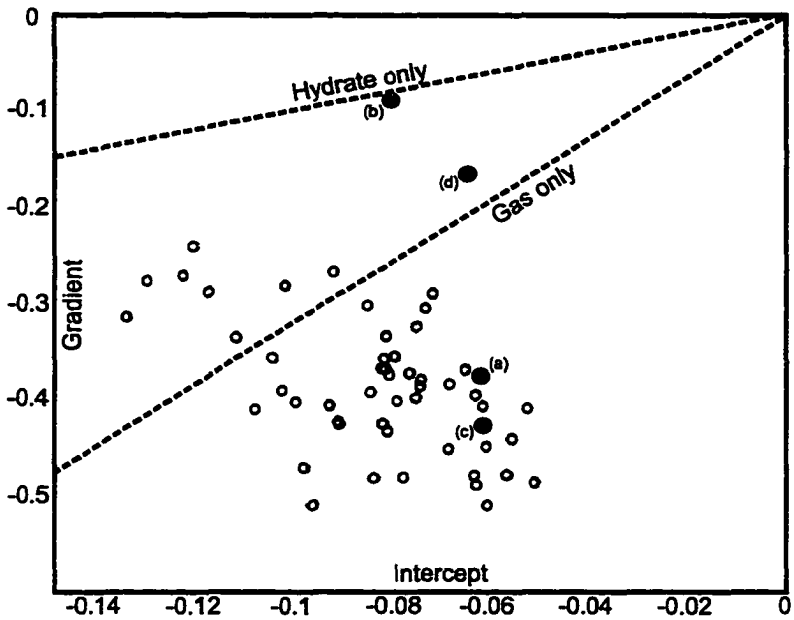

Figure 7.15 Example of extracted intercept and gradients from MC line 89-10 and COAMS (red circles). The two limits of *hydrate-only* and *gas-only* from modeling are added.

Data from the COAMS-99 survey were used only for parts of inline 41, where the BSR is clearly not affected by the receiver ghost. The maximum offset available limits the maximum angle of incidence to about 25°. In Figure 7.16, four representative examples for a BSR-AVO trend from the COAMS data are given. The corresponding

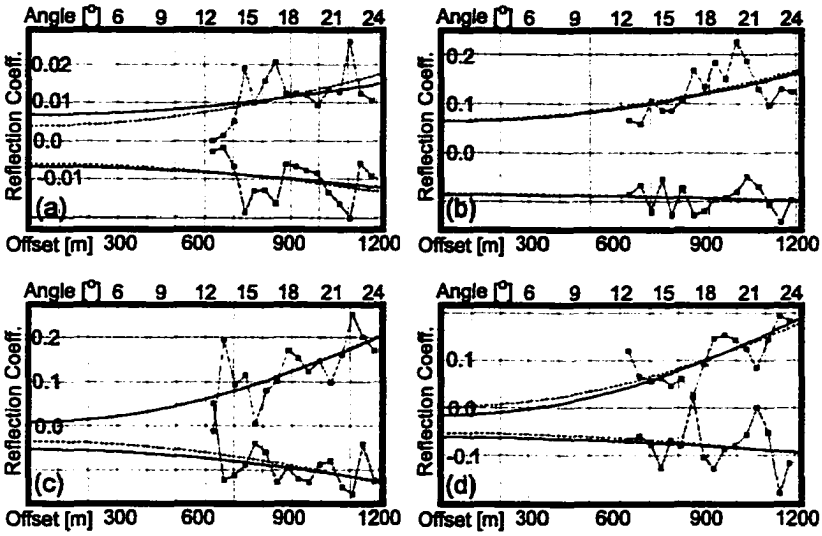

Figure 7.16 Four examples of the AVO trend of a BSR in COAMS data (from inline 41). The blue best-fit line and data points correspond to the trough and the red data points and best fit line correspond to the peak of the BSR wavelet. Related intercept (I) and gradient (G) values are as follows: (a) CMP 155775 I=-0.062, G=-0.35, (b) CMP 156975, I=-0.082 G=-0.11, (c) CMP 157775 I=-0.058 G=-0.466, (d) CMP 159775 I=-0.06 G=-0.18.

intercept and gradient values are superimposed on Figure 7.15. Again, values are negative indicating no strong cementation in the sediments above the BSR.

7.5 Frequency Dependent Reflection Coefficients and AVO Tuning

The BSR was found to be frequency dependent (Chapman *et al.*, 2001) as described in chapter 2. From modeling of vertical incidence reflection coefficients, the best model for the BSR is a thin layer of 5–10 m thickness with a strong negative velocity gradient. Velocity decreases by about 250 m/s from 1800 m/s in the hydrate-bearing sediments above to about 1550 m/s in the probably gas-bearing sediments below the BSR. This velocity gradient results in very small reflection coefficients of

the BSR for frequencies above 100 Hz which have wavelengths less than the gradient layer thickness (see Figure 2.5 in chapter 2).

How does this gradient layer affect the AVO response of the BSR? In an early now classic paper, Ostrander (1984) addressed the AVO tuning problem for a constant-velocity layer. He investigated the effect of the interference of reflections from the top and bottom of a gas layer. The tuning effect T can be expressed in terms of the NMO equation and is given by:

$$T = (1 + X^2/T_0^2 V_{rms}^2)^{-1/2}, \tag{7.3}$$

with X as offset, T_0 as zero-offset two-way-traveltime of the event and V_{rms} as the root-mean-square velocity. Amplitude attenuation or amplification due to tuning depends on the physical properties (expressed by the rms velocity) of the layer of interest and its depth, i.e. its two-way travel time T_0. This first conceptual approach was further developed by Swan (1991) and Dong (1999), who also reported a method of removing tuning effects from pre-stack seismic data. However, these methods all treat the tuning effect as the result of top and bottom reflection only. The BSR response is more complicated as it is a gradient layer that may be represented by multiple thinbeds over a very small depth range.

In general, it is expected that the intercept, i.e. the vertical incidence reflection coefficient, decreases due to the tuning effect as modeled by Chapman *et al.* (2001). The limit of BSR detectability strongly depends on the model used. If the BSR is modeled as a gradient layer with sharp edges, it is predicted to disappear at frequencies of about 100 Hz. This threshold is further reduced if the BSR is modeled with smooth edges. In a first modeling approach, the BSR AVO response was investigated using a 10 m thick and 5 m thick gradient layer with the physical properties suggested by Chapman *et al.* (2001).

Synthetic seismograms were generated with the OUTRIDER modeling software and subsequently analyzed for intercept and gradient with the AVO software by

Hampson & Russell. A Ricker wavelet was used for frequencies from 20–100 Hz and CDP gathers were generated every 5 Hz.

The intercept decreased with increasing frequency as expected. However, there is a different tuning effect for the gradient (Figure 7.17). The gradients first increase with increasing frequency until a plateau is reached. At higher frequencies the gradient strongly decreases towards zero. The frequency for which the gradient is maximum in the 10 m thick model is about 45 Hz, whereas it is about 100 Hz for the 5 m thick model. However, the corresponding intercepts for these maximum gradients are decreased by a factor of 5.

The above defined simple vector-rules are valid only for a simple BSR interface model, so these rules can be used for frequencies below 40 Hz only. If the rock-physics model by Helgerud (2000) or others are used for an inversion, tuning effects have to be build into the forward model, because otherwise the inverted physical properties are most likely not correct. Another possibility can be the removal of tuning effects from the seismic data as suggested by Dong (1999) prior to inversion. However, this seismic processing technique has to be carried out very carefully to preserve the right AVO trend in the data.

In conclusion, it can be seen that the AVO response of the BSR is very complex and dependent on the physical properties of the sediments above and below the BSR, the thickness of the gradient layer and the magnitude of the velocity decrease. From AVO data alone no final conclusion can be drawn, if the BSR is the effect of free gas below or hydrate above the interface. Also no final conclusion can be drawn which rock-physics model is correct. The *hydrate-in-pore*-model is preferred, since it fits the observed velocities from the ODP sonic log and calculated seismic interval velocities better than the *hydrate-in-frame*-model. If cementation takes places in the hydrate-bearing sediments the gradient will most likely be positive compared to the negative no-cementation values. In combination with interval velocity analyses constraining the hydrate concentration, there is a possibility to estimate the amount of free gas

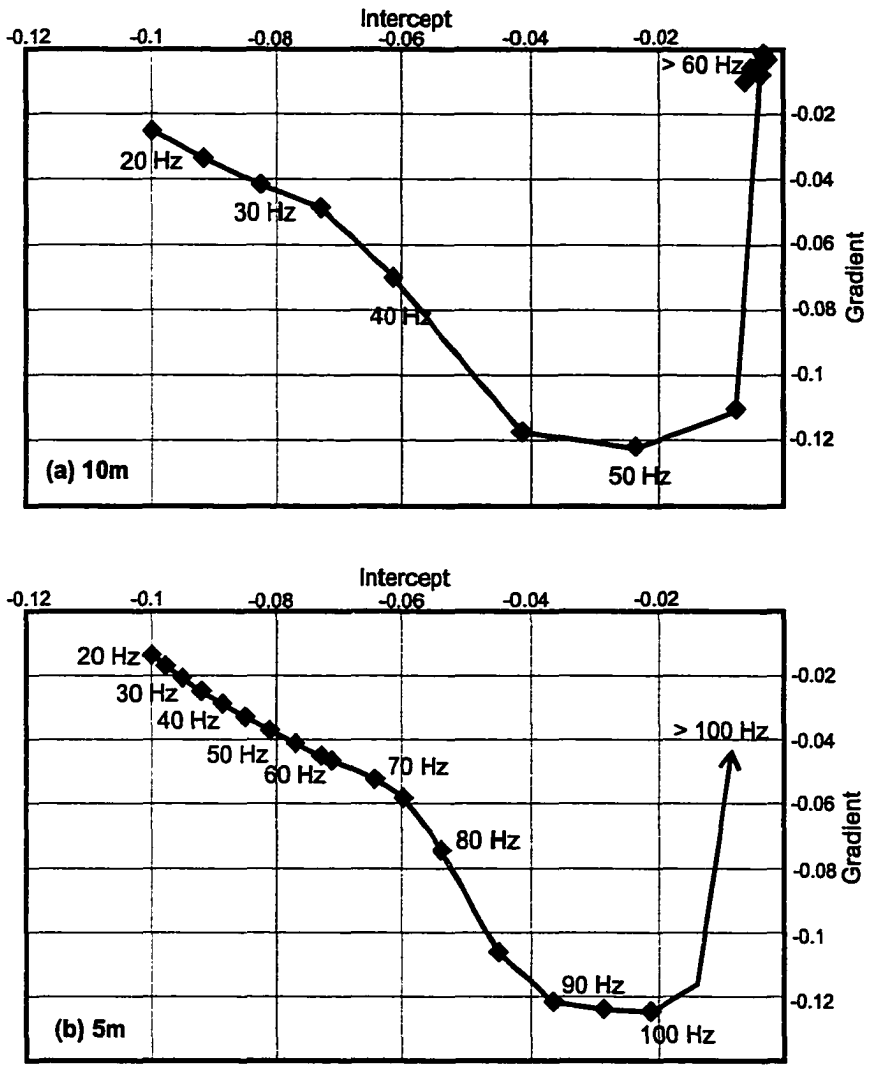

Figure 7.17 Frequency dependent intercept-gradient crossplot for a BSR gradient layer of (a) 10m and (b) 5m thickness. P-wave velocity decreases from 1800 m/s to 1550 m/s. Density is constant at 1.85 g/cm^3 and for a constant Poisson-ratio of 0.45 S-wave velocity decreases from 545 m/s above to 470 m/s below the BSR.

below the BSR. However, the AVO analyses are more complex due to the tuning effects of the gradient layer. From this analysis, inversion of AVO data to extract the

physical properties seems difficult especially given the additional problems involved with AVO, such as e.g. NMO stretch, directivity effects, multiples/ghosts and residual velocity errors due to receiver misalignments.

Chapter 8

Summary and Conclusions

8.1 Fluid Venting - Cold Vents and Blank Zones

3-D seismic analyses revealed a detailed image of a cold-vent field and gave insight into the tectonic mechanisms that control fluid/gas migration and formation of hydrate. The seismic analyses are complemented by sediment coring, geochemical analyses of pore waters, heat flow measurements and video observations with the unmanned submersible ROPOS.

The vent field is characterized by several blank zones that are related to near-surface deformation and faulting. They are 80–400 m wide and can be traced through the upper 100–200 m thick slope sediment section, but are lost in the accreted sediments that lack coherent layered reflectivity. Outside the main vent field, similar blank zones were detected at two other locations within the 3-D grid. At these locations the blank zones penetrate to greater depth below the BSR.

All observed blank zones are characterized by high amplitude rims. These rims are the interference effect of diffractions that result from relatively sharp discontinuities in the sediment physical properties at the blank zone boundary. 2-D vertical incidence seismic modeling suggests an increase in P-wave velocity inside the blank zone with only minor changes in density.

Blanking above the BSR depth is believed to be mainly the effect of increased hydrate formation within the fault plane. The fault is a conduit for upward migrating fluids and methane gas that is converted into hydrate once it reaches the hydrate stability field. Carbonate formations at the seafloor can also contribute to blanking especially at higher frequencies. Free gas inside the hydrate stability field causing

blanking may be present in case of full hydrate saturation or strong fluid flow.

Geochemical analyses of water column and pore water samples acquired at blank zone 1 were carried out by C. Solem and M. Kastner from Scripps Institute of Oceanography. These analyses give additional constraints on the nature of the blank zones and cold-vent activity. Methane concentrations of about 20 n-moles/L (about 8 times the ocean background concentration) were detected in the water column above the main blank zone of the vent field indicating free methane-gas movement through the blank zone. However, geochemical analyses of the pore fluids indicate relatively low fluid fluxes of less than 1 mm/yr and there is no heat flow anomaly present over the vent field. Venting is therefore believed to be strongly episodic but the periodicity of venting could not be determined.

Carbonate formations are a typical surface expression of fluid/gas venting and were observed at two of the blank zones at the main vent field. However, there is no seismic evidence for wide-spread carbonate formations as expressed in increased seafloor reflection coefficients. At locations of known carbonate occurrences, reflection coefficients are not increased in the low-frequency airgun multi- and single channel COAMS and Teledyne data. However, there is evidence of a carbonate pavement above blank zone 3 in the deep-towed DTAGS data that showed an increase in seafloor reflection amplitude. It can be speculated that surface-towed streamers and the lower frequencies in the COAMS and Teledyne seismic data result in a large footprint that cannot detect small-scale carbonate formations.

There is an area of about 2 km^2 in size that is characterized by increased reflection coefficients of on average 0.35 in the lower frequency seismic data. However, the observed values are not consistent with a solid carbonate pavement. The area may also be characterized by recent erosion suggested by the absence of a transparent layer that represents the last Holocene sedimentation. A possible explanation can be either a seafloor sediment that is partially cemented by carbonate or a coarser-grained layer (turbidite) with a higher sand fraction.

In general, the area of this study shows multiple evidence of enhanced fluid/gas migration along faults and increased hydrate formation. The overall amount of fluid and gas expulsion is difficult to determine from the data collected so far and will be the focus of future studies. Estimating the amount of fluid and gas expulsion and its distribution within the overlying water column is important to determine the overall fluid-budget of the accretionary prism as well as in evaluating the role of methane and methane hydrate in global climate change.

8.2 Estimating Hydrate Concentrations and BSR AVO Modeling

Gas hydrate concentrations can be determined seismically from multichannel velocity analyses. The COAMS streamer used in this study has only a limited offset range of 1200 m and was towed at depths varying from 10m to 40 m below the sea-surface. This resulted in a prominent receiver ghost, which limited vertical structural resolution and produced only a coarse interval-velocity depth-function. To calculate the varying receiver depths and offsets a new array element localization (AEL) technique was developed. The calculated interval velocities after AEL are unreasonably large compared to values obtained from previous analyses and the ODP sonic logs. The large velocities may be the effect of residual positioning errors in combination with the limited offset range. With such large uncertainty no hydrate concentrations were calculated using the COAMS interval velocities.

A rock-physics model was used to calculate elastic properties of the sediments around ODP Site 889/890. The observed velocities can best be explained by hydrate formation that mainly takes place as part of the pore volume, but small amounts of hydrate may also be formed as part of the sediment frame. The rock-physics model also provides S-wave velocities as function of hydrate concentration. However, the model does not take hydrate-cementation into account, which may result in larger

S-wave velocities. The results from the rock-physics modeling were also used in an amplitude-versus-offset (AVO) study of the BSR. The intercept-gradient (IG) form of Shuey's approximation to the full Zoeppritz equation was used which allows for a fast and simple characterization of the BSR AVO behaviour. The modeling showed that the BSR AVO response can be separated into three individual effects (fluid-replacement vectors): (a) hydrate concentration in the sediments above the BSR, (b) cementation of the hydrate, and (c) free gas concentrations below the BSR. In general, the IG crossplotting technique is able to classify the BSR response in terms of the above three effects, but the AVO response of the BSR is strongly affected by frequency. The BSR is most likely a relatively thin, 5–10 m thick gradient layer. This gradient layer results in AVO tuning effects that modify the IG-crossplot. Generally the intercept is reduced with increasing frequency, but the gradient is initially increased for intermediate frequencies and attenuated at higher frequencies.

From the analyses carried out it seems difficult to extract the physical properties P- and S-wave velocity and density from AVO data alone. In theory, the AVO method would be a tool that can distinguish between the different rock physics models of hydrate formation. However, the extracted AVO data from the 1989 MCS and COAMS show ambiguous results. Therefore no final conclusion can be drawn, whether the BSR is the effect of hydrates above the BSR only, or if free gas is present below the BSR.

References

Aki, K., and P.G. Richards, Quantitative Seismology: Theorie and methods I, W.H. Freeman Co, 1980.

Al-Chalabi, M., An analysis of stacking, RMS, average, and interval velocities over a horizontal layered ground, Geophysical Prospecting, 22, 458–475, 1974.

Arch, J. and A. Maltmann, Anisotropic permeability and turtuosity in deformed wet sediments, J. Geophys. Res., 95, B6, 9035–6045, 1990.

Bell, P.R., Methane hydrate and the carbon dioxide question, in: Carbon dioxide review, (ed) Clark, W.C., Oxford University Press, New York, 401–406, 1983.

Bily, C. and J.W.L. Dick, Naturally occurring gas hydrates in the Mackenzie Delta, N.W.T., Bulletin of Canadian Petroleum Geology, 22, 320–352, 1974.

Bohrmann G., J. Greinert, E. Suess, and M. Torres, Authigenic carbonates from the Cascadia subduction zone and their relation to gas hydrate stability, Geology, 26, 647–650, 1998.

Bouriak, S., M. Vanneste, and A. Saoutkine, Inferred gas hydrates and clay diapirs near the Storegga Slide on the southern edge of the Voring Plateau, offshore Norway, Marine Geology, 163, 125–148, 2000.

Borowski, W.S., CK. Paull, and W. Ussler III, Marine pore-water sulfate profiles indicate in situ methane flux from underlying gas hydrate, Geology, V.24, No. 7, 655–658, 1996.

Brooks, J., H. Cox, W. Bryant, M. II. Kennicutt, R. Mann, and T. MacDonald, Association of gas hydrates and oil seepage in the Gulf of Mexico, Org. Geochem., 10, 221–234, 1986.

Brooks, J.M., M.II Kennicutt, R.R. Fay, T.J. MacDonald, and R. Sassen, Thermogenic gas hydrates in the Gulf of Mexico, Science, 225, 409–411, 1984.

Buffett, B.A., Clathrate Hydrates, Ann. Rev. Earth Planet. Sci, 477–507, 2000.

Carcione, J.M., and U. Tinivella, Bottom-simulating reflectors: Sesimic velocities and AVO effects, Geophysics, 65, 54–67, 2000.

Carpenter, G., Coincident sediment slump/clathrate complexes on the U.S. Atlantic continental slope, Geo-Marine Letters, 1, 29–32, 1981.

Carson, B., E. Seke, V. Paskevich, and M. L. Holme, Fluid expulsion sites on the Cascadia accretionary prism: Mapping diagenetic deposits with processed GLORIA imagery, J. Geophys. Res., 99, 11959–11969, 1994.

Castagna, J.P., M.L. Batzle, and R.I. Eastwood, Relationships between compressional and shear-wave velocities in clastic silicate rocks, Geophysics, 50, 571–581, 1985.

Castagna, J.P., and H.W. Swan, Principles of AVO crossplotting, The Leading Edge, April Volume, 337–342, 1997.

Chapman R., J. Gettrust, D. Hannay, G. Spence, W. Wood, and R. D. Hyndman, High resolution deep towed multichannel seismic survey of deep sea gas hydrates off western Canada, Geophysics, submitted, 2001.

Chersky, N.V., V.P. Tsarev, and S.P. Nikitin, Investigation and prediction of conditions of accumulation of gas resources in gas hydrate pools, Petroleum Geology, 21, 65–89, 1985.

Claypool, G., and K.A. Kvenvolden, Methane and other hydrocarbon gases in marine sediments, Ann. Rev. Earth Planet. Sci., 11, 299–327, 1983.

Claypool, G.E., and I.R. Kaplan, The origin and distribution of methane in marine sediments, in: Natural Gases in marine sediments, ed. I.R. Kaplan, Plenum Publishing Corp., New York, 1974.

Clennell, M.B., M. Hovland, J. S. Booth, P. Henry, and W. J. Winters, Formation of natural gas hydrate in marine sediments 1. Conceptual model of gas hydrate growth conditioned by host sediment properties, J. Geophys. Res., 104, B10, 22985–23003, 1999.

Collison, N.E., and S.D. Dosso, regularized matched-mode processing for source localization, J. Acoust. Soc. Am., 107, 3089–3100, 2000.

Collett, T.S., Natural gas hydrates of the Prudhoe Bay and Kuparuk River area, North Slope, Alaska:, Amer. Assoc. of Petrol. Geolog. Bull., 77/5, 793–812, 1993.

Collett, T.S., Natural Gas Hydrate as a Potential Energy Resource, in: Natural Gas Hydrate in Oceanic and Permafrost Environments, (ed) M.D. Max, Kluwer Academic Publ., 2000.

Collet, T.S., and S.R. Dallimore, Permafrost-assiciated gas hydrate, in: Natural Gas Hydrate in Oceanic and Permafrost Environments, (ed) M.D. Max, Kluwer Academic Publ., 2000.

Curtis, W. R., Predicted geoacoustic properties of gas hydrate saturated marine sediments. MSc. Thesis, Offshore Technology Research Center, Texas A&M University, College Station, Texas, 1992.

Dallimore, S.R., T. Uchida, and T.S. Collett, Scientific Results from JAPEX/JNOC/GSC Mallik 2L-38 Gas Hydrate Research Well, Mackenzie Delta, Northwest Territories, Canada, Geological Survey Canada Bulletin 544, 1999.

Davis E.E., and R. D. Hyndman, Accretion and recent deformation of sediments along the northern Cascadia subduction zone, Geol. Soc. Am. Bull., 101, 1465–1480, 1989.

Davis E.E., R.D. Hyndman and H. Villinger, Rates of fluid expulsion across the northern Cascadia accretionary prism: Constraints from new heat flow and multichannel seismic reflection data, J. Geophys. Res., 95, 8869–8889, 1990.

Davy, H., On some of the combinations of oxy-muratic gas and oxygen, and on the chemical relations of the principles to inflammable bodies, Philosophical Transactions of the Royal Society of London, 101 (1), 1811.

Dickens, G.R., and M.S. Quinby-Hunt, Methane hydrate stability in seawater, Geophys. Res. Lett., 21, 2115–2118, 1994.

Dillon, W.P., and M.D. Max, Oceanic gas hydrate, in: Natural Gas Hydrate in Oceanic and Permafrost Environments, (ed.) M.D. Max, Kluwer Academic Publ., 2000.

Dong, W, AVO detectability against tuning and stretching artifacts, Geophysics, 64, 494–503, 1999.

Dosso, S.E., and M. Riedel, Array element localization for towed marine seismic arrays, J. Acoust. Soc. Am., 110 (2), 955–966, 2001.

Dosso, S.E., M.R. Fallat, B.J. Sotirin, and J.L. Newton, Array element localization for horizontal arrays via Occam's inversion, J. Acoust. Soc. Am., 104, 846–859, 1998.

Dvorkin, J. and A. Nur, Rock physics for characterization of gas hydrates, in: The future of energy gases. U.S. Geological Survey Professional paper 1570, 1993.

Dvorkin, J., J. Berryman, and A. Nur, Elastic moduli of cemented sphere packs, Mechanics of Materials, 31, 461–469, 1999a.

Dvorkin, J.M., M. Prasad, A. Sakai, and D. Lavoie, Elasticity of Marine Sediments: Rock Physics Modeling, Geophysical Research Letters, 26, 1781–1784, 1999b.

Ecker, C., J. Dvorkin and A. Nur, Sediments with gas hydrates: internal structure from seismic AVO, Geophysics, 63, No. 3, 1659–1669, 1998.

Elderfield H., M. Kastner and J. B. Martin, Compositions and sources of fluids in sediments of the Peru subduction zone, J. Geophys. Res., 95, 8819–8882, 1990.

Englezos, P., and P.R. Bishnoi, Prediction of gas hydrate formation in aqueous solutions, Am. Inst. Chem. Eng., 34, 1718–1721, 1988.

Fink, C. R., and G. D. Spence, Hydrate distribution off Vancouver Island from multifrequency single-channel seismic reflection data, J. Geophys. Res., 104, 2909–2922, 1999.

Fink, C.R., Methane hydrate distribution offshore Vancouver Island from detailed single channel seismic studies, MSc thesis at the University of Victoria, 1995.

Ganguly, N., G.D. Spence, N.R. Chapman, and R.D. Hyndman, Heat flow variations from bottom simulating reflectors on the Cascadia margin, Marine Geology, 164, 53–68, 2000.

Gassmann, F., Elasticity of porous media: Über die Elastizität poröser Medien, Vierteljahrsschrift der Naturforschenden Gesellschaft, 96, 1–23, 1951.

Gazdag, J., Wave equation Migration with the phase-shift method, Geophysics, 43, 1342–1351, 1978.

Gettrust, J. F. and J. H. Ross, Development of a low-frequency, deep-towed geoacoustics system, Proc. Oceans 90, 38–40, 1990.

Gettrust, J., R. Chapman, R. Walia, W. Wood, D. Hannay, D. Lindwall, G. Spence, K. Louden, and R. Hyndman, High resolution seismic studies of deep sea gas hydrate using the DTAGS deep towed multichannel system. EOS, Transactions, American Geophysical Union, 80, No.38, 439–440, 1999.

Gieskes, J.M. and W.C. Rogers, Alkalinity determination of interstitial waters of marine sediments, Journal of Sedimentary Petrology, 43, No.1, 272–277, 1973.

Ginsburg, G.D., R.A. Guseynov, A.A. Dadashev, G.A. Ivanov, S.A. Kazantsev, V.A. Soloviev, E.V. Telepnev, R. Ye. Askeri-Nasirov, A.D. Yesikov, V.I. Maltseva, Yu. G. Mashirov, and I. Yu. Shabayeva, Gas Hydrates of the southern Caspian, International Geology Review, 34, 765–782, 1992.

Ginsburg, G.D., and V.A. Soloviev, Submarine gas hydrates, (translated from Russian), Norma Publishers, St. Petersburg, Russia, 216pp, 1998.

Guerin, G., D. Goldberg, and A. Meltser, Characterization of in situ elastic properties of gas hydrate-bearing sediments on the Blake Ridge, J. Geophys. Res., 104, No. B8, 17781–17795, 1999.

Guerin, G., and D. Goldberg, Elastic wave dissipation in gas hydrates: Amplitude analysis of sonic log waveforms from the Mallik 2L-38 well, MacKenzie delta, Canada, EOS, Transactions, AGU, 80, No. 46, F503, 1999.

Hamilton, E.L., Vp/Vs and Poisson's ratios in marine sediments and rocks, J. Acoust. Soc. Am., 66, 1039–1101, 1978.

Hamilton, E.L., Geoacoustic modeling of the sea floor, J. Acoust. Soc. Am., 68(5), 1980.

Helgerud, M.B., Wave speeds in gas hydrates and sediments containing gas hydrate: A laboratory and modeling study, PhD thesis, Stanford University, 2000.

Hill, R., The elastic behaviour of crystalline aggregate, Proceedings of the Physical Society, London, A65, 349–354, 1952.

Henry P., X. Le Pichon, S. Lallemant, J.-P. Foucher, G. Westbrook, and M. Hobart, Mud volcano field seaward of the Barbados accretionary complex: a deep towed side scan sonar survey, J. Geophys. Res., 95, 8917–8929, 1990.

Holbrook, W.S., Hoskins, H., Wood, W.T., Stephen, R.A., Lizarralde, D., and Leg 164 Science PArty, Methane hydrate and free gas on the Blake Ridge from vertical seismic profiling, Science 273, 1840–1843, 1996.

Hunt, J. M., Petroleum Geochemistry and Geology, W.H. Freeman, San Francisco, 1979.

Hyndman R.D. and E. E. Davis, A mechanism for the formation of methane hydrate and seafloor bottom-simulating reflectors by vertical fluid expulsion, J. Geophys. Res., 97, 7025–7041, 1992.

Hyndman, R. D., and G. D. Spence, A seismic study of methane hydrate marine bottom simulating reflectors, J. Geophys. Res., 97, 6683–6698, 1992.

Hyndman, R.D., Wang, K., Yuan, T., and G.D. Spence, Tectonic sediment thickening: fluid expulsion and the thermal regime of subduction zeon accretionary prisms: The Cascadia Margin off Vancouver Island, J. Geophys. Res., 98, 21865–21876, 1993.

Hyndman, R.D., G.D. Spence, T. Yuan, and E.E. Davis, Regional geophysics and structural framework of the Vancouver Island Margin accretionary prism, in: Proc. of ODP Initial Reports, Vol. 146, 399–419, 1994.

Hyndman, R. D., The Lithoprobe corridor across the Vancouver Island continental margin: The structural and tectonic consequences of subduction, Can. J. Earth Sci., 32, 1777–1802, 1995.

Hyndman, R.D., T. Yuan and K. Moran, 1998. The concentration of deep sea gas hydrates from downhole electrical resistivity logs and laboratory data, Earth Planet. Sc. Lett., 172, 167–177, 1999.

Hyndman, R.D., G.D. Spence, R. Chapman, M. Riedel, and R.N. Edwards, Geophysical studies of Marine Gas Hydrates in Northern Cascadia, in: Natural Gas Hydrates: Occurrence, Distribution, and Detection, Geophysical Monograph 124, AGU, 2001.

Jansen, E., S. Befring, T. Bugge, T. Eidvin, H. Holtedahl, and H.P. Sejrup, Large submarine slides on the Norwegian continental margin: sediments, transport and timing, Marine Geology, 78, 77–107, 1987.

Kayen, R.E., and H.J. Lee, Slope stability in regions of sea-floor gas hydrate: Beaufort Sea Continental Slope, in: W.C. Schwab, Lee H.L., and Twichell D.C. (eds). Submarine Landslides: Selective Studies in the U.S., Exclusive zone, U.S. Geological Survey Bulletin 2002, 97–103, 1993.

Kennett, J.P., K.G. Cannariato, I.L. Hendy, and R.J. Behl, Carbon Isotopic Evidence for Methane Hydrate Instability During Quarternary Interstadials, Science, 288, 128–133, 2000.

Korenaga, J., W.S. Holbrook, S.C. Singh, and T.A. Minshull, Natural gas hydrates on the southeast U.S. margin: Constraints from full waveform and travel time inversion of wide-angle seismic data, J. Geophys. Res., 102 B7, 15345–15365, 1997

Kulm L. D., and E. Suess, Relationship between carbonate deposits and fluid venting: Oregon Accretionary Prism, J. Geophys. Res., 95, 8899–8915, 1990.

Kvenvolden, K., Natural Gas Hydrate: Introduction and History of Discovery, in: Natural Gas Hydrate in Oceanic and Permafrost Environments, (ed) M.D. Max, Kluwer Academic Publ., 2000.

Kvenvolden, K., Gas hydrates - geological perspective and global change, Reviews of Geophysics, 31, 173–187, 1993.

Kvenvolden, K., and L. Barnard, Gas hydrates of the Blake Ridge, Deep Sea Drilling Project Site 553, Leg 76, In: *Initial Reports of the Deep Sea Drilling Project*, ed. R. Sheridan, F. Gradstein, 75, 353–366, Washington, US Government Printing Office, 1983.

Lee, M.W., Hutchinson, D.R., Dillon, W.P., Miller, J.J., Agena, W.F., and B.A. Swift, Method of estimating the amount of in-situ gas hydrates in deep marine sediments, Marine and Petroleum Geology, 10, 493–506, 1993.

Lee, M.W., and W.P. Dillon, Amplitude blanking related to gas hydrate concentration, Marine Geophysical Researches, 22(2), 101–109, 2001.

Lee, M.W., D.R. Hutchinson, T.S. Collett, and W.P. Dillon, Seismic velocities for hydrate-bearing sediments using weighted equation, J. Geophys. Res., 101, 20347–20358, 1996.

Le Pichon X. P. Henry, and S. Lallemant, Water flow in the Barbados Accretionary Complex, J. Geophys. Res., 95, 8945–8967, 1990.

T. Lewis, P. Flueck, and J.K. Hong, Heat flow measurements, in: VENTFLUX: Piston coring and heat flow near vent sites associated with marine gas hydrates offshore Vancouver Island, CEOR Report 2000-4, G. Spence, M. Riedel and I. Novosel, Centre for Earth and Ocean Research, University of Victoria, Canada, 2000.

Lodolo, E., and A Camerlenghi, The occurrence of BSRs on the Antarctic Margin, in: Natural Gas Hydrate in Oceanic and Permafrost Environments, (ed) M.D. Max, Kluwer Academic Publ., 2000.

MacDonald, G.T., The future of methane as an energy resource, Annual Review of Energy, 15, 53–83, 1990.

MacDonald, G.T., The many origins of natural gas, J. of Petroleum Geology, 5, 341–362, 1983.

MacKay, M.E., R.D. Jarrad, G.K. Westbrook, R.D. Hyndman, and the Shipboard Scientific Party of ODP Leg 146, Origin of bottom simulating reflectors: Geophysical evidence from the Cascadia accretionary prism, Geology, 22, 459–462, 1994.

Makogon, Yu.F., V.I. Tsarev, and V.V. Cherskiy, Formation of large natural gas fields in zones of permanently low temperatures (in English): Doklady Akademii Nauk SSSR 205, 700–703, Doklady-Earth Science Section 205 (1973), 215–218, 1972.

Markl, R.G., G.M. Bryan, and J.I. Ewing, Structure of the Blake Bahama Outer Ridge, J. Geophys. Res., 75, 4539–4555, 1970.

McIver, R.D. Role of naturally occurring gas hydrates in sediment transport, American Association of Petroleum Geologists Bulletin, 66, 789-792, 1982.

Mi, Y., Seafloor sediment coring and multichannel seismic studies of gas hydrate, offshore Vancouver Island, MSc thesis, University of Victoria, 1998.

Mindlin, R.D., Compliance of elastic bodies in contact, Journal of Applied Mechanics, 16, 259–268, 1949.

Minshull, T.A., S.C. Singh, and G.K. Westbrook, Seismic velocity structure at a gas hydrate reflector, offshore western Columbia, from full waveform inversion, J. Geophys. Res., 99 B3, 4715–4734, 1994.

Mitchell, A.R., and P.G. Kelamis, Efficient tau-p hyperbolic velocity filtering, Geophysics, 55, 619–625, 1990.

Moore, J.C., A. Klaus et al., Proc. ODP, Init. Reports, College Station, TX, Ocean Drilling Program, 171A, 1998.

Neave, K.G., Judge, A.S., Hunter, J.A., and MacAulay, H.A., Offshore permafrost distribution in the Beaufort Sea as determined from temperature and seismic observations, in: Geological Survey of Canada, Current Research, Part C, paper 78-1C, 13–78, 1978.

Novosel, I., G.D. Spence, N.R. Chapman, M. Riedel, R.D. Hyndman, C. Solem, M. Kastner, and T. Hamilton, Piston Coring and Seafloor Observations of Gas Hydrates at a Vent Field, Offshore Vancouver Island, EOS, Transactions, AGU, 81, No. 48, F603, 2000.

Ostrander, W.J., Plane-wave reflection coefficients for gas sands at nonnormal angles of incidence, Geophysics, 49, 1637–1648, 1984.

Paull, C.K., W.U. Ussler III, and W.S. Borowski, Source of methane to form marine gas hydrates, in: Natural Gas Hydrates (ed) E.D. Sloan, J. Happel Jr., M.A. Hnatow, 161–176, New York, N.Y. Acad. Sci., 1994.

Paull, C.K., Matsumoto, R., Wallace, P., and *et al.*, Proceedings of the Ocean Drilling Program, Initial Reports 164, Ocean Drilling Program, College Station, TX, 623pp, 1996.

Paull, C.K., W.U. Ussler III, and W.P. Dillon, Potential role of gas hydrate decomposition in generating submarine slope failures, in: Natural Gas Hydrate in Oceanic and Permafrost Environments, (ed) M.d. Max, Kluwer Academic Publ., 2000.

Pignot, P. and N.R. Chapman, Tomographic inversion of geoacoustic properties in a range-dependent shallow water environment, J. Acoust. Soc. Am., 104, No. 3, Pt. 2, 1998.

Reuss, A., Berechnung der Fliessgrenzen von Mischkristallen auf grund der Plastizitätsbedingung für Einkristalle, Zeitschrift für angewandte Matematik und Mechanik, 9, 49–58, 1929.

Riddihough R. P., Recent movements of the Juan de Fuca plate system, J. Geophys. Res., 89, 6980–6994, 1984.

Riedel, M. and F. Theilen, AVO investigations of shallow marine sediments, Geophysical Prospecting, 49, 198–212, 2001.

Ruppel, C., Anomalously cold temperatures observed at the base of the gas hydrate stability zone on the U.S. Atlantic passive margin, Geology, 25, 699–702, 1997.

Rutherford, S.R., and R.H. Williams, Amplitude-versus-offset variations in gas sands, Geophysics, 54, 680–686, 1989.

Sassen, R., and I.R. MacDonald, Evidence for structure H hydrate, Gulf of Mexico continental slope, Org. Geochem., 22, 1029–1032, 1994.

Scholl, D.W., and A.K. Cooper, VAMPs - Possible hydrocarbon-bearing structures in Bering Sea basin, American Association Petroleum Geologists Bulletin 62, 2481–2488, 1978.

Shine, K.P., Climate Change. in: The IPCC Scientific Assessment, J.T. Hougthon, G.J. Jenkins and J. J. Ephrams eds., Cambridge Univ. Press, New York, 1990.

Shuey, R.T., A simplification of the Zoeppritz equations, Geophysics, 50, 609–614, 1985.

Singh, S.C. and T.A. Minshull, Velocity structure of a gas hydrate reflector at Ocean Drilling Program site 889 from a global seismic waveform inversion, J. Geophys. Res., 99, B12, 24221–24233, 1994.

Sloan, E.D., Clathrathe Hydrates of Natural Gas, 2nd ed. New York: Marcel Dekker, 641 p., 1998.

Smith G.C., and P.M. Gidlow, Weighted stacking for rock property estimation and detection of gas, Geophysical Prospecting, 35, 993–1014, 1987.

Spence, G.D., M. Riedel, I. Novosel, C. Solem, R.D. Hyndman, N.R. Chapman, and M. Kastner, Seafloor gas hydrates at an active vent offshore Vancouver Island: Seismic, Coring and heat flow investigations, EOS, Transactions, American Geophys. Union, 81, No. 48, F603, 2000.

Stoll, R.D., Acoustic waves in ocean sediments, Geophysics, 42, 715–725, 1977.

Suess E., G. Bohrmann, R. Huene, P. Linke, K. Wallmann, S. Lammers, H. Sahling, Fluid venting in the eastern Aleutian subduction zone, J. Geophys. Res., 103, 2597–2614, 1998.

Suess, E., M.E. Torres, G. Bohrmann, R. W. Collier, J. Greinert, P. Linke, G. Rehder, A. Trehu, K. Wallmann, G. Winkler, E. Zuleger, Gas hydrate destabilization: enhanced dewatering, benthic material turnover and large methane plumes at the Cascadia convergent margin, Earth and Planetary Science Letters, 170, 1–15, 1999.

Summerhayes, C.P., B.D. Bornhold, and R.W. Embley, Surficial slides and slumps on the continental slope and rise of South West Africa: a reconnaissance study, Marine Geology, 31, 265–277, 1979.

Swan, H.W., Amplitude-versus-offset measurement errors in a finely layered medium, Geophysics, 56, 41–49, 1991.

Thiery, R., R. Bakker, C. Monnin, ODP Leg 164 Scientific Party, Geochemistry of gas hydrates and associated fluids in the sediments of a passive continental margin, in: Gas Hydrates: Relevance to world margin stability and climate change, (ed) J.P. Henriet, and J. Mienert, London, Geological Society, 338p, 1998.

Timur, A., Velocity of compressional waves in porous media at permafrost temperature, Geophysics, 41, 621–645, 1968.

Tosaya, C., and A. Nur, Effects of diagenesis and clays on compressional velocities in rocks, Geophys. Res. Lett., 9, 5–8, 1982.

von Huene, R. and I. Pecher, Vertical tectonics and the origins of BSRs along the Peru margin, Earth Planet. Sc. Lett. 166 (1-2), 47–55, 1999 .

Walia, R., and D. Hannay, Source and receiver geometry corrections for deep towed multichannel seismic data, Geophys. Res. Letters, 26, No. 13, 1993–1996, 1999.

Warner, M., Absolute reflection coefficients from deep seismic reflections, Tectonophysics, 173, 15–23, 1990.

Westbrook, G.K. et al. (Eds.), Proceedings of the Ocean Drilling Program, Initial Report, Vol. 146 (part 1), Ocean Drilling Program, College Station, Texas, 1994.

Wood, A.B., A textbook of Sound, 578 pp. Macmillan, New York, 1941.

Wood, W.T., D.A. Lindwall, J.F. Gettrust, K.K. Sekharan, and B. Golden, Constraints on Gas or Gas Hydrate related Wipeouts in seismic data through the use of physical models, EOS, Transactions, American Geophys. Union, 81, No. 48, F639, 2000.

Wood, W.T., P.L. Stoffa, and T.H. Shipley, Quantitative detection of methane hydrate through high-resolution seismic velocity analysis, J. Geophys. Res., 99, 9681–9695, 1994.

Wyllie, M.R.J., A. R. Gregory, and G.H.F. Garnder, An experimental investigation of factors affecting elastic wave velocities in porous media, Geophysics, 23, 459–493, 1958.

Xu, W., and C. Ruppel, Predicting the occurrence, distribution, and evolution of methane gas hydrate in porous marine sediments, J. Geophys. Res., 104, 5081–5095, 1999.

Yilmaz, Ö., Seismic data processing, Society of Exploration Geophysicists, Investigations in Geophysics, No. 2, 1987.

Yilmaz, Ö., Seismic data analysis II, Processing, Inversion, and Interpretation of seismic data, Society of Exploration Geophysicists, Investigations in Geophysics, No. 10, 2001.

Yuan, T., R.D. Hyndman, G.D. Spence and B. Desmos, Seismic velocity increase and deep-sea gas hydrate concentration above a bottom-simulating reflector on the northern Cascadia continental slope, J. Geophys. Res., 101, 13665–13671, 1996.

Yuan, T., G.D. Spence, R.D. Hyndman, T.A. Minshull, and S.C. Singh, Seismic velocity studies of a gas hydrate bottom-simulating reflector on the northern Cascadia continental margin: Amplitude modeling and full waveform inversion, J. Geophys. Res., 104, 1179–1191, 1999.

Yuan, J., and R. N. Edwards, Towed seafloor electromagnetics and assesment of gas hydrate deposits, Geophysical Res. Lett., 27, 2397–2400, 2000.

Zoeppritz, R. , On the reflection and propagation of seismic waves, Erdbebenwellen VIIIB; Göttinger Nachrichten, I, 66–84, 1919.

Zühlsdorff, L., V. Spiess, C. Hübscher, and M. Breitzke, Seismic reflectivity in sediments at the eastern flank of the Juan de Fuca Ridge: Evidence for fluid migration? J. Geophys. Res., 104, 15351–15364, 1999.

Zühlsdorff, L. V. Spiess, C. Hbscher, H. Villinger and A. Rosenberger, BSR Occurrence, Near Surface Reflectivity Anomalies and Small Scale Tectonism images in a multi-frequency seismic data set from the Cascadia Accretionary Prism. Geologische Rundschau in press, 2000.

Appendix A

Array Element Localization - Theory

This section briefly presents the inverse theory that forms the basis for the AEL inversion algorithm; more complete treatments of the field can be found in Dosso and Riedel (2001).

The set of acoustic travel times $\mathbf{t}$ measured in an AEL survey can be written in general vector form as

$$\mathbf{t} = \mathbf{t}(\mathbf{m}) + \mathbf{n}. \tag{A.1}$$

In (A.1), the model $\mathbf{m}$ of unknown parameters is taken to consist of the hydrophone offsets and depths $\{x_j, z_j, j = 1, N_h\}$ and the source depth z_s. The forward mapping $\mathbf{t}(\mathbf{m})$ represents the acoustic travel times along direct and bottom-reflected ray paths between source and receivers. Finally, $\mathbf{n}$ represents the data errors (noise). The inverse problem of determining $\mathbf{m}$ from $\mathbf{t}$ is functionally nonlinear; however, a local linearization is obtained by expanding $\mathbf{t}(\mathbf{m}) = \mathbf{t}(\mathbf{m_0} + \delta\mathbf{m})$ in a Taylor series to first order about an arbitrary starting model $\mathbf{m_0}$ to yield

$$\mathbf{t} = \mathbf{t}(\mathbf{m_0}) + \mathbf{J}\,\delta\mathbf{m}, \tag{A.2}$$

where $\delta\mathbf{m}$ represents an unknown model perturbation and $\mathbf{J}$ is the Jacobian matrix consisting of the partial derivatives of the data functionals with respect to the model parameters,

$$J_{ij} = \partial t_i(\mathbf{m_0})/\partial m_j \tag{A.3}$$

Substituting $\delta\mathbf{m}=\mathbf{m}-\mathbf{m_0}$, the expansion can be written

$$\mathbf{J\,m} = \mathbf{t} - \mathbf{t}(\mathbf{m_0}) + \mathbf{J\,m_0} \equiv \mathbf{d}. \tag{A.4}$$

Equation (A.4) defines a linear inverse problem for $\mathbf{m}$ in terms of known quantities (defined as modified data $\mathbf{d}$). Since nonlinear terms are neglected in (A.4), the equations are not exact and the solution $\mathbf{m}$ may not adequately reproduce the measured data via the nonlinear forward problem. In this case, the starting model is updated, $\mathbf{m_0} \leftarrow \mathbf{m}$, and the inversion repeated iteratively until an acceptable solution is obtained.

Under the standard assumptions that the error n_i on datum t_i is due to an independent, Gaussian-distributed random process with zero mean and standard deviation σ_i, the maximum-likelihood solution of the linearized system of equations (A.4) is obtained by minimizing the χ^2 data misfit

$$\chi^2 = |\mathbf{G}\,(\mathbf{J\,m} - \mathbf{d})|^2, \tag{A.5}$$

where $\mathbf{G} = \mathrm{diag}[1/\sigma_i]$ weights the data according to their uncertainties. However, this least-squares approach is not applicable to under-determined problems, such as the AEL inversion at hand. The method of regularization provides a particularly useful approach to under-determined inversions based on explicitly including physical *a priori* information regarding the solution in the inversion. This is accomplished by minimizing an objective function ϕ which combines the χ^2 misfit with a regularizing

term that imposes the *a priori* expectation that the model $\mathbf{m}$ resembles a prior estimate $\hat{\mathbf{m}}$:

$$\phi = |\mathbf{G}(\mathbf{J}\mathbf{m} - \mathbf{d})|^2 + \mu |\mathbf{H}(\mathbf{m} - \hat{\mathbf{m}})|^2, \tag{A.6}$$

where $\mathbf{H}$ is the regularization matrix (described below), and μ is a trade-off parameter controlling the relative importance assigned to the data misfit and the *a priori* expectation in the minimization. Minimizing ϕ with respect to $\mathbf{m}$, the regularized solution is

$$\mathbf{m} = \hat{\mathbf{m}} + \left[\mathbf{J}^T\mathbf{G}^T\mathbf{G}\,\mathbf{J} + \mu\,\mathbf{H}^T\mathbf{H}\right]^{-1}\left[\mathbf{J}^T\,\mathbf{G}^T\mathbf{G}\,\mathbf{d} - \mathbf{J}\hat{\mathbf{m}}\right]. \tag{A.7}$$

The regularization matrix $\mathbf{H}$ in (A.6) and (A.7) controls the form of the *a priori* information applied in the inversion. For instance, if prior model parameter estimates $\hat{\mathbf{m}}$ are available, an appropriate regularization is given by

$$\mathbf{H} = \text{diag}[1/\xi_j], \tag{A.8}$$

where ξ_j represents the uncertainty for jth parameter estimate $\hat{m}_j$. An alternative form of regularization is to apply *a priori* information to derivatives of the model parameters. For instance, if the *a priori* expectation is that the parameters in $\mathbf{m}$ are well approximated by a smooth function of an independent variable u (with $m_j = m(u_j)$), then an appropriate choice is $\hat{\mathbf{m}} = \mathbf{0}$ and $\mathbf{H}$ consisting of the tridiagonal matrix with non-zero entries on jth row given by

$$\mathbf{H} = \text{tridiag}\left[\frac{-1}{(u_{j+1} - u_j)^2},\ \frac{u_{j+2} - u_j}{(u_{j+2} - u_{j+1})(u_{j+1} - u_j)^2},\ \frac{-1}{(u_{j+2} - u_{j+1})(u_{j+1} - u_j)}\right]. \tag{A.9}$$

Each row of $\mathbf{H}$ in (A.9) represents a discrete approximation to the second derivative operator $\partial^2/\partial u^2$. Hence, $|\mathbf{Hm}|^2$ provides a measure of the total curvature or roughness of the model. Applying this regularization minimizes the model roughness, producing the smoothest model. For either form of regularization, the trade-off parameter μ is chosen so that the χ^2 data misfit achieves its expected value of $\langle\chi^2\rangle = N$ for N data, thereby applying the *a priori* information subject to ensuring that the data are fit to a statistically appropriate level.

The AEL inversion formulated here for marine seismic arrays applies both types of *a priori* information described above. In particular, prior parameter estimates are available for the source depth and for the depth of the hydrophones adjacent to the depth sensors. The expectation that the towed array shape is smooth can be applied by minimizing the 2-D curvature. To apply simultaneously two different types of *a priori* information, an augmented objective function can be formed which includes two regularization terms

$$\phi = |\mathbf{G}(\mathbf{J}\,\mathbf{m} - \mathbf{d})|^2 + \mu_1 |\mathbf{H}_1(\mathbf{m} - \hat{\mathbf{m}}_1)|^2 + \mu_2 |\mathbf{H}_2(\mathbf{m} - \hat{\mathbf{m}}_2)|^2. \tag{A.10}$$

In (A.10), the first regularization term is taken to represent the *a priori* parameter estimates for the depth of the source and hydrophones at the depth sensors. Hence, $\hat{\mathbf{m}}_1$ consists of the prior estimates for these parameters, with zeros for the remaining parameters. The regularization matrix $\mathbf{H}_1$ is of the form of (A.8) with diagonal elements consisting of the reciprocal of the estimated uncertainty for parameters with prior estimates, and zeros for the remaining parameters. The second regularization term is taken to represent the *a priori* expectation of a smooth array shape. Hence, $\hat{\mathbf{m}}_2$ is taken to be zero, and $\mathbf{H}_2$ is of the form of (A.9) for the hydrophone position parameters, with the independent variable u in (A.9) taken to be the nominal hydrophone offsets. Rows of zeros are included in $\mathbf{H}_2$ at appropriate locations to

separate the measures of curvature in x and z. In this case, minimizing (A.10) leads to

$$\mathbf{m} = \hat{\mathbf{m}}_1 + \left[\mathbf{J}^T\mathbf{G}^T\mathbf{G}\,\mathbf{J} + \mu_1\,\mathbf{H}_1^T\mathbf{H}_1 + \mu_2\,\mathbf{H}_2^T\mathbf{H}_2\right]^{-1}\left[\mathbf{J}^T\,\mathbf{G}^T\mathbf{G}\,\mathbf{d} - \mathbf{J}\hat{\mathbf{m}}_1\right]. \quad \text{(A.11)}$$

The AEL inversion algorithm consists of an iterative application of (A.11), initiated from an arbitrary starting model. Convergence of the algorithm is based on: (i) obtaining a misfit to the measured data of $\chi^2 = N$, and (ii) obtaining a stable solution such that the rms (root-mean-square) change in the sensor positions between iterations is less than 0.1 m. Regarding the first criterion, note that although (A.11) is derived based on the χ^2 misfit for the linear inverse problem (A.4) that approximates the nonlinear problem (A.1) at each iteration, the convergence of the inversion algorithm must be judged in terms of the nonlinear misfit

$$\chi^2 = |\mathbf{G}(\mathbf{t}(\mathbf{m}) - \mathbf{t})|^2. \quad \text{(A.12)}$$

The most subtle aspect of implementing the inversion involves assigning values to the two trade-off parameters, μ_1 and μ_2, which control the balance between the data misfit and the two forms of *a priori* information. An effective procedure (Dosso *et al.*, 1998) is to set

$$\mu_2 = \beta\,\mu_1 \quad \text{(A.13)}$$

for a fixed value of β, and determine the value of μ_1 at each iteration which yields the desired χ^2 misfit. The parameter β provides a relative weighting between fitting the prior estimates (emphasized with small β) and achieving a smooth model (emphasized

with large β). The final model obtained from this procedure can then be examined to ascertain whether the value of β was appropriate based on the parameter misfit associated with the *a priori* estimates, defined by

$$\hat{\chi}^2 = |\mathbf{H}_1(\mathbf{m} - \hat{\mathbf{m}}_1)|^2. \tag{A.14}$$

To fit the prior estimates to a statistically meaningful level requires $\hat{\chi}^2 \approx \hat{N}$, where $\hat{N}$ is the number of model parameters with *a priori* estimates. If $\hat{\chi}^2 \ll \hat{N}$ for a model $\mathbf{m}$ constructed according to (A.11), then the prior information is fit more closely than is reasonable statistically, and a larger value of β is required to reduce the relative weighting of the prior information. Conversely, if $\hat{\chi}^2 \gg \hat{N}$, the prior information is not fit closely enough, and a smaller value of β is required to increase the weighting of the prior information. The inversion can be repeated with a new value of β until $\hat{\chi}^2 \approx \hat{N}$ is achieved. In practice, determining an appropriate value for β is a straightforward procedure, typically requiring two or three trial inversions for a particular problem. The value of β usually remains constant when inverting successive data sets with similar uncertainties; hence, the algorithm is appropriate for batch processing.

The above procedure reduces the problem of determining two trade-off parameters to a 1-D search for the parameter μ_1. The parameter μ_1 is chosen so that χ^2 is reduced by a controlled amount (e.g., a factor of 5) at each iteration until $\chi^2 = N$ is achieved. Controlling the reduction in χ^2 limits the change in the model at each iteration, which helps ensure that the linearization is valid and stabilizes the convergence. In practice, it is straightforward to determine the value of μ_1 which produces the desired χ^2 at a given iteration since χ^2 increases monotonically with μ_1 (this is evident from the minimization of (A.10) in which μ_1 weights the prior information at the expense of the χ^2 misfit; alternatively, it can be proved that $\partial\chi^2/\partial\mu_1$ is inherently positive (Collison and Dosso, 2000)). At early iterations an approximate value for $\mu_1$is sufficient, and

a bisection algorithm is employed. Near convergence, Newton's method is used for greater precision.

Appendix B

Geometry Definition in ITA/Insight

A typical file containing the command lines for the seismic processing in ITA/Insight is given below. For each shot gather shot point number (word 26), coordinates (UTM, WGS-84) for source easting (word 31) and northing (word 29) are defined globally. After that, each trace in that shot gather is updated based on the results of the AEL inversion. The ITA command file contains the following lines:

```
open 1 1 'il02_ael.dat'
getr 1 0
shed 31r 1 101 1 658221 0 'r'
shed 29r 1 101 1 5388394 0 'r'
shed 26r 1 101 1 500000 0 'r'
shed 3i 1 1 1 501500 0 't'
shed 37r 1 1 1 658305 0 't'
shed 35r 1 1 1 5388282 0 't'
shed 27r 1 1 1 503000 0 't'
shed 43r 1 1 1 658263 0 't'
shed 41r 1 1 1 0 0 't'
shed 49r 1 1 1 658263 0 't'
shed 47r 1 1 1 0 0 't'
shed 53r 1 1 1 139 0 't'
shed 28 1 1 1 300 0 't'
shed 33r 1 1 1 0 0 't'
shed 39r 1 1 1 -25 0 't'
```

```
shed 20r 1 1 1 0.0167 0 't'
shed 3i 2 2 1 501550 0 't'
shed 37r 2 2 1 658308 0 't'
shed 35r 2 2 1 5388278 0 't'
shed 27r 2 2 1 503100 0 't'
etc.
putb 1 0
etc.
clos 1 1
end
```

Header word	Type	Definition
26	I4	Shot point number
29	R8	Source northing
31	R8	Source easting
3	I4	CMP number
20	R4	Elevation static shift [ms]
27	I4	Receiver point (station identifier)
28	I4	Receiver offset in stations [m]
33	R8	Source elevation [m]
35	R8	Receiver northing [m]
37	R8	Receiver easting [m]
39	R8	Receiver elevation ore depth bsf [m]
41	R8	CDP northing [m]
43	R8	CDP easting [m]
47	R8	CMP northing (here equal header 41)
49	R8	CMP easting (here equal header 43)
53	R4	source to receiver distance (offset) [m]

Table B.1 Header words updated in geometry definition.

Appendix C

ITA-Insight Programs for Seismic Data Processing

After depth and offset information of each receiver in the entire line have been defined via AEL and incorporated into the appropriate header words, seismic processing can be applied to the data.

The following is a typical ITA command file for inline 2 for the **pre-stack** processing part:

```
open 1 1 'il02_ael.dat'
open 2 2 'il02_proc.dat'
COMM DO FIRST PROCESSING IN SHOT DOMAIN
bsec 1000
getr 1 0
tscl 1.0
gsft 20
shft 1 21 0
sft 1 101 -0.0186
band 10 20 160 200
gapd 0.01 0.5 0.1
band 20 30 160 200
putr 2 0
esec
clos 1 1
clos 2 2
COMM WRITE CDPS
```

```
open 1 1 'il02_proc.dat'
open 2 2 'il02_proc_cdp.dat'
srti 1 3 1 5000000 1 587 'r'
wsrt 'il02ael.srt'
bsec 50000
gets 1 0 1 101 0.0 5.0
putr 2 0 1 101 0.0 5.0
esec
clos 1 1
clos 2 2
COMM DO TRIM STATIC WITH SEAWATER VELOCITY
open 1 1 'il02_proc_cdp.dat'
open 2 2 'il02_trim.dat'
onmo 1 'watervelocity.vel'
bsec 1000000
getr 1 0
nmo2 1
trim 1.50 2.10 0.005
trim 1.50 2.10 0.004
trim 1.50 2.10 0.002
unm2 3 1 100 1
putr 2 0
esec
clos 1 1
clos 2 2
COMM DO SEMBLANCE ANALYSIS
open 1 1 'il02_trim.dat'
open 2 2 'il02_trim_hvf.smb'
```

```
COMM create super gather of 6 cdps
bsec 270
getg 1 0 1 6 0 5.0
srtm 53 1 20000
strh
hvf 220 60 400 3 1
slns 0.0 0.0 0 4 0 0
agc 2 0.2
putr 2 0
vsmb 1200.0 1900.0 1300.0 2200.0 110 110 0.025 0.9
putr 2 0
skip 1 20 'r'
esec
clos 1 1
clos 2 2
end
```

A typical **post-stack** processing file contains the following command lines:

```
open 1 1 'il02_proc_cdp.dat'
open 2 2 'il02_trimnew.stk'
onmo 1 'il02_newfinal.vel'
bsec 1000000
getr 1 0
strh
hvf 220 60 400 3 1
slns 0.0 0.0 0 4 0 0
selo 1 140.0 440.0
nmo2 1
trim 1.60 2.10 0.004
trim 1.60 2.10 0.004
stak
pack 0 0
putr 2 0
esec
clos 1 1
clos 2 2
end
```

Appendix D

Fast Phase-shift Migration in ITA

il02_trimnew.stk	! file1
il02_psfast3.mig	! file2
il02_newfinal.vel	! file3
267100 504600	! tr1,tr2
3	! icount
3.0	! Tmax
3000	! Zmax
2.01	! dx
0.25	! FRQcomp
90.0	! APERmx
2	! FRQcount
0.0 20.0 180.0	! FRQtim,FRQlow,FRQhigh
3.0 20.0 180.0	! FRQtim,FRQlow,FRQhigh
1	! Vtype
-1000	! CDP
1000 8000	! Vmin,Vmax
100.0	! Vprc
50	! VERTsmooth

Definitions:

file1: data file (stacked) to be input to migration job

file2: data file (migrated) to be output from migration job

file3: input velocity file standard ITA (ASCII) format

tr1,tr2: trace window of input and output icount: header word for specifying "tr1" and "tr2" (3 := CDP)

Tmax: maximum time to migrate in seconds

Zmax: maximum depth for migration (same system of units as velocity)

dx: interval between CDP's (same system of units as velocity)

FRQcomp: compensation factor for high-frequency attenuation caused by migration

APERmx: maximum allowable migration aperture in degrees

FRQcount: number of time-frequency definitions (min=1, max=10)

FRQtim: 2-way time when frequency definition applies

FRQlow: minimum frequency to migrate at FRQtim

FRQhigh: minimum frequency to migrate at FRQtim

Vtype: type of input velocity file

CDP: use velocity function from this CDP

Vmin,Vmax: minimum and maximum allowable INTERVAL velocities

Vprc: scale velocities by this percentage for migration

VERTsmooth: VERTICAL smoothing factor (RANGE is 0 to 100)

Appendix E

Modeling Elastic Properties of Hydrate-bearing Sediments

Rock-physic models are used in this study to predict the elastic properties of hydrate-bearing sediments. The general model for the elastic physical properties of water-saturated marine sediments is based on the *baseline model* by Dvorkin *et al.* (1999b). This model relates the elastic properties of the sediment to porosity, mineralogy and effective pressure (depth). A detailed description of the models and their original concepts can be found in Helgerud (2000).

E.1 The Baseline Model for Water-saturated Sediments

The effective bulk (K_{HM}) and shear moduli (G_{HM}) of the dry rock frame at the critical porosity (ϕ_c) can be calculated from the Hertz-Mindlin theory (Mindlin, 1949):

$$K_{HM} = \left[\frac{n^2(1-\phi_c)^2G^2}{18\pi^2(1-\nu)^2}P_{eff}\right]^{\frac{1}{3}}, \tag{E.1}$$

$$G_{HM} = \frac{5-4\nu}{5(2-\nu)}\left[\frac{3n^2(1-\phi_c)^2G^2}{2\pi^2(1-\nu)^2}P_{eff}\right]^{\frac{1}{3}}. \tag{E.2}$$

The effective pressure P_{eff} is the difference between the lithostatic and hydrostatic pressure at depth D and is given by:

$$P_{eff} = Dg(\rho_{bulk} - \rho_w), \tag{E.3}$$

where ρ_{bulk} is the bulk density of the sediment, ρ_w is the water density, and g is the acceleration due to gravity. The average number of grain contacts n is set to 9 for all calculations performed within this study.

The value ν can be calculated from the solid phase bulk (K) and shear (G) moduli:

$$\nu = \frac{3K - 2G}{2(3K + G)}. \tag{E.4}$$

The solid phase bulk (K) and shear (G) moduli for mixed mineralogy can be calculated using Hill's (1952) average formula:

$$\begin{aligned} K &= 0.5 \left[\sum_{i=1}^{m} f_i K_i + \left(\sum_{i=1}^{m} \frac{f_i}{K_i} \right)^{-1} \right], \\ G &= 0.5 \left[\sum_{i=1}^{m} f_i G_i + \left(\sum_{i=1}^{m} \frac{f_i}{G_i} \right)^{-1} \right], \end{aligned} \tag{E.5}$$

where m is the number of mineral constituents and f_i is the volumetric fraction of the i-th constituent of the solid phase. K_i and G_i are the bulk and shear modulus of the i-th constituent respectively. The solid phase density (ρ_{solid}) can be calculated using:

$$\rho_{solid} = \sum_{i=1}^{m} f_i \rho_i, \tag{E.6}$$

where ρ_i is the density of the i-th constituent.

If porosities are above the critical porosity, the dry rock bulk K_{dry} and shear G_{dry} moduli can be calculated by:

$$K_{dry} = \left[\frac{\frac{1-\phi}{1-\phi_c}}{K_{HM} + \frac{4}{3} G_{HM}} + \frac{\frac{\phi - \phi_c}{1-\phi_c}}{\frac{4}{3} G_{HM}} \right]^{-1} - \frac{4}{3} G_{HM}, \tag{E.7}$$

$$G_{dry} = \left[\frac{\frac{1-\phi}{1-\phi_c}}{G_{HM} + Z} + \frac{\frac{\phi - \phi_c}{1-\phi_c}}{Z} \right]^{-1} - Z, \tag{E.8}$$

$$Z = \frac{G_{HM}}{6} \left(\frac{9K_{HM} + 8G_{HM}}{K_{HM} + 2G_{HM}} \right).$$

If the sediment is saturated with a pore fluid of bulk modulus K_f, the bulk and shear moduli of the saturated sediments (K_{sat} and G_{sat}) can be calculated from Gassmann's equations (1951) as:

$$K_{sat} = K\frac{\phi K_{dry} - (1-\phi)K_f K_{dry}/K + K_f}{(1-\phi)K_f + \phi K - K_f K_{dry}/K}, \tag{E.9}$$

and

$$G_{sat} = G_{dry}. \tag{E.10}$$

With all elastic moduli known, the elastic wave speeds can now be calculated from:

$$V_p = \sqrt{\frac{K_{sat} + \frac{4}{3}G_{sat}}{\rho_{bulk}}}, \tag{E.11}$$

$$V_s = \sqrt{\frac{G_{sat}}{\rho_{bulk}}}, \tag{E.12}$$

with the bulk density ρ_{bulk} given as:

$$\rho_{bulk} = \phi\rho_w + (1-\phi)\rho_{solid}. \tag{E.13}$$

E.2 Hydrate Formation in the Pore Fluid

If gas hydrate forms in the pore space such that it is suspended in the pore fluid, it affects the elastic moduli of the pore fluid and the density only. The dry frame moduli are unchanged. If the volumetric concentration of gas hydrate in the pore space is given by S_h, the effective bulk modulus of the mixed pore fluid $\bar{K}_f$ can be calculated using the Reuss (1929) isostress average of the water (K_w) and gas hydrate (K_h) bulk moduli:

$$\bar{K}_f = \left[\frac{S_h}{K_h} + \frac{1-S_h}{K_w}\right]^{-1}. \tag{E.14}$$

E.3 Hydrate Formation in the Frame

If gas hydrate forms as part of the frame acting as a sediment grain, the original calculations for the dry sediment have to be redone. The presence of the hydrate reduces the original sediment porosity (ϕ) to a new value $\bar{\phi}$ as:

$$\bar{\phi} = \phi - S_h. \tag{E.15}$$

The effective mineral modulus of the gas hydrate/sediment mixture is calculated from (E.5) by replacing f_i by:

$$\bar{f}_i = f_i \frac{1-\phi}{1-\bar{\phi}}. \tag{E.16}$$

The gas hydrate is treated as additional mineral grain with

$$\bar{f}_h = \frac{S_h}{1-\bar{\phi}}. \tag{E.17}$$

E.4 Sediments With Free Gas

The presence of gas in the pore fluid is treated equivalently to the *hydrate-in-pore-space* model. Here the bulk modulus of the pore fluid ($\bar{K}_f$) is the Reuss isostress average of the water (K_w) and gas (K_g) bulk moduli for a water saturation S_w:

$$\bar{K}_f = \left[\frac{S_w}{K_w} + \frac{1-S_w}{K_g} \right]^{-1}. \tag{E.18}$$

The new bulk density is given by:

$$\rho_{bulk} = \phi(S_w \rho_w + (1-S_w)\rho_g) + (1-\phi)\rho_{solid}, \tag{E.19}$$

where ρ_w, ρ_g, and ρ_{solid} are the densities of the water, gas and the solid phases, respectively.

E.5 Cementation Model by Dvorkin and Nur (1993)

This model is valid for granular material of porosities from 30–40 %. Mechanical interaction between sediment grains takes place through the solid phase gas hydrate cement. A complete explanation of the different models and their limitations can be found in Ecker *et al.* (1998). However, this paper does contain several typos in the equations, which are corrected in the following set of equations.

The effective dry elastic moduli of hydrated sediments are given by:

$$K_{eff} = \frac{n(1-\phi_0)}{6}\left(K_h + \frac{4}{3}G_h\right)S_n, \tag{E.20}$$

$$G_{eff} = \frac{3}{5}K_{eff} + \frac{3n(1-\phi_0)}{20}G_h S_\tau, \tag{E.21}$$

where K_{eff} and G_{eff} are the dry-rock bulk and shear moduli, respectively; K_h and G_h are the bulk and shear moduli of the hydrate and ϕ_0 is the porosity of the sediment before gas hydrate formation. S_n and S_τ are proportional to the normal and shear stiffness of a cemented two-grain combination and depend on the amount of hydrate and on the grain and pure hydrate elastic moduli:

$$S_n = A_n\eta^2 + B_n\eta + C_n, \tag{E.22}$$

with

$$A_n = -0.024153 \cdot \Lambda_n^{-1.3646},$$

$$B_n = 0.20405 \cdot \Lambda_n^{-0.89008},$$

$$C_n = 0.00024649 \cdot \Lambda_n^{-1.9864}.$$

$$S_\tau = A_\tau \eta^2 + B_\tau \eta + C_\tau, \tag{E.23}$$

with

$$A_\tau = -0.1 \cdot (2.26\nu^2 + 2.07\nu + 2.3) \cdot \Lambda_\tau^{0.079\nu^2+0.1754\nu-1.342},$$

$$B_\tau = (0.0573\nu^2 + 0.0937\nu + 0.202) \cdot \Lambda_\tau^{0.0274\nu^2+0.0529\nu-0.8765},$$

$$C_\tau = 0.001 \cdot (9.654\nu^2 + 4.945\nu + 3.1) \cdot \Lambda_\tau^{0.01867\nu^2+0.4011\nu-1.8186}.$$

$$\Lambda_n = \frac{2G_h}{\pi G}\frac{(1-\nu)(1-\nu_h)}{(1-2\nu_h)} \qquad \Lambda_\tau = \frac{G_h}{\pi G} \qquad \eta = \frac{a}{R} \tag{E.24}$$

where ν and G are the grain Poisson's ratio and shear modulus, respectively and ν_h is the pure hydrate poisson's ratio. The parameter η is the ratio of the cemented contact radius to the grain radius. It depends on the hydrate saturation (S) of the pore space and can be calculated as follows if all hydrate is deposited at the grain contacts:

$$\eta = 2\left(\frac{S\phi_0}{3n(1-\phi_0)}\right)^{0.25}. \tag{E.25}$$

If the hydrate is deposited as evenly envelop-cemet, the factor η is given by:

$$\eta = \left(\frac{2S\phi_0}{3(1-\phi_0)}\right)^{0.5} \tag{E.26}$$

The elastic wave velocities are calculated using equations (E.11) and (E.12) using the saturated bulk and shear moduli as given by equations (E.9) and (E.10). In the case of the contact-cement theory, the hydrate is part of the solid phase. The solid bulk modulus needed for Gassmann's equations is given by the Reuss average (E.5).

Appendix F

List of Abbreviations

Abbreviations	Explanation
ACF	Auto Correlation Function
AEL	Array Element Localization
AGC	Automatic Gain Control
AVO	Amplitude-Versus-Offset
BSR	Bottom Simulating Reflector
bsf	Bbelow seafloor
BWT	Bottom Water Temperature
CDP	Common Depth Point
CMP	Common Mid Point
COAMS	Canadian Ocean Acoustic Measurement System
DNS	Depth of no Sulfate
DTAGS	Deep-Towed Acoustic-Geophysics System
GPS	Global Positiong System

Abbreviations	Explanation
MC	Multichannel
MCS	Multichannel Seismics
NMO	Normal Moveout
OBS	Ocean Bottom Seismometer
ODP	Ocean Drilling Program
RMS	Root-Mean-Square
SCMP	Super-Common Mid Point
SC	Single-channel
SCS	Single Channel Seismics
TWT	Two-way Traveltime
VAVO	Viscoelastic Amplitude-Versus-Offset
VIM	Vibration Insolation Module
VSP	Vertical Seismic Profiling